CHARACTERIZATION OF CRACKS ON ULTRA THIN CONTINUOUSLY REINFORCED CONCRETE PAVEMENTS

by

Johan Andries Kritzinger Gerber

*Thesis presented in partial fulfilment of the requirements for
the degree Master of Science in Engineering
at the University of Stellenbosch*

Supervisor: Prof. Kim Jenkins
Faculty of Engineering
Department of Civil Engineering

March 2011

DECLARATION

By submitting this dissertation electronically, I declare that the entirety of the work contained therein is my own, original work, that I am the owner of the copyright thereof (unless to the extent explicitly otherwise stated) and that I have not previously in its entirety or in part submitted it for obtaining any qualification.

Signature: ……………………………………

Name: Johan Andries Kritzinger Gerber

Date: ……………………………………

ABSTRACT

The southbound screener lane of the Heidelberg Traffic Control Centre received structural improvements by means of an ultra thin continuously reinforced concrete pavement (UTCRCP) overlay. This experimental overlay forms part of the South African National Roads Agency Limited's innovative highway repair strategy on existing pavements that have exceeded design life. The primary objective of this study was to characterize the UTCRCP overlay with regard to crack spacing formation under accelerated pavement testing (APT).

Characterization comprised of empirical modelling techniques, statistical analysis, non destructive testing and software simulations. Pavement deflection responses were empirically and linear elastically converted to input parameters. These parameters were used in the mean crack spacing prediction model of the Mechanistic-Empirical Pavement Design Guide (M-E PDG). Observed cracking under APT was recorded and analyzed by means of descriptive statistics. The outcome of the M-E PDG's mean crack spacing and the statistics of the observed cracking were evaluated against cncPave simulations.

Initial shrinkage crack formations ranged from 500 mm to 900 mm, with a mean spacing of 695 mm. Subsequent secondary cracking reduced the segments, delineated by initial cracking, to intervals consisting of 100 mm to 350 mm. A statistical analysis of the observed cracking indicated that traffic had little effect on the transverse crack spacing formation. The observed cracks yielded a mean spacing of 296 mm, compared to the 186 mm of the M-E PDG mean crack spacing calculation. cncPave simulations indicated that the expected range of cracking would fall between 237 mm and 350 mm with a probability of 50% that crack spacing would exceed 265 mm. The 50th percentile of the observed cracks resulted in a spacing of 233 mm. The APT project was limited to a single test section. No pavement failures occurred during the APT project. A total of 2.8 million 80 kN load repetitions were applied to the UTCRCP. However circular crack formations regarded as a punchout development have formed on the UTCRCP test section.

Circular cracks formed around weaknesses in the pavement system. The prediction of these punchout formations incorporates the mean crack spacing result. Occurrence of mean crack spacing forms part of a crack spacing distribution defined by a range. Therefore designing a punchout prediction model for UTCRCP should include the characteristics and range of the crack pattern and not merely the mean crack spacing value.

Key Words: UTCRCP, APT, Mean Crack Spacing, Punchout, Descriptive Statistics, cncPave, M-E PDG, Transverse Cracks, Dense Liquid Foundation, Elastic Solid Foundation.

SAMEVATTING

Die suidwaartse moniteerings laan van die Heidelberg Verkeersbeheer Sentrum, het strukturele verbetering ondergaan deur die konstruksie van 'n ultradun aaneen-gewapende betonplaveisel (UDAGBP) wat dien as 'n deklaag. Hierdie eksperimentele deklaag is deel van die Suid-Afrikaanse Nasionale Paaie Aggentskap Beperk (SANRAL) se vernuftige deurpadherstelstrategie vir bestaande deurpaaie waarvan die ontwerplewe verstryk het. Die primêre doel van hierdie studie is om die UDAGBP te karakteriseer, met betrekking tot kraakspasiëring, deur middel van Versnelde Plaveisel Toetsing (VPT).

Die karakteriseringsproses het bestaan uit empiriese moduleringstegnieke, statistiese ontleding, nie-destruktiewe toetsmetodologieë en sagtewaresimulasies. Die plaveisel-defleksiegedrag is empiries en liniêr elasties ontleed en omgeskakel na invoerparameters. Hierdie parameters is gebruik in die peilingsmodel vir gemiddelde kraakspasiëring van die Meganisties-Empiries Plaveisel Ontwerpsgids (M-E POG). Waargenome kraakspasiëring na die afloop van VPT is opgeteken en deur middel van beskrywende statistiek ontleed. Die resultate van die M-E POG se gemiddelde kraakspasiëring en die statistiese ontleding van die waargenome krake is geëvalueer teenoor cncPave simulasies.

Aanvanklike krimpingskrake het gevorm met wisselende kraakspasiëring tussen 500 mm en 900 mm met 'n gemiddelde spasiëring van 695 mm. Daaropvolgende krake het die aanvanklike segmente, wat gevorm het tydens die aanvanklike krimpingskrake, verkort na intervalle van 100 mm tot 350 mm. 'n Statistiese ontleding van die waargeneemde krake het aangedui dat verkeer weinig 'n aandeel het in die dwarskraak-vormingsproses. Die waargenome krake het 'n gemiddelde spasiëring van 296 mm in vergelyking met 186 mm van die M-E POG se gemiddelde kraakspasiëring berekening. cncPave simulasies het aangedui dat die verwagte kraakspasiëringsgrense tussen 237 mm en 350 mm is en 'n 50% waarskynlikheid dat die kraakspasiëring meer as 265 mm is. Die VPT projek is beperk tot 'n enkele toetsseksie. Geen plaveiselfalings is waargeneem gedurende die VPT projek nie. In totaal was 2.8 miljoen as-lasherhalings aangewend op die UDAGBP. Daar het egeter sirkelvormige kraakformasies, wat beskou word as ponsswigting, ontwikkel op die UDAGBP toetsseksie.

Sirkelvormige kraakpatrone het gevorm rondom swak plekke in die plaveisel. Die peilingsmodelle van hierdie ponsswigting maak gebruik van die gimiddelde kraakspasiëringsresultaat. Die verskynsel van gemiddelde kraakspasiëring in hierdie studie is deel van 'n kraakspasiëringsverdeling, gedefinieerd deur 'n spasiëringsgrens. Daarom moet die kraakspasiëringskarakteristieke en spasiëringsgrense in ag geneem word in die

ontwerpsproses van 'n UDAGBP ponsswigting-peilings-model, nie slegs die waarde van die gemiddelde kraakspasiëring nie.

Sleutel woorde: UDAGBP, VPT, Gemiddelde Kraakspasiëring, Ponsswigting, Beskrywende Statistiek, cncPave, M-E POG, Transversale Krake, Digte Vloeistof Fondasie, Elasties-Soliede Fondasie.

ACKNOWLEDGEMENTS

CONTENTS

LIST OF FIGURES

LIST OF TABLES

NOMENCLATURE

AC   Asphalt Concrete (asphalt)

APT   Accelerated Pavement Testing

ASB   Aggregate Subbase

BAM   Bituminous Aggregate Material

CL   Centre Line

COV   Coefficient of Variation

CRCP   Continuously Reinforced Concrete Pavement

CSIR   Council for Scientific and Industrial Research (in South Africa)

CTE   Coefficient of Thermal Expansion

DL   Dense Liquid

E-I   Echo-Impact

ES   Elastic Solid

FAT   Field Acceptance Test

FHWA   Federal Highway Administration

FWD   Falling Weight Deflectometer

HPC   High Performance Concrete

JDMD   Joint Deflection Measurement Device

KS   Kolmogorov-Smirnov (test)

LIM   Linear Induction Motor

LTE   Load Transfer Efficiency

LTPP   Long Term Performance Phase

LVDT	Linear Variable Differential Transducer
M-E	Mechanistic-Empirical
M-E PDG	Mechanistic-Empirical Pavement Design Guide (American)
MDD	Multi Depth Deflectometer
MMPDM	Mozambique Mechanistic Pavement Design Method
MLS 66	Mobile Load Simulator 66
MOR	Modulus of Rupture
NCHRP	National Cooperative Highway Research Program
NDT	Non Destructive Testing
PCC	Portland Cement Concrete
PDF	Probability Density Function
SANRAL	South African National Roads Agency Limited
SAPDM	South African Pavement Design Method
SAWS	South African Weather Serves
SRT	Specialised Road Technologies Pty Ltd
STPP	Short Term Performance Phase
TCC	Traffic Control Centre
TPB	Three Point Bending (test)
USB	Universal Serial Buss
USW	Ultrasonic Surface Wave
UTCRCP	Ultra Thin Continuously Reinforced Concrete Pavement
UTHRHPC	Ultra Thin Heavy Reinforced High Performance Concrete

1   INTRODUCTION

1.1   Development of the UTCRCP Concept

With approximately 70 percent of the South African road network surpassing its 20-year design life a need for cost effective structural improvement exists (Kannemeyer, et al. 2007). An ultra thin continuously reinforced concrete pavement (UTCRCP) or sometimes referred to as ultra thin heavy reinforced high performance concrete (UTHRHPC) is an innovative highway repair strategy proposed by the South African National Roads Agency Ltd. (SANRAL). UTHRHPC is a composite material that consists of ultra high performance concrete, fibres, steel reinforcement and additional materials. The UTHRHPC mix achieved good fatigue resistance under continuous high loads and research findings were presented at the 5th International CROW workshop in Istanbul (Buitelaar 2004). UTHRHPC had successfully been accepted into practice in European countries as a rehabilitation measure on steel bridge decks (Kannemeyer, et al. 2008).

The UTHRHPC concept was further explored in South Africa. SANRAL constructed two experimental short term performance phase (STPP) test sections in 2007 at the Heidelberg Traffic Control Centre (TCC). The two experimental test sections were constructed directly on top of natural gravel, cement treated materials and asphalt. The objective was to evaluate the performance of UTCRCP as a pavement layer under accelerated pavement testing (APT) (Kannemeyer, et al. 2007).

Two long term performance phase (LTPP) UTCRCP sections were also constructed at the Heidelberg TCC. These two LTPP sections were constructed as overlays on the existing asphalt (AC) layers that formed part of the exiting screener lanes (on ramps) onto the N3 at the Heidelberg TCC. The Heidelberg TCC, being a weigh bridge facility, could provide accurate measurements for the number of heavy vehicle axle passes and corresponding loads exerted on the LTPP sections.

UTCRCP being a state of the practice overlay methodology and the first of its kind in the world; implies that there is limited knowledge upon the characteristics of this rigid layer. The data assembled at the Heidelberg TCC STPP and LTPP sections were incorporated in the Cement and Concrete Institute of South Africa's rigid pavement design program cncPave. However to increase accuracy of the cncPave predictions regarding UTCRCP the theory must agree with reality. Therefore continuous updates are made to cncPave as new characteristics of UTCRCP are exposed and validated.

Currently the South African Pavement Design Method (SAPDM) is being revised. The majority of the South African road network consists of flexible pavements; accordingly concrete pavements are not included in the current research and development. As a result the South African industry has to rely on software such as cncPave for rigid pavement design.

1.2 Description of the Problem

After the construction of the UTCRCP layer, two different types of transverse cracking formations develop. The first type is environmentally associated transverse cracking which is primarily assigned to various thermal related activities in the pavement. Traffic induced cracking is the second type of transverse cracking to form. Initially the transverse cracks are held together by the high amount of steel reinforcement and fibres in the concrete mix. Absence of transverse contraction joints and a well defined pattern of transverse cracks are the major attributes that identify CRCPs (Selezneva, et al. 2002).

A failure phenomenon that occurs between closely spaced transverse cracks on CRCP is typically identified as structural punchout or punchout distress. The efficiency by which traffic loads are transferred across the closely spaced transverse cracks, reduces as the aggregate interlock in the cracks deteriorate due to a repetition of traffic loads. Loss of support along the pavement edge, due to base erosion and negative temperature gradients through the slab thickness, further magnify bending stresses. Passages of heavy axles causing repetitive cycles of excessive tensile bending stresses, leads to longitudinal fatigue cracking. The longitudinal crack isolates a part of the pavement to form a segment which defines the punchout (ARA, Inc., ERES Division 2003).This results in a loss of riding quality and potential hazardous driving conditions. Therefore accurate prediction of punchout distress is desirable not only for safety reasons, but also from a design perspective. The punchout distress phenomenon influences the estimated life of the pavement and the period prior to necessary maintenance. These factors are integrated with financial implications thus defying the purpose of cost effective structural improvement.

The problem that needs to be addressed is the identification of the characteristics pertaining to the spatial formation of UTCRCP transverse cracks. Transverse cracking characteristics is an important design parameter that influences load transfer efficiency, crack width, and crack spacing predictions. Proper characterization lends itself towards more accurate modelling procedures with regard to punchout distress. The facets included in the

characterization process vary, but the more important aspects are geometric and material properties of the UTCRCP, modelling techniques and observed UTCRCP cracking.

Previously a study was carried out on the characterization of spatial variability of transverse cracking on CRCP by Selezneva, et al. 2002. Good validation of methods used in the analysis process was presented in this study. The study concluded that the characteristics of transverse crack spacing contributed to the process of pavement deterioration and should be included in the prediction models of CRCP punchout distress. Consequently CRCPs are much thicker pavements than UTCRCPs and differ in mix composition, therefore CRCPs respond differently, hence having different cracking characteristics.

A more recent study conducted by Kohler and Roesler in 2006, focused on the development of crack widths under APT of CRCP. Kohler identified various surface crack formations and stated in a sub conclusion that the fundamental cause of punchout distress in the related study was due to a loss of base (USA – subbase) support enhanced by a reduction in pavement bending stiffness. The CRCP test section in the Kohler and Roesler study was constructed on bituminous aggregate materials (BAM); aggregate subbase (ASB), and compacted subgrade. The UTCRCP under current investigation was constructed on an existing flexible pavement as an overlay. Due to this variation in base and substructure support, feasible conclusions regarding fundamental causes of punchout distress remains to be investigated.

According to Kannemeyer, et al. 2008, finite element results of the two STPP UTCRCP sections (constructed on AC layers) indicated high tensile stresses at the bottom of the UTCRCP layer, approximately 450 mm from an existing crack. Expected cracking at this position was not as prominent as the observed surface cracking.

1.3 Objectives of the Study

The primary objective of this study is to characterize the spatial formation of transverse cracking on UTCRCP under accelerated pavement testing. Knowledge of the mean crack spacing excluding the characteristics of the crack pattern is not sufficient for punchout prediction. Punchout prediction models use the mean crack spacing parameter in the calculation process, but do not take account of the spacing characteristics. To achieve this objective the following secondary objectives, acting as building blocks, form the bases of this study:

1.3.1   Computation of in situ pavement parameters

Empirical and linear elastic modelling techniques for rigid pavement design and evaluation, emanating from accepted theories, will be used to determine critical pavement parameters. These parameters are used in the calculation process of the mean crack spacing. This study will evaluate the applicability of these (empirical and linear elastic) modelling techniques to UTCRCP. Empirical and linear elastic modelling techniques are usually simple to execute and give rough, but acceptable estimations of expected pavement parameters.

1.3.2   Mean crack spacing calculation

The revised American Mechanistic-Empirical Pavement Design Guide's (M-E PDG, 2004) mean crack spacing prediction model for CRCP will be used to predict the mean crack spacing on the UTCRCP. The inclusion of this prediction model in this study sets a dual objective. Firstly the study evaluates the applicability of this method for the determination of mean crack spacing on UTCRCP. Secondly this method (being empirical) will provide good insight to the sensitivity of the various factors pertaining to transverse crack spacing calculations.

1.3.3   Descriptive statistics

Crack spacing formation on UTCRCP is an uncontrollable event. To account for the spatial variation of the transverse cracking formation, descriptive statistical measures will be applied on the field observed crack spacing patterns. The aim is to characterize the spatial formation of the transverse cracks that contributes to structural punchouts, in accordance with the statistical results.

The above stated sub objectives conclude the basis from which to achieve the primary objective, however this study aims to include one more sub objective which does not form part of achieving the main objective. This sub objective is presented in Section 1.3.4.

1.3.4   cncPave evaluation

The ground for the inclusion of a cncPave evaluation is based on the scarcity of recorded data on UTCRCP crack spacing formations. cncPve is a software package that supersedes the old M10 design manual and is used in the industry for various rigid pavement designs and predictions. The objective of a cncPave evaluation would firstly be to understand the mechanisms and underlying principles of crack spacing determination, then to test the accuracy of its UTCRCP crack spacing predictions, with actual UTCRCP crack spacing data.

1.4 Scope of Works

The scope of works for this study consists of traffic simulation, data capturing, pavement modelling and the data analysis process. This section mainly outlines the limitations regarding this study. Factors contributing to the methodological limitations are delineated and discussed in the method chapter.

1.4.1 Traffic Simulation

This study is limited to a single APT field test on one test section comprising of 2.8 million applied axle load repetitions. Two available APT devices will be used to perform the number of load applications. Both devices are of the same model. The clients agreed that research may be done with their APT devices if the research project will serve the interests of the clients as being a field acceptance test (FAT) for the devices. Therefore apart from the research many other tests were also performed to satisfy the clients' requests. These tests do not form part of the study.

1.4.2 Rigid pavement modelling

UTCRCP being an ultra thin CRCP will be limited to empirical and linear elastic modelling techniques used in CRCP design processes (if applicable). This study will not deal with the structural analysis of the pavement, although the structural properties of the pavement will be briefly covered and included in relevant calculation procedures. Properties with regard to the UTCRCP layer (as reported by the contractor), are assumed to be accurate. This study will not include a laboratory testing phase to characterize the relationships that exists between the various concrete parameters of the UTCRCP mix. In the case where computer software will be used for pavement modelling or pavement response modelling, only software and free-ware available at the academic institution where this study is conducted will be considered.

1.4.3 Research equipment and data

The data collected for this study will be limited to the equipment used. Hence the methods used to characterize transverse cracking will be limited to the obtained data. In the case where more data is needed, than originally collected during the study, the source of that data will be made known explicitly. This study does not consider the methods by which data from foreign sources, outside of this study, were obtained. Conclusions regarding this study will primarily be made with regard to the data obtained by the participants in this study.

1.4.4 Data analysis and methods

Generally this aspect of research is quite broad. Due to relative recent application of UTCRCP technology, no unique methods exist to analyze the data. The study is thus limited to methods that have been proved to be applicable on CRCPs.

1.5 Content of Chapters

Chapter two is a literature study that takes the form of a funnel structure. It introduces the broad concept of CRCP then reduces it to the research objectives. The main discussions include punchout distress, rigid pavement modelling, factors that influence CRCP cracking, statistic and theoretical crack spacing evaluation methods and the development of cncPave.

Chapter three comprises of the research methodology. The research design elaborates on the project's scope of works. Elements pertaining to transverse crack spacing such as the test section, research instrumentation and data analysis procedures are introduced and discussed. Limitation factors regarding the methodology are also delineated and discussed in this chapter.

Chapter four presents the determination of mean crack spacing. This chapter presents deflection responses of the pavement that are used in a mechanistic-empirical and linear elastic modelling process. The two modelling processes, presented in this chapter, were performed to calculate specific pavement parameters that are included in the calculation procedure of the M-E PDG's prediction model of mean crack spacing.

In Chapter five the observed crack spacing distribution is discussed and presented. Descriptive statistical measures were taken to characterize the distribution. Finally a theoretical probability distribution was added to the characterized distribution.

A diagnostic investigation was launched in Chapter six centering on the performance of the UTCRCP with mean crack spacing. The cause and effect relationships of various factors contributing to crack spacing were evaluated. The effect of pavement loading to crack formation was also investigated and discussed.

Chapter seven concludes this study by summarizing all the relative points, observations, findings, suggestions and recommendations.

2 LITERATURE REVIEW

2.1 Introduction

This chapter introduces a brief structural overview of continuously reinforced concrete pavements (CRCP). The failure mechanism known as punchout distress will be probed and discussed, followed by the different modelling principles of rigid pavement design. Factors that influence transverse crack spacing will be addressed as well as methods to analyze crack spacing distributions. Theoretical modelling approaches of crack spacing distribution in combination with insights into mechanistic-empirical design procedures will be explored. Finally the Cement & Concrete Institute's (C&CI) new risk based design method for concrete roads, cncPave is presented and discussed.

The scope of the literature study was limited to relevant information pertaining to CRCP or UTCRCP. UTCRCP is a relatively new technology with limited available literature. Due to this limitation, literature regarding CRCP was reviewed and formed a suitable base from which insight into UTCRCP could be gained.

2.2 Punchout Distress in CRCP

A continuously reinforced concrete pavement (CRCP) is a type of concrete pavement that is constructed without regular transverse joints. It includes longitudinal steel bars for reinforcement that are placed continuously and sections are typically some kilometers in length. In the case of the ultra thin CRCP a steel mesh is used for reinforcement. The steel meshes are joined at the ends, providing continuous longitudinal reinforcement and as a result transverse reinforcement.

Environmentally induced transverse cracks form in CRCP after the placement of the concrete paste. This is due to concrete drying and temperature related shrinkage. These transverse cracks are retained by the longitudinal steel reinforcement and slab-base friction. The longitudinal steel also holds the formed transverse cracks tightly together so that in theory; surface water is unable to penetrate the CRCP layer.

Punchout distress is one the most severe performance problems of CRCP. A punchout (Figure 2.1) is a depression that occurs at the edge of the pavement as a result of structural failure caused by the action of heavy wheel loads after transverse cracks have suffered loss of load transfer efficiency (LTE) (Kohler and Roesler 2006).

7
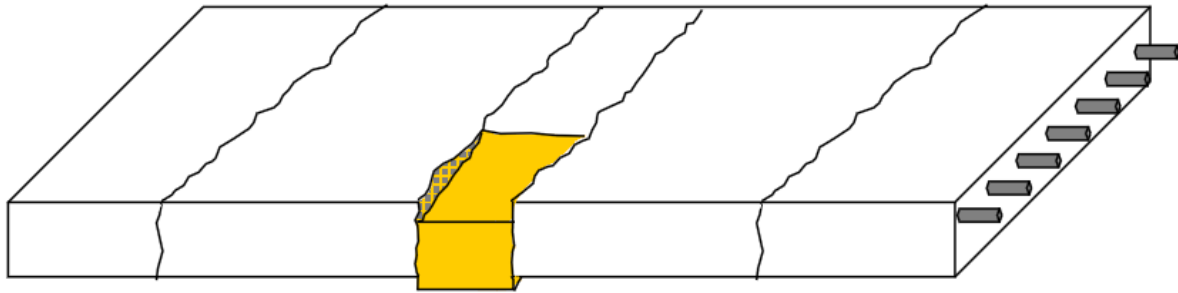
Figure 2.1. Punchout in CRCP (Kohler and Roesler 2006)

The Mechanistic-Empirical Pavement Design Guide (M-E PDG) defines a punchout as a fine longitudinal crack which forms between two transverse cracks that are closely spaced with less than 3 inches (76 mm) of spalling or 0.25 inches (6.4 mm) of faulting (ARA Inc. ERES Consultants Division 2004). Deterioration factors, such as a loss of bond at the concrete/steel interface and the forming of voids between the concrete slabs and supporting foundation both coincide with the punchout phenomenon. The supporting foundation or substructure can be divided into two classic mechanistic theories for rigid pavement design and rehabilitation procedures namely, the dense liquid (DL) foundation and elastic solid (ES) foundation.

2.3 Rigid Pavement Modelling

Mechanistic modelling of rigid pavement foundations is an important step in the design or rehabilitation process. Input parameters are generally inexpensive and easy to calculate, however development of such a model is more complex. Real soil exhibits nonlinear and in some cases visco-elasto-plastic characteristics. Experience in rigid pavement analysis and design has shown that subgrade may be modelled as linear elastic (ARA Inc. ERES Division 2003).

2.3.1 Dense liquid foundation

The most widely adopted modelling approach is the Westergaards-theory of a plate on a dense liquid (DL). The DL foundation, also known as the Winkler foundation, is the simplest foundation model and requires only one modelling parameter, the modulus of substructure reaction, k (Figure 2.2), which is the proportionality constant between the applied pressure and the load plate deflection (ARA Inc. ERES Division 2003).
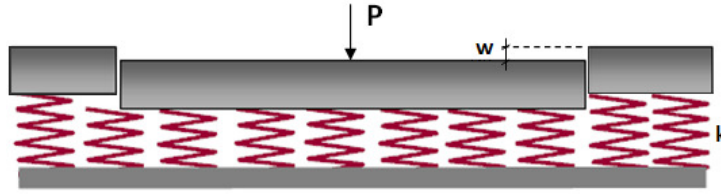
Figure 2.2 Dense liquid foundation

$$k = \frac{P}{w} \tag{2.1}$$

Where;

k =   the modulus of substructure reaction (N/mm^3)

P =   applied pressure (N/mm^2)

w =   vertical deflection (mm)

The DL foundation works on the principle that deformation is local i.e. only beneath the loaded plate and assumes zero deflection beyond the edge of the loaded plate. The substructure is elastic recoverable upon load removal and there exist no shear in between the adjacent springs. The springs have a spring stiffness equal to modulus of substructure reaction, k. In plate theory it is assumed that the plate is incompressible thus the vertical deflection, w, contributes only in the substructure deformation.

2.3.2 Elastic solid foundation

The elastic solid (ES) half space or Boussinesq subgrade idealization is often considered a more realistic representation of real soils. Deformations are global in character, that is, deformation develops not only under the loaded plate but also beyond it.
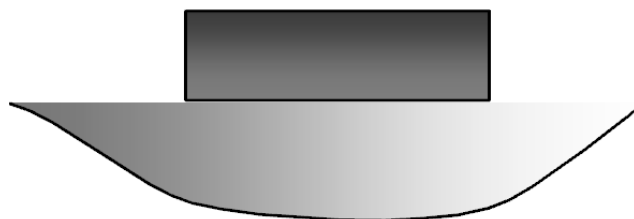
Figure 2.3 Elastic solid model (ARA Inc. ERES Division 2003)

The ES model depicted in Figure 2.3 is treated as a slab-on-grade problem. This type of model can also be considered single parametric since the only parameter required is the coefficient C (de Vos 2009).

$$C = \frac{E_s}{1 - \mu_s{}^2}$$

(2.2)

Where;

C = coefficient of elastic subgrade (N/mm^2)

E_s = elastic modulus of subgrade (N/mm^2)

μ_s = Poisson's ratio

The ES model is to some extent computationally demanding. It ascribes a higher degree of shear interaction to the subgrade than that in real soils. This model also assumes gradual decrease in deflection beyond the edges of the loaded plate.

2.3.3 Backcalculation of the Dense Liquid model

Deflection responses of real pavements are used in the ES model and DL model to estimate different parameters of the pavement structure.

Back calculation of the DL model yields a radius of relative stiffness l_k and a modulus of substructure reaction k. These parameters are ultimately used in calculating the concrete slab elastic modulus. The procedure is explained in the following steps.

Step 1: Determining the AREA parameter (A_4) of the deflection basin.

Two approaches are available for determining the pavement parameters in DL model, the AREA algorithm and the Best Fit method (FHWA-RD-00-086 2001). The Best Fit method solves for a combination of the radius of relative stiffness and coefficient of subgrade reaction the best possible agreement between the predicted and measured deflections at each sensor. Both methods are based on Westergaard's solution for interior loading on a plate. The Best Fit method yields a lower coefficient of variation in backcalculated k-values than the AREA algorithm (FHWA-RD-00-086 2001). Therefore the Best Fit method is considered the preferred backcalculation procedure. The AREA algorithm yields a parameter, A_n. The subscript number *"n"*, defines the spacing configuration of the sensors in the Area algorithm. The AREA parameter, A_n, is not truly an area, but rather has a

dimension of length, since it is normalised with respect to one of the measured deflections in order to remove the effects of load magnitude. This parameter (A_n) combines the effect of several measured deflections in a basin (FHWA-RD-00-086 2001). The AREA parameter has a unique relationship with the radius of relative stiffness and thus presents an effective method in calculating the radius of relative stiffness.

Different sensor configurations exist for the AREA algorithm. AREA algorithm number four, yielding a parameter, A_4, is traditionally used for the evaluation of concrete pavements (FHWA-RD-00-086 2001). Sensor configuration is set to 0, 300, 600 and 900 mm, thus a falling weight deflectometer (FWD) deflection bowl can be used to determine the A_4 parameter.

$$A_4 = 6 + 12 \left[\frac{d_{300}}{d_0}\right] + 12 \left[\frac{d_{600}}{d_0}\right] + 6 \left[\frac{d_{900}}{d_0}\right] \tag{2.3}$$

Step 2: Determine the radius of relative stiffness l_k

For each of the AREA algorithms the following empirical equation is used to estimate the radius of relative stiffness l_k;

$$l_k = \left[\frac{\ln \left[\frac{x_{1-AREA}}{x_2}\right]}{x_3}\right]^{x_4} \qquad \text{(FHWA-RD-00-086 2001)} \tag{2.4}$$

The advantage of the empirical Equation 2.4 is that it does not require the elastic modulus of the concrete as an input parameter to estimate the radius of relative stiffness.

Table 2.1 Coefficients for the AREA algorithm vs. radius of relative stiffness, l_k (FHWA-RD-96-198 1997)

AREA	x_1	x_2	x_3	x_4
A4	36	1812.279	-2.559	4.387

According to the M-E PDG the resulting radius of relative stiffness for a Portland cement concrete (PCC) slab should be between 22.5 in (570 mm) and 80 in (2032 mm) (ARA Inc. ERES Consultants Division 2004). The lower limit was selected based on the consideration that response of pavement systems with too low radii of relative stiffness cannot be adequately described using a slab-on-grade model. A layer elastic model is a more appropriate analytical tool and a layer elastic backcalculation procedure should be used for

backcalculation. The upper limit was assigned to recognise that backcalculation cannot also be reliable for every rigid system (FHWA-RD-00-086 2001).

Step 3: Determine the modulus of substructure k.

Westergaard's theory of an incompressible plate on a dense liquid is represented in the following equation. Equation 2.5 is valid for circular loading at the slab interior (Houben 2006).

$$k = \frac{P}{8wl^2}\left[1 + \frac{1}{2\pi}\left\{\ln\left(\frac{a}{2l}\right) + \gamma - 1.25\right\}\left(\frac{a}{l}\right)^2\right]$$ (2.5)

Where;

k =   modulus of substructure reaction (psi/in)

P =   single wheel load (lb)

w =   vertical deflection = FWD maximum deflection d_0 (in)

l =   radius of relative stiffness of concrete layer, calculated with eq.2.4 (in)

γ =   Euler's constant (= 0.5772156649)

a =   radius of circular loading area (in)

In a rigid pavement study done by the Federal Highway Administration (FHWA) on LTPP data, backcalculations of k-values were compared using the Best Fit method number four (Best Fit4 or B_4) and AREA algorithm number four (AREA4 or A_4). The following relationship was established between the Best Fit4 and AREA4 approaches, depicted in Figure 2.4 (FHWA-RD-00-086 2001).

$$k_{A4} = 1.148k_{B4} \qquad R^2 = 0.976$$ (2.6)

The R^2 value exceed 0.97 thus this linear relationship explain approximately 97 percent of the variability in the results.
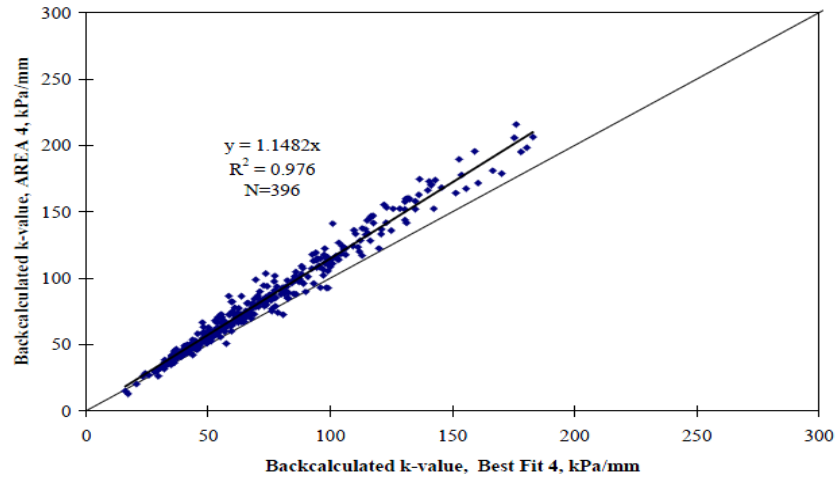
Figure 2.4 Backcalculated dynamic k-value for LTPP concrete pavement sections, AREA4 versus Best Fit 4 (FHWA-RD-00-086 2001)

Step 4: Compute the elastic modulus of the concrete

Appendix QQ from the Guide for Mechanistic-Empirical Design suggests the following equation to calculate the elastic modulus of the concrete slab (ARA Inc. ERES Division 2003).

$$E_{pcc} = \frac{12 l_k{}^4 k (1 - \mu_{pcc}{}^2)}{h_{pcc}{}^3}$$ (2.7)

Where;

E_{pcc} = elastic modulus of concrete (psi)

l_k = radius of relative stiffness of a DL model (in)

μ_{pcc} = Portland cement concrete Poisson's ratio

k = modulus of substructure reaction (psi/in)

h_{pcc} = Portland cement concrete thickness (in)

2.3.4 Backcalculation of the Elastic Solid model

Back calculation of the ES model yields a radius of relative stiffness l_e and the elastic modulus (E_s) of the pavement subgrade (substructure). These parameters are ultimately

used in calculating the elastic modulus of the concrete slab. The procedure is explained in the following steps.

Step 1: Determining the AREA parameter (A_4) of the deflection basin.

The ES model has become more widely applied since the advent of FWD backcalculation technology (Galal, et al. 1998). Prior to rehabilitation of a rubblizing contract for a portion of the US-41 in Benton Country, the Galal, et al. 1998 study used Equation 2.3 on FWD deflection bowls to estimate AREA parameter (A_4).

Step 2: Determine the radius of relative stiffness l_e

The AREA parameter, A_4, has been analytically identified as having a relationship to the radius of relative stiffness l_e of the pavement system (Galal, et al. 1998).

$$l_e = \left[\frac{ln\left[\frac{36 - AREA}{4521.676}\right]}{-3.654}\right]^{\frac{1}{0.187}}$$

(Galal, et al. 1998)   (2.8)

The same limits criterion and conditions apply to the ES radius of relative stiffness, l_e, as that of the DL radius of relative stiffness l_k.

Step 3: Calculate the elastic modulus of the subgrade by using Losberg's deflection Equation 2.9.

$$E_s = \left[\frac{2P(1 - \mu_s{}^2)}{d_0 l_e}\right]\left[0.19245 + 0.0272\left[\frac{a}{l_e}\right] + 0.0199\left[\frac{a}{l_e}\right]^2 ln\left[\frac{a}{l_e}\right]\right]$$

(2.9)

Where;

E_s =   elastic modulus of subgrade (psi)

l_e =   radius of relative stiffness of an ES model, Equation 2.8 (in)

μ_s =   subgrade Poisson's ratio (estimated value)

P =   applied load (lb)

d_0 =   maximum deflection at the centre of the load (in)

a =   load radius (in)

Step 4: Calculate the elastic modulus of the concrete

The elastic modulus of the concrete slab (E_{pcc}) can be computed from Equation 2.10.

$$E_{pcc} = \frac{6E_s l_e{}^3 (1 - \mu_{pcc}{}^2)}{h_{pcc}{}^3 (1 - \mu_s{}^2)}$$

(2.10)

Where;

μ_{pcc} =   concrete slab Poisson's ratio

h_{pcc} =   concrete slab thickness (in)

It should be noted that neither the DL foundation nor the ES model is entirely adequate, when these philosophies are applied to real soils. There are a number of influencing factors that will affect these backcalculation procedures. Some of the more significant factors include: the effect of the base layer, size of the slab and the effect of plate theory relative to elastic theory.

2.3.5 Effect of the base layer

According to Huang 1993, when a rigid pavement is constructed on an existing flexible pavement, the flexible pavement can be viewed as a composite foundation for the newly constructed rigid pavement.

Concrete pavements are generally analyzed as slab-on-grade structures with no structural contributions attributed to the underlying base or subbase layers. However it is known that these underlying layers can have a significant effect on the structural performance of the pavement, particularly if bonding between the slab and the base occurs. If such bonding is present between the layers, the effective pavement structure is now greater and the manner in which the pavement reacts to loading is altered (FHWA-RD-00-086 2001).

Khazanovich had addressed this issue with a concept of transformed sections. Thus the multi-layered pavement (slab and underlying layer(s)) is transformed to a fictitious, composite, homogeneous plate, that would exhibit the same deflection profile as the in situ system (Khazanovich 1994). For a case of two bonded plates, the flexural stiffness of the fictitious plate can be derived by using the parallel axis theorem as presented in Equation 2.11.

$$\frac{E_e h_e{}^3}{12} = \frac{E_1 h_1{}^3}{12} + E_1 h_1 \left[x - \frac{h_1}{2}\right]^2 + \frac{E_2 h_2{}^3}{12} + E_2 h_2 \left[h_1 - x + \frac{h_2}{2}\right]^2 \tag{2.11}$$

Where;

$$x = \frac{\frac{h_1{}^2}{2} + \beta h_2 \left[h_1 + \frac{h_2}{2}\right]}{h_1 + \beta h_2} \tag{2.12}$$

Therefore;

$$E_1 = \frac{h_1{}^3}{h_1{}^3 + \beta h_2{}^2 + 12 h_1 \left[x - \frac{h_1}{2}\right]^2 + 12 \beta h_2 \left[h_1 - x + \frac{h_2}{2}\right]^2} [E_e] \tag{2.13}$$

Where;

E_e =   equivalent modulus of the fictitious plate (psi)

E_1 =   modulus of the upper plate (psi)

E_2 =   modulus of the lower plate (psi)

h_e =   thickness of the fictitious plate = h_1 (assumption)

h_1 =   thickness of the upper plate (in)

h_2 =   thickness of the lower plate (in)

β =   moduli ratio = $\dfrac{E_{pcc}}{E_s}$ (FHWA-RD-00-086 2001)

Assumption;

μ_s =   fictitious plate Poisson's ratio = $\mu_1 = \mu_2$

A study conducted by Murison, et al. 2002 on ultra thin whitetopping indicated that by using a three-layer model which incorporates a degree of bond between the upper and supporting layer, better estimates critical stresses than a two-layer setup that disregards a bond between the respective layers.

As depicted in Figure 2.5, stresses are nearly reduced to a factor two by incorporating a bond in the three-layer system. The bond allows the concrete and asphalt to perform in composite action that essentially causes the layers to share loads. Bonding shifts the neutral axis in the concrete downward, reducing the tensile stress at the bottom of the concrete layer (Murison, et al. 2002).

Corner stresses will however increase at the top of the whitetopping layer and if the neutral axis shifts low enough in the concrete layer, the critical stress position will move from the edges of the slab to the corners of the slab.
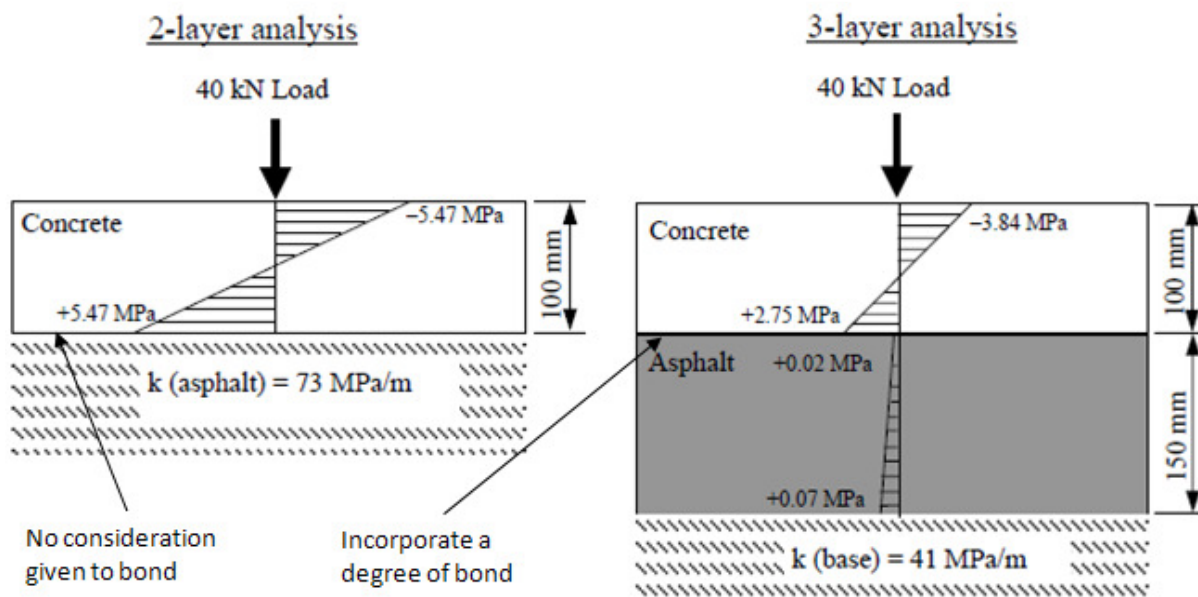
Figure 2.5 Stress distribution under a 2-layer and 3-layer analyses (Murison, et al. 2002).

2.3.6 Slab size effect

The backcalculation procedures mentioned in this section of the study are based on Westergaard's and Losberg's solutions for interior loading of an infinite plate, but concrete pavements have finite dimensions. Corvetti developed a slab size correction for square slabs that was verified (FHWA-RD-00-086 2001).

Slab size correction is a simple method to perform if the slab length is assigned properly. Due to the nature of CRCP cracking which in some cases are stated to be random, it might be better to assign slab size correction on the average mean crack spacing, if necessary.

2.3.7 Effect of plate theory relative to elastic theory

An assumption associated with plate theory is that the upper layer is incompressible. This assumption accounts primarily for the discrepancies found when the Best Fit method is evaluated against the AREA algorithm. At the location of maximum deflection i.e. under the load centre, higher inconsistencies are observed between the discussed methods. At this location the plate theory predictions of deflections deviates most from elastic theory predictions due to the compressibility of the concrete layer.

2.4 CRCP Crack Spacing

A continuously concrete pavement is effectively fully restrained in the longitudinal direction. Due to the thermal contraction and shrinkage properties of concrete, pavement cracking is inevitable. The conventional solution to counter pavement cracking is to induce transverse joints to relieve the tension of the accumulating restrained stresses. This action prevents cracks, but reduces riding quality and many failures of jointed concrete pavements are associated with the joints. An alternative is to accept that the concrete will crack and provide reinforcement to control the width of the cracks by spreading the contraction over many narrow cracks. This is the basic concept of CRCP (Jackson 1988).

Two categories of crack development are associated with CRCPs that is, environmentally related cracking and traffic induced cracks.

2.4.1 Environmentally related cracks

Environmental related cracks are associated with concrete shrinkage and concrete thermal contraction. The tendency of concrete to shrink produces longitudinal tension in the concrete and compression in the reinforcing steel. Since both materials (concrete and steel) are strong in compression, no damages normally come from expansion. However due to exothermic hydration reactions in the concrete, shrinkage takes place which induces tensile stresses in the concrete layer (Gutzwiller and Waling 1960). Eventually the resulting tensile stress exceeds the strength of the concrete and a crack forms at the weakest point (Figure 2.6).

Crack developments in CRCP due to environmentally related stresses are thought of to occur in two phases (Zollinger 2007). The initial phase consist of the formation of shrinkage cracks after construction (Figure 2.6) and are strongly associated with a cracking interval of 4.4 times the radius of relative stiffness of the pavement surface layer.
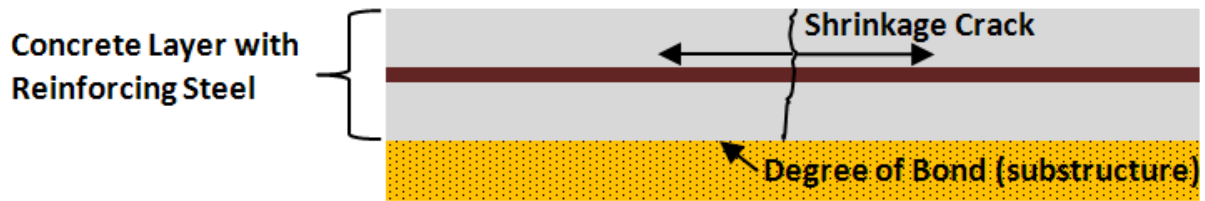
Figure 2.6 Shrinkage crack, caused by the exothermic hydration reaction. No variation in temperature i.e. bottom temperature is equal to surface temperature.

The secondary phase or secondary cracking include temperature related cracks and form on a segment delineated by the initial shrinkage cracks. Secondary cracks comprise of differential shrinkage and pavement curling induced cracks, which further relieve the pavement of existing tensile stress.

Differential shrinkage (Figure 2.7), commonly known as pavement warping occurs when the rate of shrinkage at the bottom of the concrete layer is different to the rate of shrinkage on the pavement surface (top). Thus a gradient can be ascribed to the moisture content and temperature profile in the concrete layer, which are of the characteristics of pavement warping. Warping is a permanent geometrical deformation i.e. it is a non-recoverable strain.
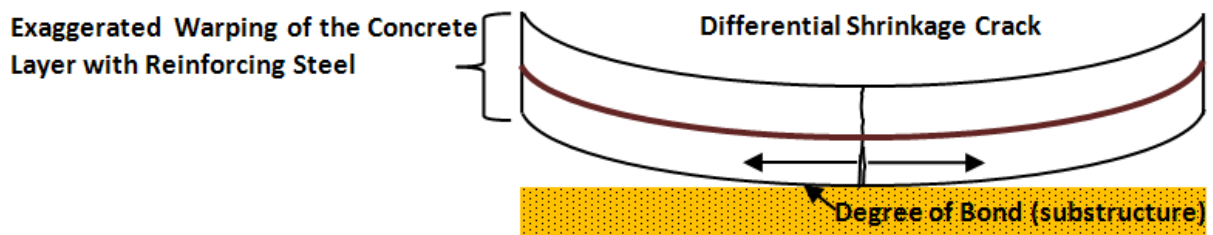
Figure 2.7 Secondary crack caused by differential shrinkage (warping). Variation in temperature i.e. bottom temperature is not equal to surface temperature.

Pavement curling occurs due to a variation of temperature gradients in the concrete layer. This pavement characteristic is associated with day and night temperature changes. The stresses induced by this variation in temperature are recoverable and not permanent as with pavement warping. Figure 2.8 depicts the curling formation of the pavement at night time and during the day. A cooler slab surface during the night induces a negative temperature gradient in the concrete slab. This results in the edges of the slab curling upward. A warmer slab surface during day time induces a positive temperature gradient in the concrete slab. Under the second condition (day time) the interior part of the pavement tend to bulge.
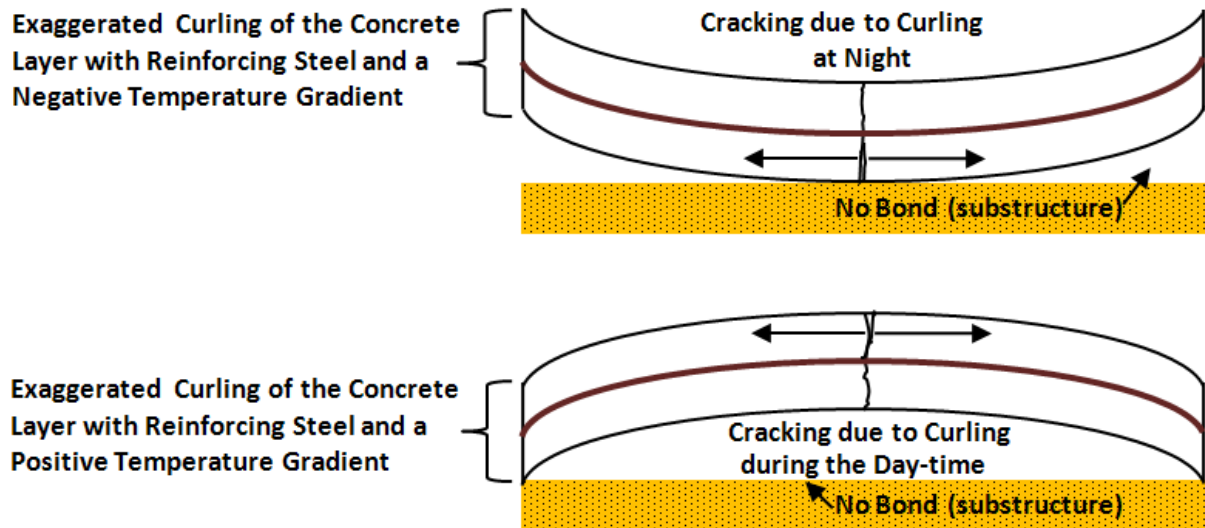
Figure 2.8 Depictions of slab curling during the day and at night with positive and negative temperature gradients respectively.

2.4.2 Traffic related cracks

Traffic related cracks are due to the flexural action of the concrete layer caused by vertical wheel loads that super impose longitudinal compressive and tensile stresses on the upper and lower positions of the concrete slab (Gutzwiller and Waling 1960). In the case where the wheel load travels across an existing deteriorating crack (Figure 2.9), tensile stresses are generated some distance away from the initial crack.
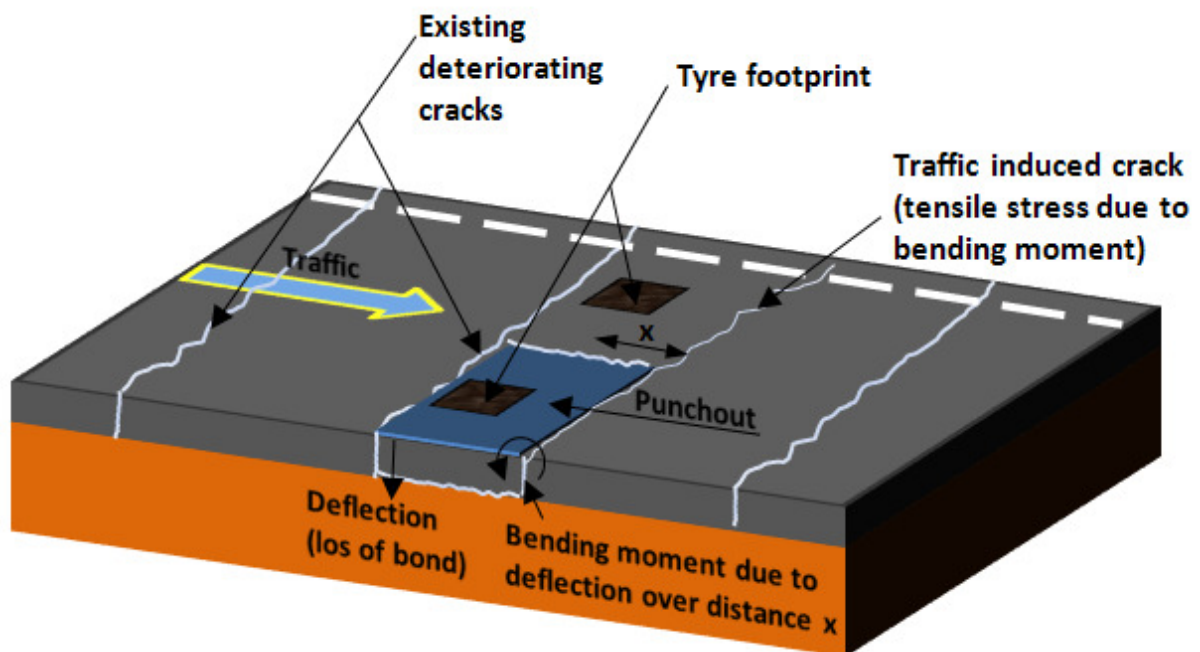
Figure 2.9 Traffic induced fatigue cracking

20

Finite element modelling done by Kannemeyer, et al. 2008 suggests that this distance for UTCRCP is approximately 450 mm. Laboratory studies have shown that cracking of concrete beams can also occur as a result of multiple applications of stresses smaller than the tensile strength of the concrete. This type of cracking is referred to as fatigue cracking (Manual M10 1995). According to Jackson 1988, the wheel load stress effects for CRCP does not become really significant until the crack spacing is less than is considered desirable. All authorities on CRCP seem to agree that the maximum desirable crack spacing is around 2.5 m (Jackson 1988).

The formation of the complete crack pattern in a given CRCP slab, results from the superposition of concrete shrinkage, temperature changes and traffic (Gutzwiller and Waling 1960). The various cracks that contribute to the complete crack pattern are depicted in Figure 2.10.
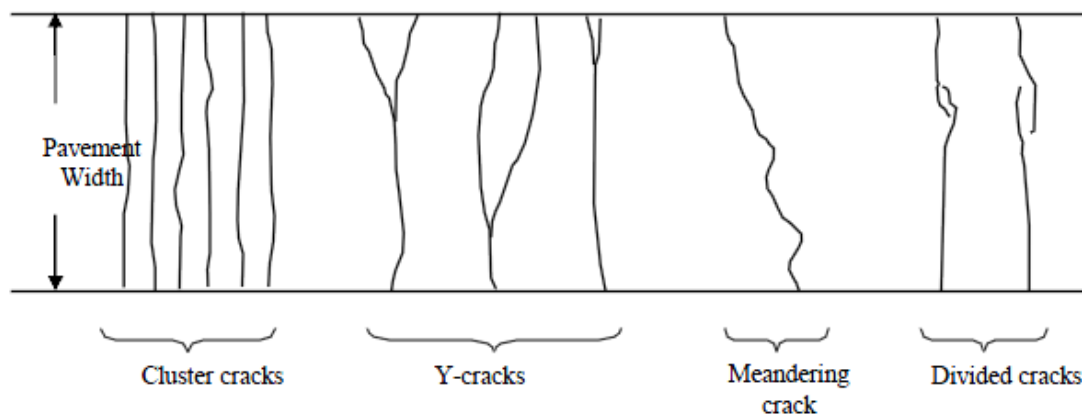
Figure 2.10 Crack shapes and patterns associated with defective passive cracks (Kohler and Roesler 2006)

Kohler and Roesler 2006 reported that divided cracks and Y-cracks have a greater tendency to deteriorate and spall more rapidly under traffic loading.

2.4.3 Factors affecting crack spacing

Several factors influence crack spacing ranging from geometrical properties to material properties. The following five factors (2.4.1.1 to 2.4.1.5) are considered to be of significant importance.

2.4.3.1 State of pavement temperature

The concrete setting temperature and the coefficient thermal expansion (CTE) have been identified as two of the most sensitive variables determining CRCP behaviour (Kohler and

Roesler 2006). The CTE describes how the size of the material changes with a change in temperature. Due to the exothermic reaction of concrete setting, construction on hot days prohibit to a degree the dissipation of the hydration energy into the atmosphere and influences the cracking patterns.

Temperature variations lead to stresses in the concrete layer as discussed in Section 2.4.1. The temperature profiles responsible for these stresses are depicted in Figure 2.11.
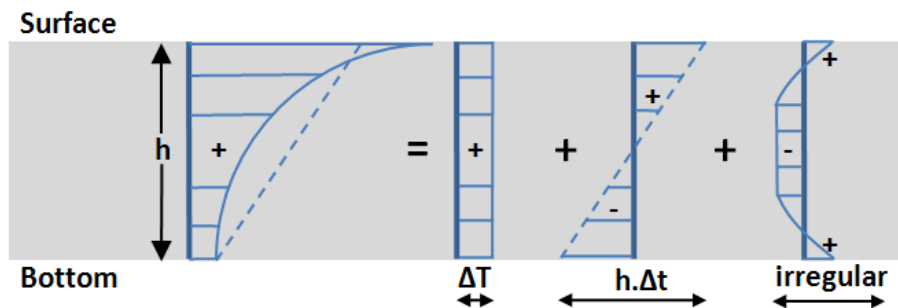
Figure 2.11 Stress inducing temperature variations in the concrete layer

Stress due to a temperature change ΔT, which is constant over the thickness of the layer is associated with concrete shrinkage. Stresses related to differential shrinkage (warping) as discussed in Section 2.4.1 are coupled with a temperature gradient $h. \Delta t$, which is constant over the thickness of the concrete layer. The variation of this temperature gradient ($h. \Delta t$), due to day and night temperature differences, contributes to the curling action of the concrete layer.

The irregular temperature profile, results in internal concrete stresses, which are only relevant for very thick concrete slabs (Houben 2006). A combination of these temperature effects contributes to the deterioration of cracks under traffic loading.

2.4.3.2 Concrete drying and shrinkage

Drying and shrinkage causes cracking in reinforced concrete, especially in the early age when the concrete tensile strength had not yet fully developed. Since drying and shrinkage have a faster development at the surface, there is a non-uniform shrinkage distribution. The pavement has the tendency to curl upward at existing cracks under such a non-uniform distribution (Kohler and Roesler 2006). This effect is commonly known as pavement warping.

2.4.3.3 Bond between the concrete and reinforced steel

Due to a variation in concrete temperature and shrinkage, stresses and strains also vary along individual pavement segments according to the distance between neighbouring cracks. The bond stress is defined by Kohler and Roesler 2006 as the interfacial shear that takes place at the boundary between the reinforcing steel surface and the concrete. The difficulty in modelling the bond stress distribution influences the accuracy of CRCP behaviour predictions.

2.4.3.4 Characteristics of reinforcing steel

Longitudinal steel reinforcement limits the degree of crack width. Tightly closed cracks allow shear transmission due to traffic across them by aggregate interlock (Jackson 1988). The latter is true for CRCPs in the absence of significant longitudinal reinforcement. In the case of the 50 mm heavily reinforced UTCRCP; the transmission of shear across the cracks are dependent on a much smaller crack width (approximately 0.02 mm) than expected CRCP crack widths. To obtain such a crack width the percentage of the reinforcing steel is increased.

The percentage of longitudinal reinforcing steel, steel diameter and the position of the steel in the concrete slab have an effect on the crack spacing of the CRCP. A higher percentage of reinforcing steel reduces the intervals of cracking and as a result a reduction in crack width. The current UTCRCP design consists of approximately 1% longitudinal steel reinforcement. Kannemeyer, et al. 2008 has reported that reinforcing steel with a diameter of 6 mm has a four to five times greater bond (concrete to steel) to the UTCRCP mix than a normal concrete mix. Field experience indicated that reinforcing steel of 5.6 mm in diameter is the optimum diameter for a 50 mm UTCRCP (Kannemeyer, et al. 2008).

2.4.3.5 Interface friction between slab and supporting base

A concrete slab sliding along the base develops friction forces which are an import factor in the early development of CRCP cracks. The most common base types for CRCP are asphalt (AC) and cement-aggregate, followed by granular bases. AC and cement-aggregate bases provide a higher degree of friction due to adhesion interlock. Prior to concrete placing Kannemeyer, et al. 2008 reported that in some sections of the Heidelberg screener lanes the reinforcing steel mesh structure used in UTCRCP was anchored to the AC base using 150 mm steel rods. It was anticipated that the anchors will restrict vertical debonding of the concrete slab to the AC base and restrict warping and curling effects along the pavement's longitudinal edge.

During the National Cooperative Highway Research Program (NCHRP), Project No. 1-37, it was found that a substantial loss of support led to an increase of slab cracking (ARA Inc. ERES Consultants Division 2004).

2.4.4 Statistical analysis of CRCP crack spacing

Descriptive statistical measures such as, mean, standard deviation, coefficient of variation (COV), kurtosis, skewness and crack spacing frequency per trail section can be computed to evaluate characteristics of crack spacing distributions.

By means of descriptive statistics a LTPP study (experiment GPS-5) conducted by Selezneva, et al. 2002 indicated that CRCP trail sections with larger crack spacing usually have a higher standard deviation of crack spacing. The coefficient of variation (COV) for the trial sections was an average value of 56%. This means that the standard deviation of the crack spacing is roughly half of the mean crack spacing. Thus, for sections with narrow mean crack spacing, the probability of the narrow crack spacing intervals being positioned next to the wide crack spacing intervals is lower compared to the sections with large mean crack spacing (Selezneva, et al. 2002).

With consideration to punchout potential, descriptive statistics of the above experiment resulted in the following. No correlation exists between mean crack spacing and the size of the segment that would develop a punchout. Therefore, the mechanistic procedure for punchout prediction cannot be based on mean crack spacing alone, but should take into account the fact that punchouts are likely to develop on narrow individual concrete segments. High variability of transverse crack spacing has a higher probability of punchout development (Selezneva, et al. 2002).

2.4.5 Theoretical modelling of CRCP transverse crack spacing

The reliability of CRCP design rests significantly on accurate characterization of the variability of transverse crack spacing. Research has indicated that contrary to the commonly held assumption of normally distributed transverse crack spacing, a Weibull distribution of transverse crack spacing is a better theoretical description of recorded transverse crack spacing results (Selezneva, et al. 2002).

To determine the probability that transverse crack spacing would occur between two crack spacing intervals Selezneva, et al. 2002 suggests the following Weibull based model.

$$Prob(L_u \geq L \geq L_l) = 100 \left[e^{-\left(\frac{L_l - L_{min}}{\alpha}\right)^\beta} - e^{-\left(\frac{L_u - L_{min}}{\alpha}\right)^\beta} \right] \tag{2.14}$$

Where;

$$\alpha = \frac{\bar{L} - L_{min}}{\Gamma\left(1 + \frac{1}{\beta}\right)} \qquad \text{(Selezneva, et al. 2002)} \tag{2.15}$$

$$\Gamma\left(1 + \frac{1}{\beta}\right) = \frac{1}{\beta} e^{\ln\left\{\frac{1}{\beta}\right\}} \qquad \text{(Selezneva, et al. 2002)} \tag{2.16}$$

$Prob(L_u \geq L \geq L_l)$ =   probability of crack spacing in the interval $L_u \geq L \geq L_l$ (%)

L_u =   upper limit of crack interval (mm)

L_l =   lower limit of crack interval (mm)

L_{min} =   minimum crack spacing (mm)

$\bar{L}$ =   mean crack spacing (mm)

α =   alpha from Equation 2.15

β =   shape parameter beta, form Equation 2.16

Γ =   gamma function

Calculation of the mean crack spacing can be done with the expression (Equation 2.17) presented in the M-E PDG. This expression contains variables with subscripts, *i*, that indicate seasonal variation.

$$\bar{L} = \frac{f'_{t28} - C_i \sigma_{0,i} \left[1 - \frac{2\zeta}{h_{pcc}}\right]}{\frac{f}{2} + \frac{U_m P_b}{c_{1,i} d_b}} \tag{2.17}$$

Where;

f'_{t28} =   concrete tensile strength in 28 days (psi)

C_i =   the Bradbury coefficient

$\sigma_{0,i}$ = Westergaard's nominal stress factor (psi)

ζ = depth to steel (in)

h_{pcc} = the concrete slab thickness (in)

f = friction coefficient

U_m = the peak bond stress (psi)

P_b = percentage of steel as a fraction

$c_{1,i}$ = the first bond stress coefficient

P_b = reinforcing longitudinal steel bar diameter (in)

The variables of mean crack spacing are discussed in greater detail in Appendix A.

2.5 The Development of cncPave

The existing South African concrete pavement design method of the Department of Transportation as stipulated in the M10 manual, *"Concrete Pavement Design and Construction"* (Manual M10 1995), essentially followed a recipe-type approach to design and used a series of nomograms. The M10 manual contained some aspects of mechanistic design, but was predominantly empirical i.e. based on experience alone (Advertorial VOL6 No1 Feb 2003). The document (M10) was not intended to cover all concrete pavement options such as inlays, overlays, and varying design periods.

2.5.1 cncRisk

The traditional approach, using single values for input parameters, was not ideal as uncertainty in the input was not translated into uncertainty in the output and therefore into the inherent risk of the design (Slavik, et al. 2004). A new design method was needed that utilized a mechanistic approach and would result in more cost effective pavements.

In support of this goal a new mechanistic risk based design method, cncRisk, was developed by the Cement & Concrete Institute (C&CI). This approach was fuelled by the fact that concrete pavements are increasingly utilized as overlays on old flexible pavements where characteristics are determined through linear elastic theory and software packages (Strauss, Slavik, et al. 2007).

Based on the requirements that the design procedure should be user friendly and that cncRisk needed to run on relatively inexpensive and readily available hardware, the use of sophisticated methods in calculating pavement response were precluded (Cement & Concrete Institute 2001). An effective but simple approach was adopted to evaluate the quality of the design and thus facilitate competent decision making. The approach used is based on the evaluation of consequences. The consequences of a certain pavement design are expressed in terms of premature failure that has to be repaired. In practice this occurs when the number of load repetitions *"n"* a pavement is expected to carry over the design period, exceeds the number of load repetitions *"N"*, the pavement can carry at an acceptable level of structural and/or functional integrity (Strauss, Slavik, et al. 2007).

The ratio *n* to *N* is called the cumulative damage (*CD*). By definition *CD = n/N*. The risk of premature failure is defined as the probability of *n* being greater than *N. R* is thus the probability (*P*) of the cumulative damage (*CD*) being greater than unity (Strauss, Slavik, et al. 2007).

$$R = P\{CD > 1\}$$
(Strauss, Slavik, et al. 2007) (2.18)

It should be mentioned that the complement of risk, i.e. 1-*R,* is often called the reliability.

Structural performance of cncRisk was based on the assumption that a crack in a concrete pavement does not signify failure. Failure is only occurring when shattered slabs develop as a result of loss of slab support and secondary cracking on the slab showing the tendency to develop punchouts (Slavik, et al. 2004).

The basic Westergaard's empirical relationship for calculating the maximum tensile stress in a concrete slab (Equation 2.19) was revised and calibrated for South African conditions.

$$Stress = f\left\{C, \frac{P}{h_1^2}, \sqrt[4]{\frac{D}{k}}\right\}$$
(Cement & Concrete Institute 2001) (2.19)

Where;

$Stress$ = maximum tensile stress close to a joint or crack in the pavement

C = coefficient depending on load/slab configuration and load transfer at a

crack or joint

D	=	slab stiffness

k	=	slab support

P	=	magnitude of the load

D	=	slab stiffness

h_1	=	slab thickness

The equation for maximum tensile stress at a joint or crack under dynamic truck loading for South African conditions (Equation 2.20.) was achieved through regression analyses in combination with finite element modelling and actual measurements of strain on concrete loads under dynamic loading.

$$Stress = k\left[\frac{(Void + 1)^{2(C-0.16)}C^{0.1.1}E_1{}^{0.6}}{h_1{}^a(h_2hE_2)^{0.08}(3\sqrt{v+1})^{0.5(C-0.16)}E_e{}^{0.5}}\right] \qquad \text{(Slavik, et al. 2004)} \qquad (2.20)$$

Where;

$Stress$ =		maximum tensile stress close to a joint or crack in the pavement

k	=	depends on wheel load and surface pressure as well as the bond between
		subbase and slab

$Void$	=	length of void below slab

C	=	load transfer coefficient

E_1	=	slab stiffness

h_1	=	slab thickness

E_2	=	subbase stiffness

h_2	=	subbase thickness

E_e	=	equivalent subgrade support stiffness

a	=	$1.95/(h^2E_2)^{0.05}$

v = speed of heavy vehicles

The expected life (N) of the pavement is calculated as presented in Equation 2.21.

$$Expected\ life\ N = a\left(\frac{stress}{strenght}\right)^{b}$$ (Cement & Concrete Institute 2001) (2.21)

Where;

$stress$ = Equation 2.20

$strenght$ = strength of the concrete

a = damage constant

b = damage factor

Many designers realize the uncertainty of concrete input parameters and consequently try to avoid the use of a single point estimates. Reasonable practical values are preferred instead. cncRisk incorporates a triangular probability distribution to express the stochastic nature (governed by the laws of probability) of the input variables (Cement & Concrete Institute 2001). According to Brian Perrie, managing director of C&CI, this stochastic approach to design, is unique in pavement design (Advertorial VOL6 No1 Feb 2003).

A triangular distribution is defined by three parameters namely a minimum practical value, the best estimate and a maximum practical value (Figure 2.12).
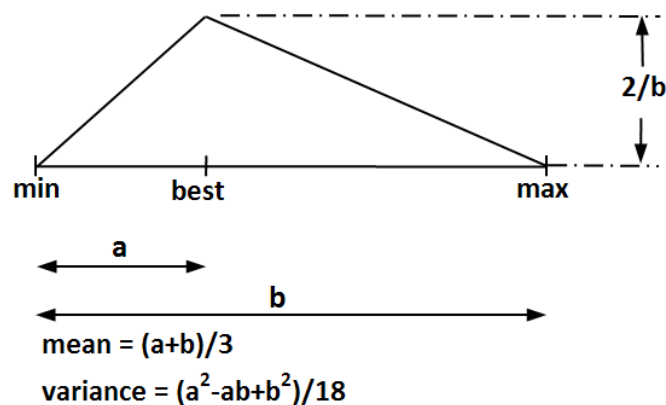
Figure 2.12 Triangle distribution of cncRisk input variables

29

cncRisk determines the risk (R, Equation 2.18) of pavement failure by calculating the stress/strength ratios of the maximum surface tensile stress near a joint or crack.

2.5.2 cncPave

An upgrade of cncRisk resulted in cncPave. The same approach was taken in cncPave, except that the risk of pavement failure was not being calculated, but rather the area of pavement failure (Strauss, Slavik, et al. 2007). cncPave has been used since 2004, but the capacity was increased in 2006 to accommodate the inclusion of UTCRCP. Experience in Europe and testing under the Heavy Vehicle Simulator (HVS) has indicated that the use of high strength concrete, steel fibres and a high percentage of steel reinforcement allow the designers to reduce the thickness of the concrete overlay to as little as 50 mm (Strauss, Slavik, et al. 2007).

Although a computer program can never replace designers' intelligence, cncPave can quickly pre-try the design, evaluate its quality, and thus facilitate competent decision making. The consequences of a certain pavement design are express in terms of decision variable, viz.
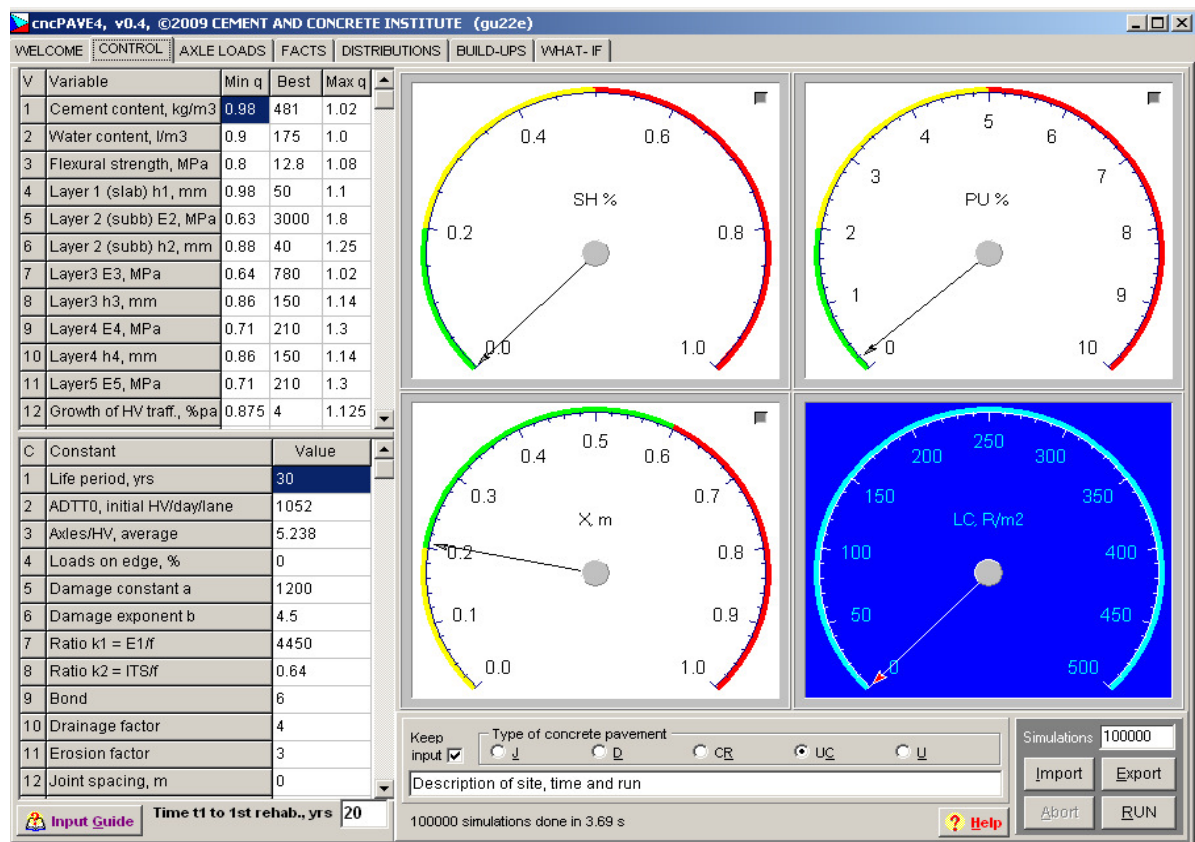
Figure 2.13 Control screen of cncPave showing input variable and outputs

30

- % shattered concrete surface (SH %)
- % pumping concrete surface (PU %)
- % faulting in the concrete (plain & dowel concrete) (FA %)
- Crack spacing (CRCP & UTCRCP) (X, m)
- Life cost of the pavement (LC, R/m2)

Pumping (Figure 2.13) is a function of: area of the pavement where the deflection exceeds a limiting value (this is a function of expected number of load applications), annual rainfall, permeability of the pavement to the surface water and erodibility of the slab support. The area of shattered slabs is a function of the area of the pavement that shows cracking as well as pumping (Slavik, et al. 2004).

In addition, probabilities of the decision variables exceeding certain limits (the confidence intervals) can be determined from the respective graphs (Figure 2.14).
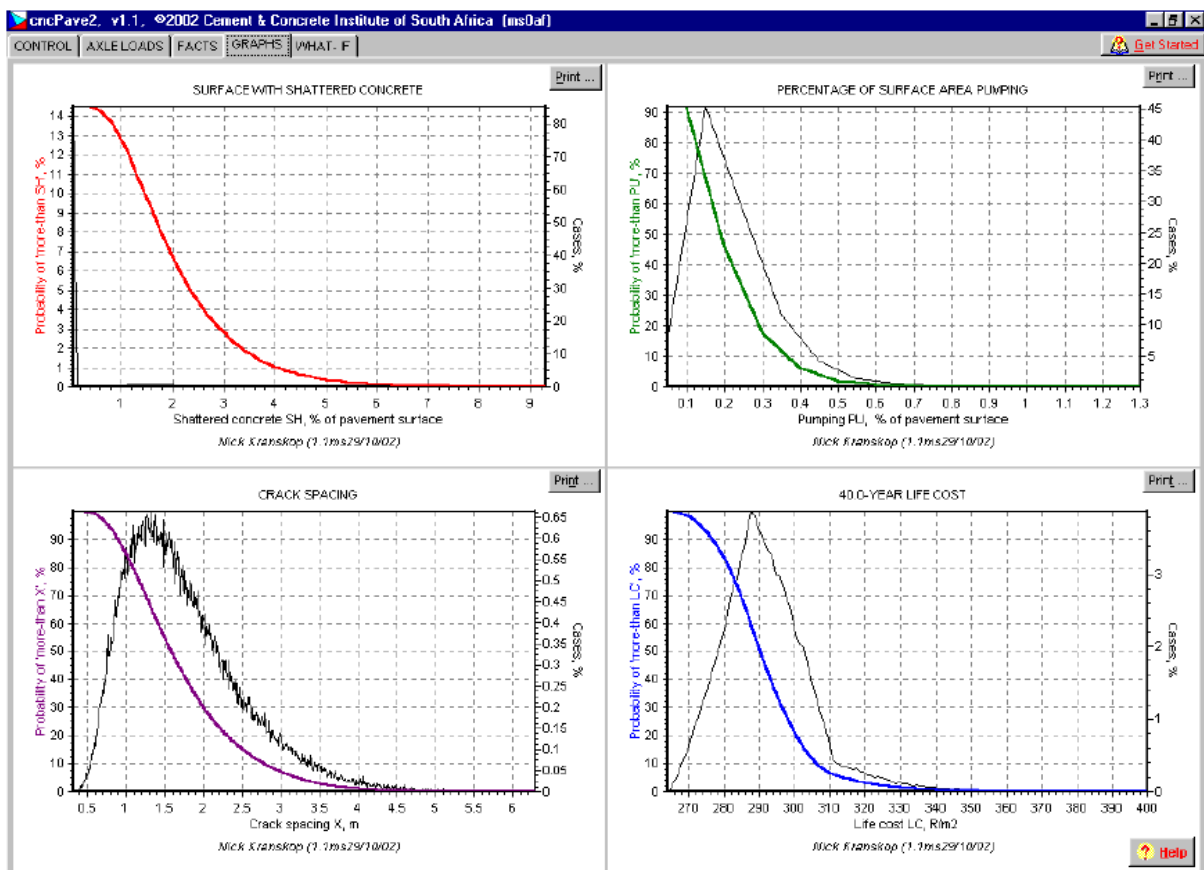
Figure 2.14 Graphs screen from cncPave showing probability distributions of the decision variables (Slavik, et al. 2004)

The current cncPave version 4.04 inludes 29 constants and 18 variables as input parameters. Of the 18 input variables, 17 have triangular distributions, while one, the

31

dynamic axle load, follows an empirical distribution. The dynamic axle load distribution was obtained by means of weigh in motion (WIM) measurements (Cement & Concrete Institute 2001)

The basic equation by which cncPave calculates crack spacing was derived from the revised American M-E PDG's approach for CRCP crack spacing developed by D.G. Zollinger, professor at Texas A&M University (Zollinger 2007). The equation as presented below was tweaked for South African conditions and included in the current version of cncPave (Strauss, Personal Communiation between P.J. Strauss and J.A.K. Gerber 2010).

$$\bar{L} = \frac{f'_{t28} - C_i \sigma_{0,i} \left[1 - \frac{2\zeta}{h_{pcc}} \right]}{\frac{f}{2} + \frac{U_m P_b}{c_{1,i} d_b}}$$ [Formerly Equation 2.17]   (2.22)

According to Slavik, et al. 2004 cracks and changes in crack patterns are still being monitored and measured for the validation and calibration of the design system.

2.6 Closure

Presented in the literature review is the most relevant information found about CRCP crack spacing. Due to the limited access to UTCRCP literature, the CRCP method of failure was explored. Punchouts occur when a thin longitudinal crack forms between two narrowly spaced transverse cracks.

The primary factors that influence transverse crack spacing are pavement temperature conditions, shrinkage due to concrete drying, the bond between the concrete and reinforcing steel, characteristics of the reinforcing steel and the interface friction between the slab and supporting substructure.

The supporting substructure can be modelled either as a dense liquid or an elastic solid structure. These two ideologies yield important pavement parameters such as the radius of relative stiffness and concrete elastic modulus which are input parameters in the Mechanistic-Empirical Pavement Design Guide's mean crack spacing formula.

Descriptive statistical measures are used to characterize transverse crack spacing distributions. Mean transverse crack spacing without the characterization thereof is not sufficient in predicting CRCP punchouts.

3 RESEARCH METHODOLOGY

3.1 Introduction

The research methodology for the characterization of transverse crack spacing distributions comprises of three sub-chapters. The first sub-chapter is the research design and comments on the scope of works. The second sub-chapter is the elements that pertain to the UTCRCP crack spacing distribution. This sub-chapter discusses the research instruments, the method of data acquisitioning, and the data analysis procedures. The third sub-chapter is the limitations chapter. In it the limitations that have affected this study are discussed.

3.2 Research Design

The Heidelberg Traffic Control Centre (TCC) APT research project was an experimental study on UTCRCP. A typical Engineering Method to transverse crack spacing characterization was adopted (Figure 3.1). This approach included a combination of simulations, data acquisitioning, modelling procedures and analysis methodologies. Each criterion of the project scope contributed uniquely to the research process and will be discussed below.

3.2.1 Traffic simulation

Traffic simulation was desired to induce pavement deterioration. The opted means of traffic simulation was a full-scale APT device, namely Mobile Load Simulator 66 (MLS 66). This type of technology gives sort after insight on pavement response, structural capacity and accurate load repetitions count under controlled circumstances in a fraction of the time of genuine (real) traffic.

The rare availability and the costs of APT projects are of the difficulties concerning the use of this technology.

3.2.2 Field data acquisition

Field data was used to validate and calibrate existing pavement modelling techniques. Pavement deflection and seismic response parameters were obtained to achieve the above stated. Varying pavement temperatures affect the deflection and seismic responses, thus pavement temperatures were monitored.

Pavement deflection response measurements are relative easy to conduct and cost effective. The quality of the data is device dependent hence a functional calibrated device was requested. As stated, deflection analysis procedures should be validated prior to pavement modelling.

Pavement seismic response testing is a type of non destructive testing (NDT) technique. Equipment is expensive and rarely available. Best results are obtained when the upper (top) pavement layer exhibits uniform, isotropic, homogeneous characteristics (FHWA-CFL/TD-09-002 2009).

Visual surveys of the pavement surface were conducted for record and reference purposes.

3.2.3 Pavement modelling techniques

Mechanistic-Empirical (M-E), linear elastic, probability distribution models and cncPave were used to derive results for transverse crack spacing analyses.

The M-E model used was not originally calibrated for UTCRCP, but for CRCP. The model considers a number of input constants and variables ranging from material and geometric properties to climatic data. The inclusion of linear elastic modelling was specifically to bridge the gaps that occurred due to the various differences between CRCP and UTCRCP. The strengths of the software used are that it can account for a loss of bond between layers in a pavement structure and that it has a relatively short analysis period.

The final modelling procedure opted for was the cncPave probability distribution program, based on the Monte Carlo simulation. This program gave insight into various calculation results especially the confidence intervals for the transverse crack spacing distribution. Due to the relevant recent development of UTCRCP, this model is based on CRCP algorithms calibrated for UTCRCP. Current research is continuously evaluated and annually incorporated in cncPave to better represent UTCRCP characteristics.

3.2.4 Transverse crack spacing analysis

Diagnostic investigations in combination with descriptive statistics lead to the conclusions of this study. Descriptive statistics were used to evaluate the characteristics of transverse crack spacing distributions (Selezneva, et al. 2002).

3.3 Elements Pertaining to UTCRCP Crack Spacing Distribution Characterization

By following the Engineering Method to characterize transverse crack spacing distributions, this section discusses in greater detail the steps enclosed by the dashed lines depicted in Figure 3.1.
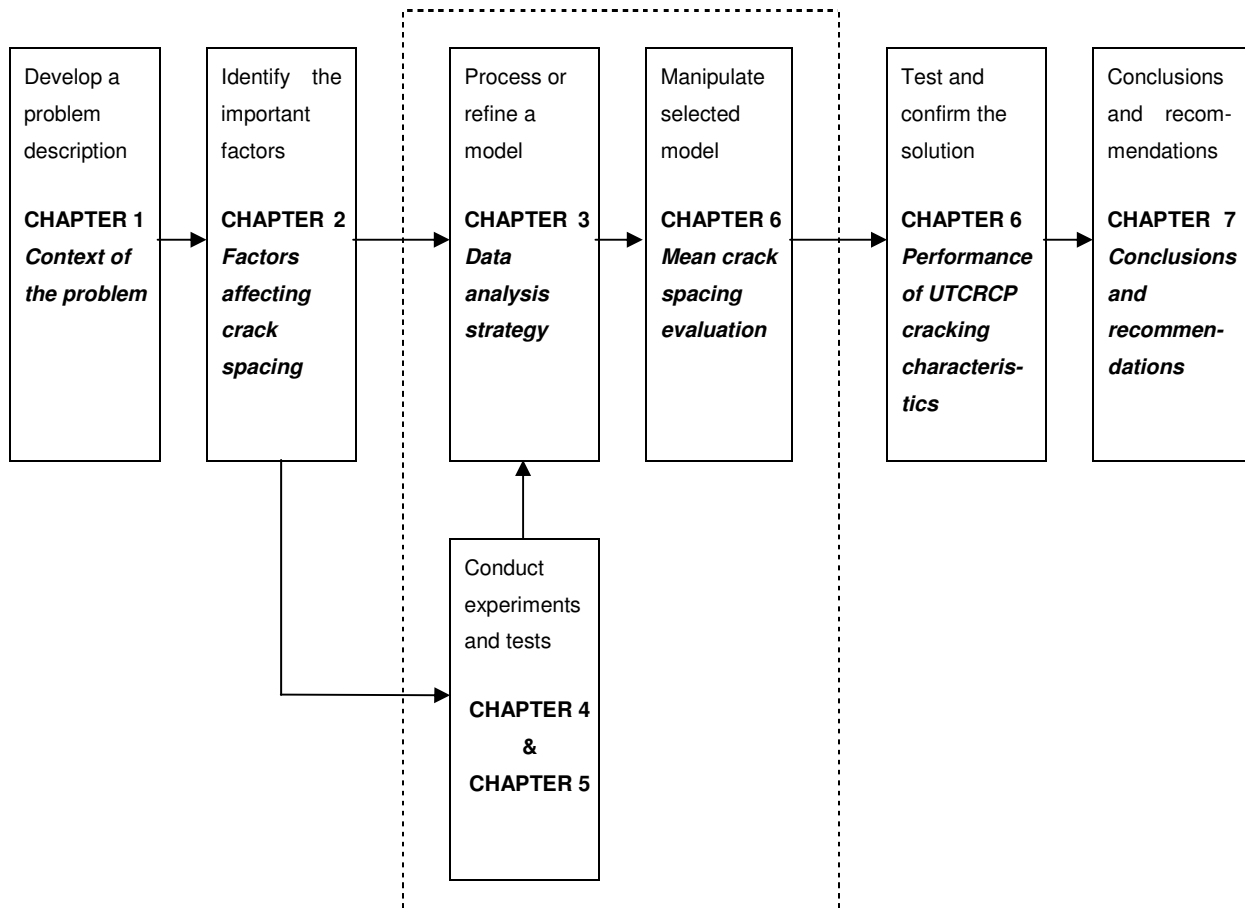
Figure 3.1 The Engineering Method

The properties of the UTCRCP field test section are briefly discussed, followed by the equipment used to obtain the necessary data. The quality of the data is examined and the methodology of interpretation and analysis is presented.

3.3.1 UTCRCP test section

Two experimental STPP UTCRCP test sections were constructed at the Heidelberg TCC in Gauteng. The results of these test sections lead to the construction of UTCRCP LTPP sections as overlays on the screener lane onramps (exits) at the TCC. The southbound screener lane is referred to as the East Bound (E) in the Africon construction report (Africon 2008). By referring to the southbound screener lane as the eastbound the actual reference is

made to the eastern side of the N3, which travels from North to South at the Heidelberg TCC. The southbound screener lane construction phase was subdivided into four sections: E1, E2, E3 & E4 (Africon 2008). This study was conducted on the southbound LTPP screener lane onramp (E4) as depicted in Figure 3.2. The test section had an average cross slope of 3.3 percent towards the V-Drain and an average longitudinal slope of 0.8 percent. A longitudinal joint separated the 2.16 m wide UTCRCP shoulder with the 5.5 m continuously casted UTCRCP traffic lane. No longitudinal joint existed between the UTCRCP traffic lane and the extension of the UTCRCP traffic lane (Figure 3.2).

Due to space constraints, traffic simulation with the APT device was applied on the right edge line (white line). Enough clearance was allowed for heavy vehicles exiting the TCC to safely pass by the test section. The position of simulated traffic met Westergaard's criterion for interior loading.
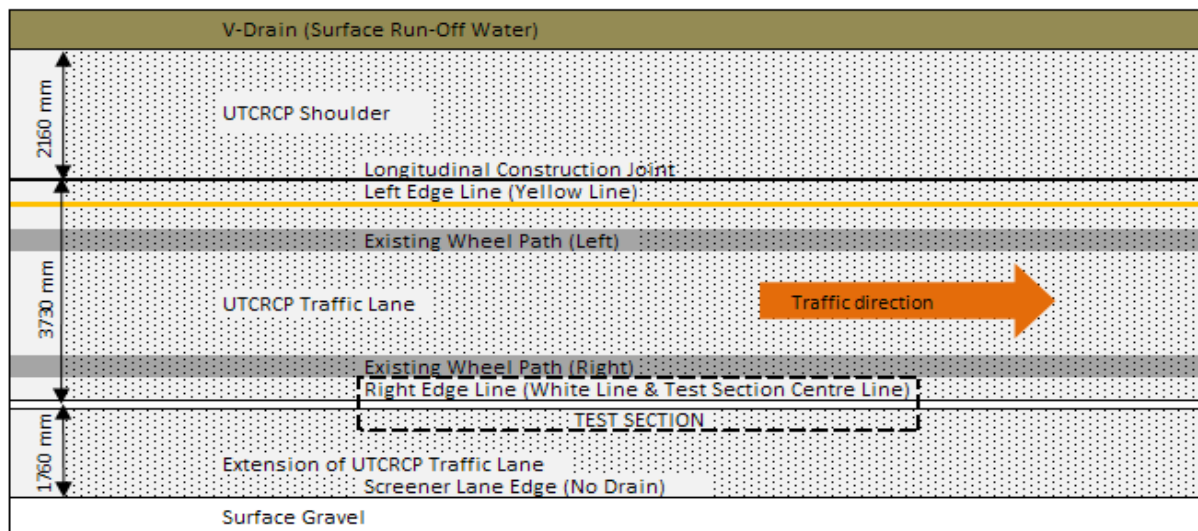
Figure 3.2 APT test section layout

Layer	Name	Thickness (mm)
	UTCRCP	50
	AC Continuously Graded Medium Grade	40
	G1 Crushed Stone Base	150
	C4 Stabilized Subbase	150
	C4 Stabilized Subbase	150
	C6 Stabilized Subbase	150
	G7 Selected Subgrade	150
	Subgrade	150
	Roadbed	Semi Infinite

Figure 3.3 Screener lane pavement structure

36

The UTCRCP overlay was constructed on the existing asphalt (AC) surface. Figure 3.3 depicts the complete pavement structure as it was recorded in the pavement's AS-BUILT drawings. Various concrete mix designs were tested in STPP test sections. The adopted concrete mix design of the southbound UTCRCP screener lane overlay is presented in Table 3.1.

Table 3.1 Concrete mix design (Africon 2008)

Material Component		Unit	Qty
Cementitious Material	**Cement**	kg/m^3	481
	PFA (pulverised fly ash)	kg/m^3	86.6
	CSF (condensed silica fume)	kg/m^3	72.2
Water (maximum)	**-**	l/m^3	175
Water/Cementitious Material Ratio	**-**	**-**	0.325
Aggregate	**6.75 mm**	kg/m^3	972
	Silica Sand	kg/m^3	683
	Steel Fibres	kg/m^3	100
	Polypropylene Fibres	kg/m^3	2
Cement Aggregate Ratio	**-**	**-**	0.39
Admixture per 100g of Cementitious Material	**Chryso Optima 100**	ml	442
	Chryso Premia 100	ml	626
Slump (Steel Fibres added)	**-**	mm	150

The average hardened concrete properties obtained by the mix design in Table 3.1 are presented in Table 3.2.

Table 3.2 Concrete mix properties (Africon 2008)

Properties	Days	Minimum	Maximum	Average
Compressive Strength (MPa)	1	34	66	50
	3	49	84	66
	7	72	92	83
	28	72	127	103
Flexural Strength (MPa)	1	5.5	10.0	7.7
	3	7.2	11.4	9.1
	7	10.2	11.6	10.8
	28	10.2	13.8	12.2

Additional information upon the construction and properties of the UTCRCP layer is presented in Appendix B.

3.3.2 Research instrumentation

Various instruments were used in this study. Traffic simulation was done by means of an APT device, namely Mobile Load Simulator 66 (MLS 66). A Falling Weight Deflectometer (FWD) and Multi Depth Deflectometer (MDD) were used to acquire deflection data. Seismic response data was obtained by using a Portable Seismic Property Analyzer (PSPA) and temperature data was monitored with a MicroDAQ data acquisition temperature logger.

In this section each instrument is discussed.

3.3.2.1 Mobile Load Simulator 66

The MLS 66 (Figure 3.4) is full scale APT device produced by MLS Test Systems (Pty) Ltd in Stellenbosch, South Africa. It is based on the design of the MLS 10 which was used in the study (de Vos 2007) for the development of the Mozambique Mechanistic Pavement Design Method (MMPDM).

Traffic is simulated on the principle of six sets of wheels connected to a rotating chain. A wheel set, also better known as a bogie, consists of a dual set of 305/70R22.5 tyres and each bogie is spaced at an offset of 3.6 m from each other. Thus one complete revolution of the chain yields six applied load repetitions. The force that drives the chain is induced by sets of linear induction motors (LIMs). The load capacities of the bogies are generated by a hydraulic system. The load of each bogie is independently adjustable. A summary of the main characteristics of the MLS66 is presented in Table 3.3.
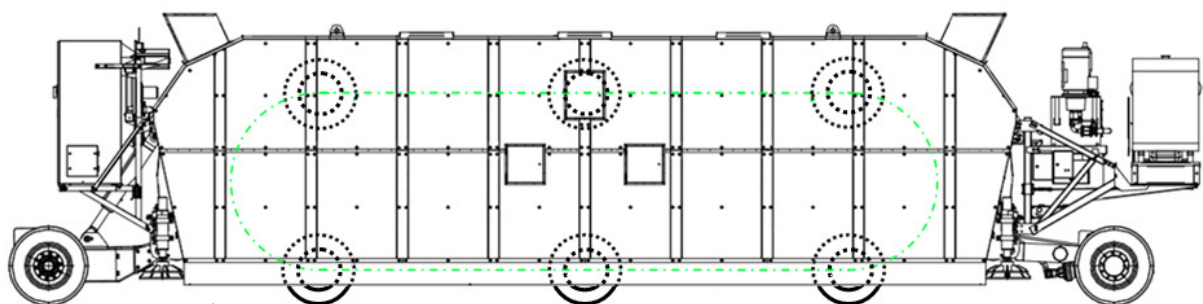
Figure 3.4 Schematic side view of the MLS 66

Table 3.3 Main MLS 66 characteristics

Overall Dimensions (m)	15x3.8x2.6	
Trafficking Wheel Speed (km/h)	Minimum	Maximum
	5.4 (1.5 m/s)	21.6 (6 m/s)
Loading Capacity (kN)	80 (adjustable)	
Load Repetition Frequency (Load Applications per Hour)	Minimum	Maximum
	1500	6000
Load Directions	Uni-directional	
Effective Trafficked Length (m)	6.6	
Traffic Mode	Channelized or Transverse Wander Distributions	
Maneuverability	Remote Controlled	

Traffic simulation was done following a specific sequence of events which included wet testing, dry testing, channelized simulation and transverse wander simulation. The alternation between wet and dry testing as well as the traffic mode and axle count at occurrence is summarized in Table 3.4. Wet testing comprises of water that is sprayed on the surface of the pavement to simulate rain or moisten conditions. The duration of a typical wet test in this study, as agreed with the South African National Road Agency Ltd (SANRAL), consisted of 40 000 axle load repetitions (approximately seven hours of continuously trafficking). Wet tests were followed by 120 000 axle load repetitions of normal trafficking (dry surface, no water added).

Pavement response was monitored under channelized and transverse wandering scenarios. Due to the tight space restrictions on the test section, transverse wandering was only applied over a distance of 200 mm to the one side of the right edge line depicted in Figure 3.2.

A total of 2.8 million axle load repetitions were applied on the UTCRCP surface at 80 kN per load application with the exception of the first 200 000 repetitions, which were conducted at 75 kN. With a damage factor of 4.5 the total equivalent number of axles adds to approximately 63 million. Traffic simulation started in March 2009 and ended in September 2009. During this autumn and winter period, traffic simulation was not done continuously, but at appointed intervals.

Table 3.4 MLS 66 test setup and load application plan

Total Axle Load Repetitions	Axle Load Repetitions	Surface Condition	Load (kN)	Tyre Pressure (kPa@25°C)	Traffic Mode	Trafficking Speed (m/s)
0	200000	Dry	75	800	Channalized	6
200000	100000	Dry	80	800	Channalized	6
300000	60000	Wet	80	800	Channalized	6
360000	120000	Dry	80	800	Channalized	6
480000	40000	Wet	80	800	Channalized	6
520000	120000	Dry	80	800	Channalized	6
640000	40000	Wet	80	800	Channalized	6
680000	120000	Dry	80	800	Channalized	6
800000	40000	Wet	80	800	Channalized	6
840000	120000	Dry	80	800	Channalized	6
960000	40000	Wet	80	800	Channalized	6
1000000	40000	Wet	80	800	Wander	6
1040000	120000	Dry	80	800	Wander	6
1160000	40000	Wet	80	800	Wander	6
1200000	120000	Dry	80	800	Channalized	6
1320000	40000	Wet	80	800	Channalized	6
1360000	120000	Dry	80	800	Channalized	6
1480000	40000	Wet	80	800	Channalized	6
1520000	120000	Dry	80	800	Channalized	6
1640000	40000	Wet	80	800	Wander	6
1680000	120000	Dry	80	800	Wander	6
1800000	40000	Wet	80	800	Wander	6
1840000	120000	Dry	80	800	Wander	6
1960000	40000	Wet	80	800	Wander	6
2000000	120000	Dry	80	800	Wander	6
2120000	40000	Wet	80	800	Wander	6
2160000	120000	Dry	80	800	Wander	6
2280000	40000	Wet	80	800	Wander	6
2320000	120000	Dry	80	800	Wander	6
2440000	40000	Wet	80	800	Wander	6
2480000	120000	Dry	80	800	Wander	6
2600000	40000	Wet	80	800	Wander	6
2640000	120000	Dry	80	800	Wander	6
2760000	40000	Wet	80	800	Wander	6
2800000						

3.3.2.2 Falling Weight Deflectometer

The FWD is a well known device that is used to obtain deflection data on pavement surfaces. A branch from Specialised Road Technologies (Pty) Ltd (SRT), situated in Boksburg Gauteng, was contracted to conduct the deflection tests with their machines.

The test section enclosed by the dashed lines in Figure 3.2 is enlarged and depicted in Figure 3.5.
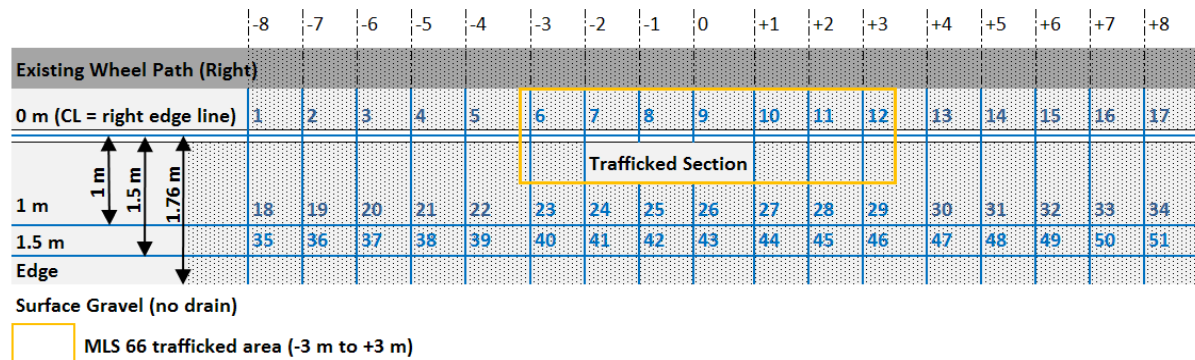
Figure 3.5 APT test section detailed layout for FWD measurements (from Figure 3.2)

A grid (blue lines Figure 3.5) was marked out on the test section to indicate where the load plate of the FWD should be positioned whilst deflection measurements were done. High density FWD tests were conducted on the test section at the various stations as follows. Station 1 to 17 was situated on the centre line (CL) of the test section, thus deflection measurement were done in the simulated wheel path. Stations 18 to 34 were at an offset of 1 m from the CL and stations 35 to 51 were at an offset of 1.5 m from the CL on the edge of the pavement. All stations were at an offset of 1 m from each other in the longitudinal direction (see top of Figure 3.5, -8 m to +8 m).

Deflection data was collected twice at all 51 stations. Once at 1.2 million applied axle load repetitions and the second time a year after the completion of the APT project. Hence no FWD data was collected at zero axle load repetitions i.e. no base line deflections. To represent interior pavement base line deflection response, stations 1 to 5, 13 to 17, 18 to 22 and 30 to 34 were selected. These stations lay outside of the trafficked section (Figure 3.5) thus it was assumed that these stations would exhibit base line deflection responses.

Deflection measurements were done in the longitudinal direction at 40kN, 60kN and 80kN falling weights for each station. The load plate radius was 150 mm and the FWD sensors conformed to the following spacing setup; 0, 200, 300, 450, 600, 900, 1200, 1500, 1800 mm from the centre of the load plate.

3.3.2.3 Multi Depth Deflectometer

A MDD measures in-situ elastic deflections or permanent deformation at various depths or layers in a pavement system. A single MDD was installed and calibrated in the centre of the test section, by the Council for Scientific and Industrial Research (CSIR) in South Africa.

41

The trafficked section enclosed by the yellow rectangle in Figure 3.5 is enlarged and depicted in Figure 3.6. The JDMD anchor rod holes will be discussed in Chapter five.
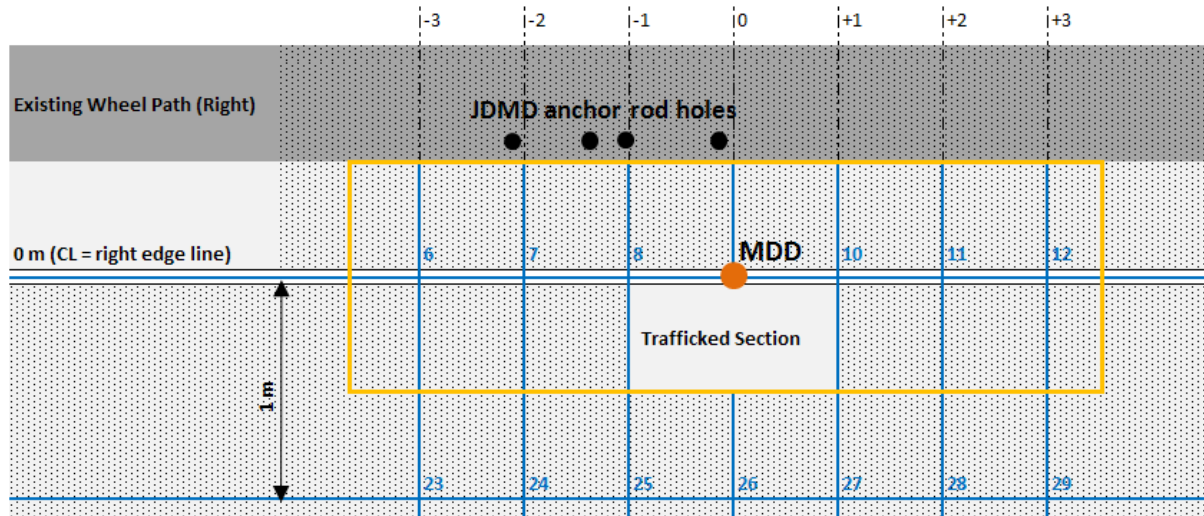
Figure 3.6 MDD position on the test section (from Figure 3.5)

The basis of the patented MDD system is a series of linear variable differential transducer (LVDT) modules that are mounted on a rod in a 39 mm diameter hole in the test section. Up to six LVDT modules can be mounted at various depths in the hole. The LVDT module measures the displacement of the soil relative to the rod to an accuracy of 10 microns.

In this study only two LVDT modules were installed. A LVDT module was installed at a depth of 20 mm in the UTCRCP layer. Another was installed at a depth of 170 mm from the UTCRCP surface i.e. approximately in the middle of the G1 granular layer. This was done to monitor in-situ pavement deflection response whilst the MLS 66 was applying axle loads to the pavement in the channelized or transverse wander mode. Deflection measurements were taken at regular intervals through the duration of the APT experimental project.

3.3.2.4 *Portable Seismic Property Analyzer*

Seismic stiffness response of the UTCRCP layer was conducted with the PSPA (Figure 3.7). The device consists of a source (S) and two receivers (R_A, R_B), packaged into a hand portable system. The PSPA is connected via USB to a laptop computer, which makes for instantaneous viewing of acquired data. The operating principle of the PSPA is based on the following. The source generates stress waves in a medium whereas the receivers detect the stress waves in the medium. The Ultrasonic Surface Wave (USW) interpretation method is then used to determine the modulus of the medium (material). This method utilizes the surface wave energy to determine the variation in surface wave velocity with wavelength.

The variability of test results with the PSPA is less than three percent without moving the device and around seven percent when the device is moved in a small area (de Vos 2007).
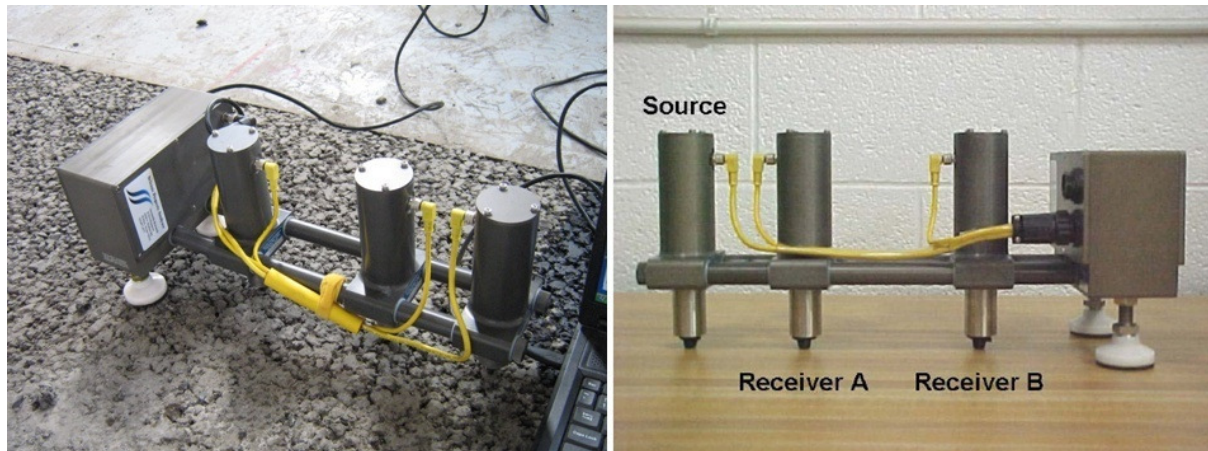
Figure 3.7 Portable Seismic Property Analyzer (PSPA)

The test section's seismic stiffness response was monitored four times consisting of the following intervals; 0, 750 000, 1 200 000 and 2 800 000 applied axle load repetitions. Measurements were taken at each station (Figure 3.8) in the longitudinal and transverse direction. This was done to monitor the deterioration of the UTCRCP layer and to evaluate if there existed a difference in the direction of deterioration due to the effects of channelized traffic loading.
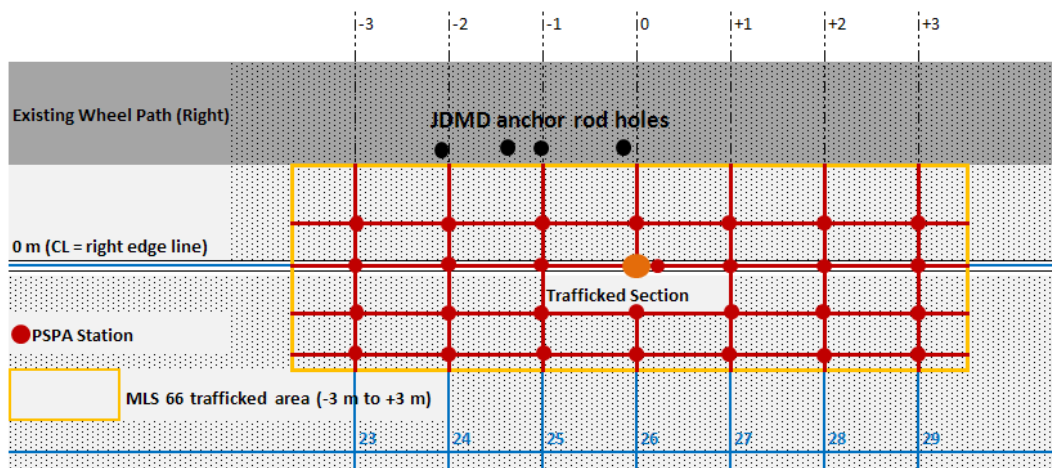
Figure 3.8 PSPA station layout on the test section

Station offsets were positioned in the channelized longitudinal wheel path i.e. on the centre line, 200 mm above and below the centre line and 450 mm below the centre line as depicted in Figure 3.8. The source-senor-spacing configuration was as follows. The distance between the S and R_A was 50.5 mm and the distance between S and R_B was 127 mm.

43

3.3.2.5 MicroDAQ Data Acquisition

A USB-73T8 MicroDAQ Data Acquisition device was used to monitor the temperature of the concrete slab. Thermocouples were installed in the pavement on the 1 m offset line (Figure 3.5) at the following depths; at the surface, depth of steel (25 mm) and at 50 mm. These temperature measurements were requirements in the M-E calculations.

3.3.3 Data

To discuss the data used in the analysis procedure it is divided into four categories consisting of deflection data, seismic response data, temperature data and visual surveys.

3.3.3.1 Deflection Data

Transverse cracks, a reduction or loss of bond between layers, moisture content and a number of other factors affect the shape of a deflection bowl. The high density of FWD measurements was used in statistical analyses, thus reducing the uncertainty of the quality of the deflection bowls. Maximum deflections varied along the test section as was expected. Similar maximum deflections were grouped as depicted in Figure 3.9 to account for the variations.
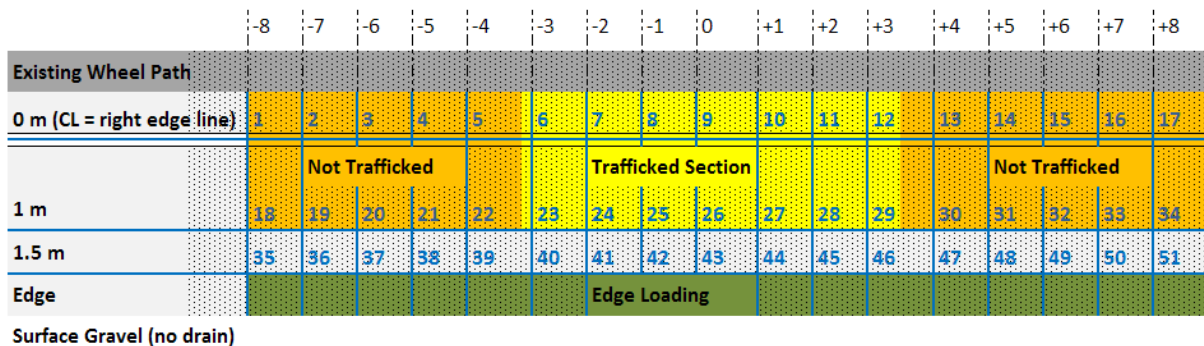
Figure 3.9 FWD maximum deflection groupings to account for variation

The sections where no applied traffic had been induced yielded the lowest maximum deflections. FWDs taken on the edge yielded the highest maximum deflections.

MDD data was captured consistently as the APT project progressed. A transverse crack formed on the 0 m transverse offset line (Figure 3.6) and grew towards the weak spot in the pavement which was the 39 mm diameter hole in which the LVDTs of the MDD were installed.

Big amounts of spalling at this crack interface lead to the termination of data capturing with the MDD at approximately 2.3 million applied axle load repetitions.

3.3.3.2 Seismic Response Data

The measured seismic response (waveform) undergoes transformation known as the Fourier transformation. This transformation step makes the determination of velocity with wavelength much easier. Coinciding with this transformation is the phase spectrum (Figure 3.10), which can be considered as an intermediate step between the time records of the waveforms and the final product i.e. the displayed data on the laptop computer.
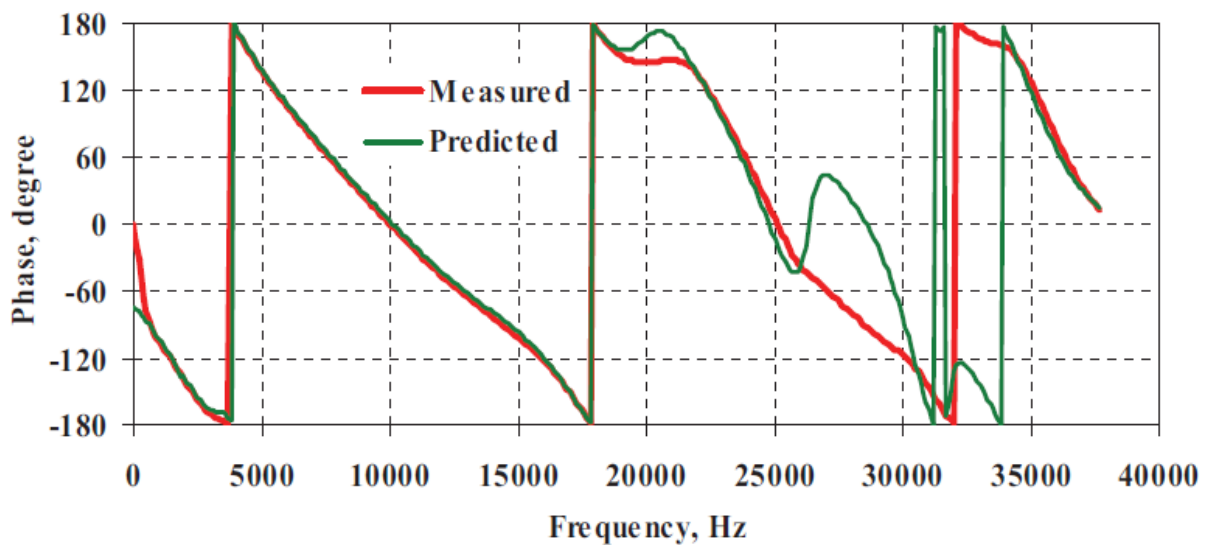
Figure 3.10 Typical phase spectra obtained from a time record

The phase spectrum consists of the measured profile and a predicted (estimated) profile. The predicted profile is used to compute the displayed data. Thus a good waveform yields a better fit between the measured and predicted phase spectrum and more precise data. Factors that influence the waveform and thus the phase spectra are the uniformity, thickness, isotropic and homogeneous characteristic of the layer under consideration.

The UTCRCP properties have not entirely conformed to the requirements for best results, mentioned in Section 3.2.2. This was evident in the phase spectra results of the obtained data. In general the PSPA measurements gave insight to the reduction characteristics of UTCRCP stiffness. A function of the PSPA known as Echo-Impact (EI) calculates layer thickness. The Echo-Impact function indicated that the layer thickness of the UTCRCP conforms to approximately 50 mm.

3.3.3.3 Temperature Data

The pavement temperatures were monitored in 24 hour cycles at 5 minute intervals. This was done during the winter period to get an indication of pavement response to ambient winter conditions at the various depths. The obtained data revealed this response in detail. Temperature data acquisitioning occurred only for a short period during the APT project and not throughout the project. This was due to an arrangement regarding the equipment. The collected data however outlined what response to expect and created the frame of reference for winter temperatures in this study.

Additional climate data comprising of the monthly precipitation records of the last ten years and the maximum ambient temperatures for the period of the UTCRCP construction phase were obtained from the South African Weather Service (SAWS).

3.3.3.4 Visual Surveys

A crack map was constructed by visually inspecting the test section and recording the cracks on scale. The distances between the cracks were measured and served as a comparison for the models and techniques used to analyze the data.

3.3.4 Data analysis strategy

The main goal of the data analyses was to characterize the transverse crack spacing distributions. The procedure consisted out of five parts; Mechanistic-Empirical Analysis Phase I, Linear Elastic Analysis, Mechanistic-Empirical Analysis Phase II, Statistical Analysis and Diagnostic Investigation. Each procedure is explained and discussed.

3.3.4.1 Mechanistic-Empirical Analysis Phase I

The objectives of this analysis were to obtain two UTCRCP variables, the radius of relative stiffness (l_k or l_e) and the concrete's modulus of elasticity (E_{pcc}). The following steps explain the procedure.

Step 1: The FWD deflection measurements were categorized as discussed in Section 3.3.3.1. The 'Not Trafficked' sections (Figure 3.9) were merged into the same group and the 'Edge Loading' FWD deflection measurements were not considered in this analysis.

Step 2: The AREA parameter (A_4) was calculated for each individual accepted deflection bowl in the categorized sections (Trafficked and Not Trafficked, Figure 3.9) using Equation 2.3.

Consider the DL-Model:

Step 3: The radius of relative stiffness (l_k) for each A_4 parameter was determined by using Equation 2.4.

Step 4: The modulus of substructure k_{A4} was calculated for each l_k using Equation 2.5.

Step 5: The modulus of substructures k_{A4} were adjusted to k_{B4} with Equation 2.6.

Step 6: The fictitious concrete elastic modulus (E_e) of each deflection bowl was determined with Equation 2.7. It was assumed that the Poisson's ratio of concrete was 0.15.

Step 7: The concrete elastic modulus (E_{pcc}) of each deflection bowl was determined with Equation 2.13.

Consider the ES-Model:

Step 8: Steps 1 and 2 were repeated.

Step 9: The radius of relative stiffness (l_e) for each A_4 parameter was determined by using Equation 2.8.

Step 10: The elastic modulus of the subgrade (E_s) was calculated for each l_e with Equation 2.9.

Step 11: The fictitious concrete elastic modulus (E_e) of each deflection bowl was determined with Equation 2.10. It was assumed that the Poisson's ratio of concrete and the subgrade was 0.15 and 0.35 respectively.

Step 12: The concrete elastic modulus (E_{pcc}) of each deflection bowl was determined with Equation 2.13.

This concludes the first phase of the M-E analysis. Two sets (DL & ES) of the desired variables, radius of relative stiffness and the elastic modulus of concrete, were calculated.

3.3.4.2 Linear Elastic Analysis

As with the first phase of the M-E analysis the objectives of this analysis were also to obtain two UTCRCP variables, the radius of relative stiffness ($l_{elastic}$) and the concrete modulus of elasticity (E_{pcc}).

The categorized FWD results (Figure 3.9) were statistically analyzed by means of maximum deflections and ranked from the 10th percentile to the 90th percentile. The linear elastic software programe BISAR 3.0 was used to simulate the 10th, 50th and 90th percentile FWD deflection bowel with a 40, 60 and 80 kN falling weight.

In each case the deflection bowl was iteratively calculated until the simulated deflection bowl was as close as possible to the measured deflection bowl without unrealistic stiffness attributed to any layers. A guide for various realistic pavement stiffness ranges were taken from the "*Over view of the South African Mechnistic Pavement Design Analysis Method*" (Theyse, de Beer and Rust 1996). The initial pavement structure is depicted in Figure 3.3.

With the resulting E_{pcc}, Equation 3.1 was substituted into Equation 3.2 to iteratively compute the radius of relative stiffness ($l_{elastic}$).

$$k = \frac{P}{8wl^2}\left[1 + \frac{1}{2\pi}\left\{\ln\left(\frac{a}{2l}\right) + \gamma - 1.25\right\}\left(\frac{a}{l}\right)^2\right] \qquad \text{[Formerly 2.5]} \quad (3.1)$$

$$l_{elastic} = \sqrt[4]{\frac{E_{pcc}h_{pcc}{}^3}{12(1 - \mu_{pcc}{}^2)k}} \qquad (3.2)$$

Where;

E_{pcc} =   elastic modulus of concrete (psi)

$l_{elastic}$ =   radius of relative stiffness calculated for the elastic model (in)

μ_{pcc} =   Portland concrete cement Poisson's ratio

k =   modulus of substructure reaction (psi/in)

h_{pcc} =   Portland concrete cement thickness (in)

Edge loading FWD results were discarded for this analysis. Only categorized FWD results that conformed to interior slab loading conditions were used.

3.3.4.3 *Mechanistic-Empirical Analysis Phase II*

The objective of the second phase of the M-E analysis was to calculate the mean crack spacing parameter ($\bar{L}$).

The variables that were successfully analyzed in the M-E Phase I and in the Linear Elastic Analysis were used in this second phase M-E analysis.

Mean crack spacing was calculated with Equation 2.17. This equation required some pavement temperature variables therefore the temperature data was analyzed and presented as a temperature profile plot along the depth of the UTCRCP.

The results of M-E phase II are various mean crack spacing lengths.

3.3.4.4 Statistical Analysis

The actual crack spacing lengths as recorded in the visuals surveys were analyzed. Descriptive statistical measures such as, mean, median, standard deviation, coefficient of variation (COV) and crack spacing frequency per trail section were computed.

The probability of transverse crack occurrence was calculated by means of Equation 2.14.

3.3.4.5 Diagnostic Investigation

In this investigation, cncPave404 simulations were evaluated with the results of the statistical analysis, M-E PDG crack spacing calculation, MDD data and the PSPA findings. Visual surveys were also considered in this chapter. Thus this investigation collectively analyzes the spectrum of data acquired in the UTCRCP APT project.

3.4 Limitations

This study is limited to a single test section. The test section as depicted in Figure 3.2 formed part of a fully functional screener lane. Thus prior to the APT project no crack growth monitoring was conducted.

Data was primarily captured during the winter season. Therefore the conclusions and assumptions based on the data were made for winter conditions. Whether warmer conditions would yield similar results remains to be investigated.

Maneuverability was restricted on the test section due to space limitations. Concrete barriers were placed between the MLS 66 and the passing traffic on the screener lane. Passing traffic had to use part of the shoulder (Figure 3.2). Under these conditions transverse wandering of the MLS 66 was limited to only 200 mm to the right (in direction of traffic) of the white edge line (Figure 3.2).

The high amount of longitudinal steel (approximately 1%) and steel fibres in the UTCRCP composition influenced the waveform quality of the PSPA device. The PSPA device as it was setup for testing had an upper limit 25 mm and a lower limit of 140 mm in terms of seismic wave penetration depth. Hence it only computed the properties of the material that were in this limit range.

3.5 Closure

The methodology in completing the required steps enclosed by the dashed lines in the Engineering Method (Figure 3.1) had been explained and discussed. The procedures as defined in the research methodology and depicted in Figure 3.11 will be presented in the chapters to follow.
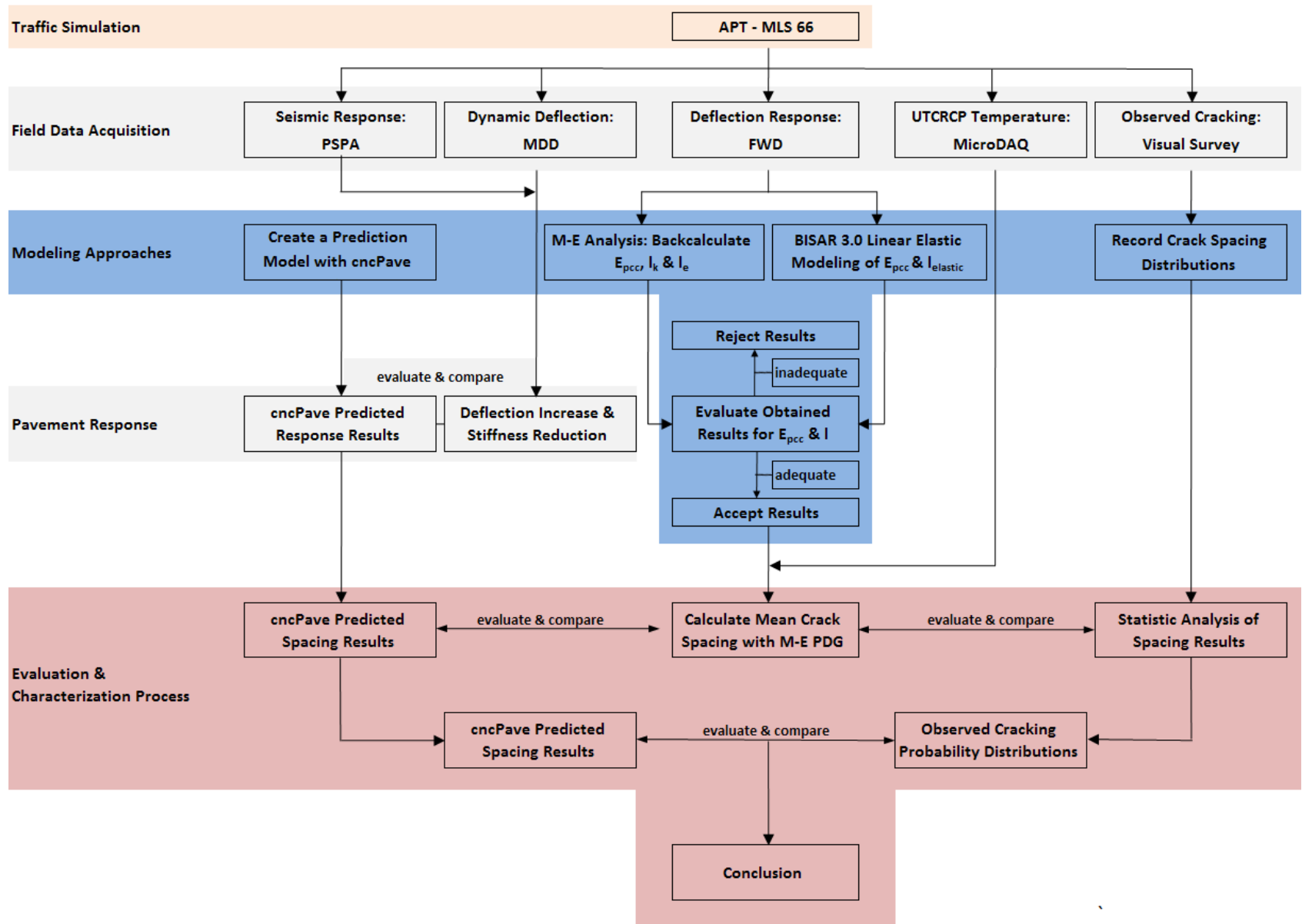
Figure 3.11 Layout of the methodology for transverse cracking characterization

51

4 DETERMINATION OF MEAN CRACK SPACING

4.1 Introduction

The outcome of this chapter is the calculated mean crack spacing for UTCRCP. Preceding the mean crack spacing calculation the radius of relative stiffness and elastic modulus of concrete should first be determined. Hence a mechanistic-empirical method was adopted followed by a linear elastic modelling procedure. Finally mean crack spacing was calculated by means of the M-E PDG's prediction model.

4.2 Mechanistic-Empirical Analysis Phase I

The FWD data results are presented in this section, followed by depictions of the calculated radii of relative stiffness and concrete elastic moduli.

4.2.1 FWD deflection results

The distribution of the FWD analysis procedure is depicted in Figure 4.1. Due to the repetition of procedures the 40 kN FWD results (pink route, Figure 4.1) will primarily be presented and discussed in this chapter. Important summaries will include the 60 and 80 kN FWD results. The complete exposition of the FWD results is presented in Appendix C.
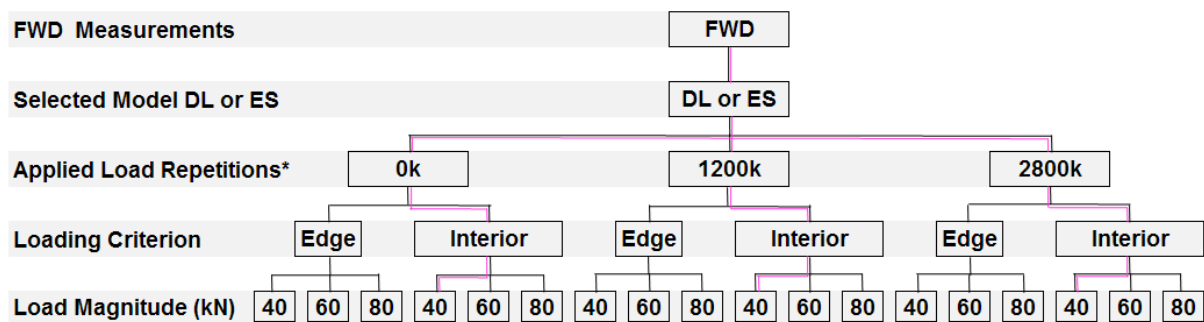
Figure 4.1 Distribution of FWD analysis procedure

Figure 4.2 depicts the longitudinal distribution of the 40 kN FWD maximum deflections. The magnitudes of the obtained deflections were fairly similar for stations situated on the centre line at the positions -8 m to -4 m. Deflection magnitudes rapidly increased for stations at

-3 m to 0 m and increased again for stations situated at 0 m to 3 m. The magnitudes of the deflections for stations situated at position 4 m to 8 m were similar.
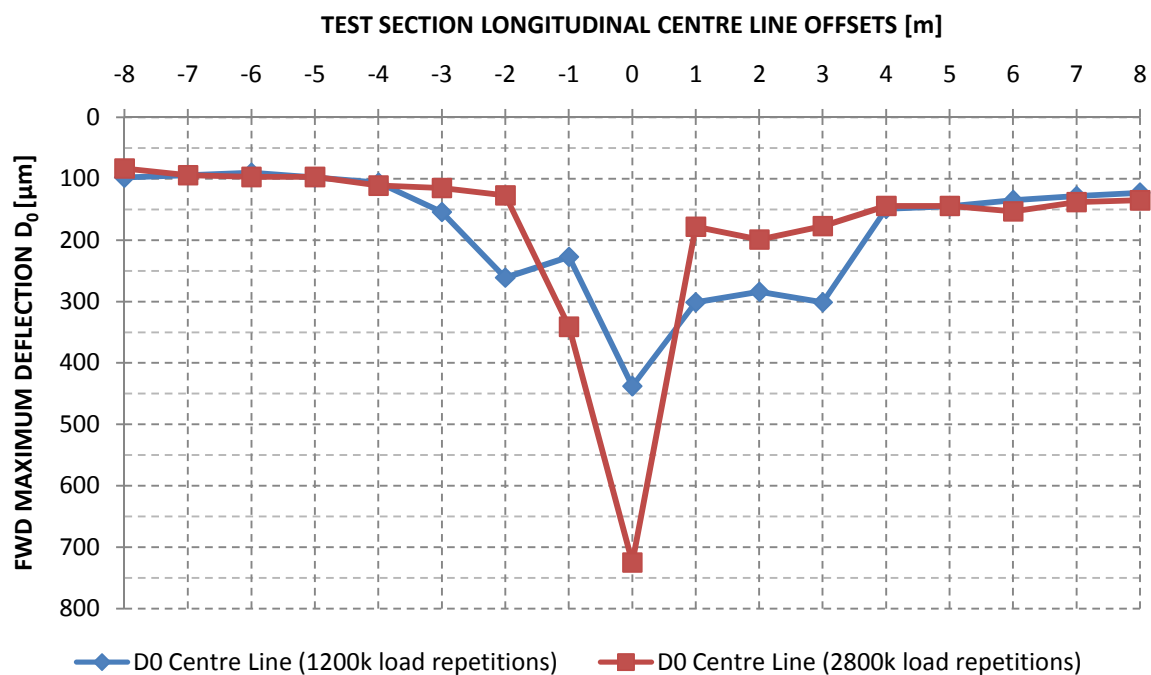
Figure 4.2 Maximum 40 kN FWD deflections along longitudinal centre line (interior)

Traffic simulation was applied between the -3 m and +3 m offsets and included seven FWD stations (Figure 3.9). Out of the seven FWD measurements conducted at 2800k load repetitions, only two (-1 m & 0 m) increased in deflection when compared to the deflections obtained at 1200k load repetitions (Figure 4.2). The increased in deflection of the two points at the -1 m and 0 m offsets, can be attributed to accumulation of pavement damage under loading, due to initial artificially induced damage. When referred to artificial induced damage, reference is made to the installation of the multi depth deflectometer (MDD) at the 0 m offset.

At both stages (1200k & 2800k) the maximum deflection was obtained at the 0 m offset. In general Figure 4.2 depicts a decrease in pavement deflection under APT. This is contrary to expectation and a possible reason for this occurrence is the compaction of the soil under APT.

Figure 4.3 presents the longitudinal distribution of the 60 kN FWD maximum deflections. The 60 kN deflections and the 80 kN deflections revealed the same trend as the 40 kN deflections. However the 40 kN case displays a greater difference between the deflections obtained at the 0 m offset during the 1200k and 2800k intervals. This phenomenon was not further investigated and falls outside the scope of this study.

53
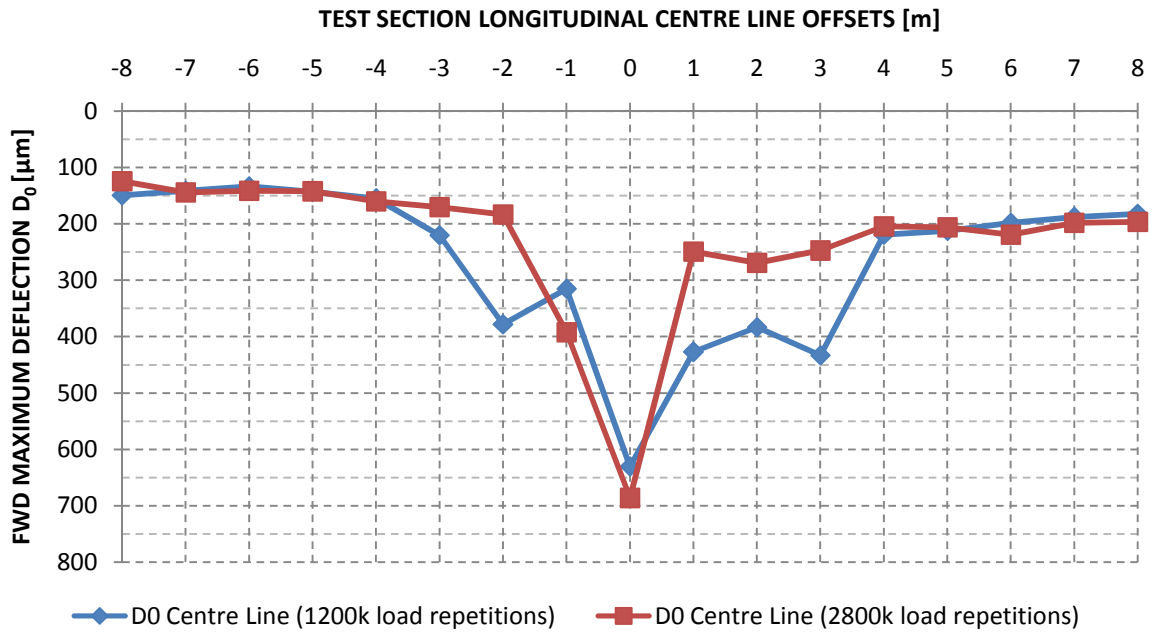
Figure 4.3 Maximum 60 kN FWD deflections along longitudinal centre line (interior)

The initial assumption that the Non-Trafficked interior sections (Figure 3.9 & Figure 4.3) could be used as an indication to the pavement's base line deflection response, yielded favourable results.
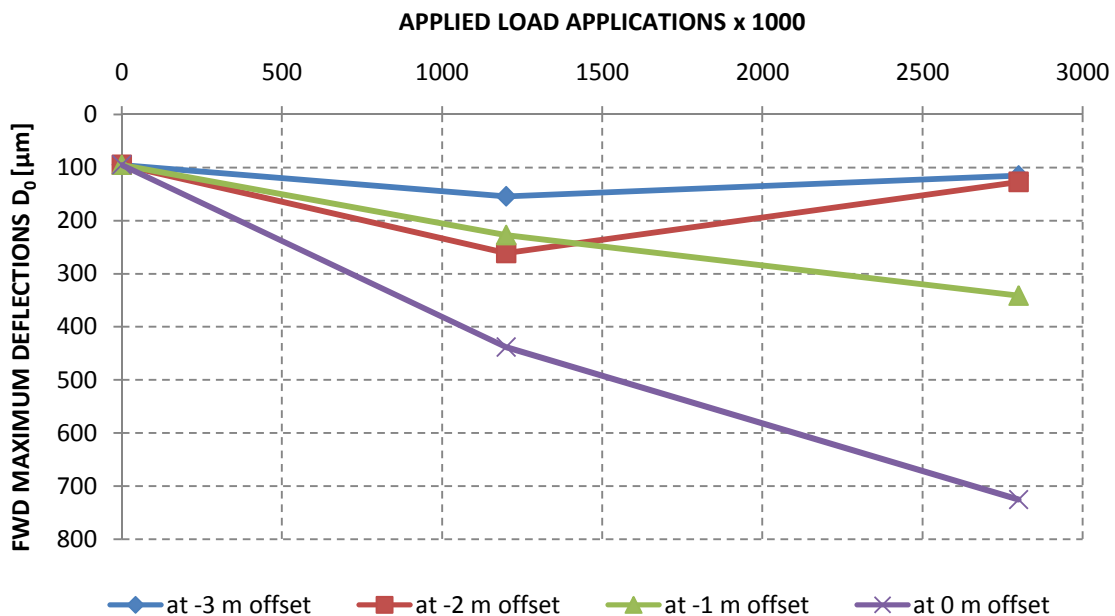
Figure 4.4 Maximum 40 kN FWD deflections at the various interior offsets

Figure 4.4 depicts the 40 kN FWD measurements at the offsets -3 m, -2 m, -1 m and 0 m. The measurements at offsets -3 m and -2 m clearly show, what was discussed as contrary to expectation, the initial increase in deflection followed by a decrease.

4.2.2 Radius of relative stiffness

The radii of relative stiffness for a DL-model and an ES-model were calculated from each deflection bowl. Depicted in Figure 4.5 are the radii of relative stiffness for a DL-model (l_k) calculated from the 40 kN FWD deflection bowls at 1200k load repetitions and 2800 load repetitions. The magnitudes of the radius of relative stiffness along the centre line of the test section were generally slightly greater at 2800k load repetitions than at 1200k load repetitions.
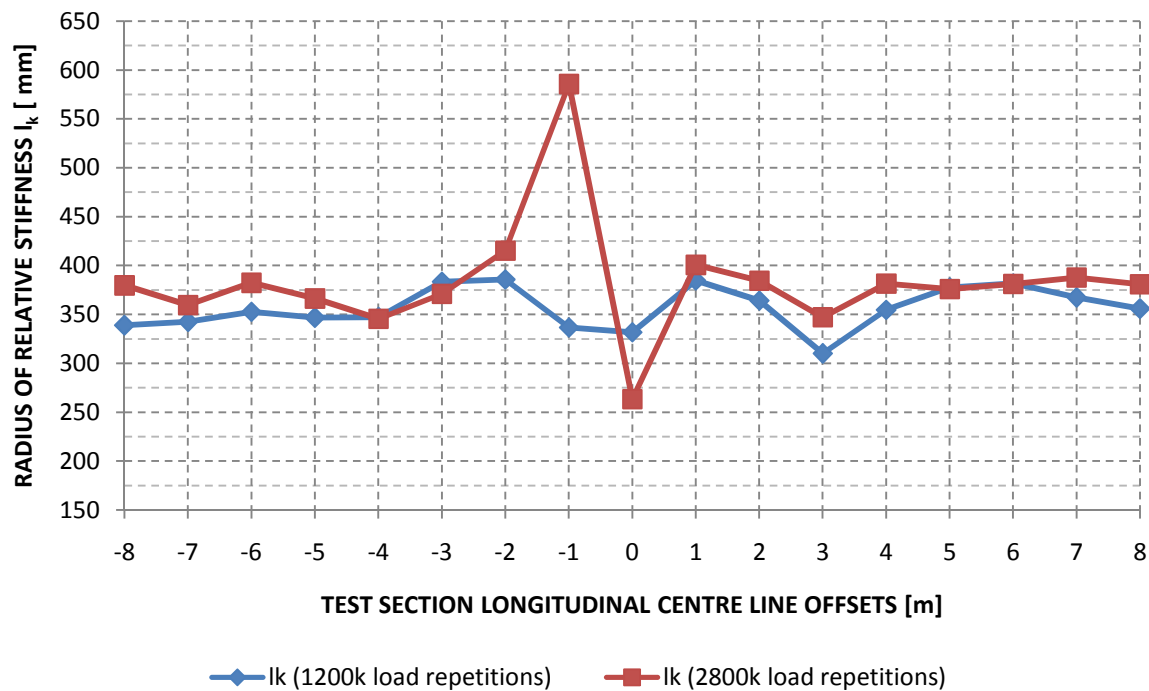
Figure 4.5 Radius of relative stiffness l_k for the DL-model along the longitudinal centre line (40 kN FWD)

The difference in magnitude between the -1 m and 0 m offsets is accounted to a loss of substructure support. According to the theory of the radius of relative stiffness (Equation 4.1)

$$l_k = \sqrt[4]{\frac{E_{pcc}h_{pcc}{}^3}{12(1 - \mu_{pcc}{}^2)k}} \qquad\qquad \text{(Formerly Equation 3.2)} \qquad (4.1)$$

55

the radius of relative stiffness (l_k) will increase if all parameters in Equation 4.1 remains constant except for a reduction in the substructure support, k. A reduction in k would result in an increase in pavement deflection. These increases in deflection are presented in Figure 4.2 at the respected offsets. It should also be mentioned that the deflection bowls at the respected offsets, decreased slowly from D_0 to D_{900} and then rapidly from D_{900} to D_{1800}. Station 8 at the offset of -1 m neighbours the centre position of the test section where spalling and pumping was observed.
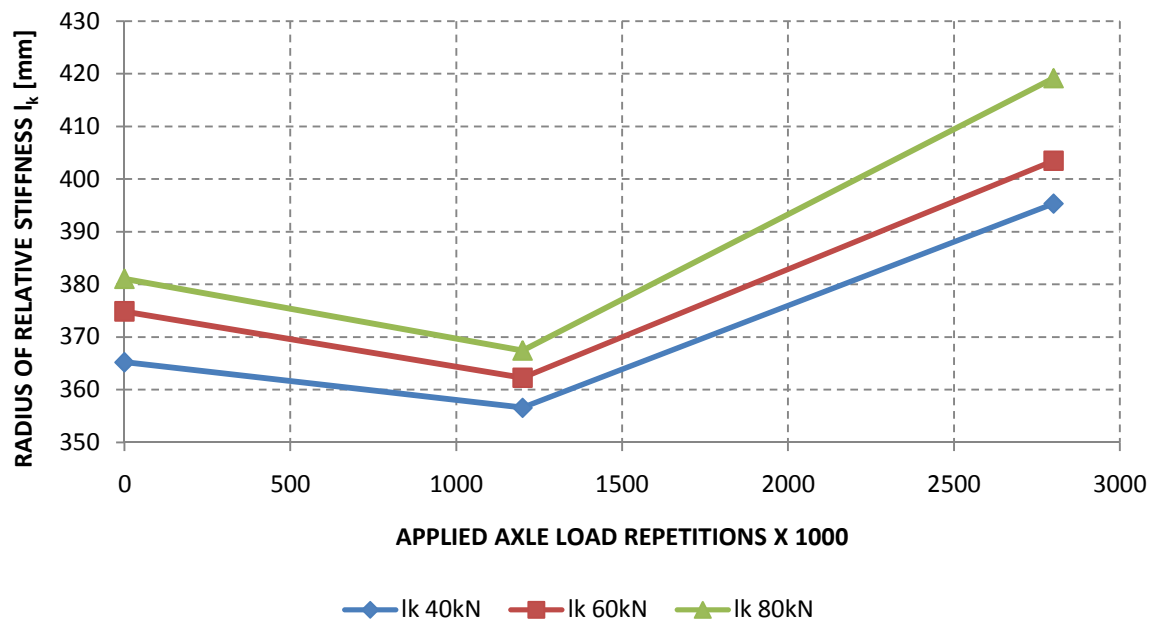
Figure 4.6 Average radius of relative stiffness for the DL-model at the indicated applied axle load repetition interval and specified FWD loading

The average radius of relative stiffness at the various intervals is depicted in Figure 4.6. A reduction in the radius of relative stiffness coincides with a reduction in pavement stiffness, according to the theory presented in Equation 4.1. However an increase in the radius of relative stiffness from the 1200k stage onwards (Figure 4.6), is attributed to an average decrease in FWD measurements at 2800k load repetitions as discussed in Section 4.2.1.

Both models indicated similar pavement responses although the magnitudes of the radii of relative stiffness for the ES-model (Figure 4.7) were slightly lower than the results of the DL-model (Figure 4.8). A similar difference in the ES and DL radius of relative stiffness was observed in FWD backcalculations done by the FHWA on LTPP test sections (FHWA-RD-00-086 2001). Figure 4.8 depicts the variation of the radii of relative stiffness with the AREA parameter A_4 for both models.
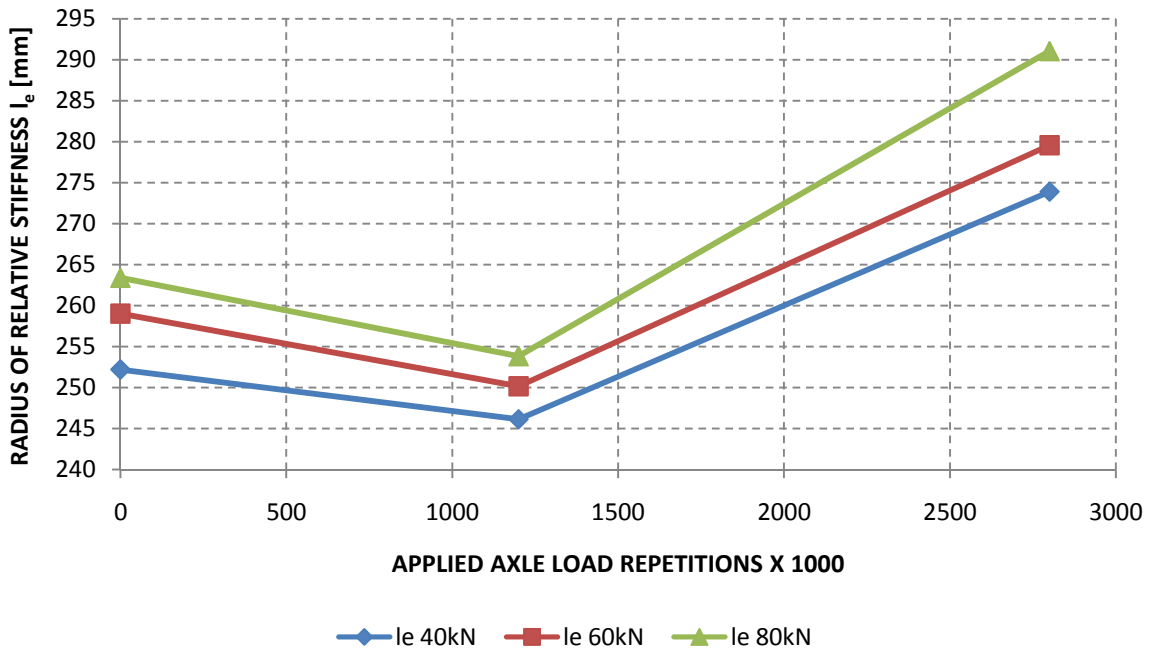
Figure 4.7 Average radius of relative stiffness for the ES-model at the indicated applied axle load repetition interval and specified FWD loading
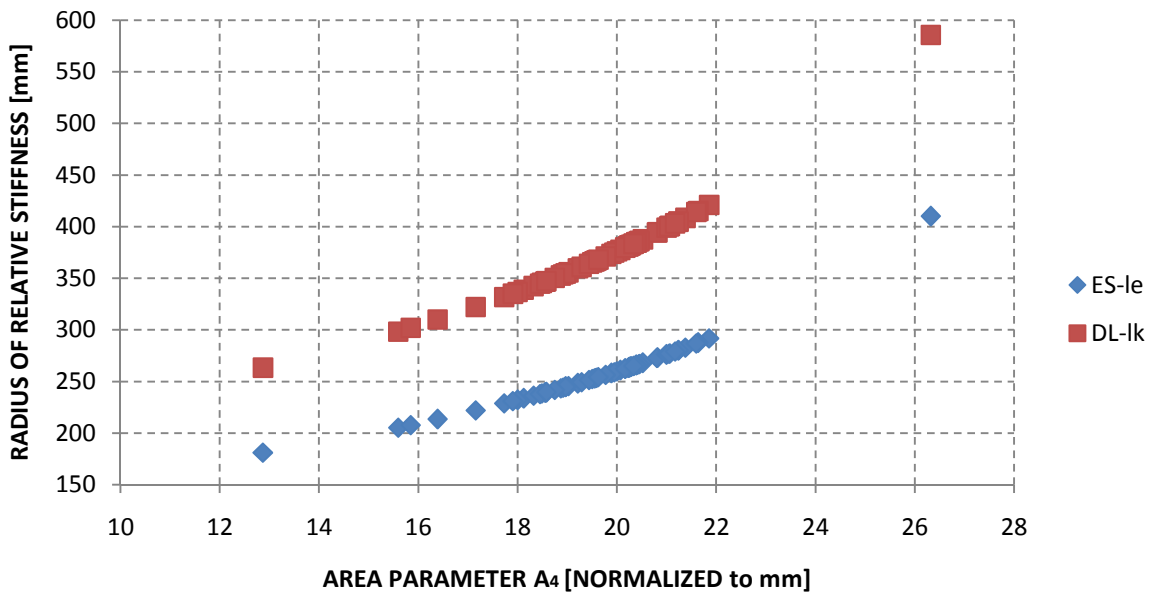
Figure 4.8 Variation of the radii of relative stiffness with the AREA parameter A_4

A greater AREA parameter yields a larger radius of relative stiffness. The magnitude of the AREA parameter is determined by the shape of the FWD deflection bowl. The lower limit for the radius of relative stiffness is set to 570 mm thus all but one of the calculated radii of relative stiffness is beneath the lower limit. This was the case for all FWD load configurations.

57

4.2.3 Elastic modulus of concrete

The backcalculated elastic modulus of the concrete layer (E_{pcc}), was done as discussed and explained in Section 2.3.3 and Section 2.3.4. The E_{pcc} for the DL-model (Figure 4.9) indicates a general increase in layer stiffness along the trafficked area for the measurements conducted at 2800k load applications in comparison with the measurements of the 1200k stage between the offsets -3 m and 3 m.
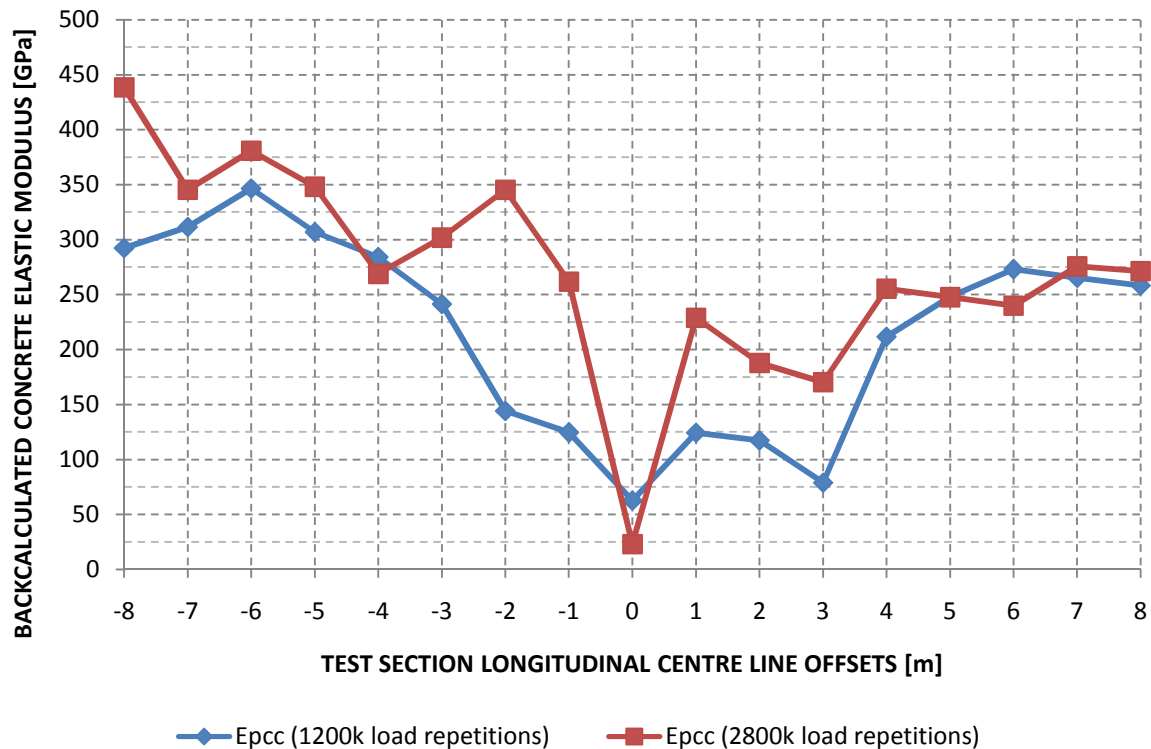
Figure 4.9 Backcalculated concrete elastic modulus for the DL-model (40 kN FWD deflection bowls)

The average E_{pcc} over the length of the tests section reduced as pavement distress was applied and increased again towards the end of the test. This phenomenon is depicted in Figure 4.10 and it replicates the trends of the radius of relative stiffness (Figure 4.6 & Figure 4.7). Figure 4.10 also indicates a difference in the magnitude of the backcalculated E_{pcc} for the three different FWD load configurations. Hence the pavement response indicates visco-elastic characteristics. A greater FWD load results in stiffer pavement response at the same applied axle load repetition interval.

58
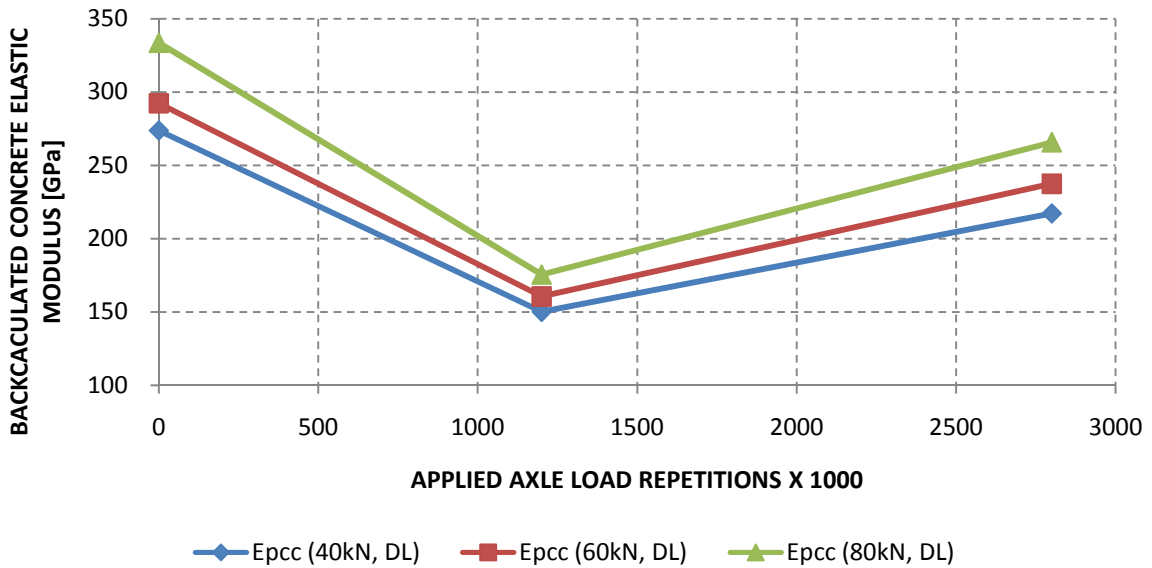
Figure 4.10 Average backcalculated concrete elastic modulus for the DL-model at the indicated applied axle load repetition interval and specified FWD loading
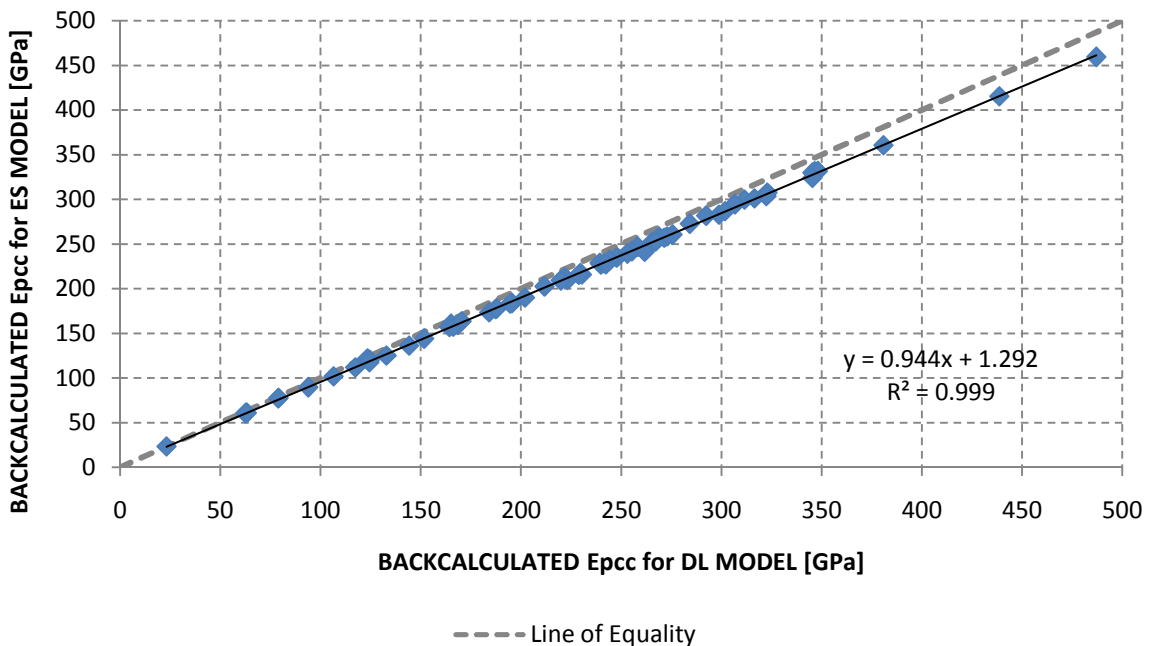
Figure 4.11 Backcalculated concrete elastic modulus E_{pcc} of the DL-model versus the ES-model (40 kN FWD deflection bowls)

According to Kannemeyer, et al. 2008 a finite element model indicated that the expected elastic modulus of the concrete should be in the interval 50 GPa to 80 GPa. The magnitudes of the various backcalculated concrete elastic moduli exceed expected values and are unrealistic. This is the case for both the DL and ES-model. The low radius of relative stiffness calculated with the AREA parameter is one of the major contributors to these

unrealistic backcalculated values. The ES-model yielded slightly lower values than the DL-model (Figure 4.11).

4.2.4 Interim conclusions

The initial assumption that the Non-Trafficked interior sections (Figure 3.9) could be used as an indication to the pavement's base line deflection response, yielded favourable results. Deflection magnitudes in these areas remained similar throughout the application of simulated traffic (Figure 4.3).

Neither the DL-model nor the ES-model yielded radii of relative stiffness between 22.5 in (570 mm) and 80 in (2032 mm). In this case the radii of relative stiffness were below 570 mm thus a linear elastic approach can be used in calculating these parameters.

The results of the low radii of relative stiffness lead to unrealistic backcalculated concrete elastic moduli.

The pavement structure displayed visco-elastic characteristics. A greater FWD load resulted in a stiffer pavement response at the same applied axle load repetition interval (Figure 4.10). Asphalt is known to have this characteristic and the UTCRCP layer was constructed on top of a 40 mm asphalt layer.

In general the M-E Analysis Phase I, yielded unfavorable radii of relative stiffness and concrete elastic modulus parameters. The radius of relative stiffness was outside of the required interval (570 mm to 2032 mm) and the backcalculated elastic modulus of the concrete greatly exceeded the expected interval of 50 GPa to 80 GPa. Therefore these parameters will not directly be used as input parameters for further investigation.

4.3 Linear Elastic Analysis

The nature of the UTCRCP system, due to its severe upper layer stiffness, requires a linear elastic modelling procedure to calculate the radius of relative stiffness and concrete elastic modulus. Since concrete overlays of flexible pavements are becoming more popular; the use of multi-layer linear elastic software programs to calculate not only residual life of the old pavement, but also its stiffness as an input into the design of overlay, is essential (Cement & Concrete Institute 2001).

4.3.1 Linear elastic modelling setup

The software that was used in the modelling procedure was BISAR 3.0 (Shell International Oil Products B.V. 1998). BISAR 3.0 calculates the stresses, strains and displacements in an elastic multi-layer system. The system consists of horizontal layers of uniform thickness resting on a semi-infinite base. The different layers extend infinitely in the horizontal directions and the material of each layer is homogeneous and isotropic. Materials are elastic and have linear stress-strain relationships. The program also accounts for partial slip between layers

Based on maximum deflection the field FWD deflection bowls representing the 10th, 50th and 90th percentile were simulated at the various stages as depicted in Figure 4.12.
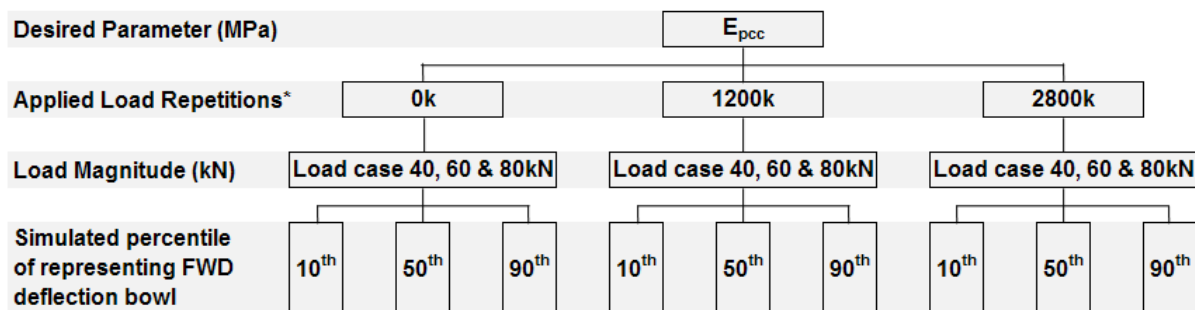
Figure 4.12 Modelling procedure representing the 10th, 50th and 90th percentile FWD deflection bowl, based on maximum deflection

A circular load was used representing the FWD load plate and full friction between the layers was assumed. Each simulated deflection bowl was iteratively adjusted to obtain the closest fit to the real measured profile.
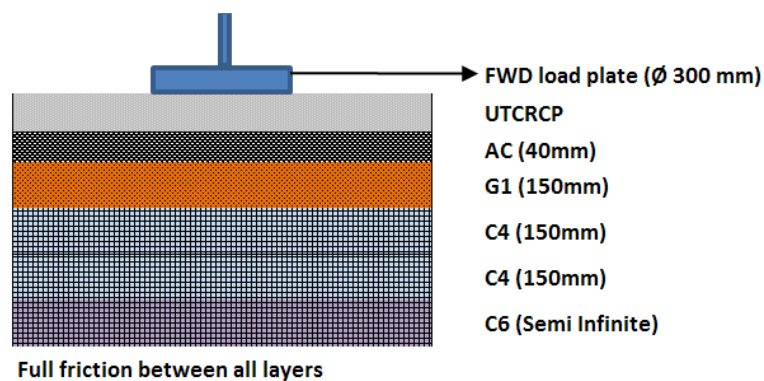
Figure 4.13 BISAR 3.0 modelling setup

4.3.2 BISAR 3.0 modelling results

The 50th percentile 40 kN FWD simulated profiles at the various stages are presented in following three Figures (Figure 4.14, Figure 4.15 & Figure 4.16). The complete exposition of the BISAR 3.0 results is presented in Appendix C.
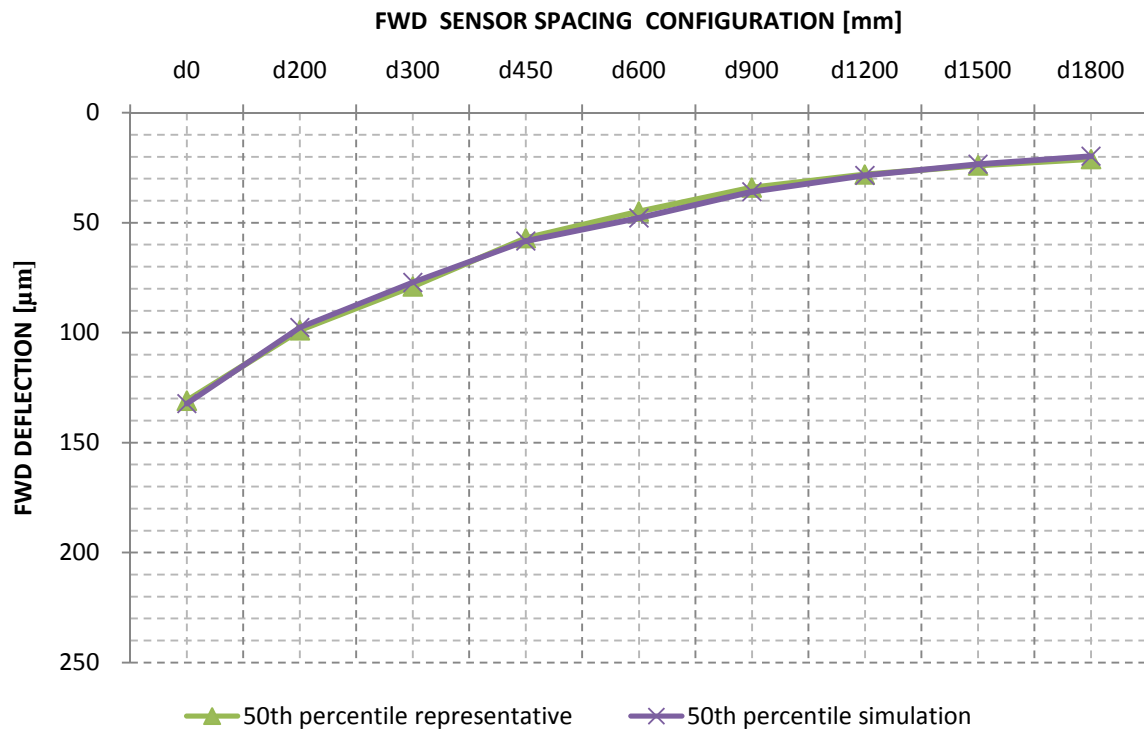
Figure 4.14 BISAR 3.0 simulated FWD deflection profile versus the measured 50th percentile FWD profile for a 40 kN deflection bowl at 0k applied axle load repetitions

The 10th, 50th and 90th simulated FWD deflection profiles displayed a close fit to the measured profiles thus supporting the decision to use a linear elastic modelling technique. However in some cases the measured deflection bowl could not be simulated with the software. Although no non-decreasing deflection bowls were used as percentile representative bowls, BISAR 3.0 was unable to simulate an obtuse angle (between 90° and 180°) that had formed between three consecutive measuring positions with reference to the pavement surface of the real FWD deflection bowl. The phenomenon (Figure 4.17) was observed at some of the 90th percentile deflection bowls, where great magnitudes of the deflection measurements were obtained.
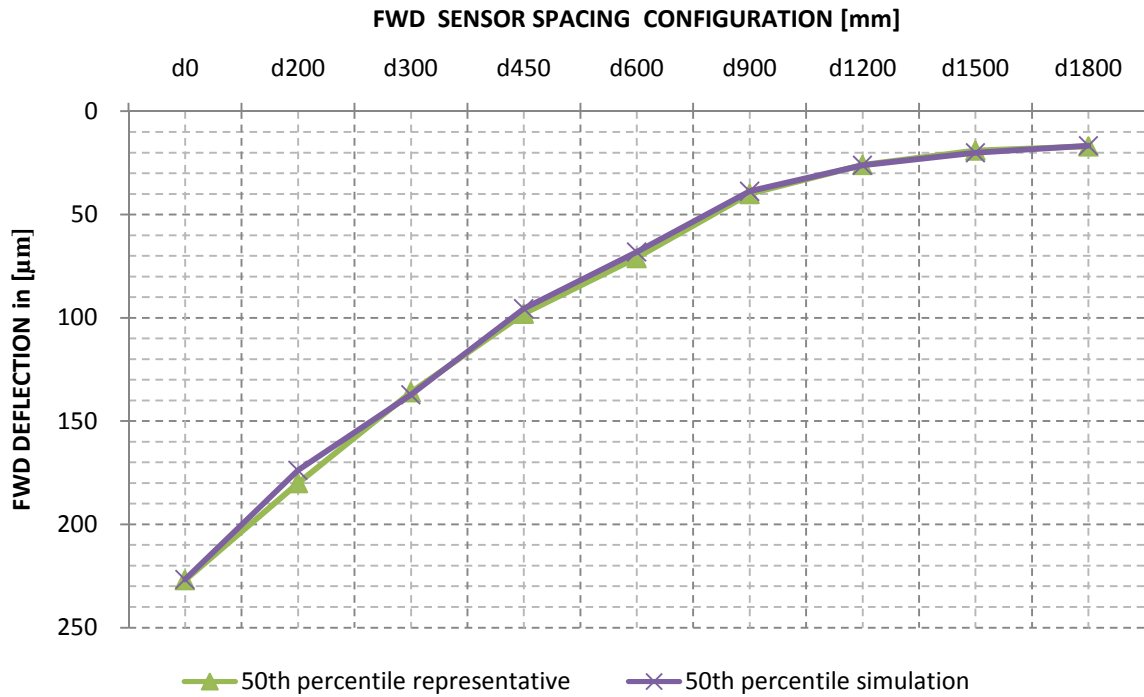
Figure 4.15 BISAR 3.0 simulated FWD deflection profile versus the measured 50th percentile FWD profile for a 40 kN deflection bowl at 1200k applied axle load repetitions
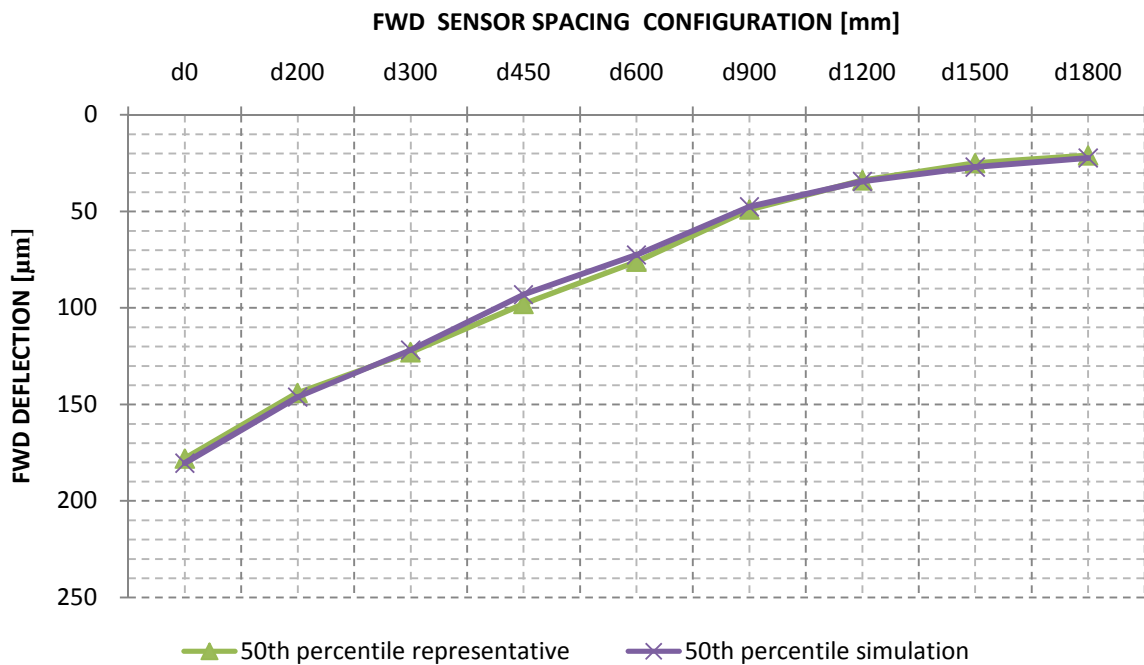
Figure 4.16 BISAR 3.0 simulated FWD deflection profile versus the measured 50th percentile FWD profile for a 40 kN deflection bowl at 2800 k applied axle load repetition

FWD SENSOR SPACING CONFIGURATION [mm]
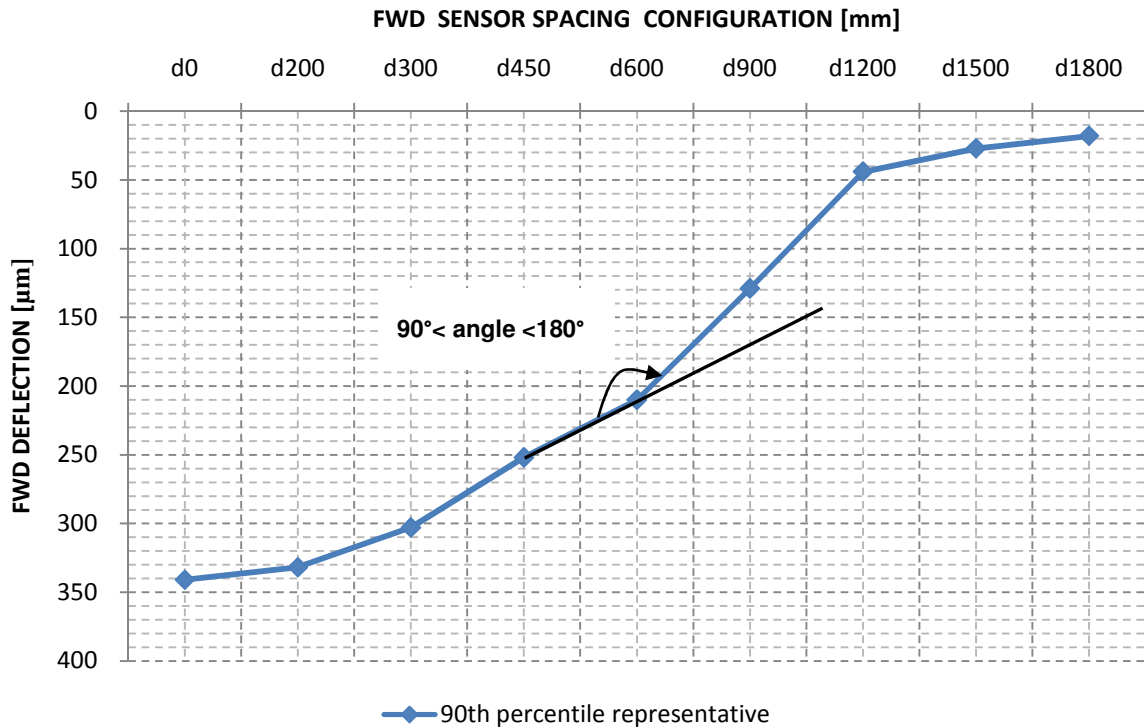
Figure 4.17 Obtuse angle formation between three consecutive deflection points on an actual (not simulated) FWD deflection profile

Deflection bowl descriptors or parameters are often used to indicate the relative structural strength contribution of the various pavement layers. A measured deflection bowl can be described in terms of three distinct zones as depicted in Figure 4.18.
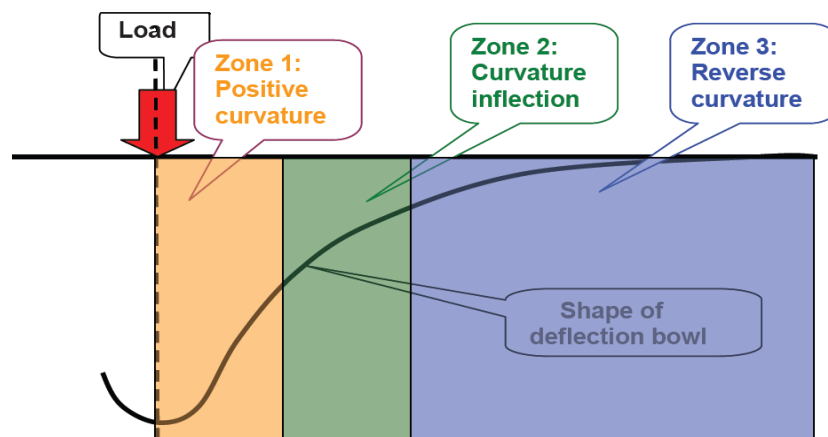
Figure 4.18 Curvature zones of a deflection bowl (Horak 2007).

Zone 1 includes the base layer index (BLI). The BLI gives on indication of the base layer structural condition (Guiama, Horak and Visser 2010). The BLI is calculated by subtracting the deflection measurement D_{300} from D_0. Zone 2 includes the middle layer index (MLI). The

64

MLI gives an indication of the subbase and selected layers' structural condition. The MLI is calculated by subtracting the deflection measurement D_{600} from D_{300}. Zone 3 includes the lower layer index (LLI). The LLI gives an indication of the condition of the lower structural layers, such as the selected and subgrade layers. The LLI is calculated by subtracting the deflection measurement D_{900} from D_{600}. Horak 2007 compiled a *"Deflection bowl parameter structural condition rating criteria"* for various pavement types (Table 4.1).

Table 4.1 Deflection bowl parameter structural condition rating criteria for various pavement types (Horak 2007)

| | Structural condition rating | Deflection bowl parameters | | | | |
		D_0 (µm)	RoC (m)	BLI (µm)	MLI (µm)	LLI (µm)
Granular Base	Sound	<500	>100	<200	<100	<50
	Warning	500-750	50-100	200-400	100-200	50-100
	Severe	>750	<50	>400	>200	>100
Cementitious Base	Sound	<200	>150	<100	<50	<40
	Warning	200-400	80-150	100-300	50-100	40-80
	Severe	>400	<80	>300	>100	>80
Bituminous Base	Sound	<400	>250	<150	<100	<50
	Warning	400-600	100-250	150-300	100-150	50-80
	Severe	>600	<100	>300	>150	>80

According to the above rating criteria, the FWD influenced the UTCRCP pavement system exceeding a depth of 900 mm. This observation is made by the change in condition of the lower selected layer as depicted in under APT (Figure 4.19). The extrapolated LLI base line condition changed from a perfect sound condition to a general warning state (1200k) and then back to a general sound condition (2800k).
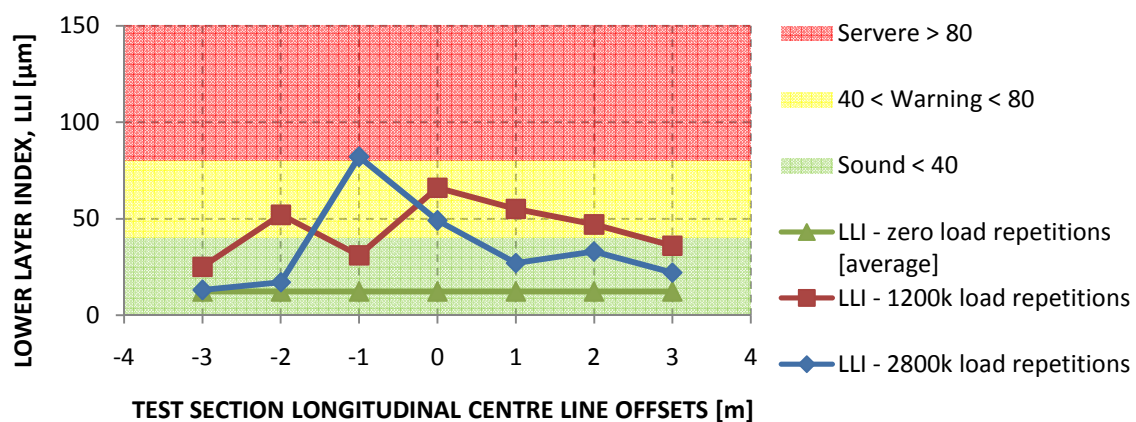
Figure 4.19 LLI of the 40 kN FWD measurements at the various load count intervals

65

The results of the BISAR 3.0 linear elastic analysis for the 50th percentile 40 kN FWD simulations are presented in Table 4.2. The layer moduli of the overlaid asphalt pavement compares favourably with the suggested moduli according to Theyse, et al. 1996 in the *"Overview of the South African Mechanistic Pavement Design Analysis Method."* The UTCRCP modulus is in the range (50 to 80 GPa) as presented in the report of Kannemeyer, et al. 2008.

Table 4.2 Layer elastic modulus of the 50th percentile 40kN FWD simulation results at the various applied axle load repetitions

Layer	Name	Layer Elastic Modulus (MPa) at the Different Stages		
		0k	1200k	2800k
	UTCRCP	55000	55000	75000
	AC (40mm)	1900	1200	3500
	G1 (150mm)	780	500	800
	C4 (150mm)	950	150	210
	C4 (150mm)	950	150	210
	C6 (Semi Infinite)	312	360	270

A very apparent occurrence in the linear elastic analysis was the stiffness reduction of the C4 cement stabilised layers. The modelled cement stabilised layers had undergone a stiffness reduction from 950 MPa to 150 MPa at 1200k load applications. Measurements at 2800k load repetitions yielded a C4 stiffness of 210 MPa, following the trend observed in Figure 4.19. The MLI supports this trend (Figure 4.20), but after 2.8 million load repetitions only two positions indicate measures of distress; the other five are similar to the extrapolated MLI base line conditions. The findings therefore cannot prove with absolute certainty that pavement substructure distress was obtained under APT. MDD data presented in Section 6.3.1, indicated that no real changes were recorded to the substructure condition.
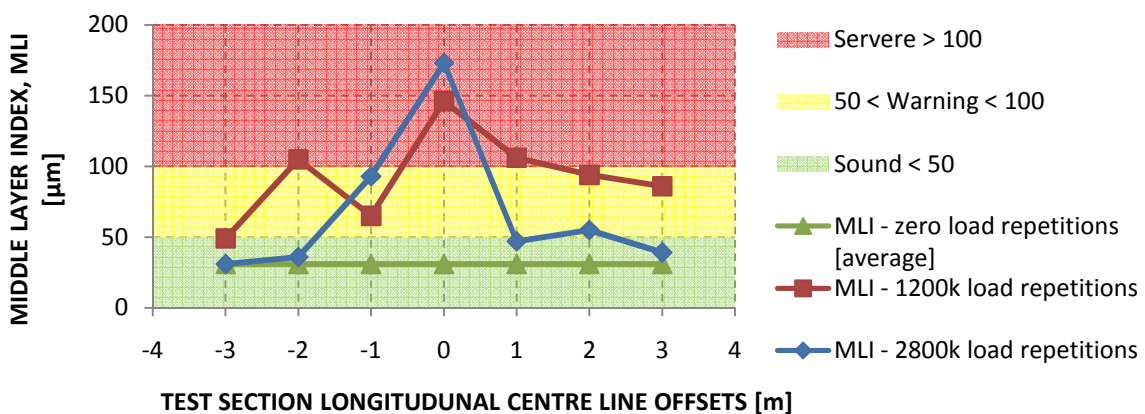
Figure 4.20 MLI of the 40 kN FWD measurements at the various load count intervals

Another structural phenomenon that was not further investigated due to project scope limitations was the increase of the UTCRCP and AC layer stiffness towards the end of the APT project. It is possible that the asphalt layer in the pavement had undergone "healing", but this would need to be verified by further investigation.

4.3.3 Elastic radius of relative stiffness

The BISAR 3.0 elastic modelling procedure yielded results of the concrete's elastic modulus, E_{pcc}. These results were used to iteratively calculate the radius of relative stiffness ($l_{elastic}$) for the elastic model as discussed in Section 3.3.4. A summary of the results are presented in the following Tables (Table 4.3, Table 4.4 & Table 4.5).

Table 4.3 The 40 kN FWD linear elastic modelling results for the concrete's elastic modulus (E_{pcc}) and radius of relative stiffness ($l_{elastic}$) at the various stages

40 kN Results	0k		1200k		2800k	
	E_{pcc}	$l_{elastic}$	E_{pcc}	$l_{elastic}$	E_{pcc}	$l_{elastic}$
	MPa	mm	MPa	mm	MPa	mm
90th percentile	36000	135	36000	180	-	-
50th percentile	55000	142	55000	180	75000	185
10th percentile	78000	143	75000	193	85000	168

Table 4.4 The 60 kN FWD linear elastic modelling results for the concrete's elastic modulus (E_{pcc}) and radius of relative stiffness ($l_{elastic}$) at the various stages

60 kN Results	0k		1200k		2800k	
	E_{pcc}	$l_{elastic}$	E_{pcc}	$l_{elastic}$	E_{pcc}	$l_{elastic}$
	MPa	mm	MPa	mm	MPa	mm
90th percentile	36000	135	40000	180	-	-
50th percentile	60000	145	60000	197	70000	170
10th percentile	80000	144	76000	191	86000	172

Table 4.5 The 80 kN FWD linear elastic modelling results for the concrete's elastic modulus (E_{pcc}) and radius of relative stiffness ($l_{elastic}$) at the various stages

80 kN Results	0k		1200k		2800k	
	E_{pcc}	$l_{elastic}$	E_{pcc}	$l_{elastic}$	E_{pcc}	$l_{elastic}$
	MPa	mm	MPa	mm	MPa	mm
90th percentile	37000	126	40000	175	50000	174
50th percentile	65000	143	60000	179	70000	177
10th percentile	80000	137	76000	189	86000	168

Generally the three different load cases yielded similar responses. The 90th percentile of the 40 kN and 60 kN load case could not be simulated due to the obtuse angle effect. The elastic radius of relative stiffness increased over the duration of traffic simulation. It was expected that the elastic modulus of the concrete would reduce as the radius of relative stiffness increased, yet the E_{pcc} either remained at fairly constant value or increased slightly as pavement distress increased.

4.3.4 Summary of results

From the linear elastic modelling results Table 4.6 was created that could be used in the calculation procedure of UTCRCP mean crack spacing. Three scenarios were created; a lower limit, best estimate and an upper limit to represent the test section properties.

Table 4.6 Results of the linear elastic modelling procedure at the various stages that will be used in the mean crack spacing calculation procedure

UTCRCP Elastic Properties	0k		1200k		2800k	
	E_{pcc}	$l_{elastic}$	E_{pcc}	$l_{elastic}$	E_{pcc}	$l_{elastic}$
	MPa	mm	MPa	mm	MPa	mm
Lower Limit	36000	135	40000	175	50000	174
Best Estimate	55000	142	60000	179	75000	185
Upper limit	80000	144	76000	189	85000	168

The lower limit was created from the 90th percentile analyses, the best estimate from the 50th percentile analyses and the upper limit from the 10th percentile analyses. In all scenarios the radius of relative stiffness is fairly low, thus indicating the severe upper stiffness of the pavement system.

4.3.5 Interim conclusions

The formation of an obtuse angle in some of the conducted field FWD measurements indicates non-linear pavement response at the respected positions. These bowls cannot be simulated with BISAR 3.0 to obtain a close fit with the real measured bowl.

The linear elastic procedure indicated subbase distress. The stiffness of the modelled cement stabilized layers reduced notably yet the results of the MLI, LLI and MDD data contradicts this statement. This argument is thus inconclusive and if only the recorded data is considered the argument leans towards no change in the subbase conditions under APT.

An element of visco-elastic response was again observed. The magnitude of the applied FWD load does slightly influence the pavement's modulus response.

4.4 Mechanistic-Empirical Analysis Phase II

The major pavement variables that are used as input parameters for the calculation of mean crack spacing are presented in this section, followed by a summary of the calculated mean crack spacing for the different limit cases.

4.4.1 Pavement temperatures

One of the input variables for the calculation of mean crack spacing is the minimum or lowest seasonal temperature of the pavement at the depth of steel. Figure 4.21 depicts a typical temperature profile in the UTCRCP on a dry winter's day.
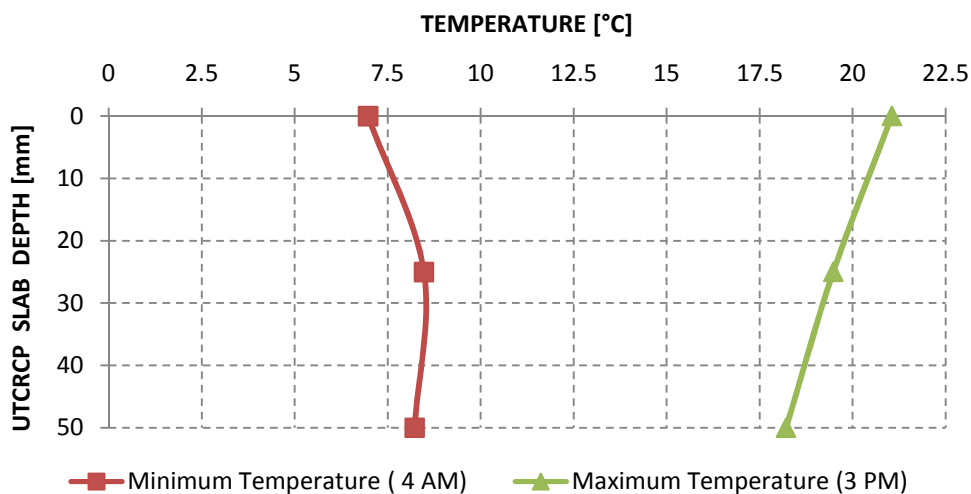
Figure 4.21 Typical temperature profiles in the UTCRCP on a winter's day

The lowest temperatures in the pavement were monitored a few hours before sunrise and the warmest temperatures were monitored three hours past midday (noon). The depth of steel in the UTCRCP is set at approximately 25 mm below the surface.

4.4.2 Calculation variables

By using Equation 4.1 to calculate the mean crack spacing a wide range of variables are included in the process. The more influential concrete, base and environmental properties are summarized in Table 4.7. These properties were extracted from the various sources as indicated in Table 4.7.

Table 4.7 Summary of the major variables used in the mean crack spacing calculation

Concrete Properties			
E_{pcc}	Concrete's Elastic Modulus	36 to 80 GPa	Bisar 3.0 Analysis
v_{pcc}	Poisson's ratio of Concrete	0.15	Assumed
α_{pcc}	The concrete coefficient of thermal expansion (quartzite)	$12.5 \times 10^{-6}/°C$	Fulton, 1977
f_{c28}	28 day concrete compressive strength	103 MPa	Africon 2008
MOR_{28}	28 Day modulus of rupture (flexural strength)	12.8 MPa	Africon 2008
ε_∞	Ultimate shrinkage	Equation A.9	Kohler and Roesler 2006
γ_{pcc}	Concrete thermal diffusivity (quartzite)	$1.39 \text{ ft}^2/\text{day}$	FHWA-ICT-09-040 2009
CC	Cement content	480 kg/m^3	Africon 2008
UTCRCP Geometric Properties			
h_{pcc}	UTCRCP layer thickness	50 mm	Africon 2008
L	Length of slab	3.7 m (144 in)	FHWA-ICT-09-040 2009
P_b	The percentage steel as a fraction	0.0094	Calculated
d_b	Reinforcing steel diameter	5.6 mm	Africon 2008
ζ	Depth to reinforcing steel (top of steel)	22.2 mm	Africon 2008
Base Properties			
f	The base friction coefficient	7.5 - 15	FHWA-ICT-09-040 2009
Environmental Properties			
Ro	Effective range in temperature for seasonal increment	23.4 °F	FHWA-ICT-09-040 2009
T_{air}	Average ambient temperature for season of construction	24 °C (75°F)	SA Weather Services
T_{steel}	Lowest average temperature at the depth of steel	8 °C (46 °F)	Figure 4.21

4.4.3 Calculated mean crack spacing

$$\bar{L} = \frac{f'_{t28} - C_i\sigma_{0,i}\left[1 - \frac{2\zeta}{h_{pcc}}\right]}{\frac{f}{2} + \frac{U_m P_b}{c_{1,i}d_b}}$$

[Formerly 2.17]   (4.2)

Equation 4.2 was used to calculate the mean crack spacing for the three cases as presented in Table 4.6. Table 4.8 presents the mean crack spacing for each limit state. The calculated mean crack spacing varies between 161 mm and 151 mm. The mean crack spacing of neither limit cases varied with more than 4 mm over the duration of the APT test.

Table 4.8 Summary of the calculated mean crack spacing from Equation 4.2

Limit Cases		Mean Spacing	Tensile Strength		Curling Stress		Friction Coefficient	Steel Restrain
		$\bar{L}$	f'_{t28}		$C_i\sigma_{0,i}\left[1 - \frac{2\zeta}{h_{pcc}}\right]$		f	$\frac{U_m P_b}{c_{1,i}d_b}$
		mm	psi	MPa	psi	MPa	-	-
Lower Limit	0k	161	1299	8.96	52	0.357	10	192
	1200k	160	1299	8.96	57	0.395	10	192
	2800k	158	1299	8.96	72	0.494	10	192
Best Estimate	0k	157	1299	8.96	79	0.545	10	192
	1200k	156	1299	8.96	86	0.593	10	193
	2800k	153	1299	8.96	107	0.741	10	193
Upper Limit	0k	152	1299	8.96	115	0.792	10	193
	1200k	153	1299	8.96	109	0.750	10	193
	2800k	151	1299	8.96	122	0.841	10	193

For comparative purposes Table 4.8 indicates that UTCRCP have a greater tensile strength capacity than recently studied CRCP sections by Erwin and Roesler 2006 (8.96 MPa versus 3.5 MPa). This is expected due to the composition of the UTCRCP mix. The UTCRCP curling stresses are greater (thinner layer) and the steel restrain is approximately 30 times

greater than studied CRCP sections. In general the results indicate that the UTCRCP layer is a harder compound than a CRCP layer yet more ductile.

4.4.4 Interim conclusions

The parameters; depth of steel, suggested slab length, concrete compressive strength and the flexural tensile strength are of the variables that directly influence the outcome of the mean crack spacing calculation.

Bradbury's coefficient to correct curling stresses for a finite slab was approximately a factor 1 indicating that the suggested slab length of 144 in (3.7 m) by M-E PDG should be adjusted for UTCRCP.

The effect of simulated traffic did not significantly affect the calculated results for mean transverse crack spacing.

4.5 Closure

More insight with regard to mean crack spacing is necessary to adjudicate the validity of the calculated mean crack spacing. Accordingly the characteristics of the observed crack spacing distributions will be discussed in the chapter to follow.

5 CHARACTERISTICS OF CRACK SPACING DISTRIBUTIONS

5.1 Introduction

This section presents the observed crack patterns of the APT UTCRCP field test, a descriptive statistical analysis thereof and a theoretical probability distribution of crack spacing occurrence.

5.2 Observed Crack Patterns

A combination of Cluster cracks, Y-cracks, Meandering cracks, Divided cracks and Longitudinal cracks, as discussed in Section 2.4.2, formed across the length of the test section. These cracks formed due to environmental related damage (non-load associated damage) and load associated damage. Transverse cracks that displayed large easy observable crack widths were labelled 'major' cracks. Some of these major cracks indicated signs of spalling and the majority of these cracks were full length cracks i.e. cracks formed across the full width of the test section, including the edge.

A series of Figures (Figure 5.1, Figure 5.2 & Figure 5.3) depicts the plan view of the entire 10 m test section after the termination of the APT test at 2.8 million load applications. Fractured cracking (Figure 5.2) consisting of the various cracks, especially fine Cluster cracks, Meandering cracks and longitudinal cracks were recorded around the centre of the test section in the vicinity of the MDD. Closely formed Meandering cracking coupled with major Y-cracks, Hair cracks (very fine cracks) and Divided Longitudinal cracks formed what could be an oval, almost circular crack pattern (Figure 5.2). A similar crack pattern which led to UTCRCP fatigue failure was observed by Kannemeyer, et al. 2008 on the UTCRCP STPP trail sections.

A continuous longitudinal crack pattern (Figure 5.1, Figure 5.2 & Figure 5.3) formed approximately 600 mm from the test section centre line (300 mm from the simulated traffic wheel-path edge) in the existing screener lane wheel path. The longitudinal cracks intersected the Joint Deflection Measurement Device's (JDMD) anchor rod holes (Figure 3.6 & Figure 5.2) which were drilled through the UTCRCP at this exact offset (600 mm from test section centre line). Short longitudinal cracks contributing to the shape of the oval crack pattern formed approximately 250 mm to 300 mm from the simulated transverse wander wheel path. According to Kannemeyer, et al. 2008 longitudinal cracks formed approximately 300 mm from the loaded area in the STPP UTCRCP trail sections.
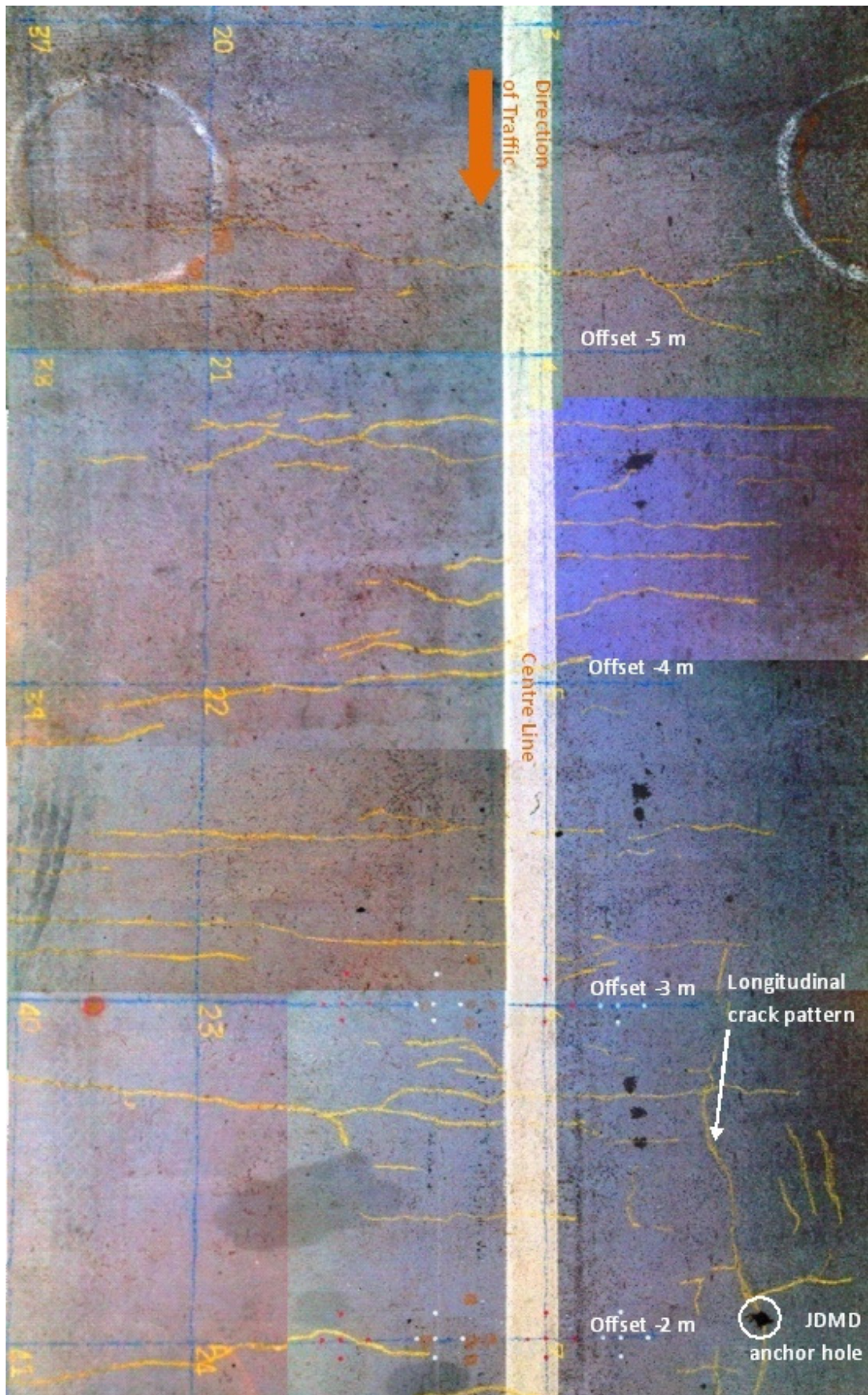
Figure 5.1 Pictorial view of cracks on test section at longitudinal offsets -5 m to -2 m at 2.8 million load applications
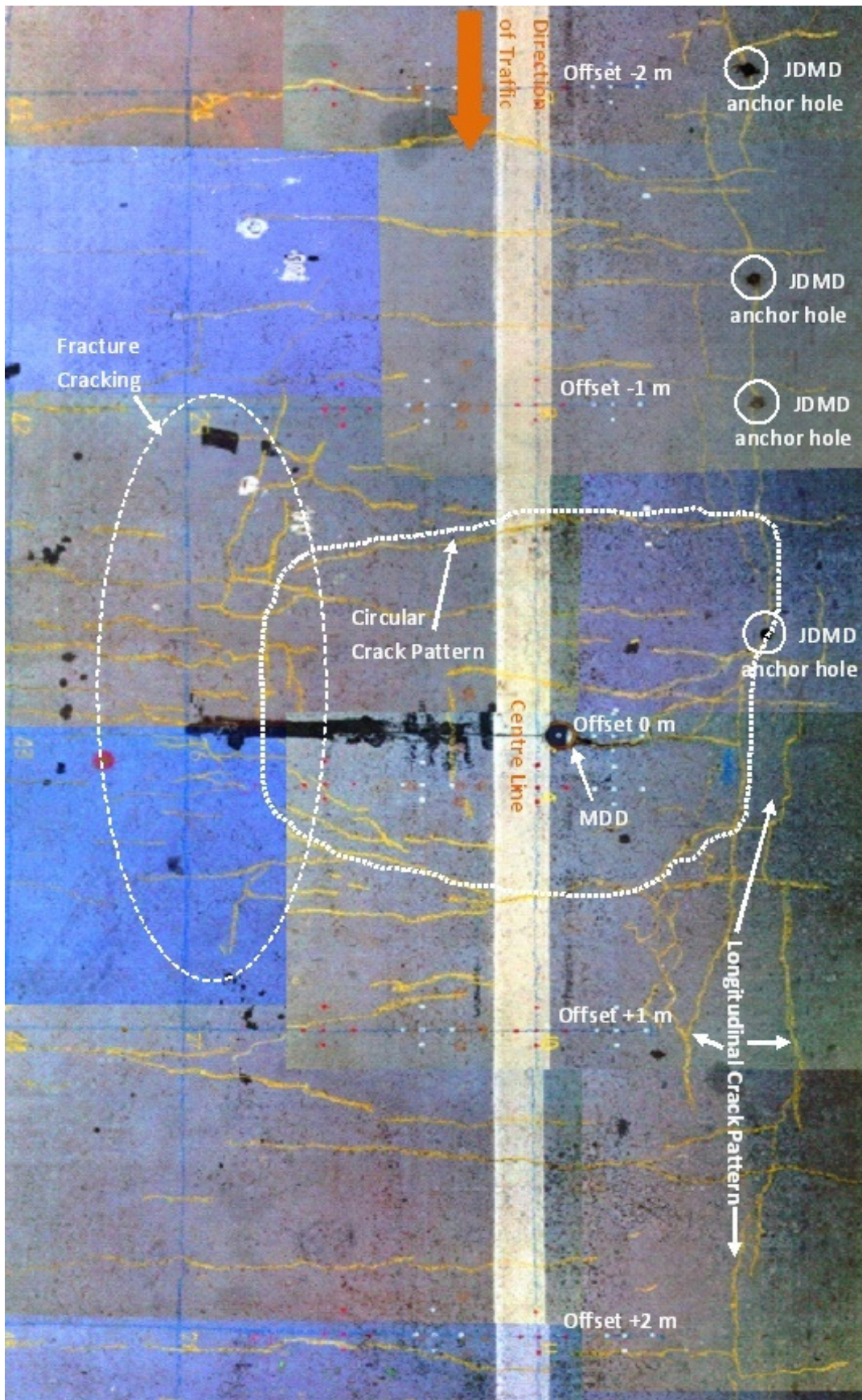
Figure 5.2 Pictorial view of cracks on test section at longitudinal offsets -2 m to +2 m at 2.8 million load applications
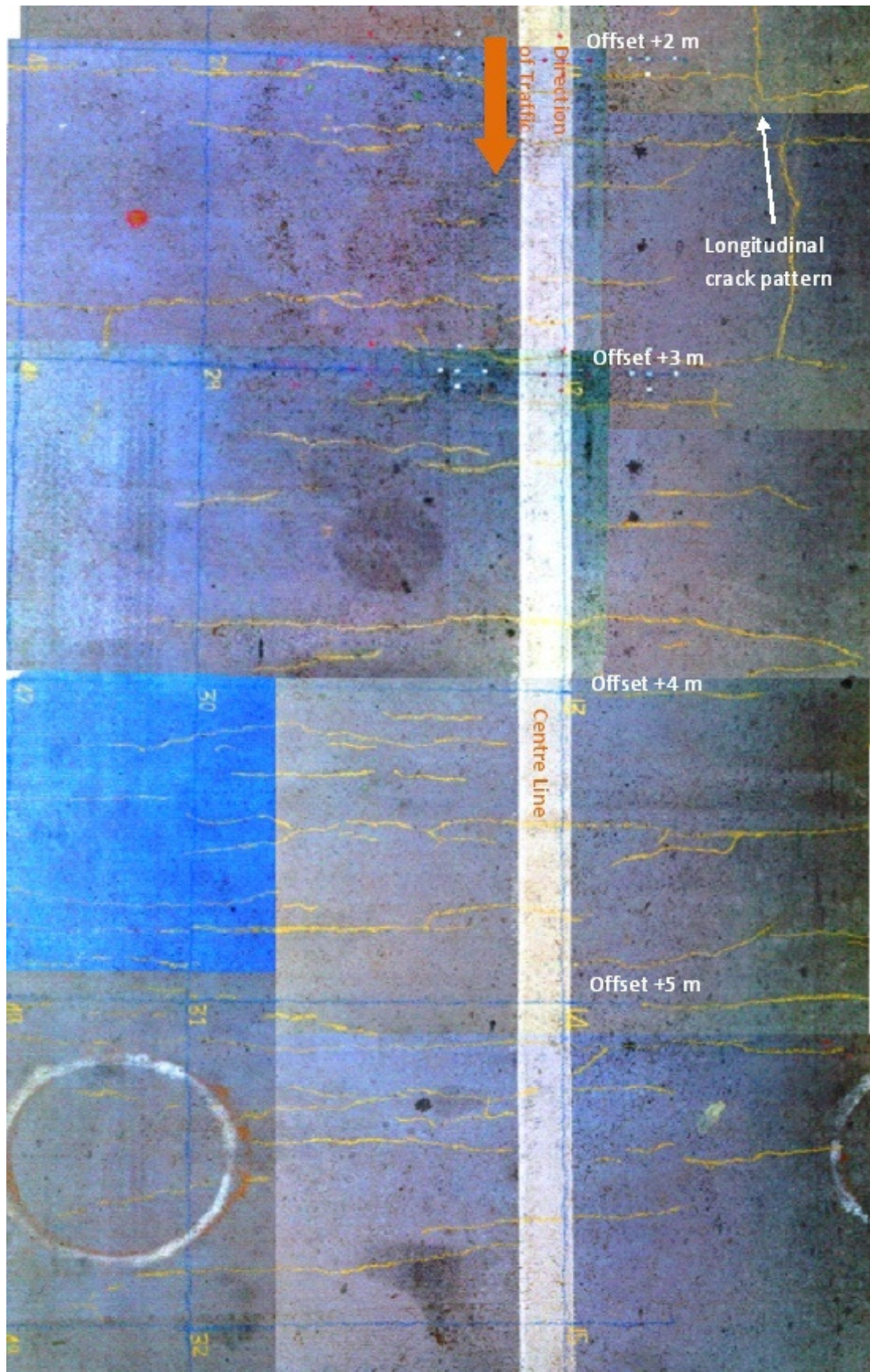
Figure 5.3 Pictorial view of cracks on test section at longitudinal offsets -2 m to +5 m at 2.8 million load applications

5.3 Descriptive Statistical Measures

The general aim with the descriptive statistical measures is to establish whether the induced traffic affected the crack formation and if so, to what extent. Initial cracking in concrete pavements is accredited to concrete shrinkage. Thereafter secondary cracking is caused by differential shrinkage and temperature related curling effects. The latter mentioned effects, in combination with traffic, results in the formation of load associated cracks.

5.3.1 Major cracks

An assumption is made that the major cracks as discussed in Section 5.2 represent the initial shrinkage cracks. These cracks display large crack widths thus is assumed to be older and have formed prior to any traffic. A statistical summary of the major crack spacing as was observed in the simulated wheel path is presented in Table 5.1.

Table 5.1 Statistical summary of the major crack spacing (initial shrinkage cracks) after 2.8 million load applications

Description of the observed cracks and offsets as depicted in Figure 5.1, Figure 5.2 & Figure 5.3	Minimum [mm]	Maximum [mm]	Mean [mm]	Median [mm]	Standard Deviation [mm]	COV [%]
Offsets -5 m to -3 m (No Traffic)	300	650	488	500	145	30
Offsets -3 m to +3 m (Trafficked)	525	900	703	688	142	20
Offsets +3 m to +5 m (No Traffic)	850	1300	1075	1075	318	30
Offsets -5 m to +5 m (All)	300	1300	695	663	243	35

Traffic was only simulated between the offsets -3 m to +3 m (Table 5.1), therefore offsets -5 m to -3 m and +3 m to +5 m carried no simulated traffic. However due to the above assumption the results of the offsets -5 m to +5 m for the major crack spacing is of primary interest. Table 5.1 indicates that the major cracks are expected to occur at an arithmetic mean distance of 695 mm having a median (middle number for a set of values arranged in order of magnitude) of 663 mm. The two parameters (mean & median) indicate a measure of location for the major crack spacing data set. The standard deviation, which indicates the measure of crack spacing spread, is 243 mm. Thus in the case of normally distributed crack spacing, the major cracks are expected to occur roughly between 452 mm and 938 mm, 68 percent of the time i.e. the intercepts of the first standard deviation is 452 mm and 938 mm. The measure of crack spacing dispersion or better described as the coefficient of variation

(COV) for the major crack spacing is 35%. This means that the standard deviation is 35% of the mean crack spacing. The real value of the COV lies in its ability to fairly compare sets of crack spacing data with different means. Figure 5.4 depicts the cumulative frequency of major crack spacing occurrence.
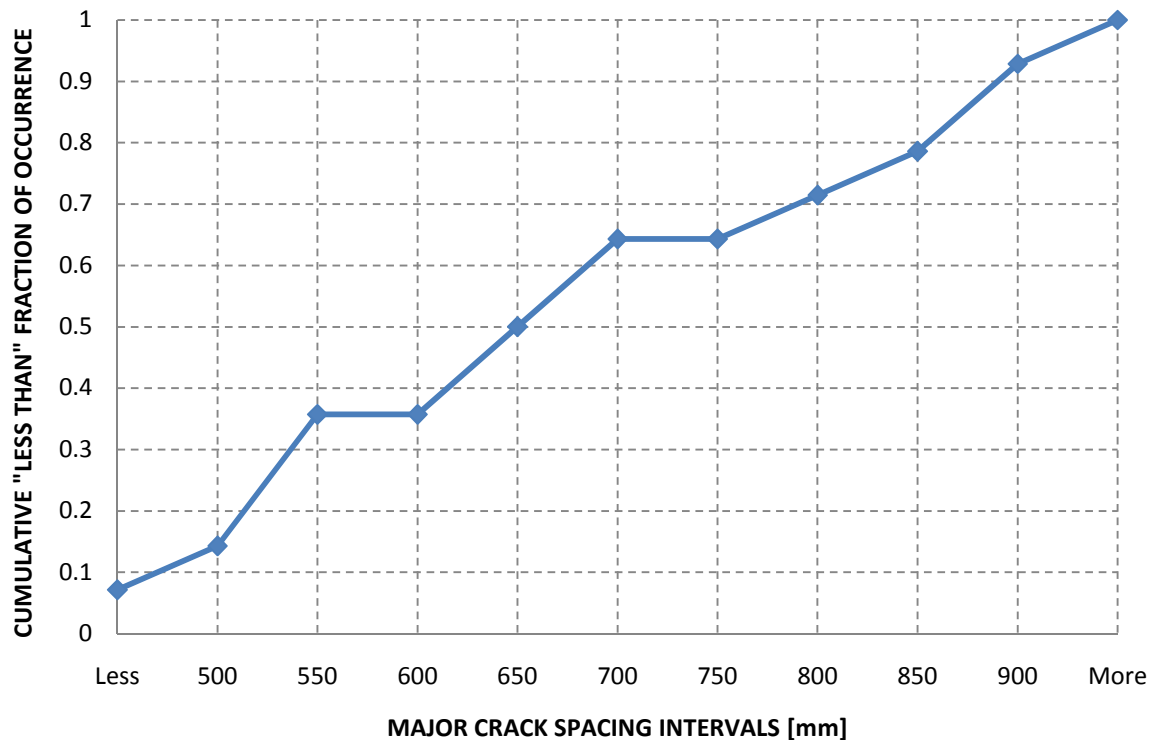
Figure 5.4 Cumulative frequency of major crack spacing after 2.8 million load applications

Half (50%) of the observed major cracks have a spacing of less than 650 mm and approximately 64% of the major cracks have a spacing of less than 700 mm. The median and the mean lies between 50% and 64% of the cumulative occurrence of crack spacing. The standard deviation of Table 5.1 indicates that if a normal distribution is assumed, approximately 10% of the Major cracks at a spacing of less than 452 mm and approximately 5% (100% - 95%, Figure 5.4) of the major cracks at a spacing greater than 938 mm would fall outside the first standard deviation. Applicability of distribution types is discussed further in Section 5.4.

Based on the shape of Figure 5.4, its slope of inclination and the statistical parameters of Table 5.1 an estimated interval of 500 mm to 900 mm is regarded as a representative interval for major crack spacing occurrence.

5.3.2 Secondary cracks

The development of secondary cracking due to differential shrinkage and environmental conditions follows the initial shrinkage (major) cracks. These cracks are much smaller in width when compared to the major crack widths. Secondary crack spacing evaluations were done at the offsets -5 m to -3 m and +3 m to +5 m where no traffic was simulated. At these offsets the cracks are solely environmentally related. A statistical summary of the secondary cracks is presented in Table 5.2.

Table 5.2 Statistical summary of the secondary crack spacing (differential shrinkage and environmental associated cracks) after 2.8 million load applications

Description of the observed cracks and offsets as depicted in Figure 5.1, Figure 5.2 & Figure 5.3	Minimum [mm]	Maximum [mm]	Mean [mm]	Median [mm]	Standard Deviation [mm]	COV [%]
Secondary Cracks (-5 m to -3 m)	100	600	325	275	182	56
Secondary Cracks (+3 m to +5 m)	150	350	217	175	68	32
All (-3 m to -5 m & +3 m to +5 m)	100	600	260	250	132	51

The statistical parameters are more meaningful when compared to the results of the major crack spacing from Table 5.1. Figure 5.5 depicts the results of the offsets -5 m to -3 m for the major and secondary cracks.
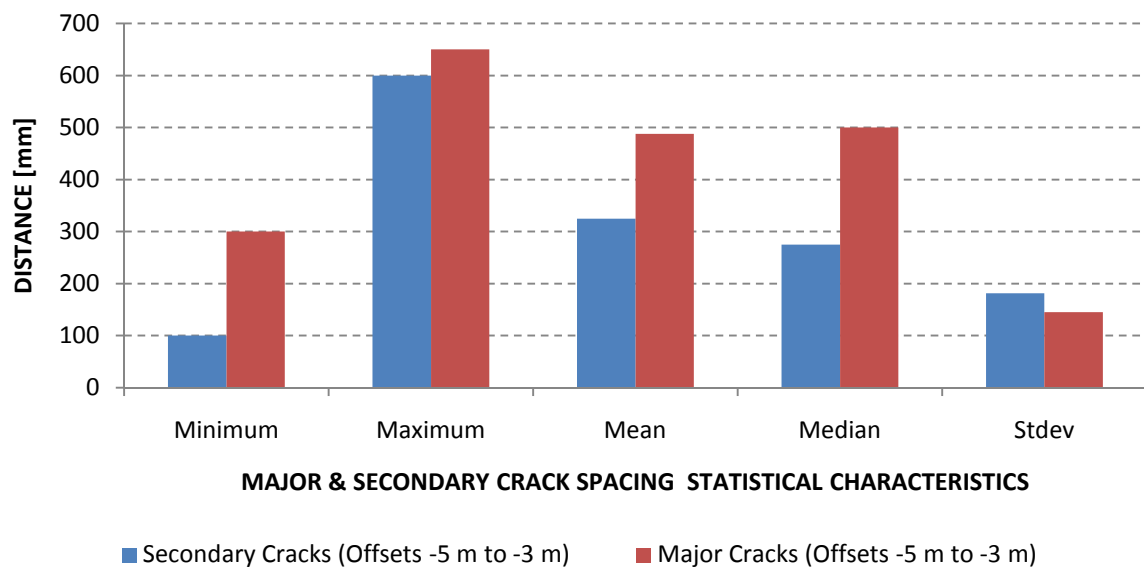
Figure 5.5 Statistical parameters of the major and secondary crack spacing after 2.8 million load applications for the offsets -5 m to -3 m

Figure 5.5 indicates, as expected, a reduction in the crack spacing for this offset. The mean major crack spacing reduced from 488 mm to 325 mm (33.4% reduction). The standard deviation of the secondary cracks increased as did the COV (Table 5.1 & Table 5.2). This means that the secondary cracking at the respected offsets resulted in an increase in the spread of the crack spacing distribution. When a similar analysis is done for the offsets +3 m to +5 m (Figure 5.6), a reduction in the standard deviation is obtained with a slight increase in the COV. This means that crack spacing dispersion for the offset +3 m to +5 m remained similar.
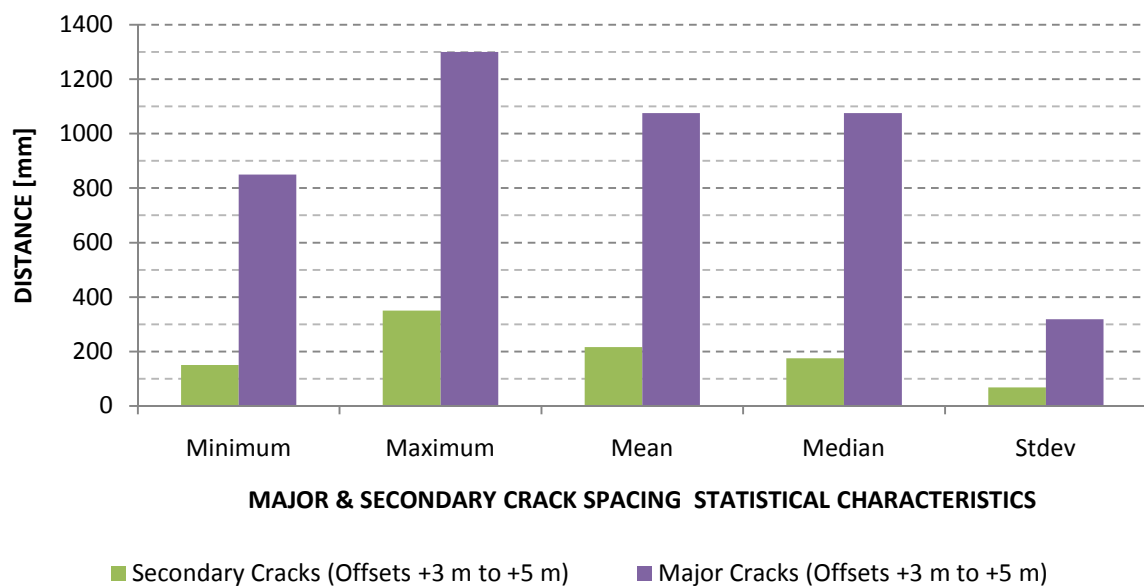
Figure 5.6 Statistical parameters of the major and secondary crack spacing after 2.8 million load applications for the offsets +3 m to +5 m

Figure 5.6 indicates a reduction in all statistical parameters. The major mean crack spacing reduced from 1075 mm to 217 mm (80% reduction). When Figure 5.6 is compared to Figure 5.5, it should be noted that secondary cracking is more prone to occur on segments (delineated by initial shrinkage cracks) of greater distance.

To evaluate the general change in crack spacing due to environmental effects, a comparison is made between the major crack spacing recorded along the offsets -5 m to +5 m (Table 5.1) and the combined secondary crack spacing offsets of -5 m to -3 m and +3 m to +5 m (Table 5.2). Figure 5.7 depicts the difference in statistical parameters, while Figure 5.8 depicts the differences in the cumulative frequencies.

80
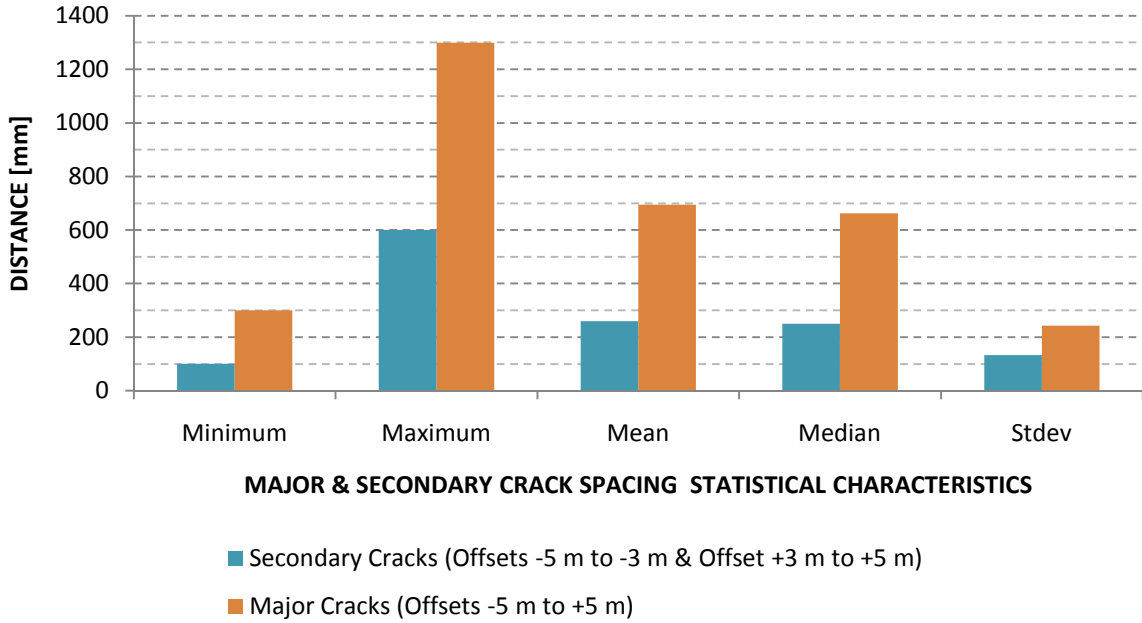
Figure 5.7 Statistical parameters of the major crack spacing (-5 m to +5 m) and the combined secondary crack spacing (-5 m to -3 m & +3 m to +5 m) after 2.8 million load applications
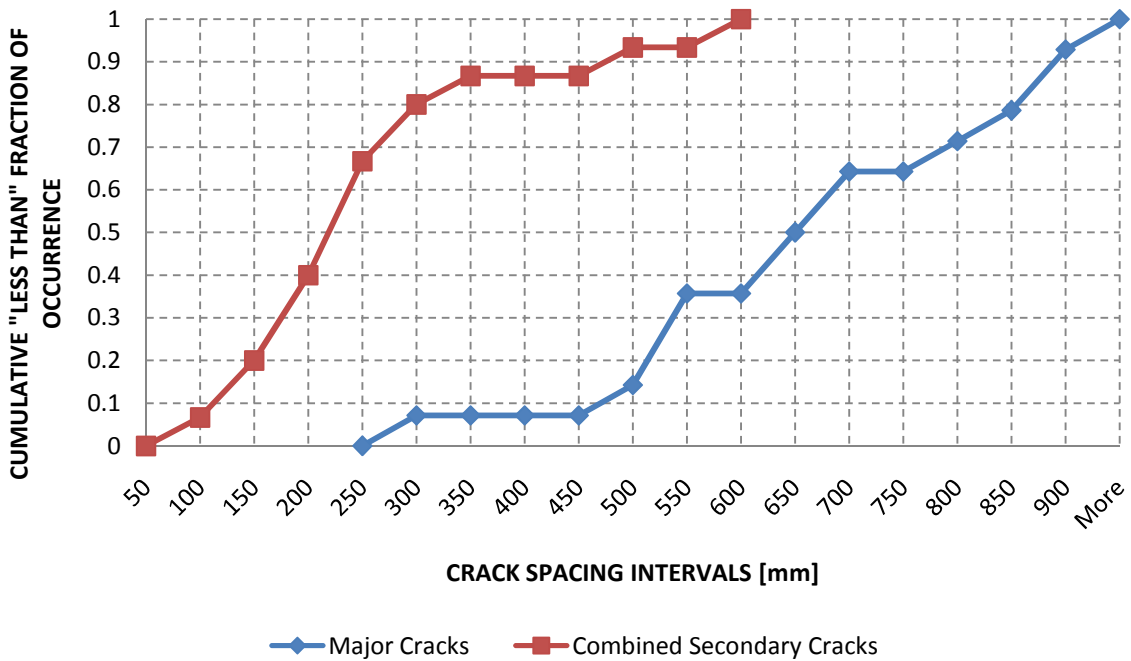
Figure 5.8 Cumulative frequency of major crack spacing and the combined secondary crack spacing after 2.8 million load applications

Although the standard deviation of the secondary cracks is less than the standard deviation of the major cracks (Figure 5.7), the measure of secondary crack spacing dispersion is higher i.e. the COV of the secondary cracking is greater than the COV of the major cracks

81

(Table 5.1 & Table 5.2). This means that the occurrence of secondary mean crack spacing in comparison with major mean crack spacing is less reliable.

The arithmetic mean spacing of the combined secondary cracks is 260 mm and the median is 250 mm (Figure 5.7). Figure 5.8 indicates that 50% of the observed combined secondary cracks have a spacing of less than 219 mm. Approximately 67% of the combined secondary cracks have a spacing of less than 250 mm and 80% of the combined secondary cracks are of a spacing less than 300 mm. If a normal distribution is assumed the intercepts of the secondary cracks for the first standard deviation is 128 mm and 392 mm respectively. If roughly similar percentages are used which delineated the major crack spacing representative interval of occurrence (10% & 95%) then a representative interval for secondary cracking would be 115 mm (10%, Figure 5.8) to 580 mm (95%). However due to scarceness of cracks beyond 350 mm, an adjustment to the delineation percentages is necessary.

Based on the cumulative frequency plot (Figure 5.8), the statistical data as presented in Figure 5.7 and the above discussions, an estimated interval of 150 mm to 350 mm is regarded as a representative interval for secondary crack spacing occurrence.

5.3.3 Load associated cracks

Traffic or load associated cracking, as discussed in Section 2.4.2, was recorded between the offsets of -3 m to +3 m. The latter offsets were exposed to initial shrinkage cracking, secondary cracking and load associated cracking. The statistical parameters of the recorded cracks after 2.8 million applied load repetitions are presented in Table 5.3.

Table 5.3 Statistical summary of the major, secondary and load associated crack spacing after 2.8 million load applications

Description of the observed cracks and offsets as depicted in Figure 5.1, Figure 5.2 & Figure 5.3	Minimum [mm]	Maximum [mm]	Mean [mm]	Median [mm]	Standard Deviation [mm]	COV [%]
Major Cracks (-5 m to +5 m)	300	1300	695	663	243	35
Major Cracks (-3 m to +3 m)	525	900	703	688	142	20
Secondary Cracks (Combined)	100	600	260	250	132	51
Load Associated Cracks (-3 m to +3 m)	125	725	325	275	182	56

The standard deviation and the measure of major crack spacing dispersion is lower along the -3 m to +3 m offsets than the respected major cracks statistical parameters of the -5 m to +5 m offsets (Table 5.3). However due to the assumption of Section 5.3.1, the results for the major crack offsets of -5 m to +5 m will be used for comparison purposes.

It is clear from Table 5.3 that the load associated cracks have the highest measure of dispersion (56%), yet when the COV is compared to the COV of the secondary cracks it exceeds only with 4%. With an assumed normal distribution and 'n mean of 325 mm the load associated cracks have intercepts of 143 mm and 507 mm at the first standard deviation. The latter intercept (first standard deviation to the right) is greater than what was obtained with the secondary cracking (no traffic) evaluation. Half (50%) of the load associated crack spacing is less than 262 mm (Figure 5.9).
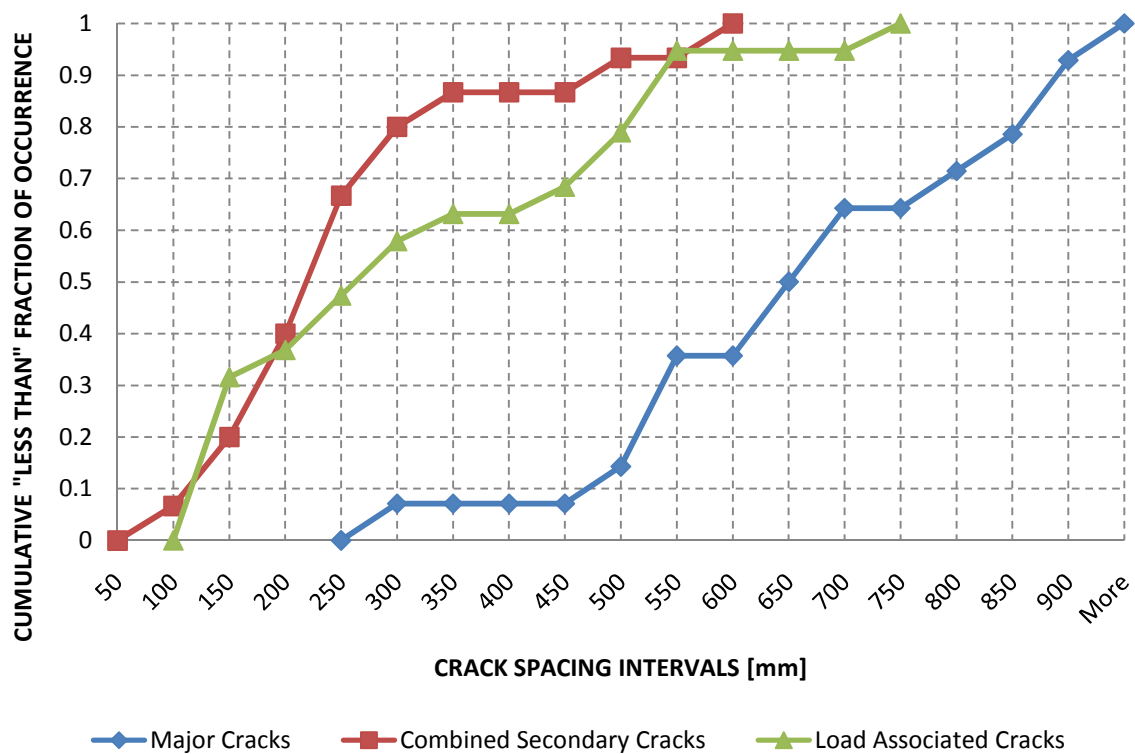
Figure 5.9 Cumulative frequency of major crack spacing, the combined secondary crack spacing and the load associated crack spacing after 2.8 million load applications

Approximately 36% of the load associated cracks have a spacing of less than 195 mm. This is similar to the secondary crack spacing evaluation. If the upper limit of the representative secondary crack interval (350 mm) is used to establish a boundary condition for the load associated cracks, an estimated 63% of the observed load associated crack spacing will be less than 350 mm (Figure 5.9).

An important factor that should be considered with the load associated cracks is the contact length of the loading wheel(s). A popular method to determine the contact area of a single wheel load is presented in Equation 5.1.

$$a = \sqrt{\frac{P}{\pi p}}$$
(Houben 2006) (5.1)

Where;

a =   radius (mm) of circular loading

P =   single wheel load (N)

p =   contact pressure (N/mm^2)

Assuming that the tyre (wheel) pressure is equal to the contact pressure the radius of an 80 kN dual wheel is 126 mm. Hence the contact length is 252 mm. Therefore if the load associated cracking mechanism of Section 2.4.2 is considered, it is expected that the loading wheel would not affect transverse crack spacing less than the length of the wheel contact. A length of 300 mm is a commonly assumed wheel contact distance (Strauss, Personal Communiation between P.J. Strauss and J.A.K. Gerber 2010).

Based on the above discussion, Figure 5.9 and Table 5.3 the simulated traffic is regarded as having little effect on the transverse crack spacing formation. Assuming that the transverse cracks of the entire test section are environmentally related cracking; then the reduction of the major crack spacing is as presented in Table 5.4.

Table 5.4 Statistical summary of the major and the secondary crack spacing after 2.8 million load applications

Description of the observed cracks and offsets as depicted in Figure 5.1, Figure 5.2 & Figure 5.3	Minimum [mm]	Maximum [mm]	Mean [mm]	Median [mm]	Standard Deviation [mm]	COV [%]
Major Cracks (-5 m to +5 m)	300	1300	695	663	243	35
Secondary Cracks (-5 m to +5 m)	100	725	296	250	163	55

The major mean crack spacing reduced from 695 mm to 296 mm (57% reduction). If a normal distribution is assumed for the secondary cracks (Table 5.4) then the intercepts of the first standard deviation would be 133 mm and 459 mm respectively.
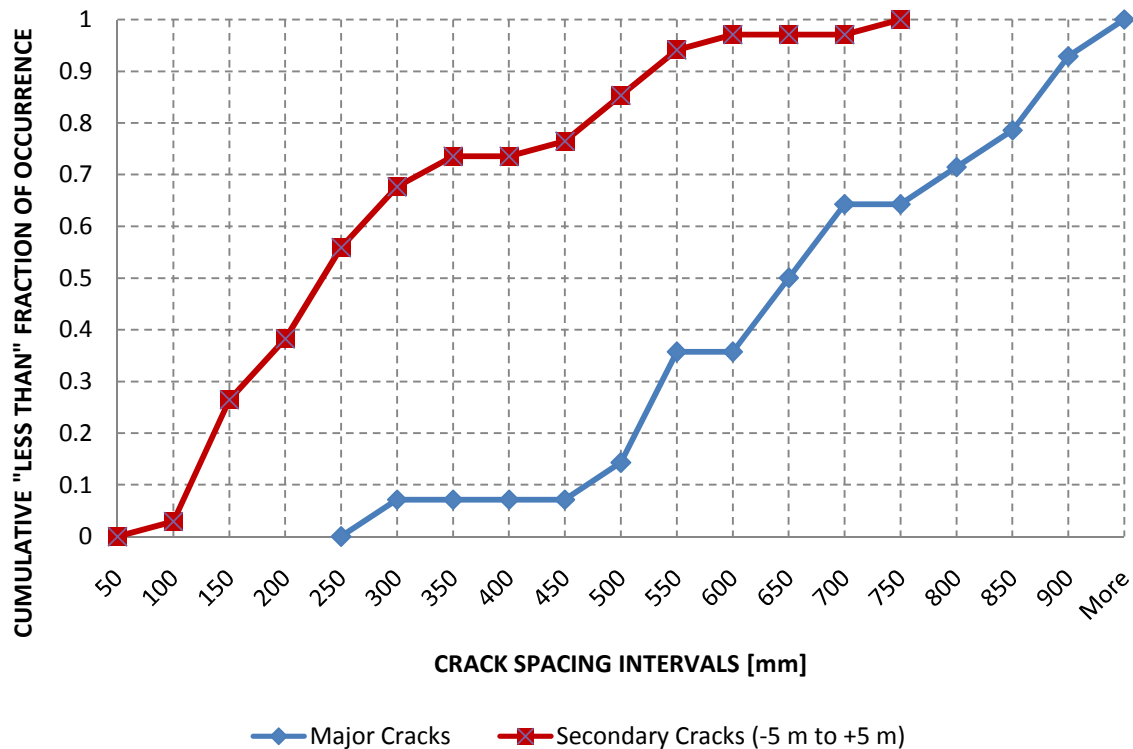
Figure 5.10 Cumulative frequency of major crack spacing and the secondary crack spacing (-5 m to +5 m) after 2.8 million load applications

Approximately 27% of the secondary crack spacing is less than 150 mm and approximately 26% is greater than 350 mm (Figure 5.10). Considering Section 5.3.2, Table 5.4, Figure 5.10 and the above discussions, an interval ranging from 150 mm to 350 mm is finally regarded as a representative interval for secondary cracking that includes the contribution of load associated transverse cracks.

It should be noted that the simulated traffic affected the longitudinal crack formation. This is deduced from Figure 5.2 and Figure 5.3. A Divided longitudinal crack formation formed along the length of the test section between the offsets -3 m to +3 m.

5.3.4 Interim conclusions

The assumption that the initial shrinkage cracks, labelled as major cracks, formed prior to any applied traffic yielded an estimated crack spacing interval of 500 mm to 900 mm.

Subsequently secondary cracking in combination with load associated cracking reduced the major crack spacing interval to approximately 150 mm to 350 mm.

It was observed in a comparison between the secondary cracks and load associated cracks that the simulated traffic had little effect on the transverse crack spacing formation (Figure 5.9). A schematic representation of the transverse crack formation for the UTCRCP layer is depicted in Figure 5.11.
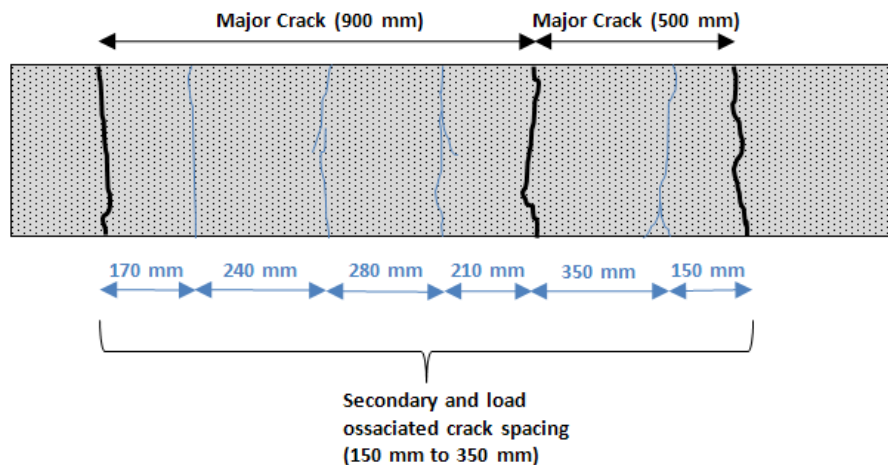
Figure 5.11 Schematic representation of the major and secondary crack spacing intervals

5.4 Probability Distributions

In Section 5.3 assumed normal distributions were used in the estimation process of the major and secondary representative crack spacing intervals. A study conducted by Selezneva, at al. 2002 indicated that a model based on the Weibull distribution can be used to represent a transverse crack spacing distribution. The parameters of the Weibull distribution provide a great deal of flexibility to model systems in which the number of failures increase with time, decrease with time or remain constant with time (Montgomery and Runger 2003). For the Weibull distribution a crack can be viewed as a failure.

5.4.1 Major crack spacing distribution

Figure 5.12 depicts a histogram of the major crack spacing and Selezvena's Weibull probability density function (PDF) as discussed in Section 2.4.5. The estimated major crack spacing representative interval is regarded as 500 mm to 900 mm (Section 5.3.1). According to the Weibull PDF of Figure 5.12, the representative interval includes 58% of the major cracks and based on the histogram, it is clear that the majority of the major cracks have

formed between 500 mm and 900 mm. The cumulative frequency plot (Figure 5.4) indicates that approximately 77% of the major cracks have formed between 500 mm and 900 mm. Therefore according to the above results, the interval 500 mm to 900 mm is confirmed to be an appropriate representative interval of major crack spacing.
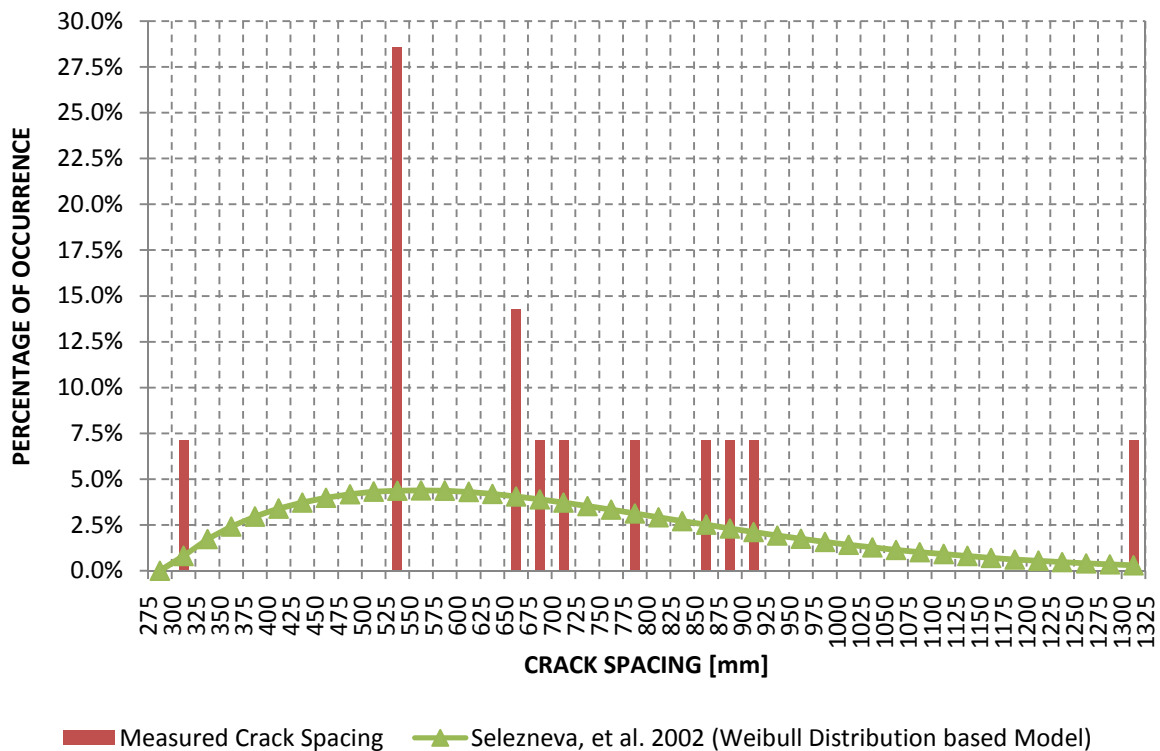
Figure 5.12 Histogram and Weibull distribution of the major crack spacing after 2.8 million load applications

The Kolmogorov-Smirnov goodness-of-fit test, as suggested by Selezneva, et al. 2002 was done to evaluate how close the Weibull distribution followed the measured crack spacing. The advantage of the Kolmogorov-Smirnov test is that unlike the chi-square test, it does not have strict rules on the required number of data groups and minimum theoretical frequencies that have to be satisfied for the test to be meaningful (Selezneva, et al. 2002). If the discrepancy between the observed crack spacing distribution $(S_n(x))$ and theoretically calculated distribution $(F(x))$ is large compared to what is normally expected from a given sample size, the model is rejected i.e. if $(F(x) - S_n(x) = D_n) > D_n^\alpha$ the model is rejected.

The magnitudes of the observed crack spacing were sorted in an ascending order and the cumulative frequency $(S_n(x))$ of the crack spacing was calculated. Likewise the theoretical cumulative frequency $(F(x))$ was calculated with the Weibull PDF of which the necessary parameters were determined from the observed crack spacing distribution. The cumulative frequencies for the major crack spacing distribution are depicted in Figure 5.13.

Table 5.5 Results of the Kolmogorov-Smirnov goodness-of-fit test for the Weibull distribution of the major crack spacing

Alpha (α)	Beta (β)	Sn(x)	F(x)	D_{max}	$D_n^{\alpha=99}$	Weibull
442.673	1.681	0.143	0.273	0.130	0.452	YES
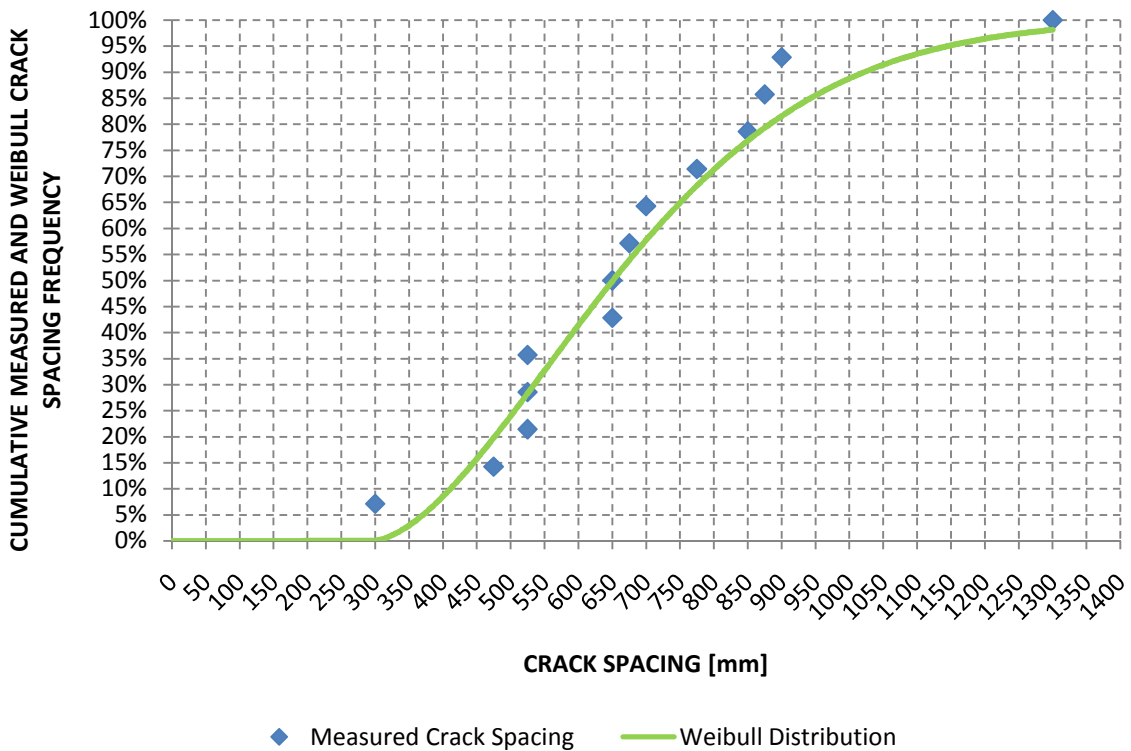
Figure 5.13 Kolmogorov-Smirnov goodness-of-fit test of the major crack spacing distribution

The observed maximum discrepancy, D_{max}, is the maximum difference between the observed cumulative frequency value $S_n(x)$ and the theoretical predicted cumulative frequency $F(x)$. For a level of significance where $\alpha = 99\%$ (not to be confused with the alpha parameter from Table 5.5) the critical discrepancy, $D_n^{\alpha=99}$ was determined as follows.

$$D_n^{\alpha=99} = 1.63n^{-0.5}$$ (Selezneva, et al. 2002)   (5.2)

Where;

88

$D_n{}^\alpha$ is defined as $P(D_n \leq D_n{}^\alpha) = 1 - \alpha$ (5.3)

The Kolmogorov-Smirnov (KS) test evaluates at the specified level of significance if the proposed distribution is an acceptable representation of the actual field data. If $D_n < D_n{}^\alpha$ then the proposed theoretical distribution is accepted, as presented in Table 5.5.

5.4.2 Secondary crack spacing distribution

Figure 5.14 depicts a histogram of the secondary crack spacing, including load associated cracks as concluded in Section 5.3.3 (Table 5.4), and the Weibull distribution.
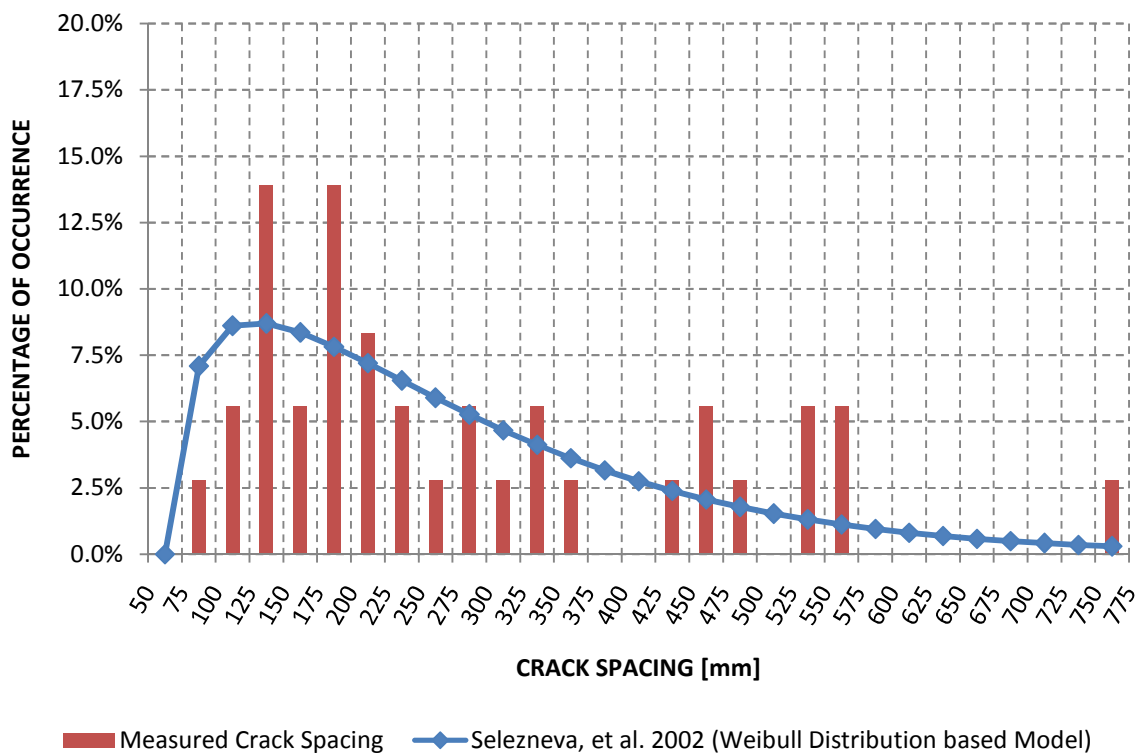
Figure 5.14 Histogram and Weibull distribution of the secondary crack spacing after 2.8 million load applications

The estimated secondary crack spacing representative interval is regarded as 150 mm to 350 mm. According to the Weibull distribution of Figure 5.14, the representative interval includes 51% of the secondary cracks and excluded the 125 mm to 150 mm interval, which includes the joint highest occurrence of secondary cracking for the test section. Based on the histogram (Figure 5.14) the majority of the secondary cracks formed between 75 mm and 375 mm. The cumulative frequency plot (Figure 5.10) indicates that approximately 70.6% of the secondary cracks spacing are between the 75 mm to 375 mm interval and

according to the Weibull distribution (Figure 5.14) 81% of the secondary cracks formed between the above interval. However due to single occurrences of crack spacing formations at the 75 mm to 100 mm and 350 mm to 375 mm intervals, the interval 100 mm to 350 mm is regarded as a better estimated interval of secondary and load associated cracking.

The Weibull distribution of the secondary cracks passed the Kolmogorov-Smirnov goodness-of-fit test and the results of this test is presented and depicted in Table 5.6 and Figure 5.15 respectively.

Table 5.6 Results of the Kolmogorov-Smirnov goodness-of-fit test for the Weibull distribution of the secondary crack spacing

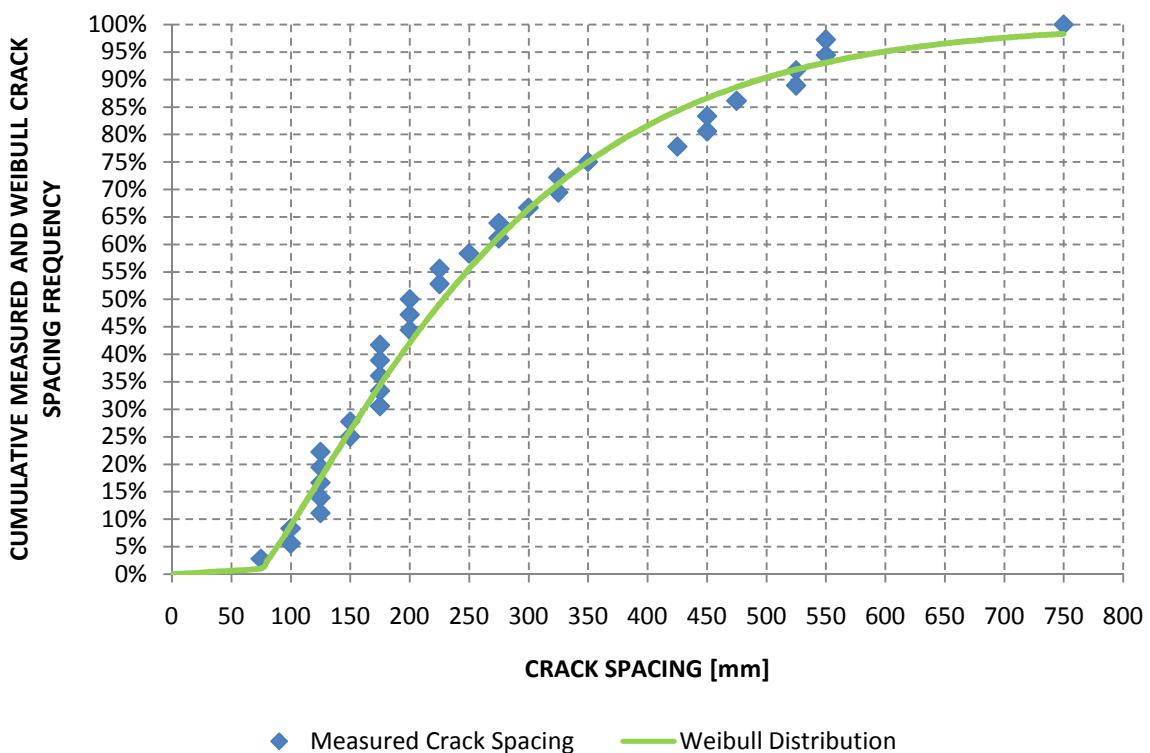| Alpha (α)	Beta (β)	Sn(x)	F(x)	D_{max}	$D_n^{\alpha=99}$	Weibull
214.05	1.216	0.417	0.343	0.073	0.272	YES

Figure 5.15 Kolmogorov-Smirnov goodness-of-fit test of the secondary crack spacing distribution

5.4.3 Interim conclusion

The initial representative intervals of the major and secondary cracks spacing, with assumed normal distributions, were 500 mm to 900 mm and 150 mm to 350 mm respectively.

Selezneva's crack spacing model based on the Weibull distribution in combination with histograms indicated that the initial estimated crack spacing intervals were correctly estimated for the major cracks and too conservative for the secondary cracks. Major crack spacing forms at a distance 500 mm to 900 mm. Subsequently secondary cracks will reduce the initial major crack spacing by forming at offsets of 100 mm to 350 mm as depicted in Figure 5.16.
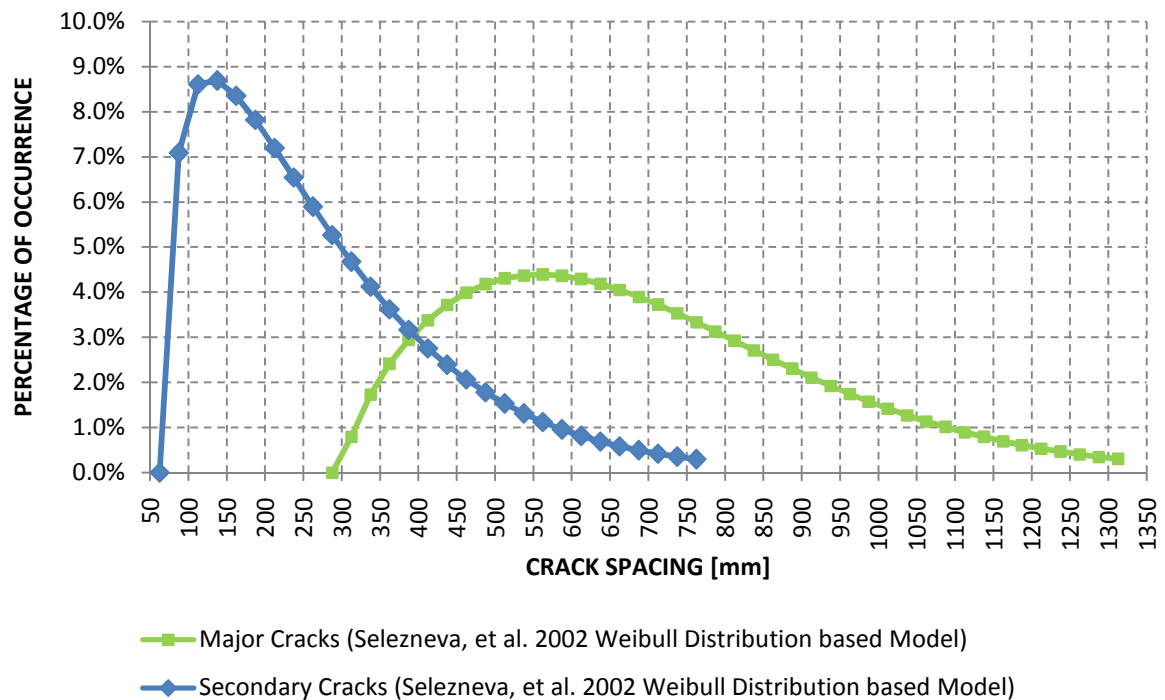

Figure 5.16 A comparison of the major and secondary Weibull crack distributions

Finally, Figure 5.17 schematically depicts the formation of major cracks and the subsequent reduction due to secondary and load associated cracks.
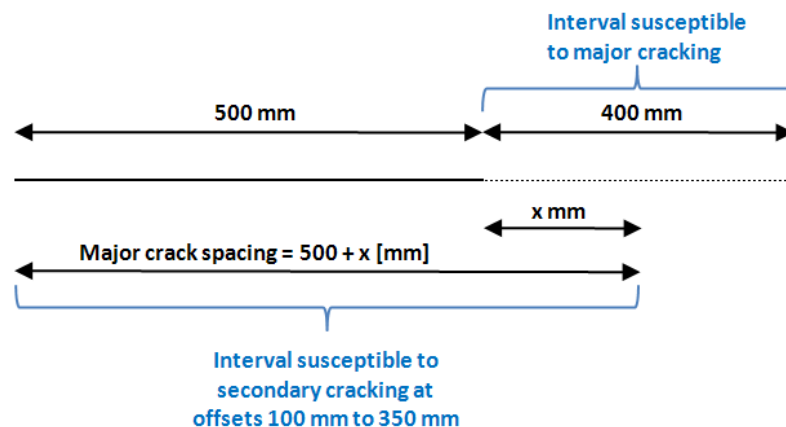
Figure 5.17 Schematic representation of crack formation on UTCRCP

91

5.5 Closure

Initial shrinkage cracks, labelled as major cracks, formed on the test section at intervals between 500 mm and 900 mm. Subsequently these crack spacing were reduce by the formation of secondary cracks. The majority of secondary cracks formed at a spacing ranging from 100 mm to 350 mm.

The simulated traffic had little effect on the transverse crack spacing formation. The contact length of a typical heavy vehicle wheel is between 250 mm to 300 mm. Due to the nature of load induced cracks, the loading wheel has little effect on a crack spacing that is of smaller magnitude than the contact length of the load wheel. However the simulated traffic had an effect on the longitudinal cracking formation and the formation of a circular crack pattern at the centre of the test section. The APT project yielded no punchouts.

The observed crack spacing characteristics will diagnostically be investigated with regard to the mean crack spacing calculated with the M-E PDG procedure and a cncPave analysis in the chapter that follows.

6 PERFORMANCE OF UTCRCP: CRACKING CHARACTERISTICS

6.1 Introduction

This section introduces diagnostic investigations done with modelled pavement characteristics from the software cncPave, version 4.04. cncPave is a concrete pavement design tool developed to assist with decision making regarding the various uncertainties of concrete pavement design. Consequently cncPave was used to compare, evaluate and asses the calculated, modelled and measured crack spacing characteristics. The investigation concludes with the development of a modulus adjustment factor derived from the pavement's performance responses.

6.2 Mean Crack Spacing Evaluation

Apart from the input parameters used in the M-E Analysis Phase II and estimated pavement properties of the linear elastic analysis, cncPave required further input parameters with regard to genuine traffic and region climate. The former was studied in detail by Slavic and Bosman 2007. Therefore traffic input parameters were taken exactly as stipulated by Slavic and Bosman 2007. The necessary climatic data was obtained from the South African Weather Service (SAWS).

6.2.1 Calculated, modelled and measured mean crack spacing

A cncPave model of UTCRCP with a 30 year design life was used for the evaluation process. The time to the first rehabilitation was set to 20 years and exponential traffic growth (4% per annual) was selected. The exponential traffic growth yielded approximately 61 million axle load repetitions over the 30 year life period thus setting common ground to compare the results of the APT project that consisted of approximately 63 million effective axle load repetitions (damage factor of 4.5). Table 6.1 presents a summary of the cncPave input parameters that were used in the evaluation process. The input variables take the form of a triangular distribution, as discussed in Section 2.5.1. The method of input requires a best estimated value, followed by two factors (min and max, Figure 6.1) which complete the triangular distribution.

Table 6.1 cncPave 4.04 input variables and constants for the UTCRCP analysis

No.	Variables	Min	Best	Max	Constants	Value
1	Cement content, kg/m^3	0.98	481	1.02	Life period, yrs	30
2	Water content, l/m^3	0.9	175	1.0	ADTTO, initial HV/day/lane	1052
3	Flexural strength, MPa	0.8	12.8	1.08	Axles/HV, average	5.238
4	Layer1 (slab) h1, mm	0.98	50	1.1	Load on edge, %	0
5	Layer2 (subbase) E2, MPa	0.63	3000	1.8	Damage constant a	1200
6	Layer2 (subbase) h2, mm	0.88	40	1.25	Damage exponent b	4.5
7	Layer3 E3, MPa	0.64	780	1.02	Ratio k1 = E1/f	4450
8	Layer3 h3, mm	0.86	150	1.14	Ratio k2 = ITS/f	0.64
9	Layer4 E4, MPa	0.71	210	1.3	Bond	6
10	Layer4 h4, mm	0.86	150	1.14	Drainage factor	4
11	Layer5 E5, MPa	0.71	210	1.3	Erosion factor	3
12	Growth of HV traffic, % p.a.	0.875	4	1.125	Joint spacing, m	0
13	Speed of HV, ave km/h	0.91	80	1	Steel diameter, mm	5.6
14	Contact pressure, MPa	0.9	0.7	1.1	Steel spacing, mm	50
15	Annual rain fall, mm p.a.	0.7	587	1.3	Aggregate crushing value	20
16	Daily temperature cycle, ºC	0.6	18	1.5	Aggregate type	1
17	Joint movement, mm	0.1	0	2.5	Aggregate size, mm	6.7
18	Void extra Vex, m	0.01	0	2	Cement type	1
19					Aggregate content factor	0.55
20					Fibre content, kg/m^3	100
21					Fibre factor	0.6
22					Relative humidity, %	85

Figure 6.1 depicts the summary of the various mean crack spacing results comprising of the M-E PDG calculation, cncPave model and the field conducted measurements on the UTCRCP test section. After 100 000 simulations, cncPave predicted that 50% of the crack spacing distribution will be of a value greater than 206 mm. This value is situated between the M-E PDG calculation and the 50th percentile of secondary crack spacing.
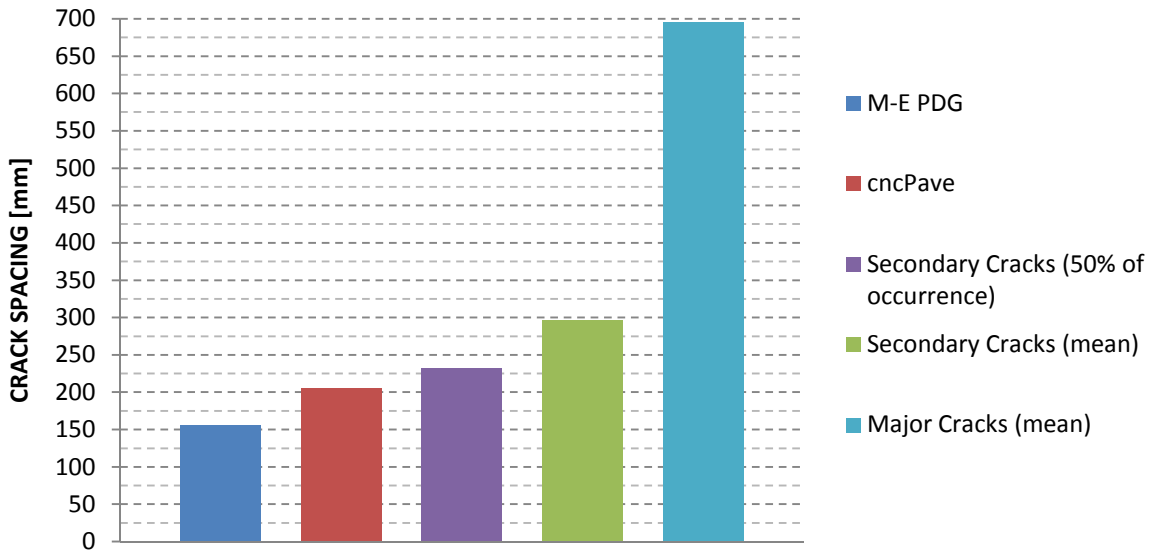
Figure 6.1 Summary of the various calculated, modelled and field-measured mean crack spacing results

The M-E PDG and cncPave prediction model results are within the expected interval of secondary cracking (100 mm to 350 mm) as discussed in Section 5.5. The M-E PDG yields mean crack spacing and the cncPave model yields a 50% greater than probability of occurrence. Both prediction models are sensitive to the input parameters and hence a variation of crack spacing results are obtained for the various combinations of input parameters.

6.2.2 Sensitivity of the M-E PDG mean crack spacing prediction model

A sensitivity analysis was done on the M-E PDG mean crack spacing prediction model. The Best Estimate 1200k result from Table 4.8 was used in this evaluation. Depicted in Figure 6.2 is a summary of the variation for the calculated mean crack spacing due to a change in a specific variable.

In each analysis only one variable was subjected to change whilst the rest remained at fixed magnitudes for the Best Estimate 1200k scenario. However, if the most favourable combination of variation in variables is chosen to increase the crack spacing the calculated mean crack spacing results to 304 mm and the most unfavourable condition yields a value of 68 mm. This situation stresses the importance of good variable cause-and-effect relation in proportion with each other.

The relationship between modulus of rupture (MOR) and the concrete compressive strength (f_{c28}) is one of the more important examples.
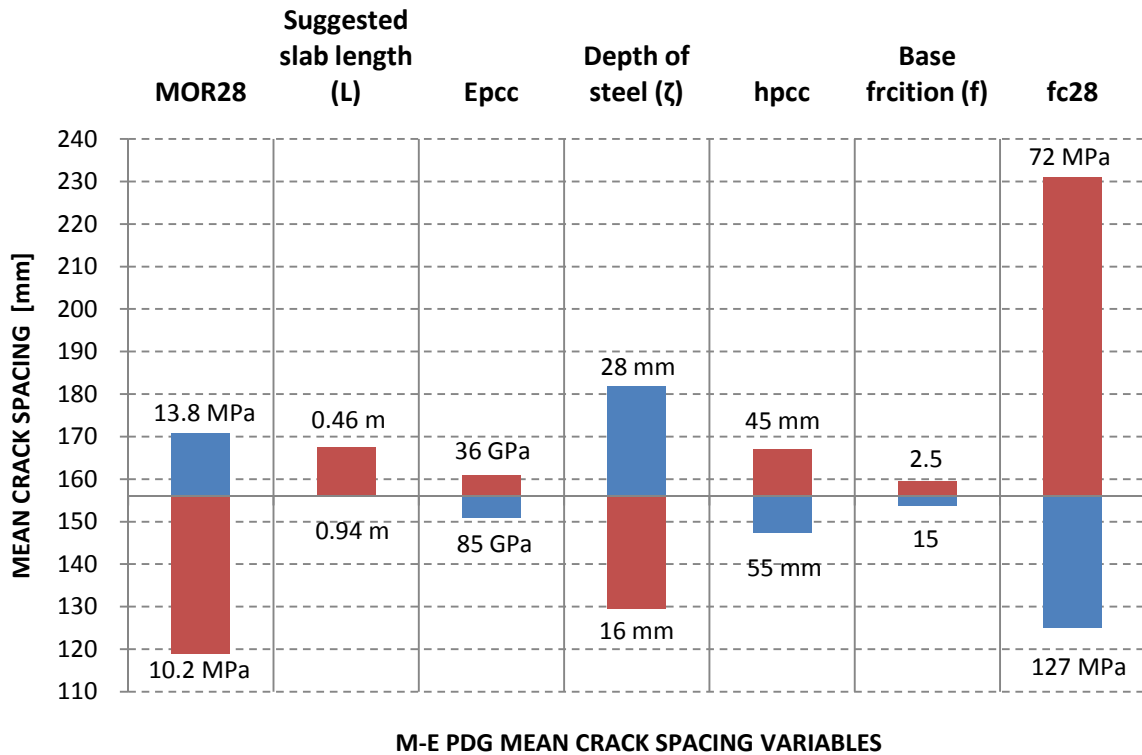
95

Figure 6.2 The sensitivity of the M-E PDG prediction model due to a variation in variables

An increase in MOR and a decrease in the compressive strength yielded mean crack spacing closer to the field measured magnitudes. Even though the concrete mix contains a high amount of steel fibres that would increase the MOR, the corresponding compressive strength is also required for a good crack spacing estimation.

Due to the developing nature of the UTCRCP concrete mix an existing relationship between these two parameters could not be found. However, according to work done by Ramadoss and Nagamani 2008 on a similar high performance concrete (HPC) mix the following relationship was obtained.

$$MOR = 0.019 f_{c28}^{1.425}$$ (6.1)

The steel fibres in the mix were crimped, 36 mm in length with a diameter of 0.45 mm (Ramadoss and Nagamani 2008). This relationship does not simulate the UTCRCP conditions but gives an estimated relationship between the MOR and concrete compressive strength for heavy fibre reinforced HPC. Selecting a concrete compressive strength of 100 MPa yielded a MOR of 13.5 MPa with Equation 6.1.

The other main variable influencing the mean crack spacing is the depth of the longitudinal steel placement. Steel depth was varied over a distance of two steel bar diameters i.e. one steel bar diameter above and one steel bar diameter below the designed depth of the reinforcing steel. This variation considers then the depth of the steel when the reinforcing meshes overlaps. Due to rigid construction measures the depth of steel is unlikely to be in excess of 22.2 mm (designed depth). In the case where the steel meshes overlap the depth of steel is likely to be approximately 16 mm. Therefore the depth of steel remained at 22.2 mm in the mean crack spacing calculation procedure.

The elastic modulus of the concrete and base friction parameters had the smallest influence on the crack spacing outcome, but the thickness of the UTCRCP layer contributed to some extent. The nature of the project, being the first UTCRCP LTPP sections, included thorough monitoring of the construction process thus resulting in good quality control of the layer thicknesses. Hence the layer thickness with a magnitude of 50 mm was still selected in the mean crack spacing calculation procedure.

Finally the M-E PDG suggests a slab length 144 in (3.7 m) for mean crack spacing calculation. Section 4.4.4 concluded that the suggested slab length should be adjusted for UTCRCP, hence the new suggested slab length was set equal to the mean crack spacing of the major cracks (approximately 700 mm (28 in)) measured on the test section. The suggested slab length was further varied one standard deviation to the left (460 mm) and to the right (940 mm). The former case (460 mm) exceeds the maximum radius of relative stiffness (193 mm) by a factor of two. If the slab is thus centrally loaded it is still capable of incorporating the radius of relative stiffness to all directions in the horizontal plane. The slab length was selected at 700 mm.

The combination of the above discussed variables resulted in a mean crack spacing of 186 mm. The M-E PDG prediction model for mean crack spacing results in a seasonal increment for mean crack spacing, hence the current prediction of 186 mm is approximately 110 mm less the observed secondary mean crack spacing, but is between the 175 mm to 200 mm interval which has the joint highest occurrence of secondary crack spacing (Figure 5.14).

6.2.3 *Sensitivity of the cncPave prediction model*

The WHAT-IF experiments in cncPave allow the user to vary a single input parameter and instantly view the outcome of a selected output parameter. Crack spacing was selected as the preferred output parameter. A trend similar to the M-E PDG sensitivity analysis was observed for the flexural strength (MOR).

It is continuously stressed in the literature how important the bond friction factor is between the newly overlain UTCRCP on top of an existing pavement as part of a rehabilitation action. The bond friction factor is to influence the curling stresses, layer permeability and crack development, yet a variation in the bond friction parameter yield no difference in the results of mean crack spacing.

The thickness of the UTCRCP layer had an opposite response to mean crack spacing than what was found with the E-M PDG prediction model. The thickness of the layer was also varied from 45 mm to 55 mm resulting in mean crack spacing of magnitudes 181 mm to 230 mm respectively. The daily temperature cycle also influenced the cncPave prediction model for mean crack spacing. A warmer temperature cycle yielded smaller mean crack spacing than a cooler temperature cycle indicating that UTCRCP cracking is seasonal related. Warmer conditions increase the heat of the hydration reaction which catalyzes the shrinkage process thus ultimately increasing the strain at steel depth. A greater strain at the depth of steel requires more (or greater) transverse cracks to reach a state of stress equilibrium hence a smaller magnitude for mean crack spacing.

A variable that had not previously been investigated is the effect of steel fibres in the concrete mix. The M-E PDG prediction model does not regard this variable as an input parameter. Figure 6.3 depicts the effect of the fibre factor on the 50th percentile crack spacing result.
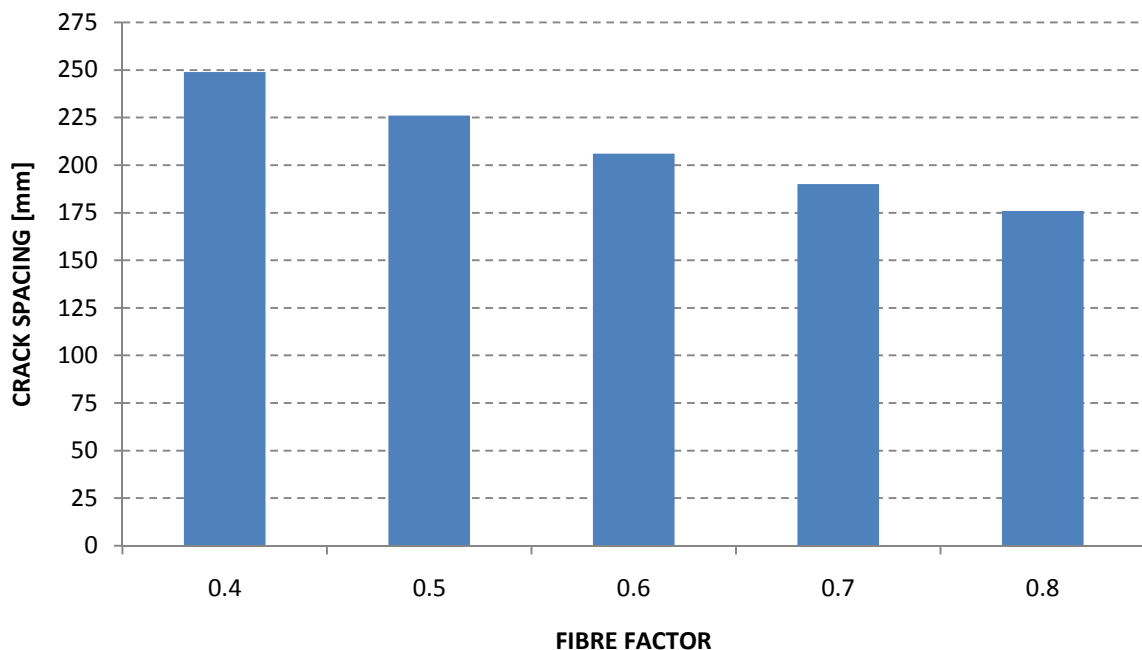

Figure 6.3 The effect of the fibre factor on the 50th percentile crack spacing result

The fibre factor depends on the fibre type, material characteristics, fibre shape, length and diameter (cncPave 4.04, 2009). The guideline in cncPave regarding the fibres in the UTCRCP concrete mix indicates that a fibre factor between 0.5 and 0.8 should be selected. If the steel fibres tend to be brittle 0.02 should be subtracted from the select factor. If the fibre factor should be 0.7 instead of the selected 0.6 then the result of crack spacing would compare well with the investigated combination of the M-E PDG prediction model (Figure 6.4).
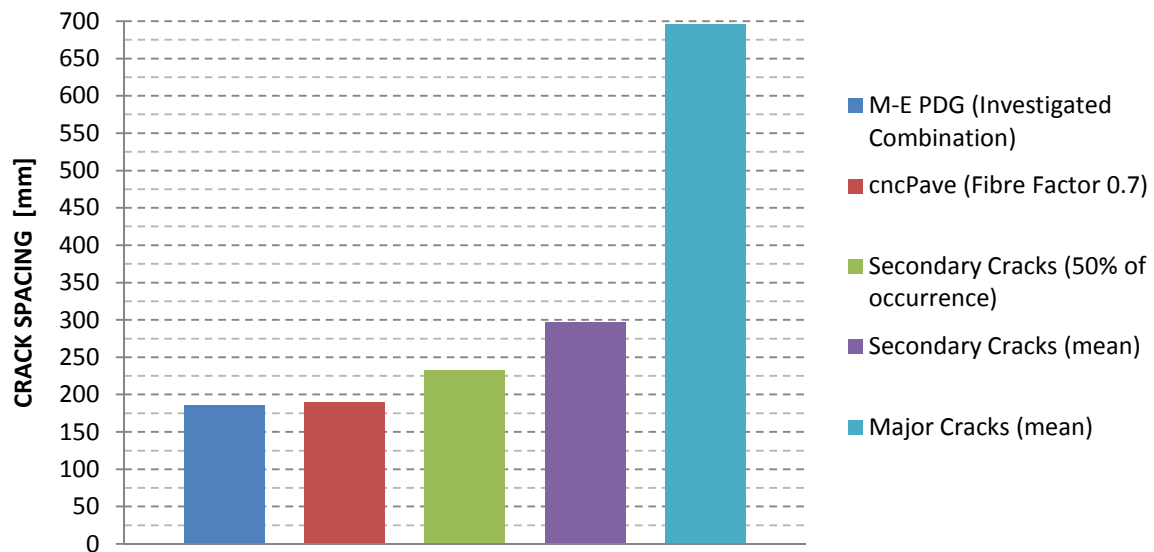

Figure 6.4 Summary of the various calculated, modelled and field-measured mean crack spacing result subsequent to sensitivity analyses

It is not impossible for the steel fibre factor to 0.7 if the age of the pavement is considered. The UTCRCP overlay is approximately in its second year of a 30 year design life period therefore the properties of the steel fibre can be considered to be above the average (0.65) steel fibre factor. Both prediction models still yield smaller crack spacing results after the sensitivity analyses than what was recorded on the test section.

6.2.4 Evaluation of the field-measured mean crack spacing results

Apart from the method of measuring crack spacing which was discussed in Section 5.3, there is no direct variable that influences the measured mean crack spacing. Therefore resulting attributes that influence crack spacing are used to evaluate the measured mean crack spacing.

The argument concerning the relative young age of the pavement holds firm for the following case. It is expected that more cracks will develop as the age (i.e. shrinkage) of the pavement

increases, resulting in a smaller mean crack spacing than observed in this study. This statement coincides with the results of the cncPave prediction model depicted in Figure 6.5 and Figure 6.6.
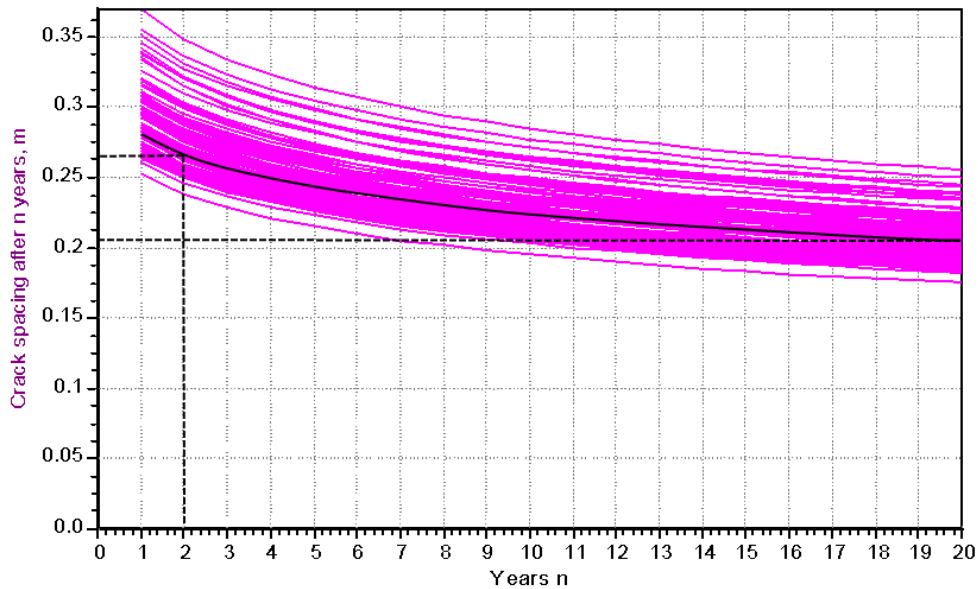

Figure 6.5 Build-ups of the cncPave crack spacing intervals over the duration of pavement life
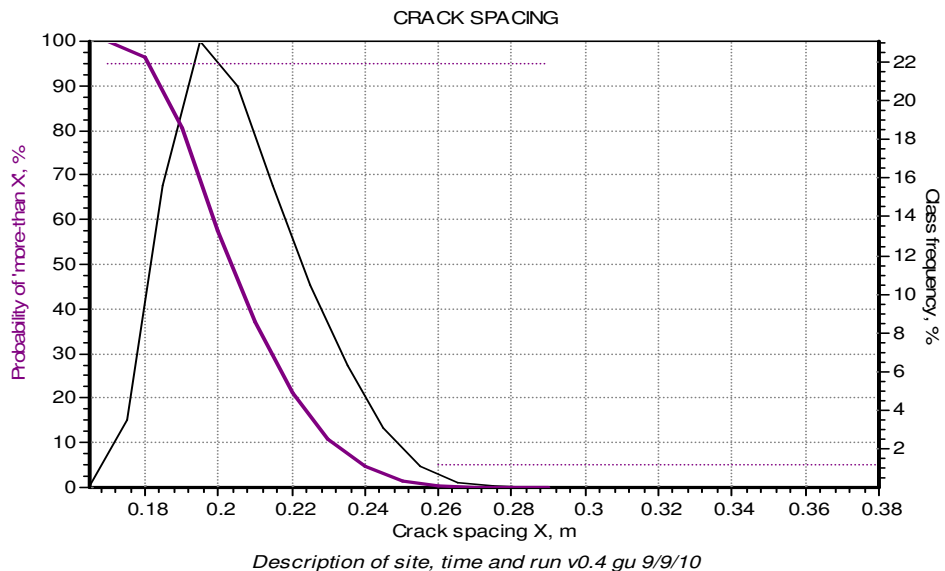

Description of site, time and run v0.4 gu 9/9/10

Figure 6.6 cncPave predicted crack spacing confidence intervals

Figure 6.5 indicates that the cncPave prediction model has a transverse crack spacing distribution ranging from 175 mm to 260 mm, 20 years after construction.

The confidence intervals (Figure 6.6) depicts that 95% of the crack spacing is greater than 180 mm, 5% of the crack spacing beyond 240 mm and 50% of the cracks are greater than 206 mm. However, two years after construction the transverse crack spacing distribution ranges from 237 mm to 350 mm, with a probability that 50% of the cracks will be greater than 265 mm (Figure 6.5). This probability matches the 50 percentile (233 mm) of the secondary cracks (Figure 5.10 and Figure 6.1).

6.2.5 Interim conclusion

The relationship of the MOR (flexural strength) and the concrete compressive strength significantly influences the result of the mean crack spacing as determined via the M-E PDG prediction model. A good understanding of this relationship for the UTCRCP mix would yield less uncertainty in calculating the mean crack spacing with the M-E PDG prediction model.

The suggested slab length of approximately 700 mm in the M-E PDG's mean crack spacing calculation should scientifically be validated by further research. Approximations were made on visual surveys only that were statistically analyzed.

The cncPave prediction model has a smaller range for crack spacing occurrence than what was observed in the field. In the second year after the construction of the UTCRCP layer cncPave predicts crack spacing ranging from 237 mm to 350 mm with a 50% greater than value of 265 mm. The observed crack spacing indicates a range of 100 mm to 350 mm with a 50% greater than value of 233 mm. A decrease in the measured mean crack spacing will occur as the age of the pavement increase.

6.3 Pavement Loading Response

This section investigated characteristic pavement response under simulated traffic. Pavement response characteristics are used in the construction of models. Hence the aim of this investigation was to include pavement response in the calculation process of crack spacing intervals.

6.3.1 Dynamic deflection response

The pavement's dynamic deflection response was measured with a MDD as discussed in Section 3.3.2.3. Figure 6.7 schematically depicts the positions of the two LVDTs of the MDD system.
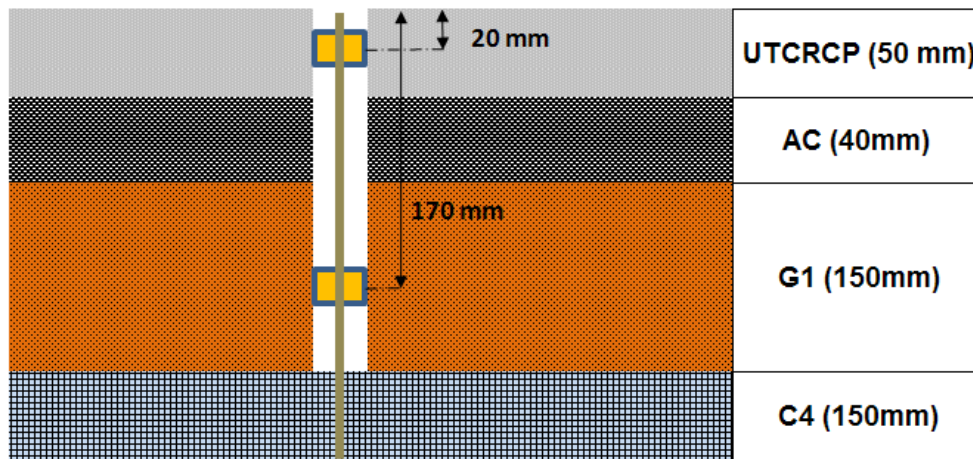
Figure 6.7 Schematic section view of the MDD installation

Deflections were measured relative to the pavement's static surface position. The results of the MDD measurements under wet and dry trafficking conditions are depicted in Figure 6.8.
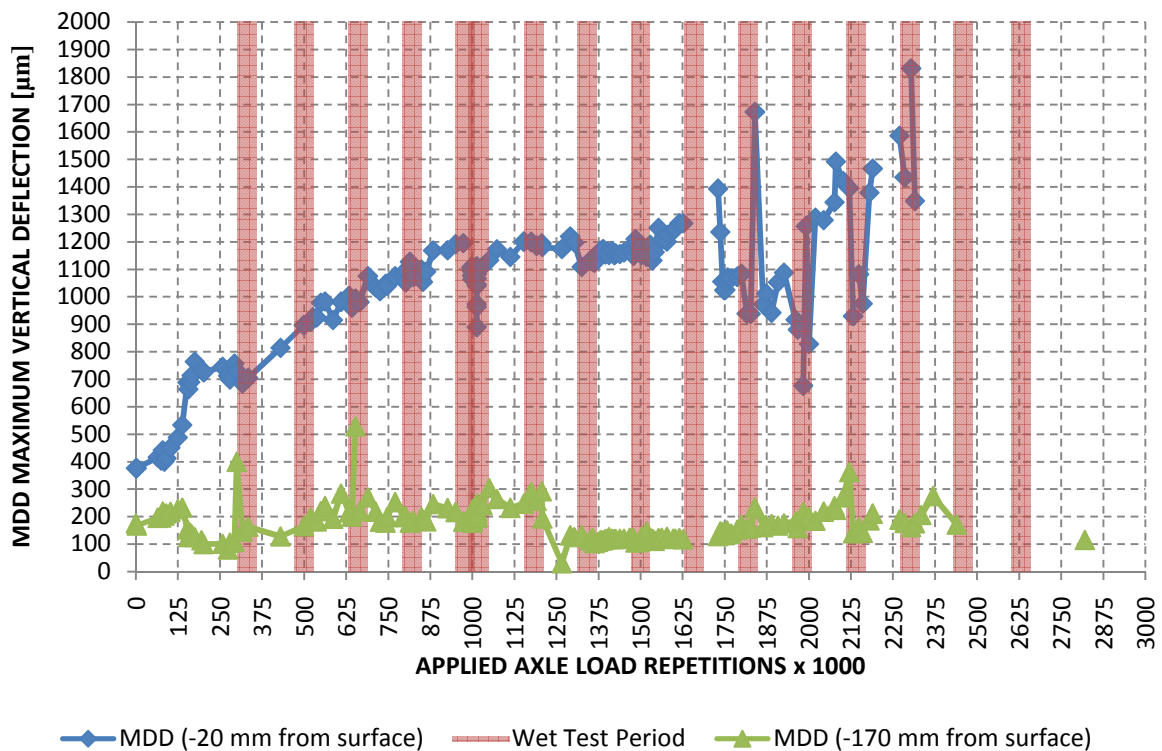

Figure 6.8 Maximum MDD dynamic deflections over the duration of the APT project

The dynamic deflection in the G1 subgrade remained fairly constant over the duration of the APT project, contrary to the deflection response of the UTCRCP. The UTCRCP's dynamic deflection response increased significantly after approximately 200 000 applied load axle repetitions, when the applied loads were increased from 75 kN to 80 kN. Steady increase in

102

deflection continued to 1 million load applications. The reduction in the maximum deflection at 1 million load applications is due to the application of transverse wandering. Transverse wandering was postponed at 1.16 million load application and reintroduced at 1.64 million load applications (See Table 3.4).

An increase in the UTCRCP layer deflection was observed in the later stages (1.64 million to 2.8 million) of the APT project. Similar UTCRCP responses were obtained under wet trafficking by Hugo, et al. 2008 on the STPP trail sections in Heidelberg.

The difference in the measured deflection responses of the UTCRCP layer and the G1 granular subbase is discussed mentioning two possible theories. The first theory regards the UTCRCP as a very rigid plate thus distributing the force of the applied wheel over a large area. A 'sandwich' effect is created by the underlying C4 cement stabilized layers acting as an anvil, trapping the weaker (less stiff) G1 granular and AC layers. The deflection measured at the UTCRCP layer is thus absorbed by these two layers. Under such conditions pumping due to fatigue is expected. Heavy pumping under wet conditions was observed in the vicinity of the MDD at roughly 1.5 million load applications.

The second more plausible theory presumes that the difference in deflection can be ascribed to the alteration of the pavement system. A 39 mm diameter hole is necessary to install the MDD system. A 4x4 mm grove was cut into the pavement surface on the 0 m transverse offset line to install and protect the MDD data acquisition cable, thus inducing a transverse crack. The alteration in the pavement system localized stresses resulting in an increased fatigue process. The maximum FWD deflection was measured at this position of which the magnitude greatly exceeded all other deflection measurements (Figure 4.2). Under wet conditions water had easy access to the substructure resulting in pumping and the formation of a void with possible localized delamination of the UTCRCP layer (no coring was done). The formation of the void induced the circular crack patterns as discussed in Section 5.2.

The expected value of surface deflection estimated by the cncPave prediction model is 108 μm. This value was obtained by implementing the applied load distribution of heavy vehicle axles as stipulated by Slavik and Bosman 2007. Magnitudes of approximately 1800 μm were measured with the MDD near the termination of the APT project, vastly exceeding the predicted deflection.

6.3.2 Seismic response

The pavement's seismic response was monitored with the PSPA as discussed in Section 3.3.2.4. Figure 6.9 depicts the schematic representation of the measurement positions under the trafficking wheel of the MLS 66.
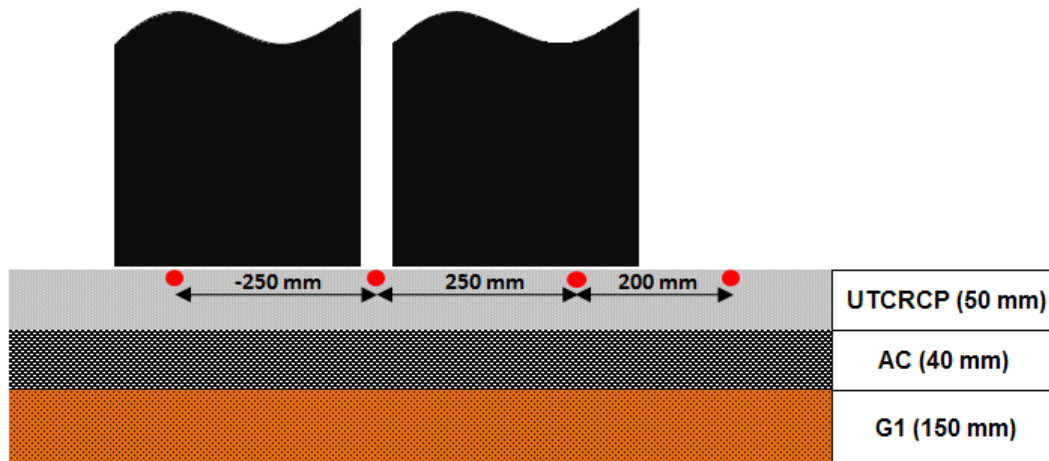

Figure 6.9 Positions of PSPA measurements under the MLS 66 trafficking wheel

Due to the composition of the pavement structure, temperature and moisture content were identified as influencing factors. The stiffness of the AC layer is subjective to load frequency and temperature and the stiffness of the G1 granular subbase layer is influenced by moisture. According to Nazarian, et al. 2002 the modulus of the subbase materials can be related to the moisture content.

The stiffness of the UTCRCP is not directly affected by the identified influencing factors, but the UTCRCP stiffness is directly affected by the stiffness of the underlying layers. As a result the measured UTCRCP seismic stiffness is a composite stiffness. To account for the variation in temperature difference in the AC layer the composite UTCRCP seismic stiffness results were normalized to 25 °C with Equation 6.2, as stipulated in the PSPA test protocol (FHWA-CFL/TD-09-002 2009).

$$E_{25} = \frac{E_t}{1.35 - 0.014t} \tag{6.2}$$

The results of the average longitudinal UTCRCP composite stiffness ratios over the duration of the APT project are presented in Figure 6.10.
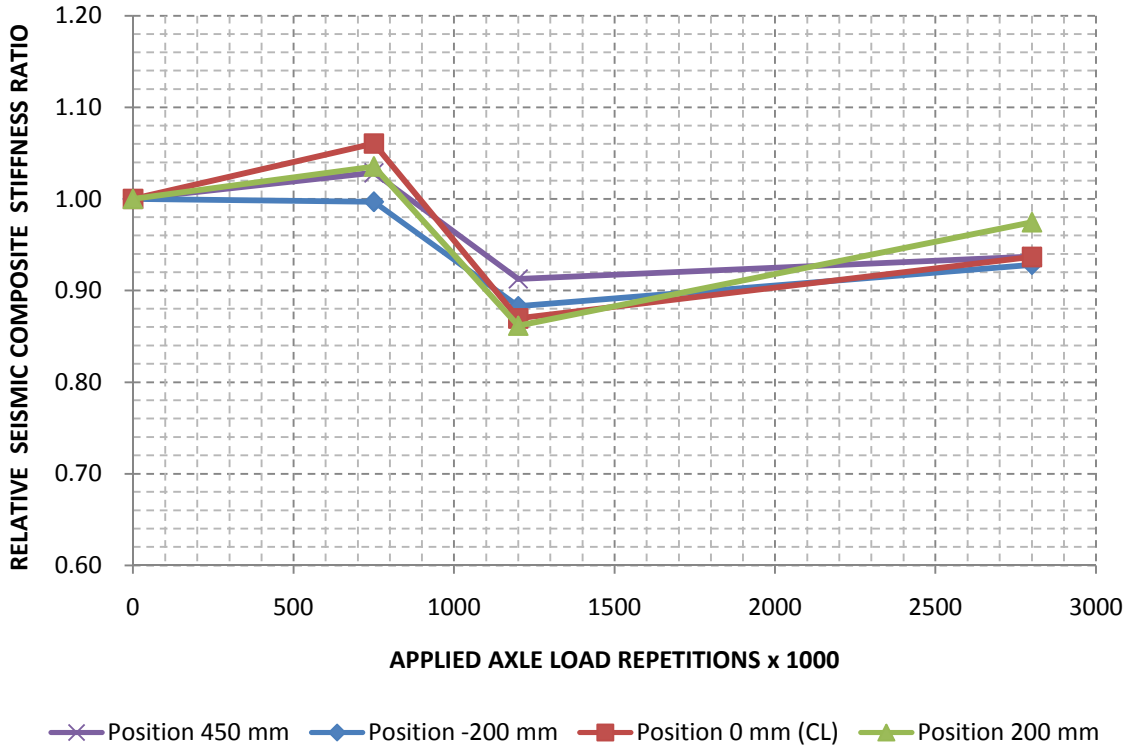
Figure 6.10 Average longitudinal UTCRCP's relative composite seismic stiffness at the various load application intervals

The majority of the composite stiffness values increased from the start of the project to the 750 000 load repetition stage. The increase in composite stiffness can be contributed to compaction of the previous non-trafficked section and possible increase of the moisture content in the G1 granular layer. Cyclic wet trafficking was introduced from 300 000 applied load applications thus it is possible that the G1 layer exhibits responses near an optimum moisture content. Research done by Nazarian, et al. 2002 depicted in Figure 6.11, illustrates the seismic modulus response of subbase material under moistened conditions.
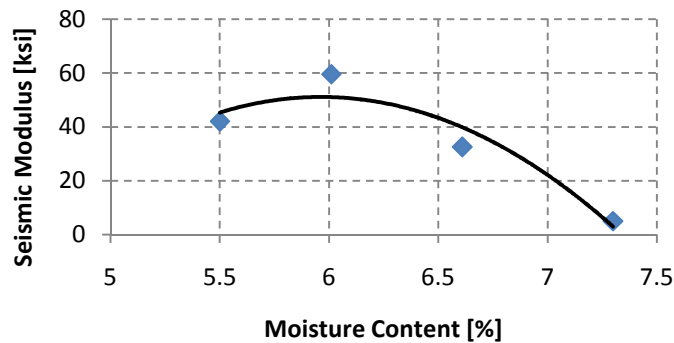

Figure 6.11 Variation in modulus with moisture under constant compaction effort (Nazarian, et al. 2002)

105

A reduction in seismic stiffness after the 750 000 axle load measurements coincides with the application of transverse wandering at 1 million load applications. From Figure 6.11 it is also expected that the seismic modulus of the G1 layer would decrease if exposed to more moisture subsequent reaching the optimum moisture content. Similar to the 'healing' effect observed with the FWD deflection responses the seismic stiffness response indicates a gradual increase from the 1.2 million load repetition stage to the termination of the project at 2.8 million load applications. Note should be taken that the third and fourth set of PSPA readings i.e. the 1.2 million and 2.8 million were taken approximately one year apart.

Similar trends were observed for the average transverse UTCRCP relative-composite-seismic-stiffness results. There existed no definite difference between the longitudinal and transverse results apart from a higher degree of scatter in the transverse results.

6.3.3 Development of a deflection to modulus adjustment factor

The seismic stiffness results as presented and discussed in Section 6.3.2 was used to develop a UTCRCP deflection to modulus adjustment factor. The average 40 kN FWD maximum deflections for the intervals zero, 1.2 million and 2.8 million applied load applications were evaluated with the corresponding relative seismic stiffness ratios. Due to the restricted number of data point this function as depicted in Figure 6.12 is interpreted as a rough estimation of the existing relationship between the UTCRCP deflection and seismic responses.
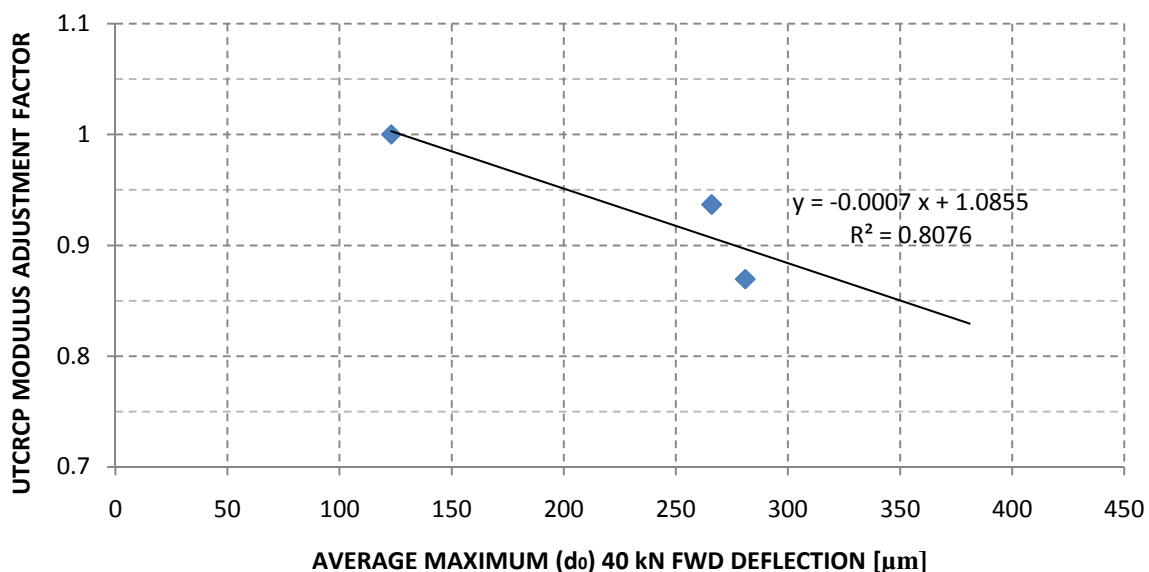

The chart shows UTCRCP MODULUS ADJUSTMENT FACTOR (y-axis, 0.7 to 1.1) versus AVERAGE MAXIMUM (d_0) 40 kN FWD DEFLECTION [μm] (x-axis, 0 to 450). Trend line equation: $y = -0.0007x + 1.0855$, $R^2 = 0.8076$

Figure 6.12 The deflection to modulus adjustment factor derived from UTCRCP performance

$$MAF = -0.0007d_0 + 1.0855 \qquad\qquad (6.3)$$

By obtaining a relationship between the concrete compressive strength and elastic modulus of the UTCRCP layer the effect of a deteriorating elastic modulus can be exhibited in the concrete compressive strength. As discussed in Section 6.2.5 the relationship between the concrete compressive strength and modulus of rupture is of significant importance in the calculation of the mean crack spacing with the M-E PDG prediction model. Thus by conducting FWD deflection tests, a UTCRCP modulus adjustment factor (MAF) can be obtained with Equation 6.3. This MAF will account for the deterioration of the effective stiffness of the UTCRCP.

6.3.4 Interim conclusions

The installation of the MDD prior to APT caused artificial damage to the pavement system. This damage encouraged a localized stress focal point thus exhibiting altered field responses under APT. Channelized traffic loading with the MLS 66 had little to no effect on the orientation (longitudinal or transverse) of the seismic response measured with the PSPA.

A relationship in the reduction of seismic modulus and an increase in pavement surface deflection had been noted and depicted in Figure 6.12. The current relationship is limited to three data points, thus development of a stronger model requires further research. A modulus adjustment factor can combine in situ pavement responses with developed laboratory testing.

6.4 Closure

The cause and effect relationships of the various influencing parameters and observations contributing to the crack spacing prediction models were evaluated by means of sensitivity analyses. The sensitivity analyses served as processes of elimination for uncertainties regarding the crack spacing parameters. Hence this concludes the diagnostic investigation of the UTCRCP test section.

7   CONCLUSIONS AND RECOMMENDATIONS

7.1 Introduction

The conducted study investigated the characteristics of transverse cracking on a UTCRCP test section under APT. This section presents the findings and conclusions pertaining to this study. Furthermore this section also includes recommendations for future research regarding UTCRCP.

7.2 Summary of Findings

This section summarizes the discoveries and findings that were made during the study.

7.2.1 Calculation of pavement parameters using empirical methods

An increase in the pavement's deflection response under APT resulted in an increase in the magnitude of the empirically determined radius of relative stiffness. The majority of the results were below the lower limit of this method, as stipulated by the M-E PDG. This resulted in unrealistic calculations of the UTCRCP concrete elastic modulus. The method was deemed inappropriate for the specific UTCRCP system.

7.2.2 Calculation of pavement parameters using linear elastic methods

Linear elastic pavement modelling using Bisar 3.0 and Westergaard's model for interior rigid pavement loading yielded good results. The modelling process indicted a form of visco-elastic pavement response and subbase (cement stabilized) distress. The distress was accounted to the APT.

Non-linear pavement deflection responses were identified by the formation of an obtuse angle in some of the FWD deflection plots.

7.2.3 M-E PDG mean crack spacing calculation

Mean crack spacing was initially calculated to 156 mm. This result was affected by a range of factors such as the concrete mix characteristics, pavement geometric properties and climatic conditions. The more important aspects were identified as the depth of steel placement in the UTCRCP, the suggested slab length for modelling, concrete compressive

strength and the modulus of rupture. The mean spacing included only environmentally associated cracks and did not consider the effect or contribution of traffic related cracks and did not yield a close approximation for the seasonal estimated value of mean crack spacing as was measured. A shortfall of this model for the current study was the exclusion of the effect high amount of steel fibres had on the concrete mix and on the concrete's characteristics. The model was greatly influenced by the relationships of the various input parameters. Contrary to literature, the base friction factor i.e. the bond between the UTCRCP and the AC did not notably influence the outcome of the mean crack spacing calculation.

7.2.4 Observed crack spacing

Initial transverse shrinkage cracks were labelled as major cracks and formed at an average spacing of 695 mm, within a popular range consisting of 500 mm to 900 mm. Subsequent formations of secondary cracks formed at an average spacing of 296 mm within an estimated range of 100 mm to 350 mm. It was observed that segments delineated by large magnitudes of initial crack spacing, were more prone to secondary cracking than segments delineated by an initial spacing of lesser magnitude.

The simulated traffic did not decrease the measure of secondary crack spacing and is considered as having little effect on the transverse crack spacing formation of the UTCRCP system. No punchouts were recorded during the test and therefore the characterization of the contributing cracks could not be made. However circular crack patterns were observed which indicate similar means of failure as reported by Kannemeyer, et al. 2008 on the Heidleberg TCC STPP sections.

7.2.5 Crack spacing evaluation

The descriptive statistical analysis indicated that secondary cracks have formed between 100 mm to 350 mm. This included a mean spacing of 296 mm and a probability that 50% of all cracks consist of crack spacing greater than 233 mm. Two years subsequent to the UTCRCP construction, the build-ups of the cncPave prediction model indicated that cracks will form between 237 mm and 350 mm, with a probability that 50% of the cracks will be greater than 265 mm. Thus the predicted ranges of cracks are within the measured ranges.

A sensitivity analysis of the M-E PDG mean crack spacing indicated the importance of established relations between the concrete mix characteristics for proper modelling. The relationships of the concrete compressive strength, modulus of rupture and elastic modulus

of the concrete is necessary for more accurate modelling. The suggested relationships yielded a recalculated mean crack spacing of 186 mm.

Both prediction models predicted a mean spacing or 50% greater than probability within the estimated representative secondary crack spacing interval (100 mm to 350 mm). One difference of the M-E PDG's mean crack spacing prediction model and the cncPave model is that the cncPave model accounts for steel fibres in the concrete mix. This has a significant influence on the crack spacing results.

7.2.6 Load response evaluation

The method of obtaining dynamic deflection response caused artificial damage to the pavement structure. This led to a localized stress focal point.

The direction of loading with the MLS 66 did not influence the seismic response results of the pavement.

7.3 Conclusions

This section concludes findings pertaining to the UTCRCP models, transverse cracking and applied methods.

7.3.1 UTCRCP modelling

By using deflection responses of the FWD the in situ elastic modulus of the concrete could be modelled by simulating the deflection bowl on a linear elastic program. The result of the modulus can be used to calculate the radius of relative stiffness of the UTCRCP layer. Empirical modelling techniques for the calculation of these two parameters as investigated by this study should not be considered for UTCRCP.

The load magnitude of the FWD did not significantly influence the modelled and calculated parameters, although the AC base did respond in a visco-elastic manner.

7.3.2 Crack spacing characteristics

Initial shrinkage cracks form at a spacing between 500 mm and 900 m, followed by secondary cracking consisting of offsets between 100 mm to 350 mm (Figure 5.17). The UTCRCP cracks consist primarily of Y-cracks and Divided cracks. Meandering cracks and

Cluster cracks forms around pavement weak spots i.e. spots that are damaged. Longitudinal cracks forms approximately 300 mm from the wheel path edge.

Transverse crack spacing is not significantly affected by traffic, however traffic does affect the formation of longitudinal cracks.

7.3.3 Research equipment

Seismic wave propagation by means of the PSPA can be use to evaluate the changes in the stiffness of the UTCRCP. The orientation of the device does not play a significant role in the seismic response of the UTCRCP.

7.4 Summary of Contributions

The summary of contributions comments on the significance of the conclusions and the practical implications thereof.

7.4.1 Significance of the conclusion

Based on the FWD deflection results, the study concludes that UTCRCP can be modelled as a layered linear elastic system. Parameters obtained from such modelling are sufficient to serve as variables that are used in prediction models. Calculations of mean crack spacing are sensitive to the relationships of the various input parameters. Therefore the characteristics of concrete mix and the relationships of these characteristics must be established.

The crack pattern on the UTCRCP surface can be represented by a Weibull distribution. Thus statistic analysis and predictions can be made by using this distribution.

7.4.2 Practical implications

cncPave predicts crack spacing occurrence of smaller dispersion than what was observed in the field. Necessary adjustments to this software may be needed to increase the predicted crack spacing range.

7.5 Recommendations for Future Research

The following recommendations for future research are made by the experience obtained, results achieved, findings made and diagnostic investigations reported upon in this study.

1) It is recommended that more UTCRCP sections should be inspected with regard to cracking formation. A higher number of observations will result in less uncertainty about the variance and patterns of the developed cracks. Also greater number in observed spacing can contribute to the accuracy of the cncPave program.
2) Laboratory testing should be done on the UTCRCP mix, establishing the relations of the characteristics that are subject to the mix properties. Specific interests relating to the concrete compressive strength, modulus of rupture, elastic modulus of the concrete and concrete shrinkage should be explored. To summarize, it is recommended to conduct a study on the fracture mechanics of UTCRCP.
3) Alternative methods of dynamic deflection response should be considered. The MDD disrupts the natural response of the pavement under loading due to the hole in the pavement that is needed for installment. It is recommended that research be done for example, on accelerometers as a data capture device for dynamic deflection responses. This is device is smaller than the MDD and much easier to install.
4) The contribution of the asphalt base layer to the UTCRCP should be researched for two separate cases. The first case being the effect of structural support and thus contribution to deflection under dynamic loading response. The second case being the measure of friction provided by the existing asphalt surface to the bottom of the UTCRCP layer.
5) Acquiring more data can yield to a stronger relation of the Modulus Adjustment Factor.

The fulfillment of the above suggested research themes would increase the knowledge upon the characteristics of UTCRCP. Such characteristics will contribute uniquely to the design process of the UTCRCP as an overlay.

7.6 Closure

The Heidelberg Traffic Control Centre APT research project was done as an independent study on UTCRCP. The content reported in this thesis reflects the view of the author who is responsible for the facts and the accuracy of the data presented.

8 REFERENCES

Advertorial. "CncPave takes off." *CONCRETE trends*, VOL6 No1 Feb 2003: 1.

Africon. *HEIDELBERG TRAFFIC CONTROL CENTRE, THE REHABILITATION OF THE SCREENER LANES, UTCRCP CONSTRUCTION REPORT.* First Draft, Pretoria: Africon Engineering International (Pty) Ltd, 2008.

ARA Inc. ERES Consultants Division. *Guide for Mechanistic-Empirical Design, PART 3. DESIGN ANALYSIS, CHAPTER 4. DESIGN OF NEW AND RECONSTRUCTED RIGID PAVEMENTS.* NCHRP 1-37A, Washington: Transportation Research Board, 2004.

ARA Inc. ERES Division. *Guide for Mechanistic-Empirical Design OF NEW AND REHABILITATED PAVEMENT STRUCTURES; APPENDIX QQ: STRUCTURAL RESPONSE MODELS FOR RIGID PAVEMENTS.* NCHRP, APPENDIX QQ:, Washington: Transportation Research Board, 2003.

ARA, Inc., ERES Division. *Guide for Mechanistic-Empirical Design OF NEW AND REHABILITATED PAVEMENT STRUCTURES; APPENDIX LL: PUNCHOUTS IN CONTINUOUSLY REINFORCED CONCRETE PAVEMENTS.* NCHRP, APPENDIX LL:, Washington: Transportation Research Board, 2003.

Buitelaar, P. *Heavy Reinforced Ultra High Performance Concrete.* 5th International CROW workshop in Istanbul 2004, Hojbjerg,Denmark: Contect Aps, 2004.

Cement & Concrete Institute. "The Use of Concrete In Developing Long-Lasting Pavement Solutions for the 21st Century." *SEVENTH INTERNATIONAL CONFERENCE ON CONCRETE PAVEMENT.* Disney's Coronado Springs Resort Lake Buena Vista, FL 32830: International Society for Concrete Pavements, 2001. 133 - 148.

de Vos, E.R. *BEN SCHOEMAN CONTINUOUSLY REINFORCED CONCRETE PAVEMENT TESTING SCOPING REPORT.* Scoping Report, Pretoria: BKS (Pty) Ltd, 2009.

de Vos, E.R. *PERFORMANCE CHARACTERIZATION OF CEMENT TREATED SAND BASE MATERIAL OF MOZAMBIQUE.* MSC Thesis, Stellenbosch: University of Stellenbosch, 2007.

FHWA-CFL/TD-09-002. *PORTABLE SEISMIC PROPERTY ANALYZER Identification of Asphalt Pavement Layers.* Report No. FHWA-CFL/TD-09-002, 12300 West Dakota Avenue Lakewood, CO 80228: Federal Highway Administration (FHWA), 2009.

FHWA-ICT-09-040. *MECHANISTIC-EMPIRICAL DESIGN CONCEPTS FOR CONTINUOUSLY REINFORCED CONCRETE PAVEMENTS IN ILLINOIS.* Final Report, Urbana-Champaign: University of Illinois at Urbana-Champaign, 2009.

FHWA-RD-00-086. *Backcalculation of Layer Parameters for LTPP Test Sections, Volume I: Slab on Elastic Solid and Slab on Dense-Liquid Foundation Analysis of Rigid Pavements.* FHWA-RD-00-086, Washington: Transporation Research Board, 2001.

FHWA-RD-96-198. *LTPP DATA ANALYSIS, Phase 1: Validation of Guidelines for k-Value Selection and Concrete Pavement Performance Prediction.* FHWA-RD-96-198, Georgetown: U.S Department of Transportation Federal Highway Administration, 1997.

Fulton, F.S. *CONCRETE TECHNOLOGY A SOUTH AFRICAN HANDBOOK.* Johannesburg: Portland Cement Institute, 1977.

Galal, K.A., B.J. Coree, J.E. Haddock, and T.D. White. *STRUCTURAL ADEQUACY OF RUBBLIZED PCC PAVEMENT.* MSCE Report, West Lafayette, Indiana 47906: Indiana Department of Transportation, 1998.

Guiama, D., E. Horak, and D.T. Visser. *COMPARATIVE STUDY OF NON-DESTRUCTIVE FIELD TESTING DEVICES ON BSM-EMULSION.* M Thesis, Pretoria, South Africa: University of Pretoria, 2010.

Gutzwiller, M.J., and J.L. Waling. *Experimental Continuously-Reinforced Concrete Pavements: Ptogress Report--1959.* Bulletin 238, Purdue University: Highway Research Board, 1960.

Horak, E. *Surface Moduli Determined with the Falling Weight Deflectometer Used as a Benchmarking Tool.* Research Report, Pretoria, South Africa: University of Pretoria, 2007.

Houben, L.J.M. *STRUCTUAL DESIGN OF PAVEMENTS, PART 5 DESIGN OF CONCRETE PAVEMENTS.* Report CT4860, Netherlands: L.J.M. Houben, 2006.

Huang, Y.H. *Pavement Analysis and Design.* Englewood Cliffs, New Jersey 07632: Prentice-Hall, Inc., 1993.

Hugo, F, E.R. de Vos, H Tayob, L Kannemeyer, and M Partle. *INNOVATIVE APPLICATIONS OF THE MLS10 FOR DEVELOPING PAVEMENT DESIGN SYSTEMS.* Third International Conference on APT in Madrid 2008, Stellenbosch: Institute for Transport Technology, Stellenbosch University, South Africa, 2008.

Jackson, P A. *Continuously reinforced concrete pavement: A literature review.* Contracter Report 127, Crowthorne, Berkshire UK: Transport and Road Research Laboratory, 1988.

Kannemeyer, L, B.D Perrie, P.J. Struass, and L du Plessis. *Ultra-Thin CRCP: Modelling, Testing under Accelerated Pavement Testing and Field Application for Roads.* Research Report, Pretoria: SANRAL, 2008.

Kannemeyer, L, B.D. Perrie, P.J. Struass, and L du Plessis. *Ultra Thin Continuously Reinforced Concrete Pavement Research in South Africa.* Research Report, Pretoria: SANRAL, 2007.

Khazanovich, L.E.V. *STRUCTURAL ANALYSIS OF MULTI-LAYERED CONCRETE PAVEMENT SYSTEMS.* Thesis, URBABA CHAMPAIGN: UNIVERSITY OF ILLINOIS, 1994.

Kohler, E, and J Roesler. *ACCELERATED PAVEMENT TESTING OF EXTENDED LIFE CONTINUOUSLY REINFORCED CONCRETE PAVEMENT SECTIONS.* Project IHR - R32, Urbana-Champaign: Department of Civil and Environmental Engineering University of Illinois at Urbana-Champaign, 2006.

Manual M10. *CONCRETE PAVEMENT DESIGN AND CONSTRUCTION.* Manual, Pretoria, South Africa: DEPARTMENT OF TRANSPORT, 1995.

Montgomery, D.C, and G.C Runger. *APPLIED STATISTICS AND PROBABILITY FOR ENGINEERS THIRD EDITION.* New York: John Wily & Sons Inc., 2003.

Murison, S, A Shalaby, and T Smith. *ULTRA-THIN WHITETOPPING IN CANADA: STATE-OF-PRACTICE.* 4th Transportation Specialty Conference of the Canadian Society for Civil Engineering, Winnipeg: University of Manitoba, 2002.

Nazarian, S, D Yuan, V Tandon, and M Arellano. *Quality Management of Flexible Pavement Layers with Seismic Methods.* Research Report 1735-3F, El Paso: The University of Texas at El Paso, 2002.

Ramadoss, P, and K Nagamani. "TENSILE STRENGTH AND DURABILITY CHARACTERISTICS OF HIGH-PERFORMANCE FIBER REINFORCED CONCRETE." *The Arabian Journal for Science and Engineering* (The Arabian Journal for Science and Engineering), 2008: Volume 33, Number 2B.

Selezneva, O, M Darter, D Zollinger, and S Shoukry. *Characterization of Transverse Cracking Spatial Variability Using LTPP Data for CRCP Design.* For A2K05(2) Session

entitled, Spatial Variability in Pavement Engineering, Washington: Transportation Research Board, 2002.

Shell International Oil Products B.V. *BISAR 3.0 Software Package.* Koningin Julianaplein 15, 2595 AA The Hague, Netherlands: Bitumen Business Group, 1998.

Slavik, M, and J Bosman. *TRAFFIC LOADING ESTIMATED FROM COUNTS.* Power Point Presentation, Pretoria: BKS, 2007.

Slavik, M., B. D. Perrie, and P. J. Strauss. "LIFE COSTING AND RELIABILITY CONCEPTS IN THE CONCRETE PAVEMENT DESIGN: THE SOUTH AFRICAN APPROACH." *9th International Symposium on Concrete Roads.* Istanbul, Turkey: C&CI, 2004. 9.

Strauss, P.J. *Personal Communiation between P.J. Strauss and J.A.K. Gerber.* Pretoria, South Africa: Stellenbosch University, 2010.

Strauss, P.J., M. Slavik, L. Kannemeyer, and B.D. Perrie. "UPDATING CNCPAVE: INLCUSION OF ULTRA THIN CONTINUOUSLY REINFORCED CONCRETE PAVEMENT (UTCRCP) IN THE MECHANISTIC, EMPERICAL AND RISK BASED CONCRETE PAVEMENT DESIGN METHOD." *International Conference on Concrete Roads (ICCR2007).* Midrand, South Africa: Cement & Concrete Institute, 2007. 204-218.

Theyse, H.L, M de Beer, and F.C Rust. *Overview of the South African Mechanistic Pavement Design Analysis Method.* Pretoria: CSIR, 1996.

Zollinger, D. *THE MECHANISTIC APPROACH BEHIND THE DESIGN FOR CRC PAVEMENT CRACKING IN THE 200X AASHTO GUIDE.* Proceedings of the International Conference on Concrete Roads (ICCR2007), Texas A&M University: Document Transformation Technologies cc, 2007.

APPENDICES

of

CHARACTERIZATION OF CRACKS ON UTCRCP

CONTENTS

A. APPENDIX A – CALCULATION OF MEAN CRACK SPACING

CONTENTS

A.1 M-E PDG Mean Crack Spacing Prediction Model

Calculation of the mean crack spacing can be done by the expression (Equation A.1) presented in the M-E PDG. This expression contains variables with subscripts, i, that indicate seasonal variation.

$$\bar{L} = \frac{f'_{t28} - C_i \sigma_{0,i} \left[1 - \frac{2\zeta}{h_{pcc}} \right]}{\frac{f}{2} + \frac{U_m P_b}{c_{1,i} d_b}}$$

(A.1)

Where;

f'_{t28} =   concrete tensile strength in 28 days (psi)

C_i =   the Bradbury coefficient

$\sigma_{0,i}$ =   Westergaard's nominal stress factor (psi)

ζ =   depth to steel (in)

h_{pcc} =   the concrete slab thickness (in)

f =   friction coefficient

U_m =   the peak bond stress (psi)

P_b =   percentage of steel as a fraction

$c_{1,i}$ =   the first bond stress coefficient

P_b =   reinforcing longitudinal steel bar diameter (in)

A.2 Concrete 28-day Tensile Strength

The variable f'_{t28} can be estimated by using Equation A.2. The modulus of rapture (MOR) also commonly known as flexural strength can be determined by a three point bending (TPB) tests.

$$f'_{t28} = 0.7MOR_{28} \tag{A.2}$$

A.3 Bradbury Coefficient

The Bradbury coefficient (C_i) is used to correct curling stress in finite concrete slabs. Interior and edge corrections can be calculated as follows.

$$C_i = 1 - \frac{2\cos\lambda\cosh\lambda(\tan\lambda + \tanh\lambda)}{\sin 2\lambda_i \sinh 2\lambda_i} \tag{A.3}$$

And;

$$\lambda = \frac{L}{l_i\sqrt{8}} \tag{A.4}$$

Where;

L =   slab (segment) length M-E PDG suggests 144 inches (in)

l_i =   radius of relative stiffness (in)

A.4 Westergaard's Nominal Stress Factor

$$\sigma_{0,i} = \frac{E_{pcc,i}\varepsilon_{tot-\Delta,i}}{2(1 - \mu_{pcc})} \tag{A.5}$$

Where;

$E_{pcc,i}$ =   concrete modulus of elasticity (psi)

$\varepsilon_{tot-\Delta,i}$ =   equivalent total strain difference between the slab surface and slab bottom

μ_{pcc} =   Poisson's ratio of the concrete

A.4.1 The equivalent total strain

The equivalent total strain difference ($\varepsilon_{tot-\Delta,i}$) can be computed as with Equation 2.22.

$$\varepsilon_{tot-\Delta,i} = \alpha_{pcc}\Delta t_{eqv,i} + \varepsilon_{\infty}\Delta\left(1 - rh_{pcc}^{3}\right)_{eqv} \tag{A.6}$$

Where;

α_{pcc} =   coefficient of thermal expansion (CTE) for concrete (1/°F)

$\Delta t_{eqv,i}$ =   the equivalent temperature (°F)

ε_{∞} =   concrete ultimate shrinkage strains

$\Delta\left(1 - rh_{pcc}^{3}\right)_{eqv}$ = relative humidity difference between pavement surface and bottom

A.4.2 Equivalent temperature

The equivalent temperature ($\Delta t_{eqv,i}$) is determined as follows.

$$\Delta t_{eqv,i} = \frac{R_{0,i}}{2CF}\left(1 - e^{-\frac{h_{pcc}}{12}\sqrt{\frac{2\pi}{\gamma_{pcc}^{2}}}}\right) \tag{A.7}$$

And;

$$CF = 1.000 + 0.1116h_{pcc}^{3/2} - 0.565h_{pcc} + 0.685h_{pcc}^{1/2} \tag{A.8}$$

Where;

$R_{0,i}$ =   effective range in temperature (Table A.1) (psi)

γ_{pcc} =   the concrete thermal diffusivity (Table A.2) (ft^2/day)

Table A.1 Effective temperature rages (FHWA-ICT-09-040 2009)

Minimum Seasonal Ambient Temperature (°F)	Effective Range in Temperature (R_0)
< 40	21.5
40 to 60	23.4
60 to 80	25.7
> 80	30.1

3

Table A.2 Concrete thermal diffusivity (FHWA-ICT-09-040 2009)

Coarse Aggregate Type	Concrete Thermal Diffusivity (ft^2/day)
Quartzite	1.39
Limestone	1.22
Dolomite	1.20
Granite	1.03
Rhyolite	0.84
Basalt	0.77
Syenite	1.00
Gabbro	1.00
Chert	1.39

A.4.3 Ultimate shrinkage strains.

Concrete ultimate shrinkage (ε_∞) values typically vary between 415 x 10$_{-6}$ and 1070 x 10$_{-6}$ in./ in. When specific shrinkage data is unavailable, the ultimate shrinkage can be taken as 780 x 10$_{-6}$ in./in. per ACI 209 (1992) recommendations (FHWA-ICT-09-040 2009).

The following formula is recommended by Kohler and Roesler.

$$\varepsilon_\infty = C_1 C_2 \left(26 w^{2.1} (f'_{c28})^{-0.28} + 270 \right)$$ (A.9)

Where;

ε_∞ =   ultimate shrinkage (micro strain)

C_1 =   cement type factor: 1.0 for type I, 0.85 for type II and 1.1 for type III

C_2 =   type of curing factor: 0.75 if steam cured, 1.0 if cured in water or 100%

         humidity and 1.2 if sealed during curing (curing compound)

w =   water content for the mix under consideration (lb/ft^3)

f'_{c28} =   28-day compressive strength (psi)

A.4.4 Relative humidity difference between the slab surface and bottom

The relative humidity difference between the pavement surface and bottom $\Delta\left(1 - rh_{pcc}{}^3\right)_{eqv}$ is calculated using Equation A.10 (FHWA-ICT-09-040 2009).

$$\Delta\left(1 - rh_{pcc}{}^3\right)_{eqv} = 0.2\left(0.0028h_{pcc}{}^2 - 0.107h_{pcc} + 1.4292\right) \tag{A.10}$$

The use of this equation assumes a wet, freezing climatic zone with a minimum ambient humidity range of 50 to 95 percent.

A.5 Peak Bond Stress

The peak bond stress (U_m) is calculated is follows (FHWA-ICT-09-040 2009).

$$U_m = 0.0020k_1 \tag{A.11}$$

$$k_1 = 1000(0.1172f'_{c28}) \tag{A.12}$$

Where;

k_1 =   bond slip coefficient

f'_{c28} =   28-day compressive strength (psi)

A.6 First Bond stress Coefficient

The first bond stress coefficient ($c_{1,i}$) is calculated iteratively as follows (FHWA-ICT-09-040 2009).

$$IF = \ \overline{L}_\iota - L_{seed} < 0.01 \ then \ c_{1,i} = c_{1,seed}$$

$$ELSE \ c_{1,seed} = 0.577 - 9.499E10^{-9}\frac{\ln\varepsilon_{tot-\zeta max}}{\left(\varepsilon_{tot-\zeta max}\right)^2} + 0.00502L_{seed}(\ln L_{seed}) \tag{A.13}$$

Where;

L_{seed} =   seed crack spacing value (in)

$\varepsilon_{tot-\zeta max}=$ total maximum strain at the depth of steel (strain)

A.6.1 Total maximum strain at the depth of steel.

The total maximum strain at the depth of steel $\left(\varepsilon_{tot-\zeta max}\right)$ is calculated as follows (FHWA-ICT-09-040 2009).

$$\varepsilon_{tot-\zeta max} = \Delta T_{\zeta max}\alpha_{pcc} + \varepsilon_{shr} \tag{A.14}$$

Where;

$\Delta T_{\zeta max}=$ maximum concrete temperature difference from the concrete set temperature

at the steel depth (°F)

α_{pcc} = coefficient of thermal expansion (CTE) for concrete (1/°F)

ε_{shr} = unrestrained concrete drying shrinkage at the steel depth (strains).

A.6.2 Maximum concrete temperature difference

The maximum concrete temperature difference from the concrete set temperature at the steel depth ($\Delta T_{\zeta max}$) is calculated as follows (FHWA-ICT-09-040 2009).

$$\Delta T_{\zeta max} = \frac{IF\ T_{set} > T_{steel,min}\ then, T_{set} - T_{steel,min}}{Else\ 0} \tag{A.15}$$

Where;

T_{set} = concrete set temperature at depth of steel (°F)

$T_{steel,min}$ = minimum average temperature at depth of steel (°F)

A.6.3 Concrete set temperature at depth of steel

The concrete set temperature at depth of steel (T_{set}) is the temperature at which the concrete layer exhibits zero thermal stress. This value is evaluated as follows (FHWA-ICT-09-040 2009).

$$T_{set} = CC * 0.59328 * H * 0.5 * 1000 * \frac{1.8}{1.1 * 2400} + T_{air} \tag{A.16}$$

$$H = -0.0787 + 0.007 T_{air} - 0.00003 \, T_{air}^2 \tag{A.17}$$

Where;

CC =   cement content of the concrete mixture (lb/yd³)

H =   heat of hydration (KJ/g)

T_{air} =   average seasonal ambient temperature (°F)

The allowable range for this formula is from 60 to 120 °F (Kohler and Roesler 2006).

A.6.4 Unrestrained concrete drying shrinkage at the depth of steel

The unrestrained concrete drying shrinkage at the depth of steel (ε_{shr}) is calculated as follows (FHWA-ICT-09-040 2009).

$$\varepsilon_{shr} = \varepsilon_\infty \left(1 - rh_{pcc}^3\right) \tag{A.18}$$

Where;

ε_∞ =   ultimate shrinkage (microstrain)

rh_{pcc} =   relative humidity in the concrete at the depth of steel as a fraction

A.6.5 Relative humidity in the concrete at the depth of steel

The relative humidity in the concrete at the depth of steel (rh_{pcc}) can be calculated as follows (Kohler and Roesler 2006).

$$rh_{pcc} = rh_a + (100 - rh_a) f(t) \tag{A.19}$$

$$f(t) = \frac{1}{\left(1 + \frac{t}{35}\left(25.4\zeta * 1.35^{\frac{w}{c} - 0.19}\right)\right)} \tag{A.20}$$

Where;

rh_a =   average ambient relative humidity annually or monthly

t =   drying time (days)

w/c =   water/cement ratio

B. APPENDIX B – AFRICON UTCRCP CONSTRUCTION REPORT

HEIDELBERG TRAFFIC CONTROL CENTRE

THE REHABILITATION OF THE SCREENER LANES

UTCRCP CONSTRUCTION REPORT

OCTOBER 2008

FIRST DRAFT

Prepared for:

Prepared by:

Africon Engineering International (Pty) Ltd
P O Box 905
PRETORIA
0001

Contact Person: Estimé Mukandila
Tel: 012 - 427 2515
Fax: 427 2777
e-mail: estimem@africon.co.za

TABLE OF CONTENTS

1. INTRODUCTION

The project entails the rehabilitation of the Heidelberg Traffic Control Centre screener lanes situated approximately 10 km south-east of Heidelberg on route N3-11 in the Gauteng Province.
This project has served as an experimental section for the newly South African technology of Ultra Thin Continuously Reinforced Concrete Pavement (UTCRCP).

The traffic control centre consists of two facilities, namely the western control centre adjacent to the north-bound carriageway of the freeway and the eastern control centre adjacent to the southbound carriageway of the freeway. On- and off-ramps provide access to the control centre from the freeway.

As part of the pavement rehabilitation design, a 50 mm thick UTCRCP layer was specified on sections of the screener lanes exhibiting symptoms of distress. The 50 mm UTCRCP is specified to be constructed as an overlay either over existing asphalt surfaced sections after localized repairs were completed or after new pavement layers were constructed on asphalt surfaced sections that required deep pavement rehabilitation action. It should be note that the function of the asphalt layer underneath UTCRCP was to avoid or to reduce the occurrence of pumping as much as possible.

This project was subdivided into the following sections:
- East Bound (E):
    o Section E1 (CH 0.000 – CH 0.188): UTCRCP placed over localized repaired asphalt;
    o Section E2 (CH 0.188 – CH 0.237 and CH 0.247 – CH 0.277): UTCRCP over new pavement layers;
    o Section E3 (CH 0.237 – CH 0.247): Weigh In Motion (WIM) Continuously Reinforced Concrete Pavement (CRCP) slab;
    o Section E4 (CH 0.277 – CH 0.844): UTCRCP placed over localized repaired asphalt, this section contained also 4 loops CRCP slabs.
- West Bound (W):
    o Section W1 (CH 0.000 – CH 0.209 and CH 0.289 – CH 0.303): UTCRCP placed over localized repaired asphalt;
    o Section W2 (CH 0.209 – CH 0.259 and CH 0.269 – CH 0.289): UTCRCP over new pavement layers;
    o Section W3 (CH 0.259 – CH 0.269): WIM CRCP slab.
- West Access ramp: UTCRCP over new pavement layers.

Note that:
- UTCRCP on sections E2 and W2 was constructed on the following layers:
    o 2 Emulsion Treated Base (ETB) layers of 150mm and 140mm thick respectively;
    o A 50mm Continuously graded asphalt(AC), medium grade;
    o On E2 only: a Bitumen Treated Base (BTB) correction layer under AC of 25mm to 60mm.
- UTCRCP on West Access ramp was constructed on the following layers:
    o 150mm G7 selected layer;
    o 150mm C3 subbase layer;
    o 150mm ETB layer;

    o 50mm AC medium grade.

After completion of three trial sections to finalize the proposed mix design and the construction methodology, this UTCRPC construction project started on 25 May 2008, and was completed successfully on 02 September 2008.

2. MIX DESIGNS

The project specifications included a proposal of UTCRCP mix design, as shown in Table 2.1.

The Contractor submitted two mix designs made with the same components except that the water/cement ratios (W/C ratio) were respectively 0.27 and 0.31, as shown in Table 2.2.

The Contractor's mix design was used as base during the three trial sections organised on site. In order to obtain workability of concrete without loosing the specified strengths, the W/C ratio and admixture (Chryso Optima 100) content of this mix were varied as indicated in table 2.3.

After performing the third trial section, the selected mix design for the rest of the work was mix 7 as described in table 2.4).

TABLE 2.1: CONCRETE MIX DESIGN AS PROPOSED IN PROJECT SPECIFICATIONS			
Component Material		**Unit**	**Qty**
Cementitious material	Cement	Kg/m^3	480
	PFA	Kg/m^3	87
	CSF	Kg/m^3	72
Water (maximum)		l/m^3	175
Water / cementitious materials ratio			**>0.40**
Aggregate	6.75 mm	Kg/m^3	972
	Silica sand	Kg/m^3	684
	Steel fibres	Kg/m^3	100
	Polypropylene fibres	Kg/m^3	2
Cement / Aggregate ratio			0.39
Admixture per 100 kg of cementitious materials	Optima	ml	376
	Premia	ml	626
Slump (before steel fibres are added)		mm	
Slump (after steel fibres are added)		mm	
Compressive Strength	24 h	MPa	40
	3 days	MPa	
	7 days	MPa	
	28 days	MPa	90
Flexural Strength	24 h	MPa	
	3 days	MPa	
	7 days	MPa	
	28 days	MPa	10

TABLE 2.2: CONCRETE MIX DESIGN SUBMIT BY THE CONTRACTOR

Component Material		Unit	Qty
Cementitious material	Cement	Kg/m³	481
	PFA	Kg/m³	86.6
	CSF	Kg/m³	72.2
Water (maximum)		l/m³	175
Water / cementitious materials ratio			**0.27 & 0.31**
Aggregate	6.75 mm	Kg/m³	972
	Silica sand	Kg/m³	683
	Steel fibres	Kg/m³	100
	Polypropylene fibres	Kg/m³	2
Cement / Aggregate ratio			0.39
Admixture per 100 kg of cementitious materials	Optima	ml	375
	Premia	ml	626
Slump (before steel fibres are added)		mm	
Slump (after steel fibres are added)		mm	120
Compressive Strength	24 h	MPa	36.5
	3 days	MPa	
	7 days	MPa	72.0
	28 days	MPa	
Flexural Strength	24 h	MPa	6.3
	3 days	MPa	
	7 days	MPa	
	28 days	MPa	12

TABLE 2.3: Variation of W/C ratio during trial section

Trial section	Date	W/C	Chryso Optima 100 [ml/100kg of cementitious mat.]	Mix name
Trial section 1	23 June 2008	0.278	376	Mix 1
Trial section 1	23 June 2008	0.291	376	Mix 2
Trial section 1	23 June 2008	0.300	376	Mix 3
Trial section 1	23 June 2008	0.310	376	Mix 4
Trial Section 2	21 July 2008	0.313	376	Mix 5
Trial Section 2	21 July 2008	0.325	438	Mix 6
Trial Sectiom3	22 July 2008	0.325	442	Mix 7
Trial Sectiom3	22 July 2008	0.320	442	Mix 8

TABLE 2.4: CONCRETE MIX DESIGN ADOPTED AFTER TRIAL SECTIONS (MIX 7)			
Component Material		**Unit**	**Qty**
Cementitious material	Cement	Kg/m^3	481
	PFA	Kg/m^3	86.6
	CSF	Kg/m^3	72.2
Water (maximum)		l/m^3	175
Water / cementitious materials ratio			**0.325**
Aggregate	6.75 mm	Kg/m^3	972
	Silica sand	Kg/m^3	683
	Steel fibres	Kg/m^3	100
	Polypropylene fibres	Kg/m^3	2
Cement / Aggregate ratio			0.39
Admixture per 100 kg of cementitious materials	Chryso Optima 100	ml	442
	Chryso Premia 100	ml	626
Slump (before steel fibres are added)		mm	
Slump (after steel fibres are added)		mm	150
Compressive Strength	24 h	MPa	54.8
	3 days	MPa	81.0
	7 days	MPa	
	28 days	MPa	106.2
Flexural Strength	24 h	MPa	7.16
	3 days	MPa	10.24
	7 days	MPa	
	28 days	MPa	11.87

3.   CONSTRUCTION METHODOLOGY

3.1   Placement of Side-Forms and Mesh

3.1.1   Placement of Side-forms

As the UTCRCP was designed to be placed on top of an asphalt layer, a rectangular metallic tube or a metallic lipped channel (see Figure 1 and Figure 2) meting the layer thickness specified were used as side-forms
To avoid corner break of the UTCRCP, corner chamfrain (15mmx15mm) was constructed on the side edge of UTCRCP. A piece of wood (with triangle section) was mounted on the side-forms for this purpose (see Figure 3).

The side-forms were anchored to the asphalt by mean of metal pegs.

Figure 1: Rectangular metallic tube side-forms of UTCRCP	*Figure 2: Metallic lipped channel side-forms of UTCRCP*
Figure 3:Chamfrain side-form	*Figure 4: Anchoring of mesh in bottom layer and using of concrete blocs spacer*
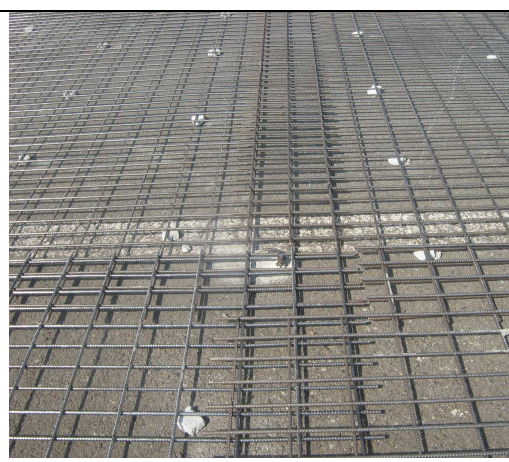
3.1.2 Placement of mesh

A 50mm x 100mm high strength steel mesh was used as reinforcement in the UTCRCP.

This mesh is consisted of:
- 5.6mm diameter longitudinal bars spaced at 50mm's; and
- 5.6 mm diameter transversal bars spaced at 100mm's.

The mesh was placed with the longitudinal bars in the road traffic direction.

Two challenges in the operations were:
- to maintain the mesh at the mid position within the 50 mm concrete layer thickness; and
- to control the overlap area of adjacent meshes so that the total thickness of the steel in the concrete shouldn't be more than 3 mesh bars (one on top of the other), as shown on Figure 5 and Figure 6, which yields a total of 16.8mm of reinforcement thickness representing 34% of the UTCRCP thickness; an additional 4th mesh bar would bring the thickness of steel in the UTCRCP thickness to 45%, which didn't leave enough cover.

In order to maintain the reinforcement position, the mesh was placed on top of concrete spacer blocs to ensure a 25mm space from the bottom surface, and anchored with nails and pegs in the bottom surface, as shown on figure 4.

To control the thickness of steel on the overlap areas (see Figure 5), the adjacent meshes were placed alternatively as follow:
- overlap in longitudinal direction: if the first mesh has transversal bars on top, the consecutive mesh should have transversal bars in the bottom; and
- overlap in transversal direction: if the first mesh has longitudinal bars on top, the consecutive mesh should have longitudinal bars in the bottom.

Figure 5A and Figure 5B show the longitudinal and transversal overlaps, and Figure 6 and Figure 7 illustrate these two cases with photos.

At places where there were overlap in both the longitudinal and traversal directions, as showed in Figure 5, some bars were cut to left only a reinforced thickness of 3 bars as explain in a previous paragraph. This operation was done in such a way to ensure a continuity of reinforcement in both longitudinal and traversal directions
Note that an overlap of at least 20mm was allowed in each direction.
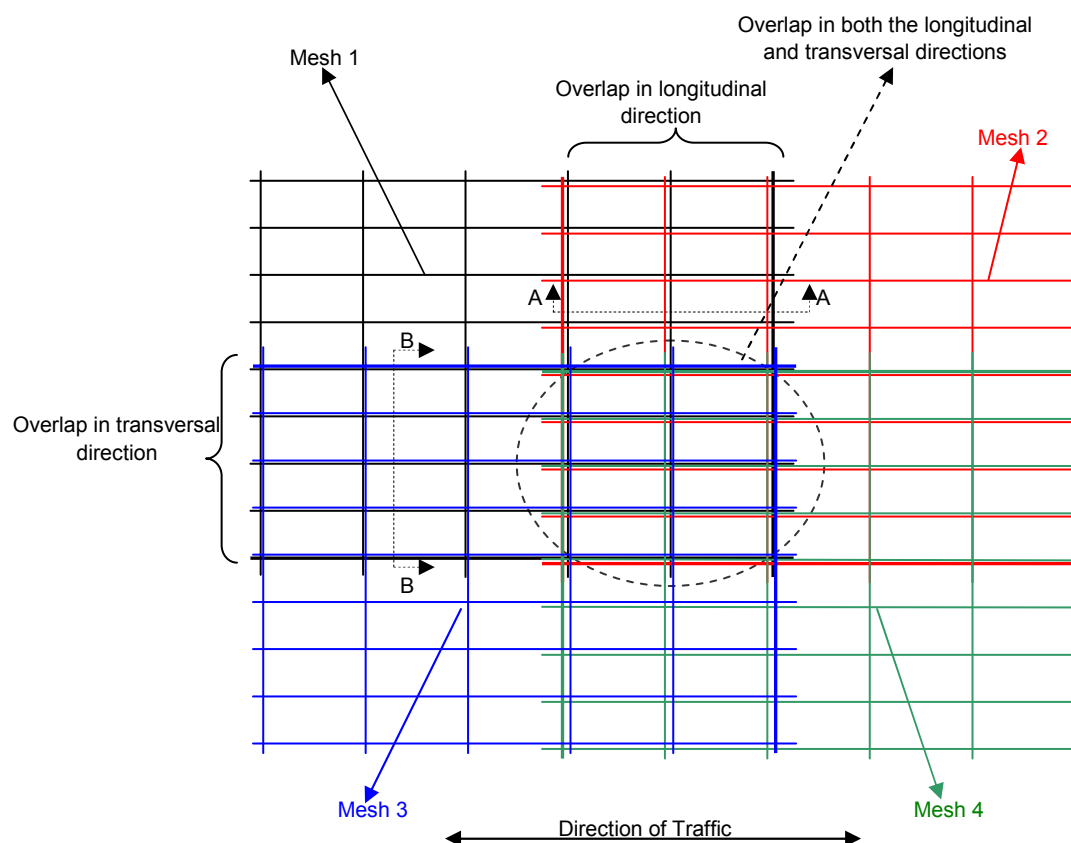
Figure 5: Sketch of general overlap between high tensile strength steel meshes
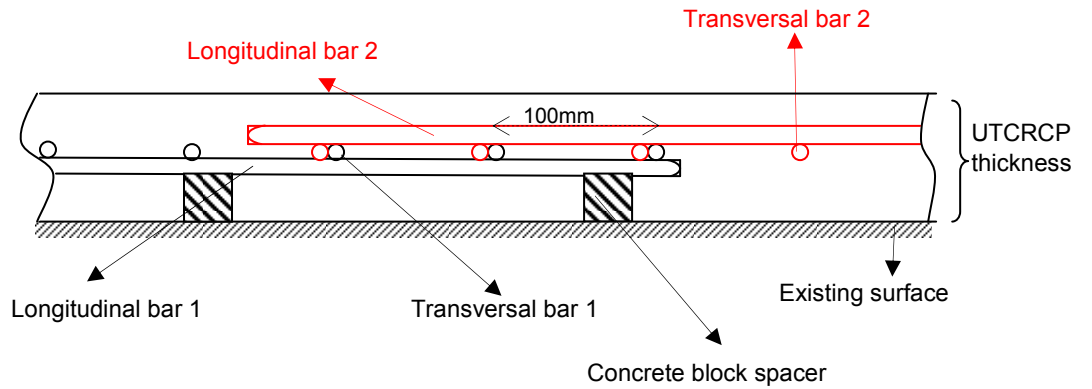
Figure 5A: Section A-A: overlap in longitudinal direction
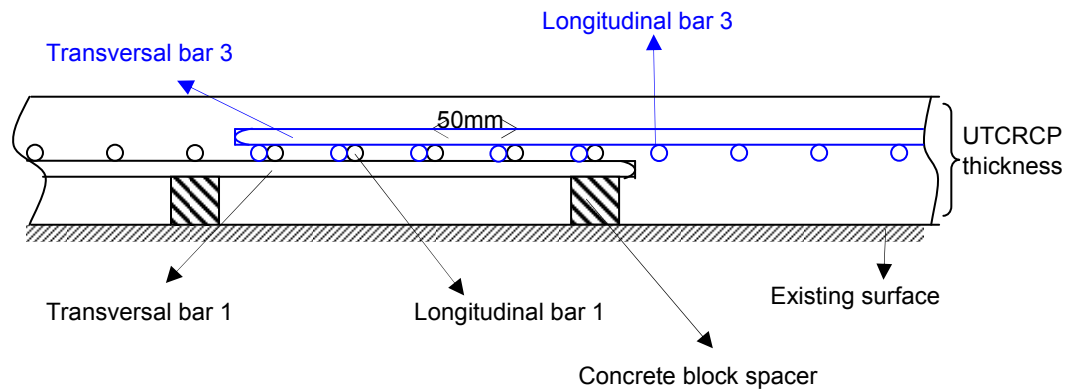
Figure 5B: Section B-B: overlap in traversal direction

| Figure 6: Overlap in longitudinal direction | Figure 7: Overlap in transversal direction |
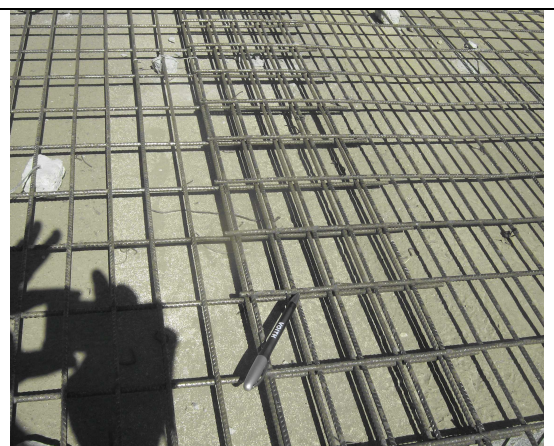
The possible use of 100mm X 200mm high strength steel mesh (more available than size 50mm X100mm) was investigated in an experiment on the West bound section from CH 0.012 to the end. To get the same pattern as 50mmX100mm steel mesh, two 100X200mm meshes were superposed. The same principle as the overlap technique abovementioned was used except for positions of longitudinal and transversal bars that were placed in order to get respectively 50mm and 100mm spacing between each other. In this case the overlap area present a steel reinforcement with at least 5 bars one on top of another. Since the minimum number allowed was 3 bars, as mentioned above, this method required that transversal and longitudinal bars had to be removed at overlap areas, either during the manufacturing process or by cutting some bars in the construction process (as explained previously).

This process has was found to be time consuming and requested a lot of attention to get the reinforcement correct.

3.1.3   Formwork on longitudinal joints

2 types of longitudinal joints were tested on site:
-   Joint using Y12 tie bars with Hex coupling nut to link the two meshes each side of the joint. The link was done through the Hex coupling nut that connected together the tie bars of each side of the joint (type 1 longitudinal joint). This joint type is sketched in Figure 8 and illustrated in Figure 10; and
-   Joint using continuity of mesh through the joint (Type 2 longitudinal joint): as sketched on Figure 9 and illustrated in Figure 11, the reinforced mesh passed between a top and a bottom side-works which were screwed together, after part of joint was firstly casted and cured, the top and the bottom side-form could been taken out without damaging the reinforcement. In order to control the final level of UTCRCP and to avoid unevenness of the top of side-form due to screwing operation, it was necessary to used a correction plat between the top and the bottom side-form; the correction plat was a 25mmX5mm steel; this plat was accompanied with a sponge for proofing purpose during concrete vibration (see Figure 12).
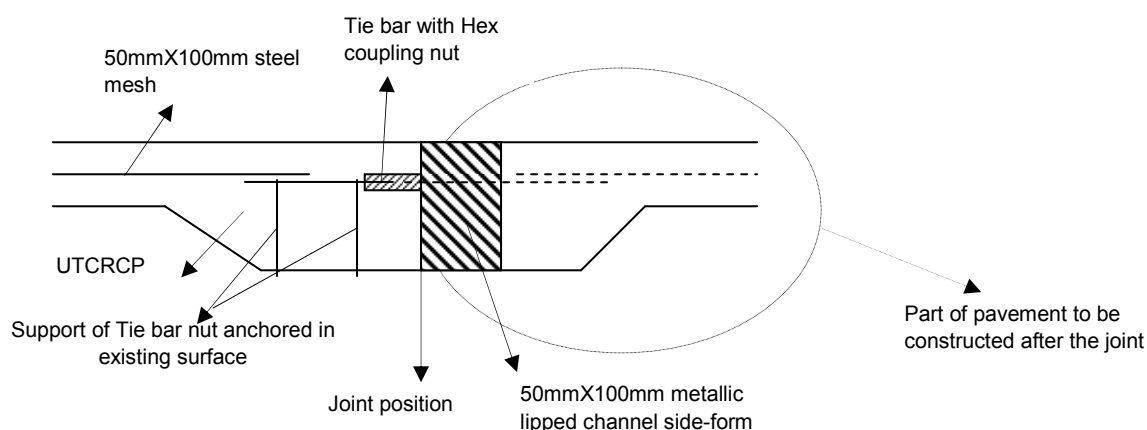
Figure 8: Sketch of form-work of joint using tie bars with Hex coupling nut (Type 1 longitudinal joint)

50mmX100mm steel mesh passing through the mesh

Top side-form: 38mmX20mm rectangular tube

UTCRCP

Part of pavement to be constructed after the joint

Top side-form: 50mmX20mm rectangular tube

Joint position

Bottom side-form: 75mmX75mm square tube
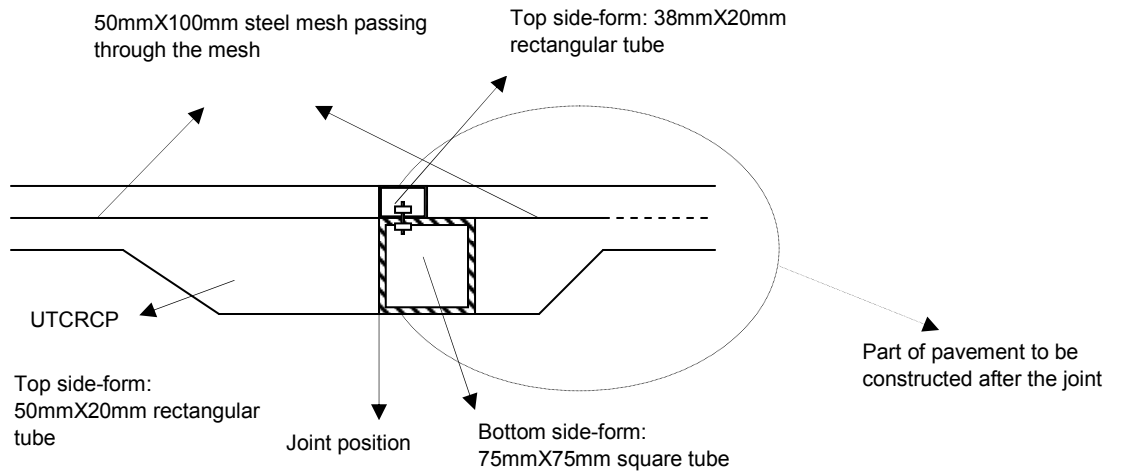
Figure 9: Sketch of form-work of joint with reinforcement mesh trough it (type 2 longitudinal joint)

Figure 10: form-work of joint using tie bars with Hex coupling nut (Type 1)
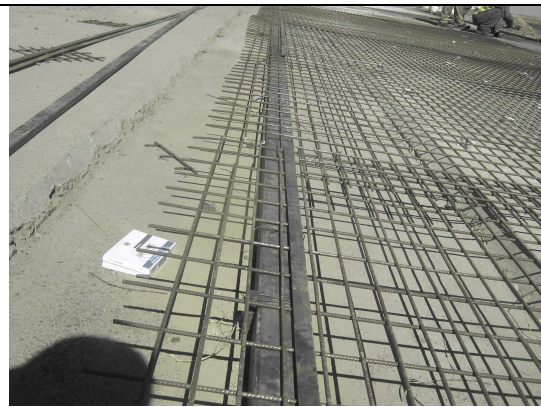
Figure 11: form-work of joint with reinforcement mesh trough it (Type 2)
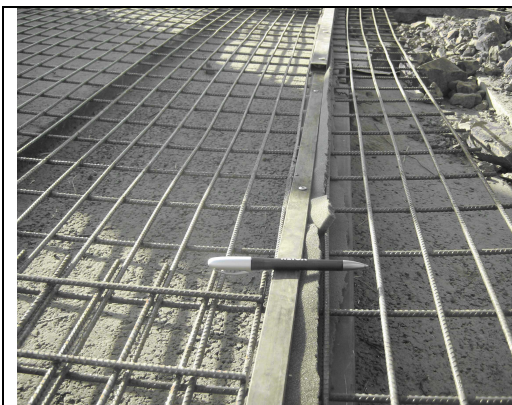
Figure 12: Correction plate and sponge for longitudinal joint side-form

Figure 13: Reinforcement for anchor beam

3.1.4 Anchor beam

Anchor beams were made with concrete as specified for UTCRCP, and the steel mesh was folded and used as reinforcements, as shown in Figure 13.
Positions of different beams in the project were shown on the as-built documents (AB1 form, and drawings).

3.1.5 Observations

With the technique described above, reinforcement mesh did not show much buckling-up during placement and the concrete cover on top of the reinforced mesh was sufficient.

Because the use of anchor nail and peg and the placement of joint side–form were manual tasks, they are time consuming.

3.2 PREPARATIONS AND MIXING OF MATERIALS

3.2.1 Mixing equipment

The mix of UTCRCP was prepared in pan mixer (two unites: a small mixer of 400 kg and a big mixer of 720kg) mounted on a truck, as depicted in Figure14. The pan mixer was provided with a shearing device (see Figure 15), which allowed intimate and homogeneous mix between different components.

3.2.2 Preparation of mixing components

The sand, cementitious materials (cement, fly ash, condense silica fume) and polypropylene fibres were pre-batched prior in the factory and bagged (see Figure 16). Workers on site only had to mix the aggregates (also pre-batched and bagged), as shown in Figure 17, with the pre-batched dry mixture described above and the steel fibres (see Figure 18) by adding them into the mixer.

3.2.3 Mixing process

The mixing process was as followed (see Figure 19):
- First the aggregates,
- Secondly the pre-batched dry mix, all were mixed in 1 to 2 minutes; then
- The water blended with additives (Chryso Optima 100 and Chryso Primia 100) and the mixing carry on for additional 2 to 2.5 minutes; the mix should appear workable before
- Adding, lastly, the steel fibres and mix for 1 minute more. Steel fibres were spread in the mix progressively in the same direction as mixer rotation to avoid the "snow ball effect" of steel fibre that caused segregation.

3.2.4 Observations

The pan mixer seemed to be an important tool in the mixing process that enhance the homogeneity of different components due to the shear strength produced

A part of pan mixer operation, the other steps in the mixing process were manual.

Figure 14: Mixer pan

Figure 15: inside of mixer pan

Figure 16: Pre-batched cementitious materials + sand + Polypropylene fibres

Figure 17: Pre-batched aggregates

Figure 18: Bag containing steel fibres

Figure 19: Mixing in process

3.3   LAYING AND COMPACTION OF CONCRETE

3.3.1   Process

The UTCRCP casting process was as followed:

- The mixed concrete from the mixer is poured and sprayed all over the prepared area. Workers manually sprayed the fresh concrete using rakes and shoves, as shown on Figure 20;
- The pocket vibrator was used to give initial compaction and vibration to the concrete, the vibrator was applied against the mesh to shake the entire area (see Figure 21);
- The concrete was then rolled with a oscillating triple roller screed, this equipment included 2 normal rollers to level and roll the concrete surface, and 1 oscillating roller that provided additional compaction to the concrete. The Oscillating triple roller screed is depicted in Figure 22 and Figure 23
- After compaction, a straight edge was used to get a more levelled surface (see Figure 24) and the surface was hand floated, as shown on Figure 25
- Finally the surface was textured and impregnated with curing compound

Figure 20: Pouring and spraying of fresh concrete

Figure 21: Concrete vibration using pocket vibrator

Figure 22: Oscillating triple roller screed

Figure 23: Oscillating triple roller screed in action

Figure 24: Levelling with straight edge	*Figure 25: Hand floating of UTCRCP surface*
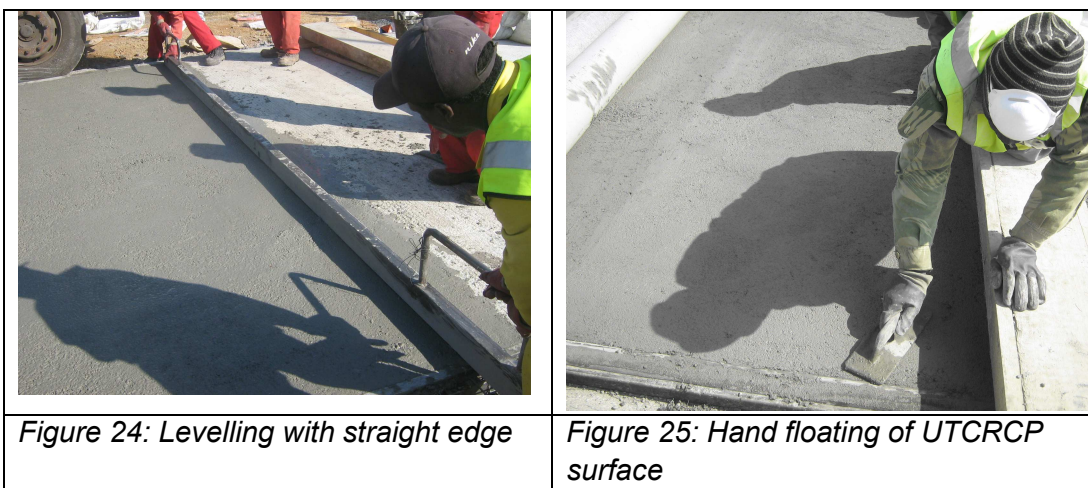
3.3.2   Observations

The use of the Oscillating triple roller screed increased the production rate significantly.

It was found that the pocket vibrator could not achieve sufficient compacting energy especially under the reinforcing mesh. Although the oscillating action of the oscillating triple roller screed provided additional compaction energy, a proper device designed to allow correct compaction under the steel mesh might be required. One of the solutions could be to equip one of the 2 remaining rollers of the oscillating triple roller screed with a vibrating action in addition to the oscillating action.

3.4   JOINTS

3 types of joints were constructed on this project:
Longitudinal joints, isolation joints and construction joints.

3.4.1   Longitudinal Joints

Longitudinal joints were constructed at places where the total width of the UTCRCP was to large to be placed in one operation. This was the case at 2 positions in East bound section:
-   Position 1: from CH 0.00 to CH 0.115; and
-   Position 2: from CH 0.777 to the END
As explained in **3.1.3**, two types of longitudinal joints were constructed: Type 1 longitudinal joint and Type 2 longitudinal joint.

Each of these type longitudinal joints was constructed in 2 different profiles:
-   oblique edge profile (as designed in project specifications) this profile is depicted in Figure 26) and;
-   straight edge profile, this was an experimental profile implemented on site (see Figure 27).
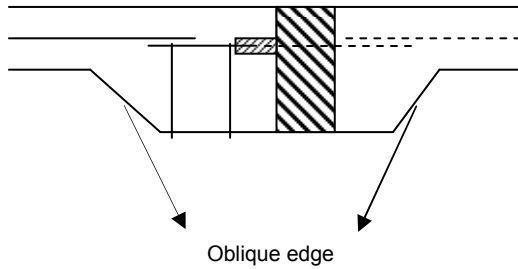
Figure 26: Oblique edge profile of Longitudinal Joint.
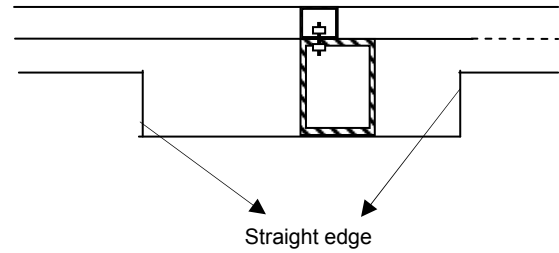
Figure 27: Straight edge profile of Longitudinal Joint

Four different varieties of longitudinal joints were constructed:
- Type 1 longitudinal joint with oblique edge profile (Position 1 from CH 0.000 to CH 0.020);
- Type 1 longitudinal joint with straight edge profile (Position 1 from CH 0.078 to CH 0.115);
- Type 2 longitudinal joint with oblique edge profile (Position 1 CH 0.020 to CH 0.040); and
- Type 1 longitudinal joint with straight edge profile (Position 1 CH 0.041 to 0.078 and Position 2).

The longitudinal joint was constructed as follow:
- Side form work, as mention in **3.1.3**
- Casting of first side of longitudinal joint: Figure 28 and Figure 29 presented the first side casted of respectively Type 1 longitudinal joint and Type 2 longitudinal joint
- Tie reinforcement of second side to the reinforcement of first side: Fig 30 and Figure 31 show respectively the second side Y12 tie bars coupled to the first side Y12 tie bars and the second side mesh tie to the first side mesh.
- Casting of second side of longitudinal joint

Figure 28: First side of type 1 longitudinal joint

Figure 29: First side of type 2 longitudinal joint

Figure 30: Second side Y12 tie bars coupled to first side Y12 tie bars

Figure 31: Second side mesh tie to first side mesh
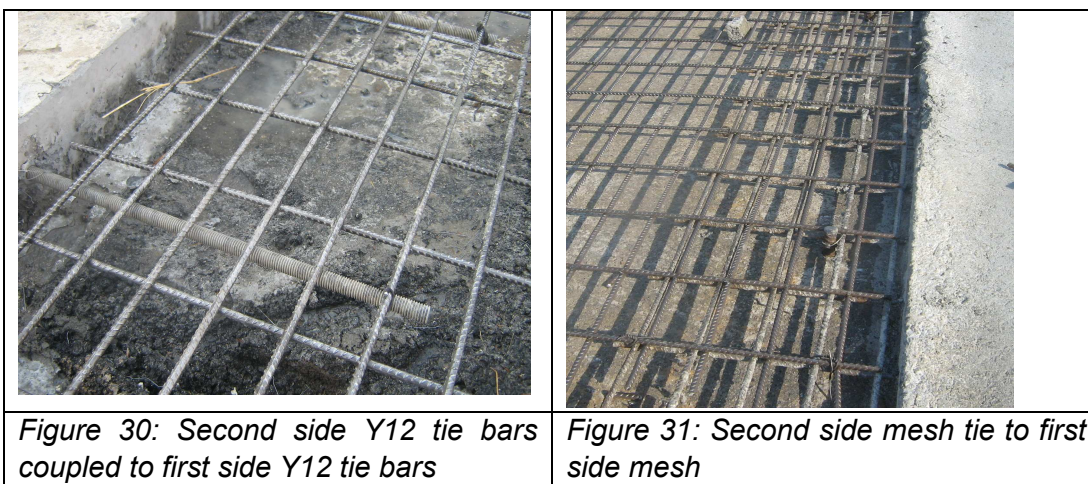
3.4.2   Isolation Joints

Isolation joints were constructed between UTCRCP and CRCP at the WIM and loop slab. Mild steel bars (of 40mm in diameter and 500mm in length) were used as dowels at a spacing of 375mm, as shown on Figure 32.

A 12mm joint left between the UTCRCP and the CRCP (see Figure 33) was filled with cold poured liquid self levelling ultra low modulus silicon.

Figure 32: 40mm mild steel dowels in isolation joint between UTCRCP and CRCP slab

Figure 33: 12mm joint between UTCRCP and CRCP
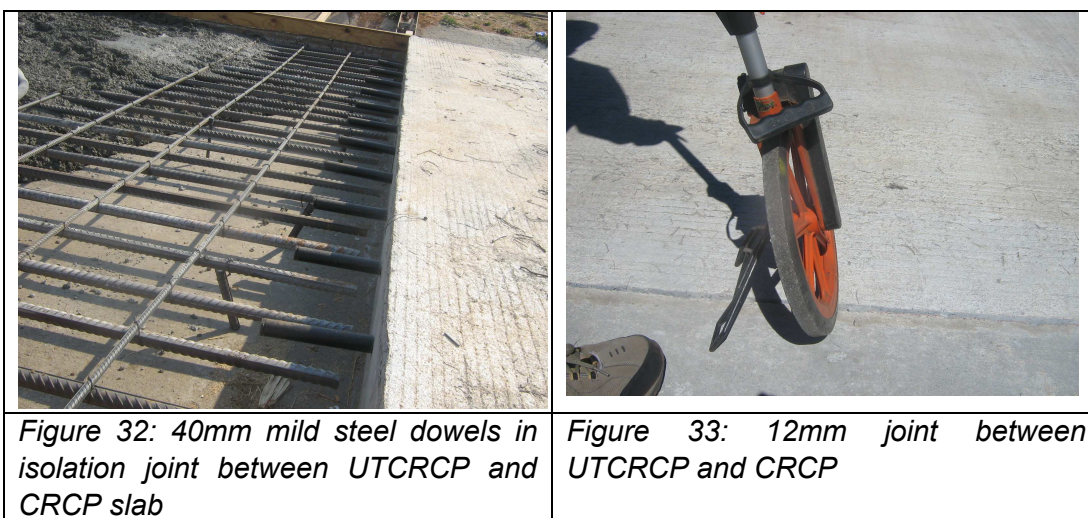
3.4.3   Construction Joints

Construction joints were constructed at the end of day-work section or when the concrete supply was insufficient. The construction joint was made with a sponge underneath the mesh (see Figure 34) tie to a Piece of wood placed on top of mesh (see Figure 35)

No groove was made between new and old concrete in the construction joint.

| Figure 34: Placing construction joint: sponge underneath of mesh. | Figure 35: Placing construction joint: piece of wood on top of mesh |

3.4.4 Observations

All the longitudinal joints using Y 12 tie bars with a hex nut (type 1) displayed cracks a few days after concrete placement (see Figure 36) while for the same period of observation no noticeable cracks were found on joints using mesh through it (type 2), as shown in Figure 37. The presence of cracks in type 1 joint could be due to the fact that the continuity of reinforcement was interrupted between two consecutive tie bars. It should also be noted that the type1 joint seemed to be more expensive than the type 2 joint.

The construction joint without groove did show a good bound between the new and the old concrete; and no noticeable crack through the thickness of the UTCRCP was found.
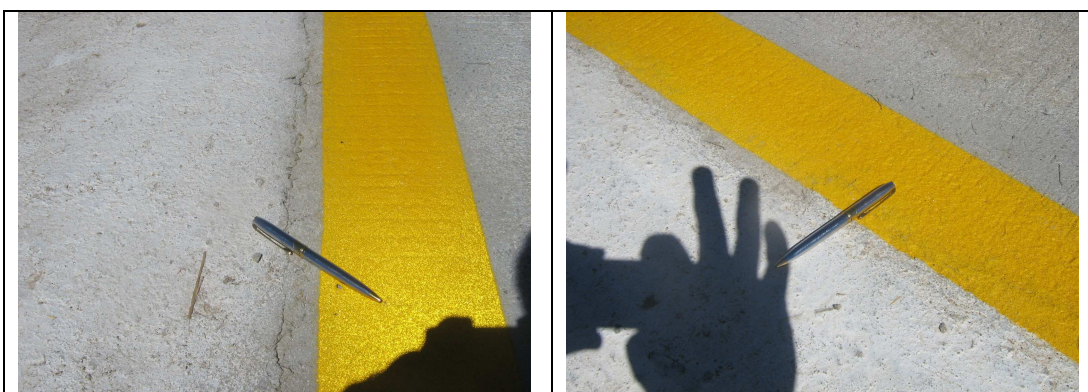
| Figure 36: Crack in longitudinal joint with Y 12 tie bars. | Figure 37: No crack appear on the longitudinal joint with mesh trough it |

3.5 Texturing Of Concrete Surface

Two types of concrete surface texturing were experimented on this project:
Tinning finish and stiff broom finish.
- The tinning or grooving finish used a rack to give to the surface it finished texture (see Figure 38). The action of the rack could easily result in steel fibres being racked from surface instead of getting the grooving effect needed. The method also

appeared to be more inconsistent. The tinning finishing was applied on the East bound section from CH 0.000 to CH 0.636 and on the West access ramp, before shifting in stiff broom finish.

- The stiff broom finish was used as shown in Figure 39, the East bound section from CH 0.635 to the End and in the West bound sections.

Figure 38: Tinning surface finishing.	*Figure 39: Stiff broom surface finishing*
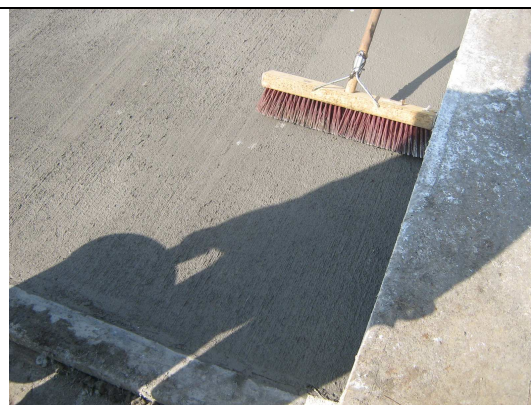
It was found in general for better texture, the finish should take place 15 to 20 minutes after floating to allow initial hardening of the concrete.

3.6   Curing Of Concrete

The curing of concrete was done using a solvent type resin-based curing compound; this operation was done just after surface texturing (see Figure 40). In general white-pigmented resin-based curing compound was applied (West access ramp and East bound: CH 0.00 – CH 0.777), as shown in Figure 41.

At the end of the project (East bound: CH 0.777 – END and West bound), the contractor ran out of white-pigmented resin-based curing compound, thus a none-pigmented resin-based curing compound was used.

At some places where none-pigmented curing compound was used, minor transversal cracks appeared; while, in general, places where white-pigmented curing compound was applied non apparent cracks were displayed. This could probably be due to the light-reflection power of white-pigmented curing compound, which slowed down the water evaporation from fresh concrete.

On East bound section from CH 0.736 to CH 0.777, , curing with plastic sheeting was tested in addition to curing compound as shown in Figure 42.
It was found that:
- Plastic sheeting laid over a fresh curing compound prevented the curing to stick to the UTCRCP surface (see Figure 43).
- Since plastic sheeting could easily be blown away by the wind, it became a hazardous object for the traffic near the highway.
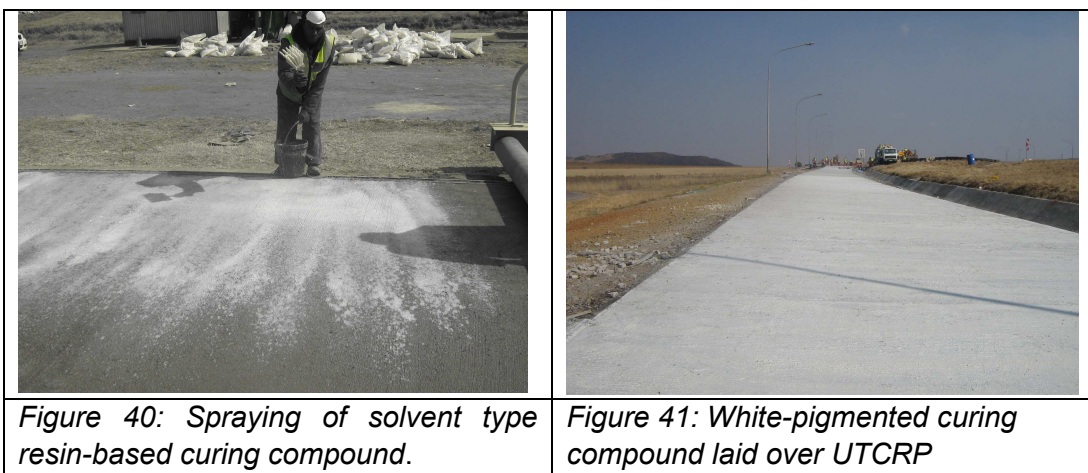
Figure 40: Spraying of solvent type resin-based curing compound.	*Figure 41: White-pigmented curing compound laid over UTCRP*
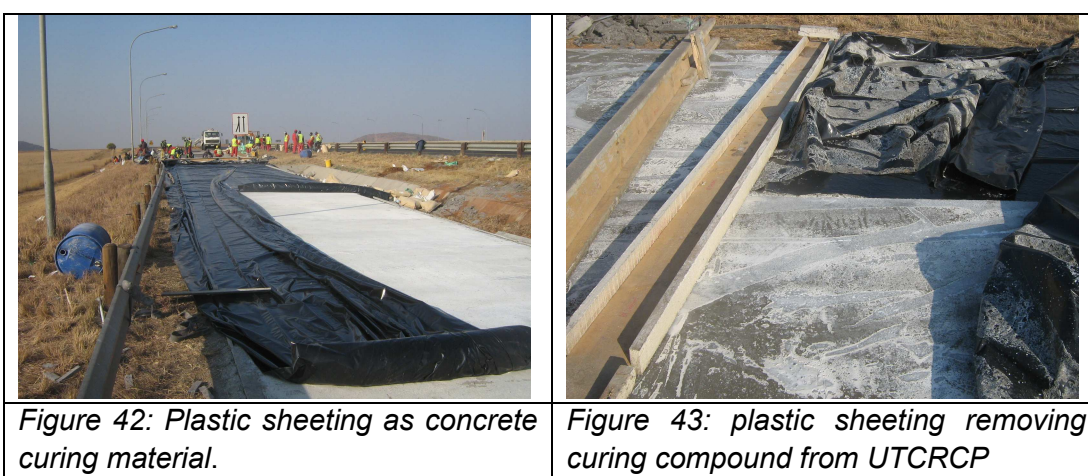
Figure 42: Plastic sheeting as concrete curing material.	*Figure 43: plastic sheeting removing curing compound from UTCRCP*

3.7   PRODUCTION RATE

A daily production rate in term of length of UTCRCP placed or in term of volume of UTCRCP placed was estimated as follow;

- The total mixing time detailed in **3.2.3** is 2+2.5+1= 5.5 minutes, if 2 minutes was allowed for manual loading of materials in the mixer and 2 minutes allocated to pour and empty concrete from the mixer, the total time would be 9.5 minute, rounded to 10 minutes. Thus = cycle time of one operation = 10 minutes (1);
- Daily working time = 8 hours = 480 minutes (2);
- Daily number of operation cycle: (2)/(1) = 480/10 = 48 (3);
- Capacity of big mixer as mentioned in **3.2.1** = 720 kg (4)
- Daily production: (4)*(3) = 720*48 = 34560 kg (5)
- Average width of UTCRCP = 5m (6)
- Average thickness of UTCRCP = 0.05m (7)
- Area of section of UTCRCP : (6)*(7) = 5* 0.05 = 0.25 m^2 (8)
- The estimated specific mass of UTCRCP = 2400 kg/m^3 (9)
- Daily volume of UTCRCP placed: (5)/(9) = 34560/2400 = 14.4 m^3 (10)
- Length of road placed per day : (10)/ (8) = 14.4/0.25= 57.6m

The average length of daily placing of UTCRCP, as obtained from the section constructed every day was 55.4m (representing 13.85m^3 of UTCRCP placed per day), this value is very close to the calculated.

Thus for a mixer of 720kg, a daily production rate of between 55 and 60m can be expected, or a daily UTCRCP volume placed of between 13m^3 and 15m^3

4. TESTS RESULTS

In this project the following control tests were done:
- Concrete compressive strength using 100X100X100 mm cube
- Concrete flexural strength using 100X100X300 mm beam;
- Concrete flexural toughness using centrally loaded round panel (600mm diameter and 50mm thick);
- Consistency and workability test: slump test on fresh mix before introducing fibres.

Note that the results of these test presented below, are untreated ("raw results"), without any discard of outliers.

4.1 Concrete Compressive Strength

The compressive strength showing average, maximum and minimum for 1, 3, 7 and 28 days UTCRCP are given in Table 4.1 and the Graph 4.1 indicates the evolution of compressive strength with the time.

It could be concluded that:
- The 1day range of compressive strength was between 34Mpa and 66Mpa with an average of 50Mpa;
- At 3 days, the period after which the road was opened to traffic, the strength ranged is between 49Mpa and 84Mpa with an average of 66Mpa;
- At 28 days, the compressive strength could reach a maximum value of 127Mpa with a minimum of 72Mpa and an average of 103Mpa.

Table 4.1: Compressive strength [Mpa]

concrete age [day]	average	Maximum	Minimum
1	50	66	34
3	66	84	49
7	83	92	72
28	103	127	72

Graph 4.1 Compressive strength vs. Time relationship for UTCRCP
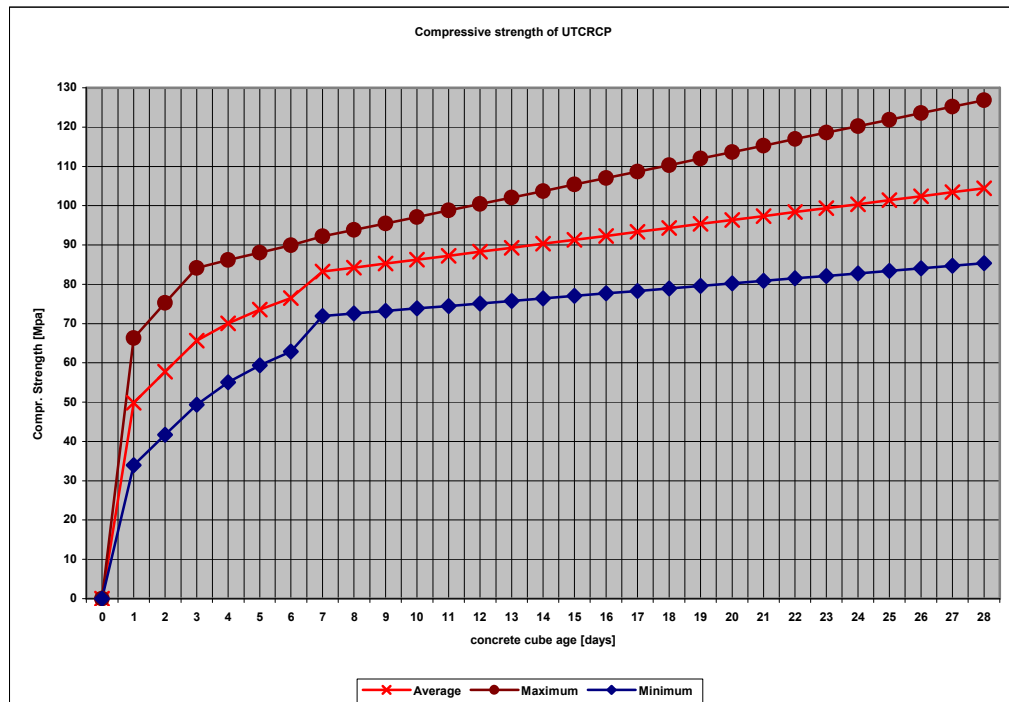
4.2 Concrete Flexural Strength

The beam flexural strength of UTCRCP showing average, maximum and minimum value for 1, 3, 7 and 28 days UTCRCP are given in Table 4.2 and the Graph 4.2 indicate the strength vs. time relationship.

It can be seen that:
- After 1day, the flexural strength ranged between 5.5Mpa and 10Mpa with an average of 7.7Mpa;
- At 3 days, period after which the road was opened to traffic, the strength ranged between 7.2Mpa and 11.4Mpa with an average of 9.1Mpa;
- At 28 days, the compressive strength could reach a maximum value of 13.8Mpa with a minimum of 10.2Mpa and an average of 12.2Mpa

The graph is flattens after 7days concrete age, which represents a slow gain in strength from this date.

Table 4.2: Beam Flexural strength [Mpa]

concrete age [days]	average	Maximum	Minimum
1	7.7	10.0	5.5
3	9.1	11.4	7.2
7	10.8	11.6	10.2
28	12.2	13.8	10.2

Graph 4.Flexural strength vs. Time relationship for UTCRCP
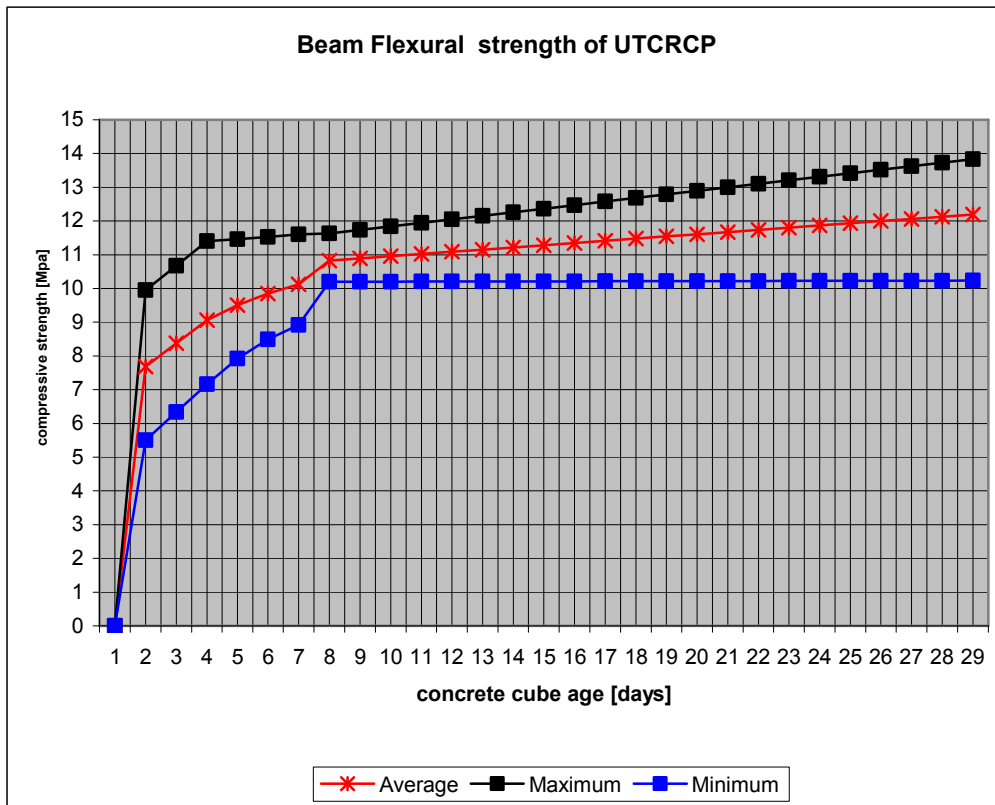
4.3   Concrete Flexural Toughness Using Centrally Loaded Round Panel

Flexural toughness was tested on 28 days old UTCRCP; all maximum Loads with the correspondent deflections are given in Table 4.3

It could be seen that:

- the maximum load could go up to 52.26kN with a minimum of 28.50kN and an average of 37.2kN
- the deflection reached a maximum of 11.48mm with a minimum value of 1.32mm and an average of 5.64mm

Table 4.3: Maximum Load with it correspondent deflection

Cast Date	Disc No	Max Load (kN)	Deflection (mm)
23-Jun	2306a	52.260	4.35
23-Jun	2306b	38.092	1.32
23-Jun	2306c	45.537	5.99
21-Jul	kp1	38.944	1.89
21-Jul	kp2	34.474	1.34
21-Jul	kp3	34.674	2.53
21-Jul	kp4	33.341	2.11
21-Jul	kp5	48.516	4.83
21-Jul	kp6	32.463	2.40
08-Aug	kp17a	28.501	10.60
08-Aug	kp17b	29.777	8.60
08-Aug	kp17c	34.138	11.48
17-Aug	kp28a	34.212	9.08
17-Aug	kp28b	37.790	8.29
17-Aug	kp28c	35.301	9.84
	average	37.201	5.643
	Maximum	52.260	11.476
	Minimum	28.501	1.323

Graph 4.3: Maximum round panel load vs. deflection

Africon
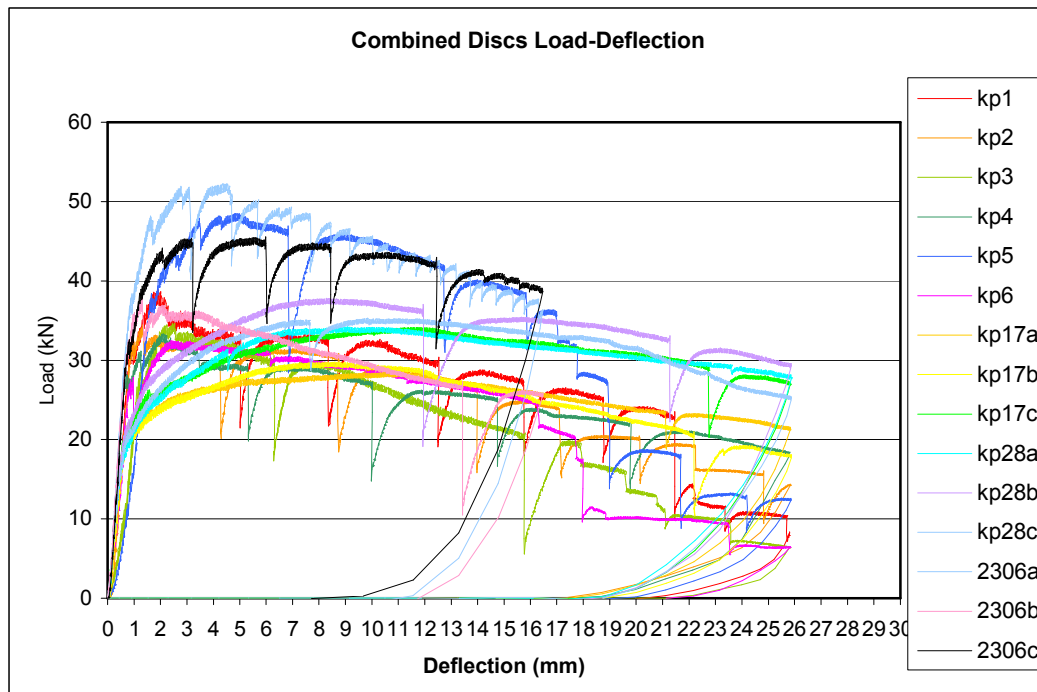
4.4 CONSISTENCY AND WORKABILITY TEST: SLUMP TEST

Generally, the slump test on this project was done on concrete before addition of steel fibres, and the results of this test was not consistent; it was difficult to correlate the slump with the UTCRCP strength. However the slump varied between 90 and 208.

As mention in **2**, the workability of the concrete mix was found to be better with a W/C ratio of around 0.325, this value fluctuated on site between 0.320 and 0.330.

4.5 OBSERVATIONS

In general compressive strength and flexural strength obtained in this project were higher than those required in the project specifications, as can be seen in table 4.4.

Table 4.4: comparison of designed strength specified and average strength obtained on site

	Contract specifications		site	
	1day	28days	1day	28days
Compressive strength [Mpa]	40	90	50	103
Flexural strength [Mpa]	-	10	7.7	12.2

The inconsistency of the slump compared to the concrete strength could possibly be due to the good quality of UTCRCP mix design; the concrete strength requirement was achieved within a large range of slump (between 90 and 208). Another explanation of the inconsistency of the slump could be the presence in the concrete sample of some steel fibres remained from the previous mixing. However, the slump should be controlled to avoid voids or segregation in the concrete.

5. CONCLUSIONS AND RECOMMENDATIONS

The rehabilitation of screener lanes using Ultra Thin Continuously Reinforced Concrete Pavement (UTCRCP) technology conducted in Heidelberg from June 2008 to September 2008 was considered to be successful in terms of the identification of a basic construction methodology of this newly South Africa implemented technology. The UTCRCP was constructed as an overlay on repaired existing asphalt or, where major pavement distresses occurred, on top of a new pavement structure which included an asphalt surfacing. The presence of asphalt beneath the UTCRCP was to prevent pumping.

After performing 3 trial sections the mix design selected in term of workability and concrete strength requirement had fairly the same composition then the others tested except for a water/cement ratio of 0.325 and the increase in the additive Chryso Optima 100 from 376 to 442 ml per 100kg of cementitious materials.

In general the UTCRCP construction required a lot of manual operations which could enhance labour intensive construction.

50mm thick UTCRCP did not leave enough room for placing of reinforcement, and the following considerations were addressed:

- Curling and warping of reinforcement steel mesh lead to a reduction of concrete cover; to prevent buckling-up of the reinforcement mesh nails and peg anchored in the existing surface were used in addition to cover bloc to maintain steel mesh at correct position.
- An alternate technique of placing steel meshes allowed a maximum of 3 mesh bars (one on top of another) in longitudinal or transversal overlap areas. In cases where overlap occurred in both longitudinal and transversal directions, the extra mesh bars were cut off to leave only 3 bars which assured continuity between consecutive meshes.

The possibility of use of 100mm X 200mm high strength steel mesh (more available size than 50mm X 100mm) was experimented on site, by superposing them to get a same pattern as 50mm X 100mm mesh. This process was found to be time consuming and required a lot of attention to get the reinforcement correct.

The pan mixer, using shear strength during mixing process, seemed to be an appropriate on-site equipment for the UTCRCP. On the other hand, the use of the Oscillating triple roller screed increased the production rate significantly and provided additional compacting energy to pocket vibrator. However compaction and vibration techniques needed more refinement such as the addition of a vibration action to the Oscillating triple roller screed in addition to the oscillation action.

Two types of longitudinal joints were experimented on site, and the longitudinal joint using Y 12 tie bars with hex nut displayed cracking a few days after concrete placement whilst for the same period of observation no noticeable cracks were found on the joint using mesh through it. The presence of cracks in the first type of joint could be due to the fact that the continuity of reinforcement was interrupted between two consecutive tie bars. Thus the longitudinal joint using mesh through it seemed to be more efficient in terms of cost consideration.

The construction joint made without the groove specified in the project showed a good bound between the new and the old concrete; and not noticeable crack through the thickness of the UTCRCP was found. This technique could also save the use of silicon sealant application in the joint (as required in the project specifications).

From the 2 types of texturing were used on site (tinning finish and hard bloom finish), and the tinning finish appeared more inconsistent due to the type of tool used that tended to rack steel fibres on UTCRCP surface instead of getting the grooving effect

The white-pigmented resin-based curing compound had an efficient curing effect on concrete. Some sections cured with none-pigmented resin-based compound seemed to display some minor transversal cracks, this could be explained by a lack of light reflexion of the none-pigmented compound which acted toward rapid water evaporation from concrete.

It was found that the simultaneous use of curing compound and the plastic sheeting as curing (as required in the project specifications) was difficult because the fresh curing compound sticked to the plastic instead of sealing the UTCRCP. On other hand, curing

with plastic sheeting became a hazardous object for the traffic near the highway when it was blown by the wind.

The daily production rate of this labour intensive construction using a 720kg pan mixer was estimated between 13m^3 and 15m^3 or in term of length of road constructed; 55m to 60m

The average compressive strength and the average beam flexural strength were found to be higher than the required strength in the project specification. The site average compressive strength at 1 day and at 28 days were respectively 50Mpa and 103Mpa, while project specifications required respectively 40Mpa and 90Mpa. The average beam flexural strength on site at 28 day was 12,2Mpa while the project specifications required 10Mpa after 28 days. Thus the UTCRCP mix design could be regarded as an acceptable mix design, however one should consider that a very strong concrete is a source of possible cracks.

This newly implemented South Africa technology of UTCRPC construction started on 25 May 2008 was conducted and completed successfully on 02 September 2008.

C. APPENDIX C – FWD DATA RESULTS

CONTENTS

Table of Figures

List of Tables

C.1 FWD Data Results

This subsection includes the complete exposition of the FWD data results discussed in Section 4.2.1. Figure C.1 depicts the stations of the load plate positions.

C.1.1 FWD stations layout
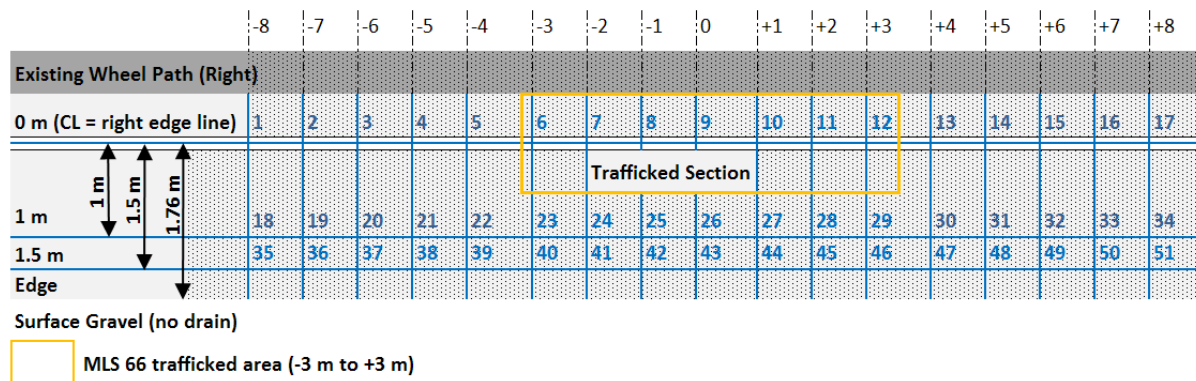
Figure C.1 APT test section detailed layout

C.1.2 FWD deflection bowl data records

All deflections are in μm.

Table C.1 FWD 40 kN deflection bowls at 1200k applied axle load repetitions

	d_0	d_{200}	d_{300}	d_{450}	d_{600}	d_{900}	d_{1200}	d_{1500}	d_{1800}
Station 1	98	73	56	41	31	24	19	17	14
Station 2	94	70	54	39	31	23	19	16	13
Station 3	90	69	54	39	31	23	20	17	16
Station 4	98	72	57	40	33	25	20	17	15
Station 5	106	81	63	45	35	26	21	18	16
Station 6	154	126	108	79	59	34	24	17	15
Station 7	261	240	199	140	94	42	27	19	17
Station 8	227	180	136	98	71	40	26	19	17
Station 8/9*	214	179	162	112	82	40	26	19	18
Station 9	438	338	272	185	126	60	31	20	19
Station 9/10*	443	347	276	192	132	63	32	23	19
Station 10	301	255	219	160	113	58	33	23	20
Station 9/10*	349	298	245	168	114	55	32	24	20
Station 11	284	236	193	137	99	52	32	22	20
Station 11/12*	289	240	193	134	90	48	30	23	21
Station 12	301	213	163	111	77	41	29	23	20
Station 13	149	113	91	66	51	38	29	23	17

Station 14	145	116	97	71	55	36	27	21	18
Station 15	135	112	93	68	51	33	26	21	17
Station 16	128	100	82	61	47	32	25	20	18
Station 17	123	93	75	55	43	31	25	21	16
Station 18	177	117	85	54	42	29	24	21	19
Station 19	-	-	-	-	-	-	-	-	-
Station 20	104	82	65	46	38	28	26	21	20
Station 21	-	-	-	-	-	-	-	-	-
Station 22	156	110	85	58	44	32	27	23	21
Station 23	149	124	103	75	57	39	31	26	23
Station 24	200	167	138	101	77	50	38	31	26
Station 25	304	251	217	164	125	76	50	36	29
Station 26	219	181	151	111	84	51	37	29	26
Station 27	219	177	147	109	84	55	40	34	28
Station 28	190	158	134	103	82	55	43	34	28
Station 29	196	167	143	111	88	56	41	33	29
Station 30	-	-	-	-	-	-	-	-	-
Station 31	-	-	-	-	-	-	-	-	-
Station 32	-	-	-	-	-	-	-	-	-
Station 33	-	-	-	-	-	-	-	-	-
Station 34	-	-	-	-	-	-	-	-	-
Station 35	431	333	268	173	101	40	24	20	21
Station 36	-	-	-	-	-	-	-	-	-
Station 37	249	192	151	99	64	31	24	21	18
Station 38	-	-	-	-	-	-	-	-	-
Station 39	266	210	173	121	88	49	35	27	24
Station 40	545	461	382	270	189	88	49	35	29
Station 41	629	597	508	381	291	175	108	70	46
Station 42	923	828	731	560	420	212	106	55	33
Station 43	817	703	578	419	287	121	58	39	29
Station 44	654	529	448	334	243	126	70	48	34
Station 45	630	553	473	351	252	133	75	47	35
Station 46	660	521	424	295	202	98	63	47	40
Station 47	-	-	-	-	-	-	-	-	-
Station 48	-	-	-	-	-	-	-	-	-
Station 49	-	-	-	-	-	-	-	-	-
Station 50	-	-	-	-	-	-	-	-	-
Station 51	-	-	-	-	-	-	-	-	-

* Intermediate stations as depicted in Figure 3.5

Table C.2 FWD 60 kN deflection bowls at 1200k applied axle load repetitions

	d_0	d_{200}	d_{300}	d_{450}	d_{600}	d_{900}	d_{1200}	d_{1500}	d_{1800}
Station 1	149	113	88	64	50	38	32	27	23
Station 2	141	106	84	61	49	36	31	26	22
Station 3	133	103	81	59	47	36	31	26	23
Station 4	143	107	86	61	49	38	32	27	22
Station 5	155	118	95	69	53	38	32	27	23
Station 6	220	180	154	117	88	53	35	28	24
Station 7	378	361	289	203	138	65	41	31	27
Station 8	315	259	190	138	102	60	40	31	27
Station 8/9*	294	246	218	157	117	63	43	33	27
Station 9	630	499	391	263	181	90	48	34	29
Station 9/10*	606	484	374	261	181	89	49	35	29
Station 10	427	365	316	233	167	89	52	35	30
Station 9/10*	486	417	345	240	166	82	49	36	30
Station 11	383	323	267	191	142	79	49	36	30
Station 11/12*	406	340	274	190	130	72	47	36	31
Station 12	433	297	235	159	111	61	44	37	32
Station 13	219	165	135	100	79	58	44	35	29
Station 14	212	169	141	106	82	56	42	33	27
Station 15	198	165	140	103	80	53	41	32	27
Station 16	188	148	123	93	73	50	40	31	27
Station 17	182	140	113	85	68	50	39	32	26
Station 18	270	177	132	85	63	44	37	31	27
Station 19	-	-	-	-	-	-	-	-	-
Station 20	156	123	99	71	56	42	37	33	30
Station 21	-	-	-	-	-	-	-	-	-
Station 22	228	162	124	87	67	49	41	36	32
Station 23	222	184	155	115	89	61	48	41	36
Station 24	288	239	200	147	114	76	59	48	40
Station 25	443	364	316	240	183	113	77	57	44
Station 26	320	261	219	163	125	78	58	47	38
Station 27	318	259	214	161	124	82	62	50	41
Station 28	283	235	198	154	123	84	65	53	43
Station 29	292	245	210	166	132	87	65	52	44
Station 30	-	-	-	-	-	-	-	-	-
Station 31	-	-	-	-	-	-	-	-	-
Station 32	-	-	-	-	-	-	-	-	-
Station 33	-	-	-	-	-	-	-	-	-
Station 34	-	-	-	-	-	-	-	-	-
Station 35	669	477	381	243	142	61	36	31	30
Station 36	-	-	-	-	-	-	-	-	-
Station 37	343	276	211	140	94	50	39	34	31
Station 38	-	-	-	-	-	-	-	-	-
Station 39	357	285	237	171	126	76	54	45	38
Station 40	776	693	551	387	270	135	76	56	45

Station 41	810	794	674	516	387	231	147	94	69
Station 42	1192	1056	923	763	543	263	139	80	53
Station 43	1142	943	777	576	395	178	91	61	63
Station 44	913	759	647	472	355	197	117	80	65
Station 45	872	801	690	536	374	218	145	78	59
Station 46	887	719	579	411	289	152	100	75	64
Station 47	-	-	-	-	-	-	-	-	-
Station 48	-	-	-	-	-	-	-	-	-
Station 49	-	-	-	-	-	-	-	-	-
Station 50	-	-	-	-	-	-	-	-	-
Station 51	-	-	-	-	-	-	-	-	-

* Intermediate stations as depicted in Figure 3.5

Table C.3 FWD 80 kN deflection bowls at 1200k applied axle load repetitions

	d_0	d_{200}	d_{300}	d_{450}	d_{600}	d_{900}	d_{1200}	d_{1500}	d_{1800}
Station 1	197	151	116	86	68	51	43	36	30
Station 2	182	136	110	81	65	48	41	35	31
Station 3	169	131	105	77	62	46	41	36	31
Station 4	183	138	111	81	66	50	42	35	30
Station 5	196	151	122	90	70	51	43	36	31
Station 6	275	227	196	149	114	71	49	38	32
Station 7	487	440	368	258	177	88	56	42	35
Station 8	386	319	234	173	129	80	56	44	37
Station 8/9*	360	307	262	201	155	87	60	46	37
Station 9	798	622	489	325	224	115	65	46	37
Station 9/10*	701	576	446	315	219	113	66	47	37
Station 10	516	459	392	297	212	114	68	47	38
Station 9/10*	579	509	437	298	209	106	66	48	39
Station 11	470	427	328	234	176	100	65	48	40
Station 11/12*	498	445	333	235	164	93	61	48	41
Station 12	517	374	294	202	143	81	59	47	42
Station 13	280	214	177	132	106	77	60	47	39
Station 14	267	216	181	139	109	75	57	45	37
Station 15	254	212	182	136	107	73	56	45	36
Station 16	241	192	160	124	98	69	54	43	37
Station 17	235	183	150	114	92	67	53	44	35
Station 18	356	230	172	114	83	58	49	42	38
Station 19	-	-	-	-	-	-	-	-	-
Station 20	201	159	131	93	74	56	49	43	38
Station 21	-	-	-	-	-	-	-	-	-
Station 22	289	207	160	115	89	66	56	48	42
Station 23	292	242	206	154	120	83	66	56	49
Station 24	368	307	256	191	149	102	80	64	53
Station 25	567	466	404	307	234	147	102	75	59

Station 26	413	334	282	212	163	104	78	63	52
Station 27	406	332	274	208	162	109	84	67	56
Station 28	369	307	260	203	164	115	89	72	59
Station 29	379	319	273	217	173	117	87	69	59
Station 30	-	-	-	-	-	-	-	-	-
Station 31	-	-	-	-	-	-	-	-	-
Station 32	-	-	-	-	-	-	-	-	-
Station 33	-	-	-	-	-	-	-	-	-
Station 34	-	-	-	-	-	-	-	-	-
Station 35	832	611	474	330	186	83	52	46	44
Station 36	-	-	-	-	-	-	-	-	-
Station 37	416	342	266	179	122	69	55	48	43
Station 38	-	-	-	-	-	-	-	-	-
Station 39	425	347	292	216	163	102	75	61	50
Station 40	956	884	711	501	347	177	108	79	66
Station 41	1075	939	792	620	505	282	182	124	93
Station 42	1456	1247	1064	829	621	323	178	104	94
Station 43	1366	1128	941	675	474	236	125	87	82
Station 44	1134	919	775	573	439	248	149	109	81
Station 45	1152	1045	820	616	476	283	167	109	90
Station 46	1078	889	719	531	378	209	141	106	89
Station 47	-	-	-	-	-	-	-	-	-
Station 48	-	-	-	-	-	-	-	-	-
Station 49	-	-	-	-	-	-	-	-	-
Station 50	-	-	-	-	-	-	-	-	-
Station 51	-	-	-	-	-	-	-	-	-

* Intemediate stations as depicted in Figure 3.5

Table C.4 FWD 40 kN deflection bowls at 2800k applied axle load repetitions

	d_0	d_{200}	d_{300}	d_{450}	d_{600}	d_{900}	d_{1200}	d_{1500}	d_{1800}
Station 1	83	66	52	42	33	26	21	18	15
Station 2	94	70	55	42	35	27	23	20	17
Station 3	97	79	65	48	37	27	22	19	16
Station 4	97	76	61	45	35	27	22	19	16
Station 5	111	83	66	47	36	27	22	19	16
Station 6	115	89	74	54	43	30	24	21	18
Station 7	127	111	91	70	55	39	30	25	20
Station 8	341	332	303	252	210	129	44	27	18
Station 9	725	433	280	169	106	58	32	26	20
Station 10	178	144	123	98	76	49	34	25	21
Station 11	199	165	135	104	80	47	33	26	20
Station 12	177	129	102	82	63	41	31	26	20
Station 13	144	123	95	71	56	40	31	23	20
Station 14	144	116	93	72	55	40	30	23	19

Station 15	153	121	99	76	61	43	34	27	20
Station 16	138	110	91	69	56	40	30	24	18
Station 17	135	106	88	67	53	38	29	23	17
Station 18	81	65	53	40	33	28	25	21	18
Station 19	134	108	84	55	40	30	25	21	19
Station 20	107	83	65	50	40	32	28	23	20
Station 21	131	99	79	57	45	34	28	24	21
Station 22	123	99	81	61	47	36	30	25	21
Station 23	126	102	86	67	52	40	33	27	23
Station 24	139	109	92	69	53	42	35	30	27
Station 25	155	120	96	74	59	42	33	23	19
Station 26	284	194	140	97	70	46	34	28	23
Station 27	180	152	128	101	78	56	42	30	26
Station 28	213	176	149	115	91	61	46	35	28
Station 29	212	173	147	114	90	62	47	37	30
Station 30	206	171	145	112	87	59	46	37	26
Station 31	232	183	148	115	90	61	46	35	29
Station 32	192	145	115	85	67	51	40	31	25
Station 33	163	130	107	83	65	47	36	29	22
Station 34	145	107	90	70	57	43	34	28	23
Station 35	456	408	334	295	268	151	98	63	45
Station 36	575	412	392	297	212	152	81	50	40
Station 37	391	317	264	203	156	94	58	42	28
Station 38	337	261	201	140	98	54	39	31	27
Station 39	350	314	270	213	163	99	65	48	36
Station 40	487	429	369	285	229	131	84	60	46
Station 41	491	457	403	326	263	172	118	80	55
Station 42	840	676	597	442	351	203	117	64	42
Station 43	623	452	339	231	158	73	47	36	32
Station 44	466	410	355	284	224	145	97	69	49
Station 45	814	729	631	493	317	195	109	64	44
Station 46	593	451	341	237	168	93	67	52	43
Station 47	497	470	419	343	272	169	104	75	50
Station 48	835	732	641	499	396	230	137	87	59
Station 49	853	694	583	477	329	196	125	79	52
Station 50	551	476	390	296	221	123	78	53	40
Station 51	482	373	305	224	162	88	58	44	36

Table C.5 FWD 60 kN deflection bowls at 2800k applied axle load repetitions

	d_0	d_{200}	d_{300}	d_{450}	d_{600}	d_{900}	d_{1200}	d_{1500}	d_{1800}
Station 1	124	99	80	63	50	39	33	27	23
Station 2	144	102	82	60	50	39	33	28	24
Station 3	141	116	96	72	57	41	34	29	24
Station 4	142	112	90	69	54	41	34	29	24
Station 5	160	123	97	73	58	43	37	31	26
Station 6	170	130	107	82	65	48	38	33	28
Station 7	183	161	131	102	81	58	47	39	32
Station 8	392	375	351	301	237	148	61	40	28
Station 9	686	497	340	208	139	79	50	39	31
Station 10	249	200	171	139	109	74	52	41	33
Station 11	269	225	183	142	112	71	50	39	31
Station 12	247	182	147	118	93	65	50	41	33
Station 13	204	169	137	107	86	62	49	38	32
Station 14	206	168	135	106	86	63	50	39	31
Station 15	219	171	144	113	91	66	52	40	32
Station 16	198	160	135	105	87	63	48	38	32
Station 17	196	155	129	103	83	60	47	37	30
Station 18	122	99	80	63	54	44	39	33	28
Station 19	200	153	117	81	60	46	40	35	30
Station 20	160	123	98	76	62	50	43	36	31
Station 21	192	147	117	88	70	53	45	37	32
Station 22	184	146	120	92	73	57	49	40	34
Station 23	192	152	127	101	82	62	52	46	38
Station 24	207	160	132	101	82	64	55	45	38
Station 25	224	173	141	112	90	65	50	39	31
Station 26	384	263	192	139	103	70	55	44	36
Station 27	258	217	183	144	115	81	64	46	40
Station 28	308	253	216	171	138	96	74	56	45
Station 29	306	249	210	170	135	94	71	57	45
Station 30	302	251	209	167	132	92	72	57	45
Station 31	336	267	221	172	137	95	72	55	46
Station 32	275	210	168	127	105	81	63	49	37
Station 33	241	191	157	122	99	73	57	46	36
Station 34	213	161	136	109	91	69	56	45	35
Station 35	496	445	378	343	255	186	119	88	64
Station 36	631	470	432	343	188	174	98	61	72
Station 37	467	368	325	265	198	145	85	59	46
Station 38	437	343	268	193	138	84	62	50	43
Station 39	488	419	353	288	218	137	94	68	52
Station 40	631	549	511	372	285	173	117	87	68
Station 41	662	531	507	410	330	222	159	116	92
Station 42	875	723	681	551	395	243	146	106	64
Station 43	722	597	460	320	218	119	77	67	52
Station 44	637	560	476	385	297	199	136	98	77

Station 45	954	924	759	613	431	267	148	99	72
Station 46	736	628	470	332	243	144	105	81	67
Station 47	696	639	559	467	363	235	157	112	81
Station 48	988	873	787	612	483	292	178	122	87
Station 49	951	809	716	570	412	251	163	115	80
Station 50	708	605	496	378	289	169	113	78	59
Station 51	652	493	405	304	224	131	91	72	60

Table C.6 FWD 80 kN deflection bowls at 2800k applied axle load repetitions

	d_0	d_{200}	d_{300}	d_{450}	d_{600}	d_{900}	d_{1200}	d_{1500}	d_{1800}
Station 1	166	133	104	84	68	53	45	37	31
Station 2	178	138	108	83	69	54	45	37	31
Station 3	183	152	127	94	76	55	46	39	33
Station 4	188	149	118	92	73	57	46	39	33
Station 5	209	159	126	95	76	58	49	41	35
Station 6	241	172	142	109	88	65	52	44	38
Station 7	236	222	169	133	108	79	65	53	43
Station 8	416	410	401	362	275	184	82	54	40
Station 9	763	514	391	242	171	102	68	53	42
Station 10	318	255	215	179	140	97	70	55	44
Station 11	347	272	225	184	142	93	68	52	41
Station 12	313	257	189	153	123	87	67	55	43
Station 13	263	215	175	140	115	86	67	53	44
Station 14	267	220	177	139	114	85	67	52	42
Station 15	282	219	186	147	122	89	70	55	44
Station 16	267	210	176	141	116	85	66	52	42
Station 17	260	201	169	135	111	81	64	51	40
Station 18	164	133	107	85	72	60	52	45	37
Station 19	250	204	148	105	81	63	56	48	41
Station 20	209	163	130	102	85	68	59	49	42
Station 21	250	193	155	118	94	72	61	51	43
Station 22	253	192	159	124	101	79	66	55	47
Station 23	249	202	170	136	110	85	71	61	52
Station 24	267	212	174	136	111	87	74	62	50
Station 25	293	228	186	147	120	87	67	53	43
Station 26	475	327	243	177	135	94	73	60	49
Station 27	340	283	240	192	154	113	88	67	57
Station 28	398	331	282	224	182	129	100	78	64
Station 29	408	326	274	223	179	129	100	79	63
Station 30	395	330	277	221	178	125	98	78	64
Station 31	445	351	291	226	183	129	97	75	60
Station 32	359	276	221	172	143	110	86	66	52
Station 33	316	251	210	164	134	99	78	63	50
Station 34	285	213	180	147	123	95	75	61	49

Station 35	553	420	426	380	281	213	145	100	83
Station 36	624	474	495	362	242	185	127	61	52
Station 37	562	413	379	303	239	173	133	82	62
Station 38	489	427	336	244	180	114	86	71	60
Station 39	581	493	422	346	266	173	122	91	71
Station 40	712	629	575	433	317	214	147	112	90
Station 41	735	617	584	462	373	263	188	133	106
Station 42	934	780	790	644	465	287	168	114	78
Station 43	775	682	550	395	278	158	108	87	73
Station 44	760	661	592	498	369	242	174	128	100
Station 45	1108	835	851	725	545	303	192	122	95
Station 46	819	702	585	421	315	192	143	112	91
Station 47	828	748	681	575	452	298	201	145	105
Station 48	1057	955	883	688	557	337	215	160	107
Station 49	1097	918	850	665	503	310	205	147	101
Station 50	828	704	595	461	358	213	143	103	80
Station 51	734	610	502	381	293	173	124	97	87

C.1.3 Maximum 40 kN deflections
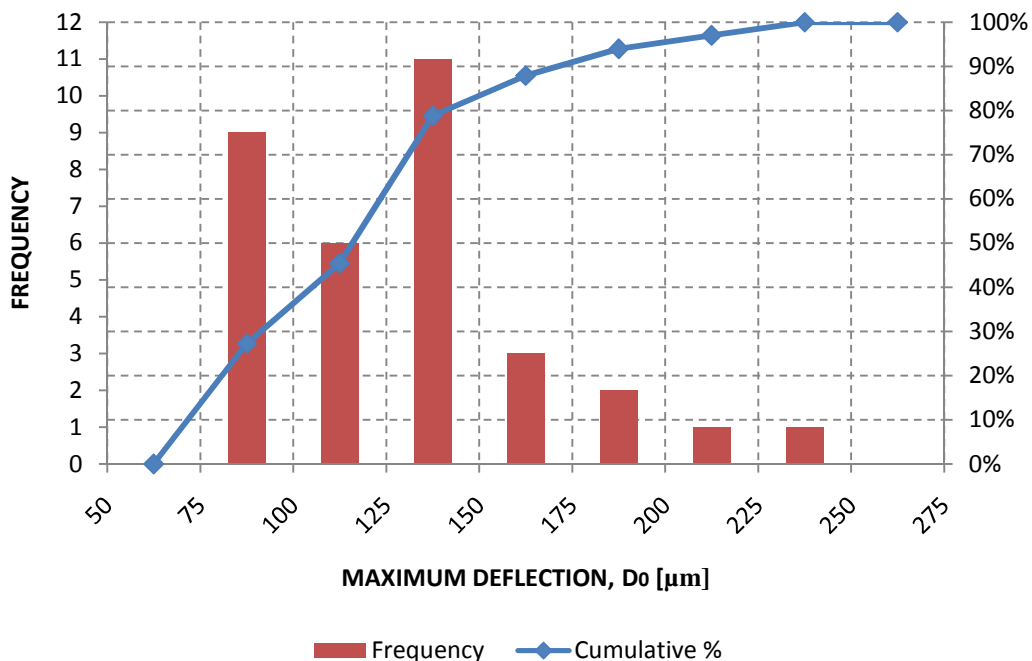
Figure C.2 Maximum 40 kN FWD interior deflections (D_0) at zero axle load repetitions
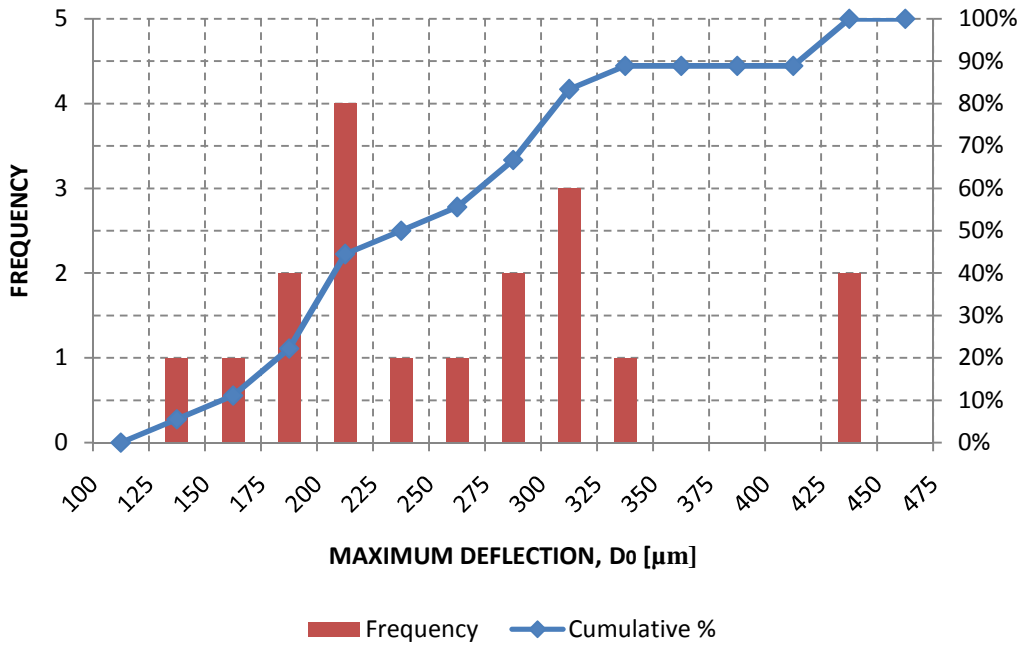
Figure C.3 Maximum 40 kN FWD interior deflections (D$_0$) at 1200k axle load repetitions
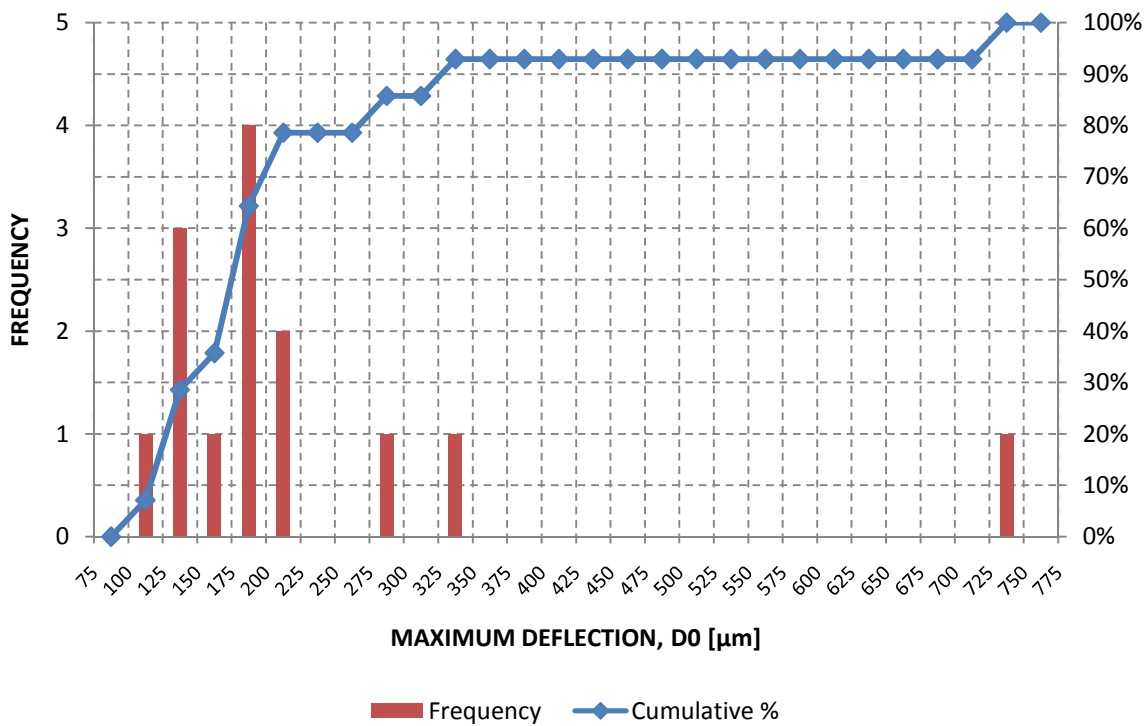
Figure C.4 Maximum 40 kN FWD interior deflections (D$_0$) at 2800k axle load repetitions

C.1.4 Maximum 60 kN deflections
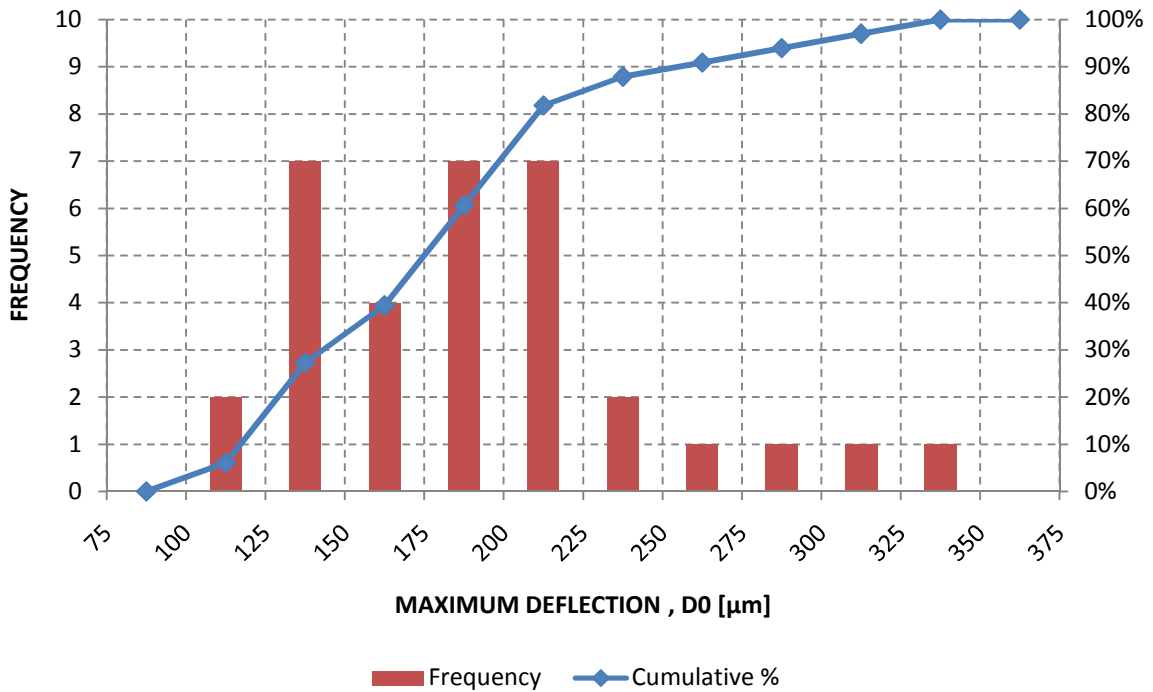
Figure C.5 Maximum 60 kN FWD interior deflections (D$_0$) at zero axle load repetitions
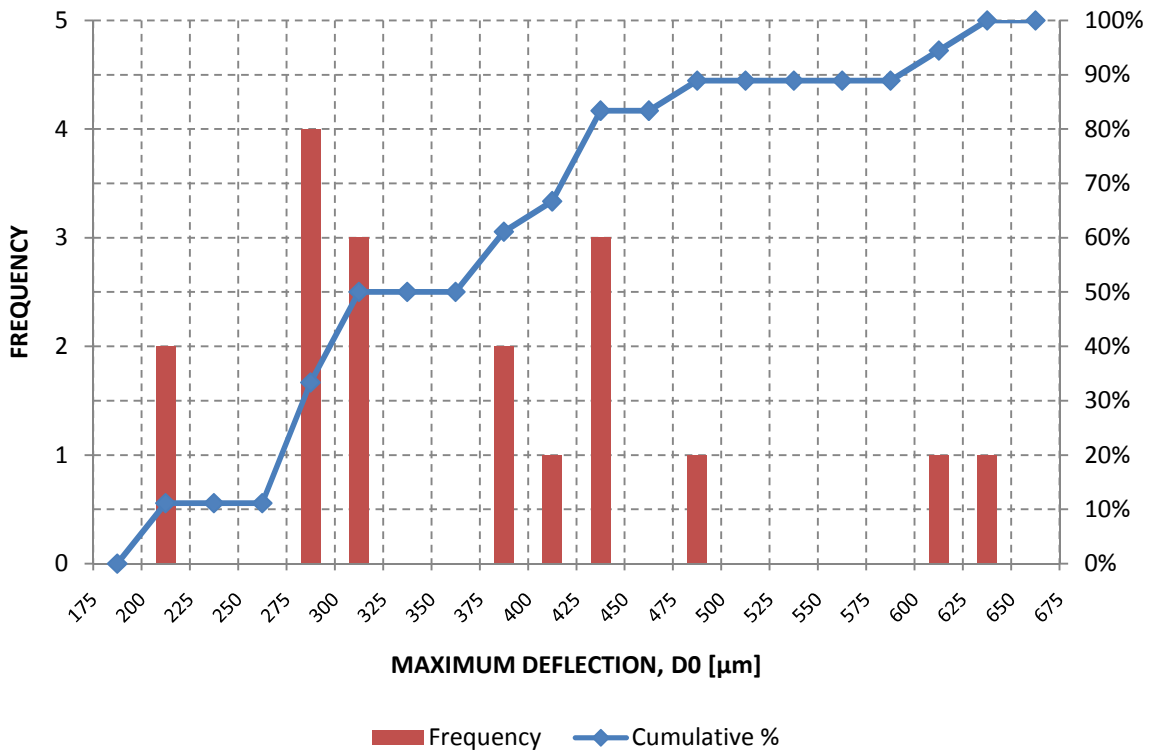
Figure C.6 Maximum 60 kN FWD interior deflections (D$_0$) at 1200k axle load repetitions
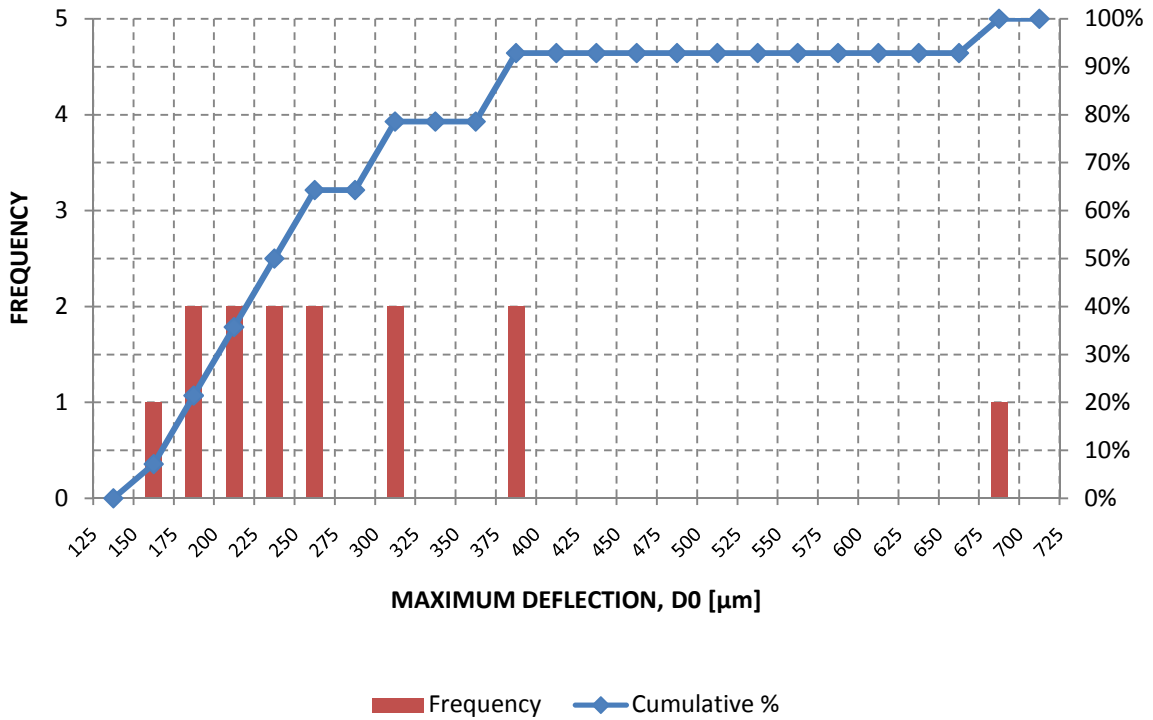
Figure C.7 Maximum 60 kN FWD interior deflections (D$_0$) at 2800k axle load repetitions

C.1.5 Maximum 80 kN deflections
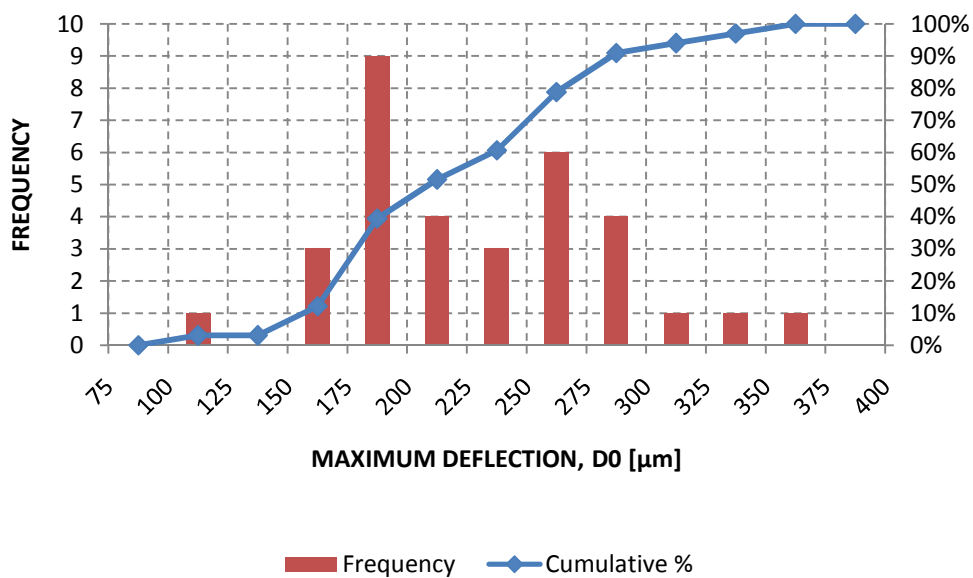
Figure C.8 Maximum 80 kN FWD interior deflections (D$_0$) at zero axle load repetitions
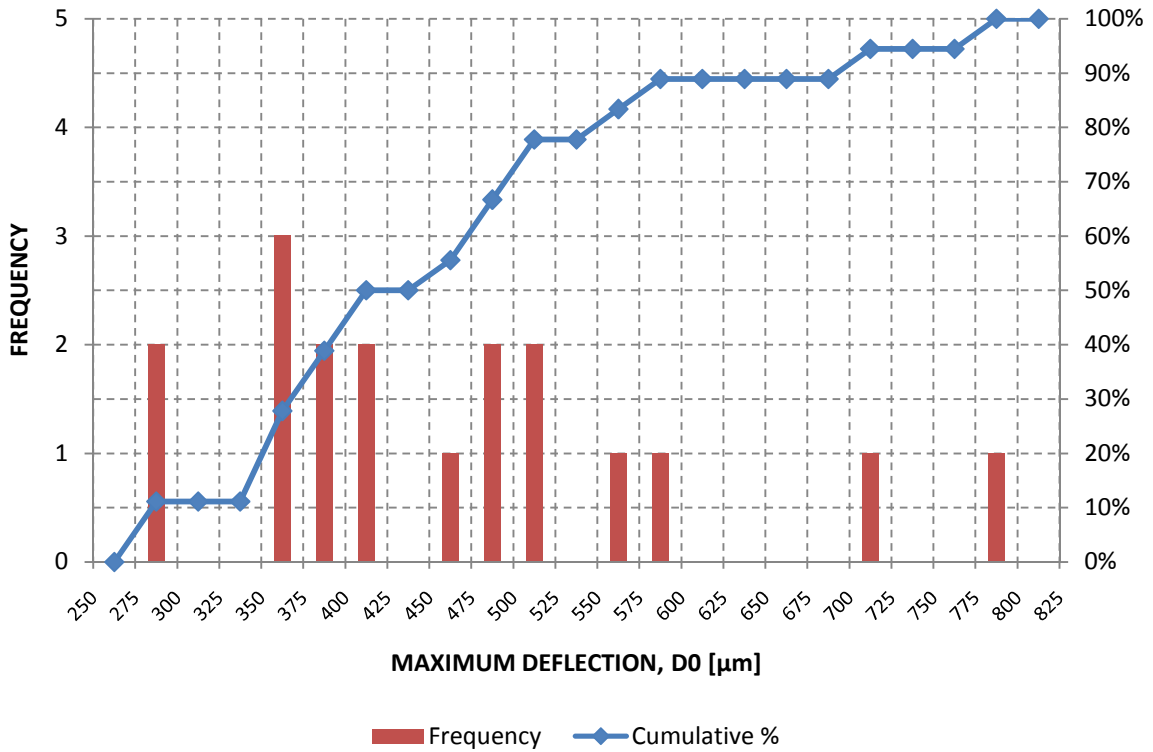
Figure C.9 Maximum 80 kN FWD interior deflections (D$_0$) at 1200k axle load repetitions
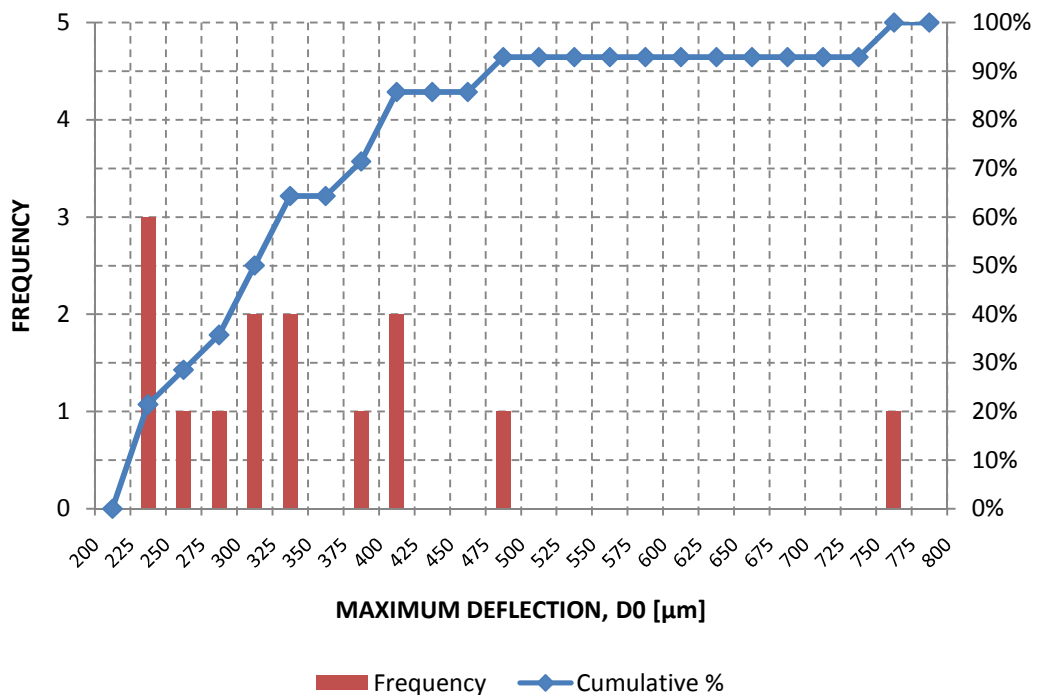
Figure C.10 Maximum 80 kN FWD interior deflections (D$_0$) at 2800k axle load repetitions

C.1.6 Maximum deflections along pavement interior
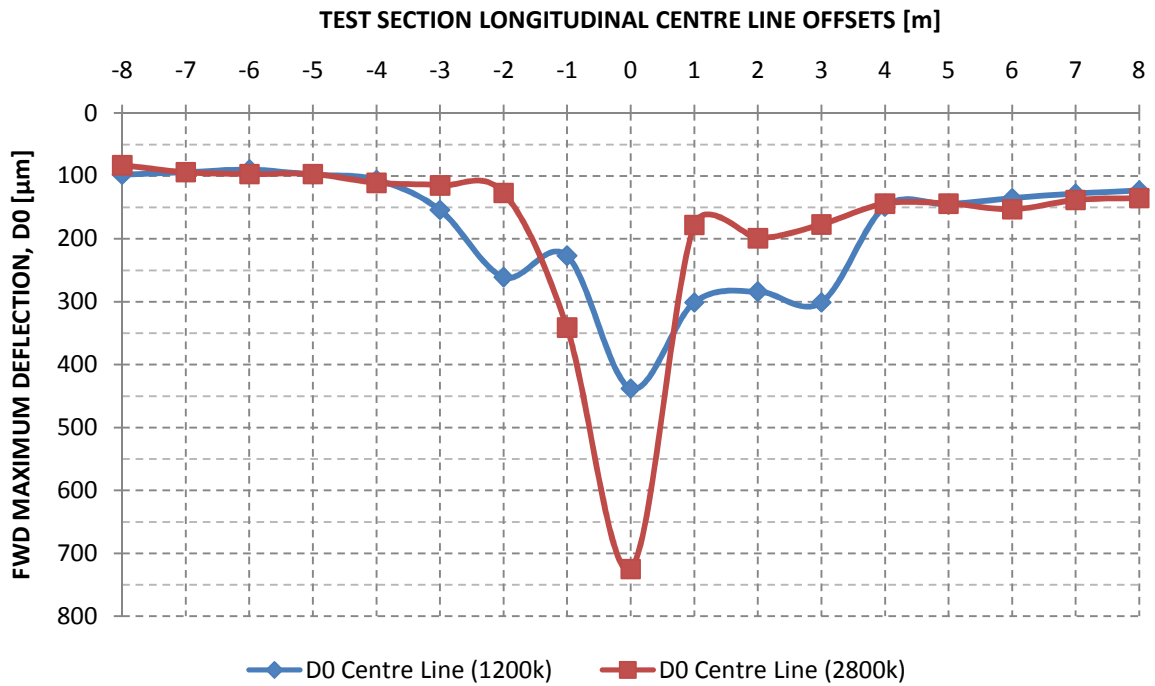
Figure C.11 Maximum 40 kN FWD deflections along longitudinal centre line
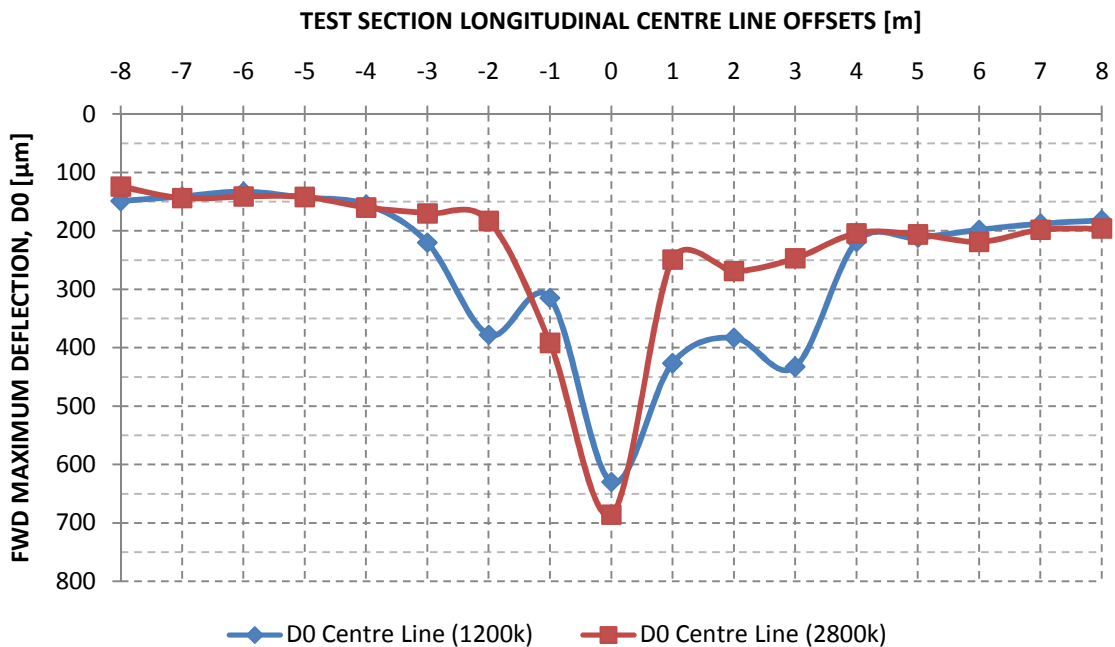
Figure C.12 Maximum 60 kN FWD deflections along longitudinal centre line
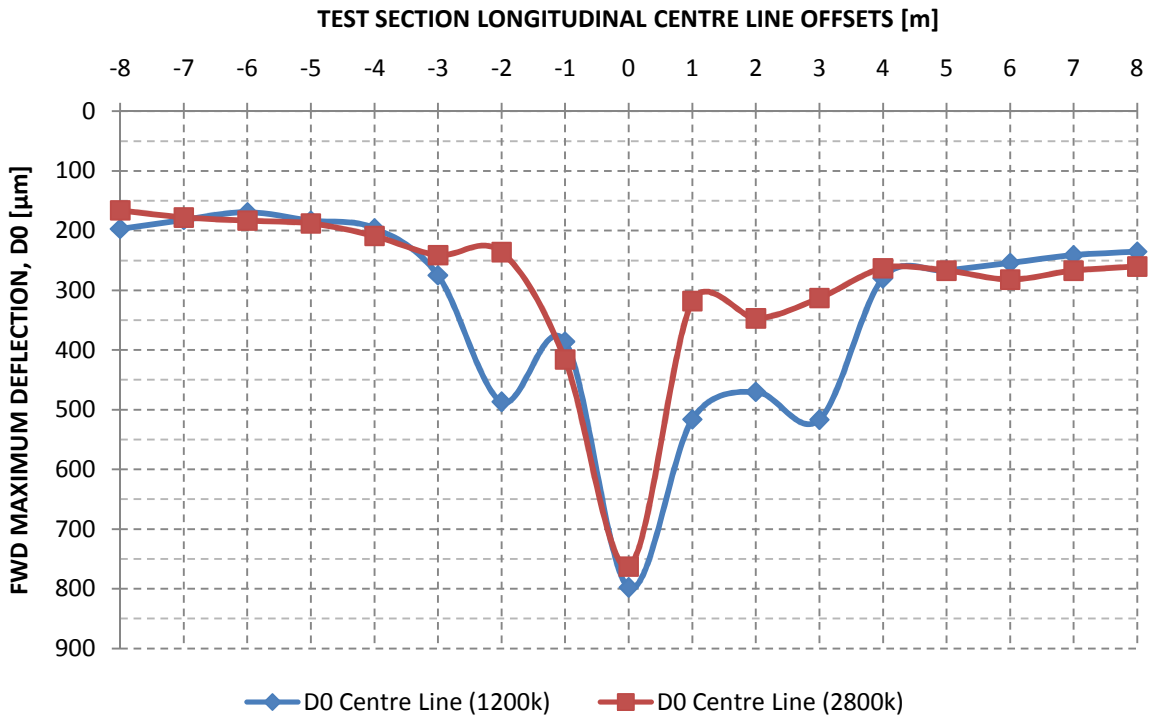
Figure C.13 Maximum 80 kN FWD deflections along longitudinal centre line

C.1.7 Edge loading deflections
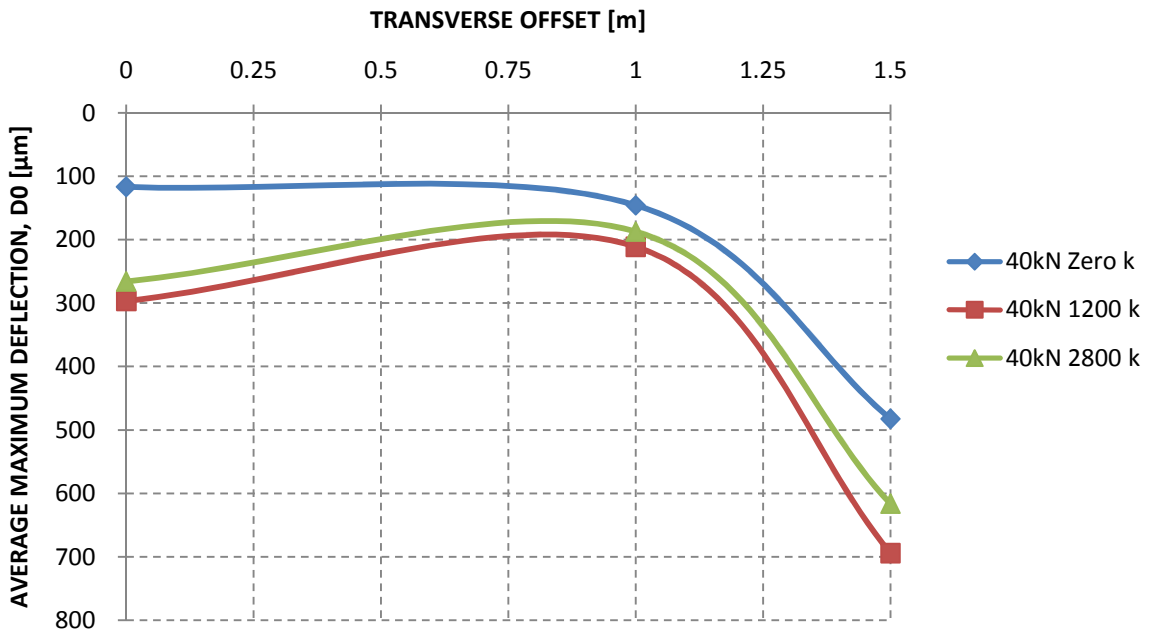
Figure C.14 FWD 40 kN transverse deflection profile (centre to edge)
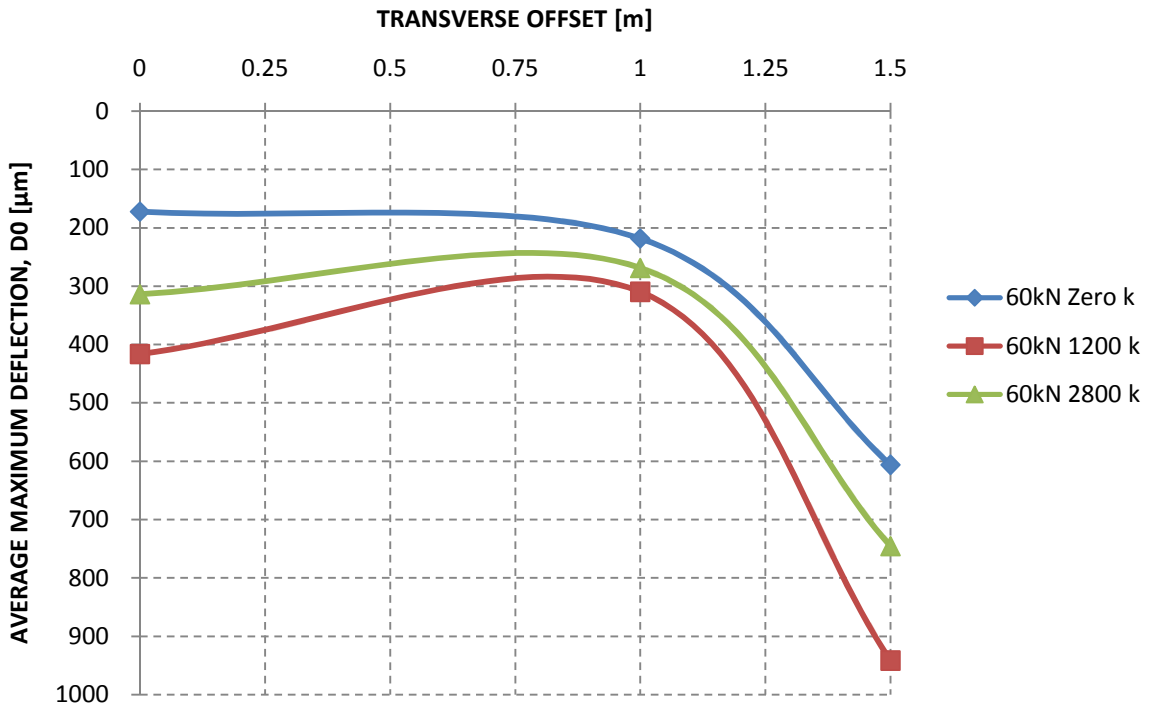
Figure C.15 FWD 60 kN transverse deflection profile (centre to edge)
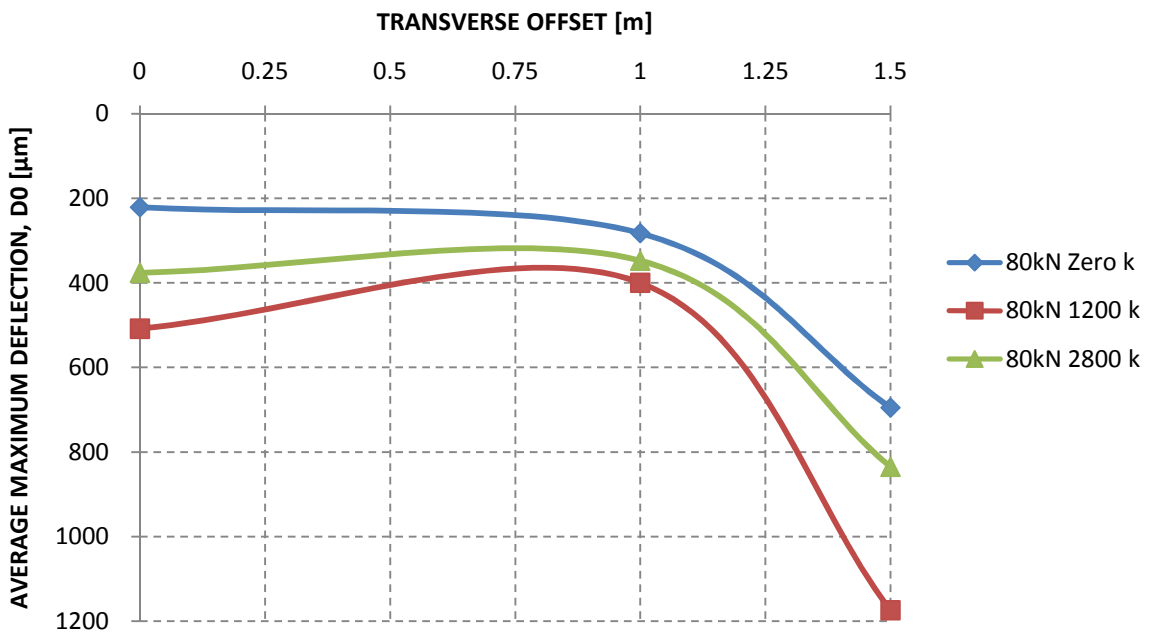
Figure C.16 FWD 80 kN transverse deflection profile (centre to edge)

C.2 Radius of Relative Stiffness Results

C.2.1 DL-model radius of relative stiffness (l_k) plots
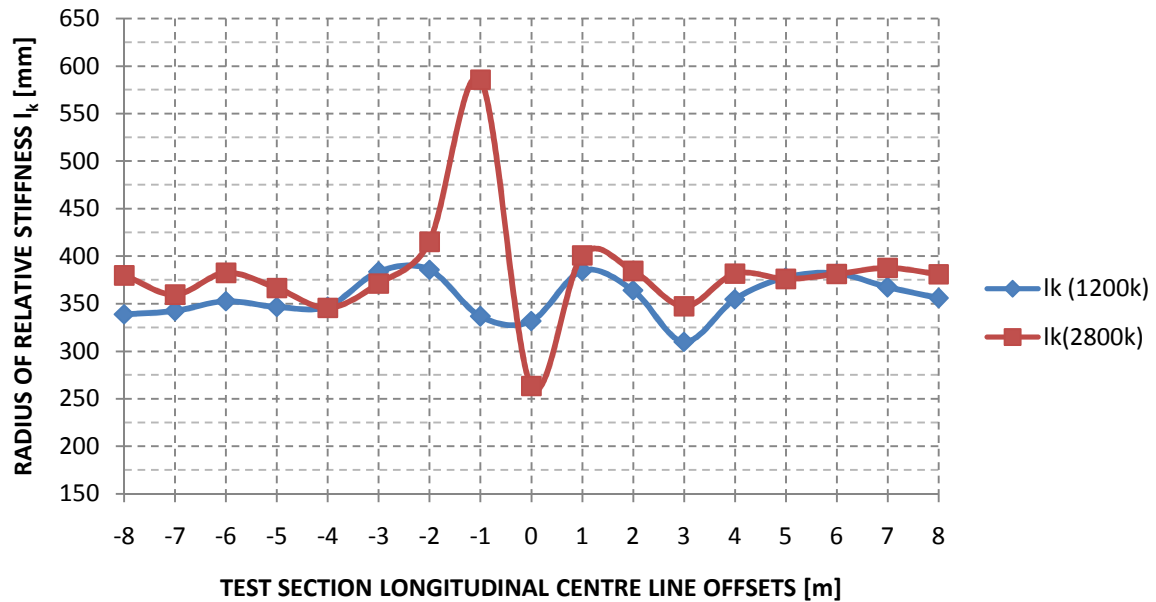
Figure C.17 Radius of relative stiffness l_k for the DL-model along the longitudinal centre line (40 kN FWD)

Figure C.18 Radius of relative stiffness l_k for the DL-model along the longitudinal centre line (60 kN FWD)

Figure C.19 Radius of relative stiffness I_k for the DL-model along the longitudinal centre line (80 kN FWD)
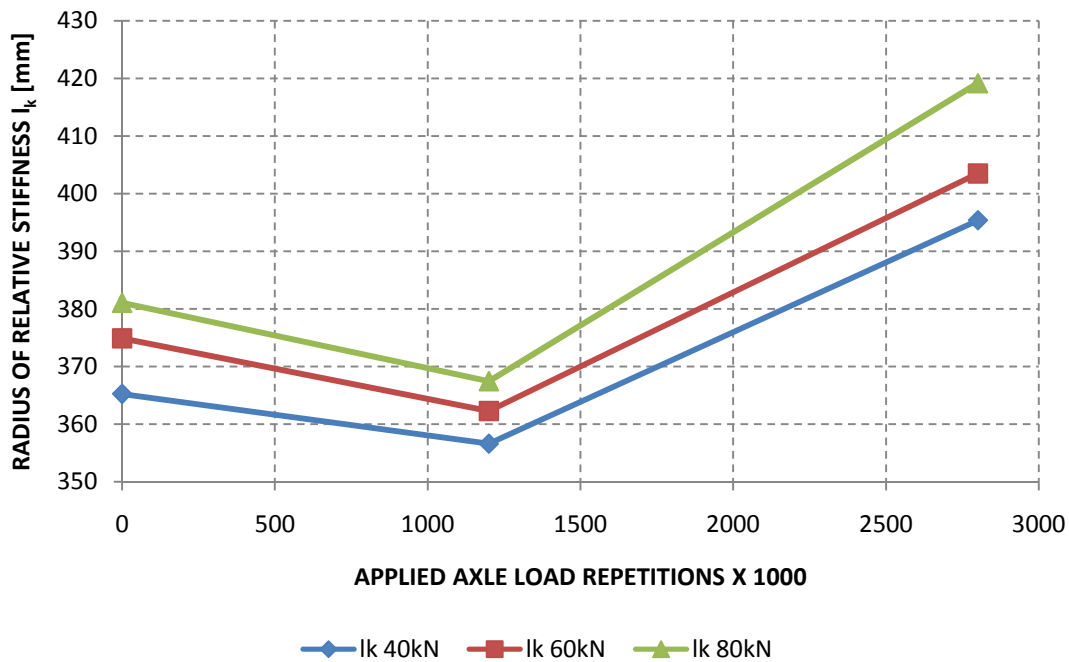
Figure C.20 Average radius of relative stiffness for the DL-model at the indicated applied axle load repetition interval and specified FWD loading

C.2.2 ES-model radius of relarive stiffness (I_e) plots
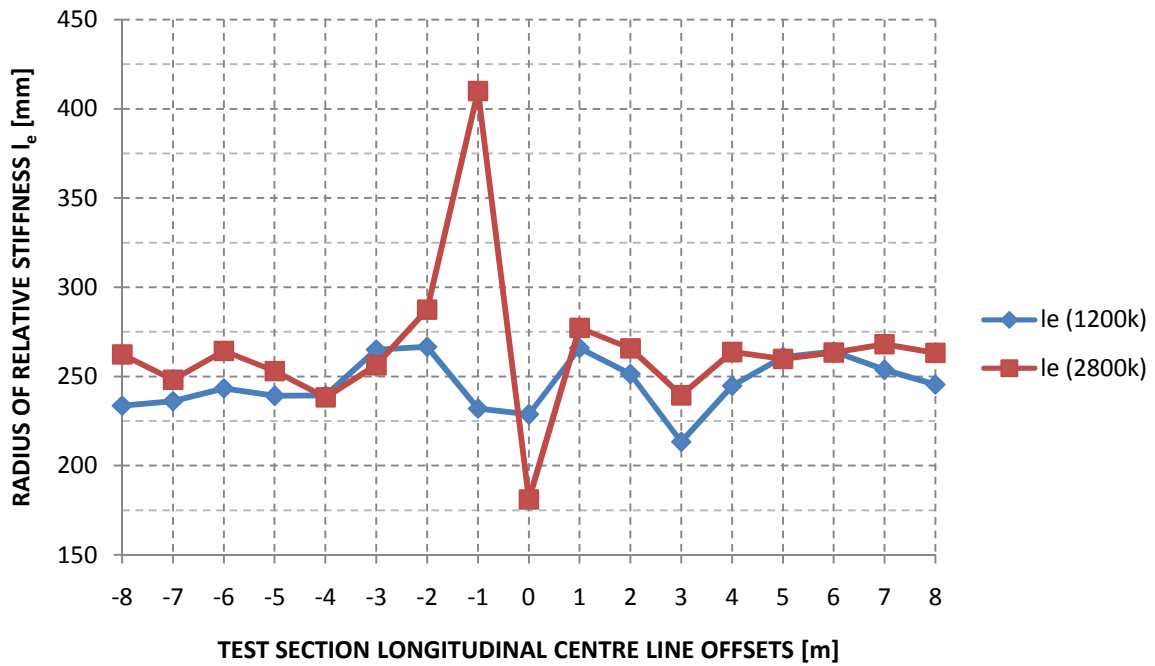
Figure C.21 Radius of relative stiffness I_e for the ES-model along the longitudinal centre line (40 kN FWD)
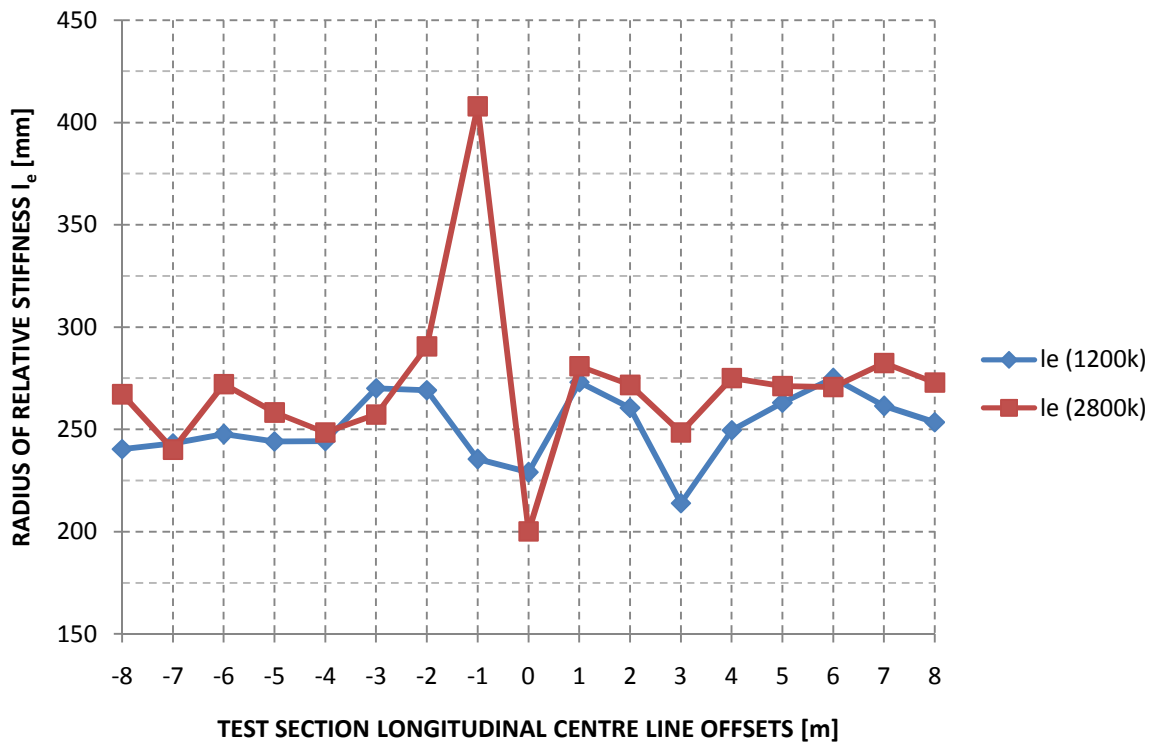
Figure C.22 Radius of relative stiffness I_e for the ES-model along the longitudinal centre line (60 kN FWD)
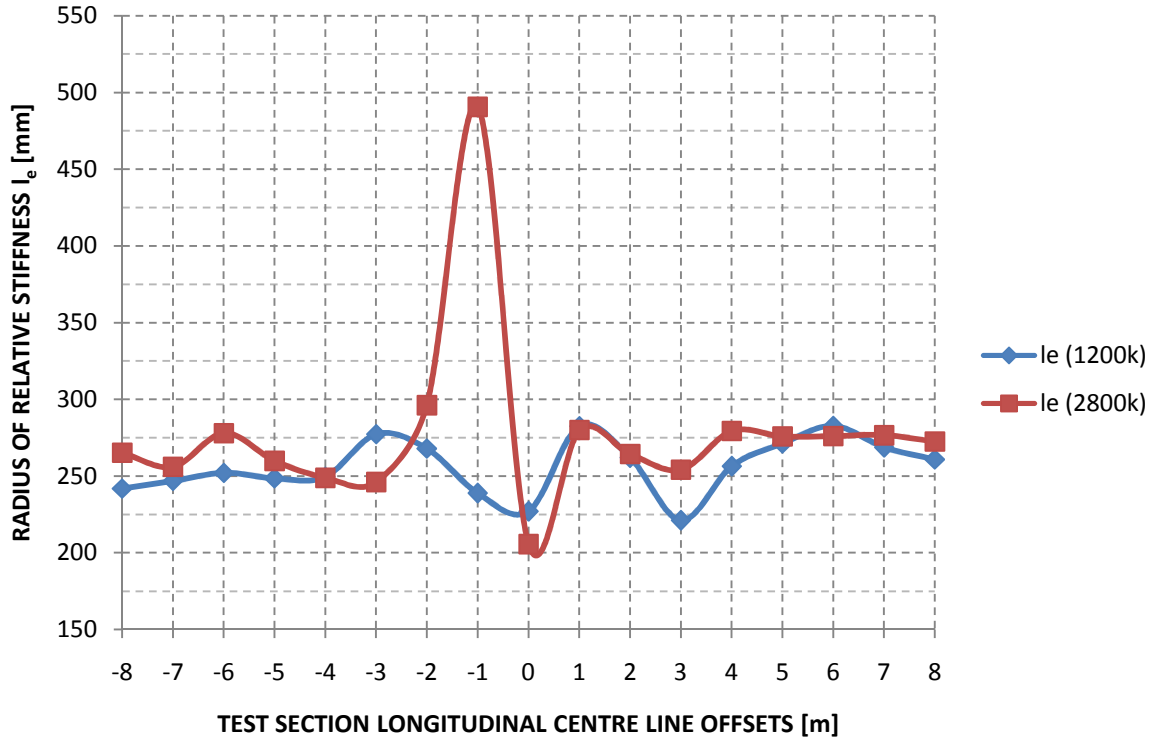
Figure C.23 Radius of relative stiffness Iₑ for the ES-model along the longitudinal centre line (80 kN FWD)
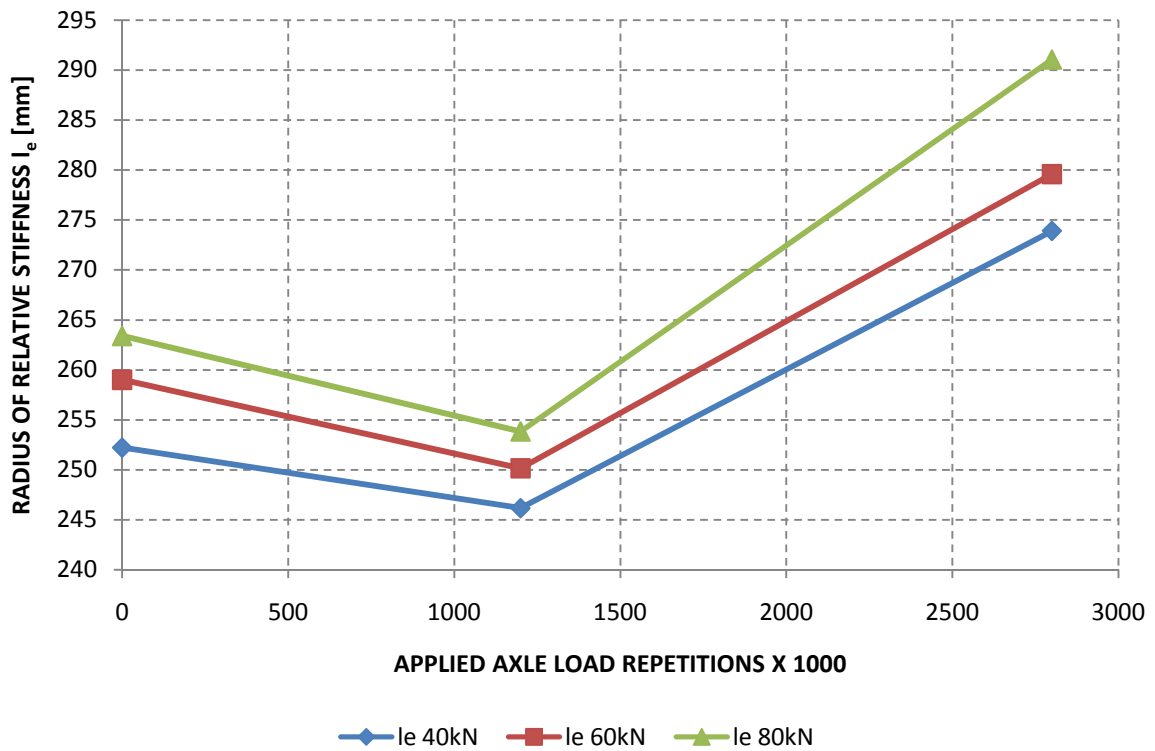
Figure C.24 Average radius of relative stiffness for the ES-model at the indicated applied axle load repetition interval and specified FWD loading

C.3 Elastic Modulus of Concrete Results

C.3.1 DL-model concrete elastic modulus
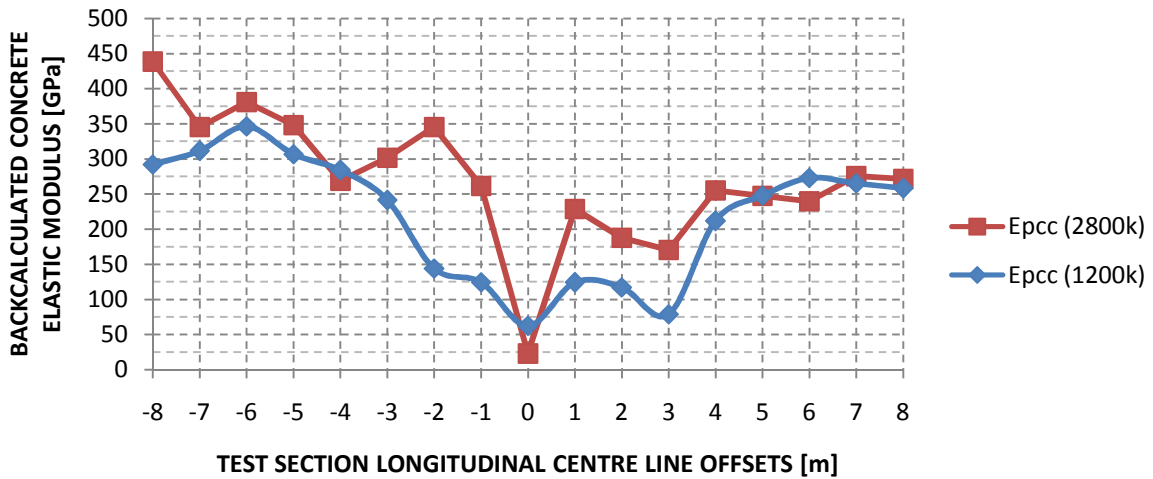
Figure C.25 Backcalculated concrete elastic modulus for the DL-model (40 kN FWD deflection bowls)
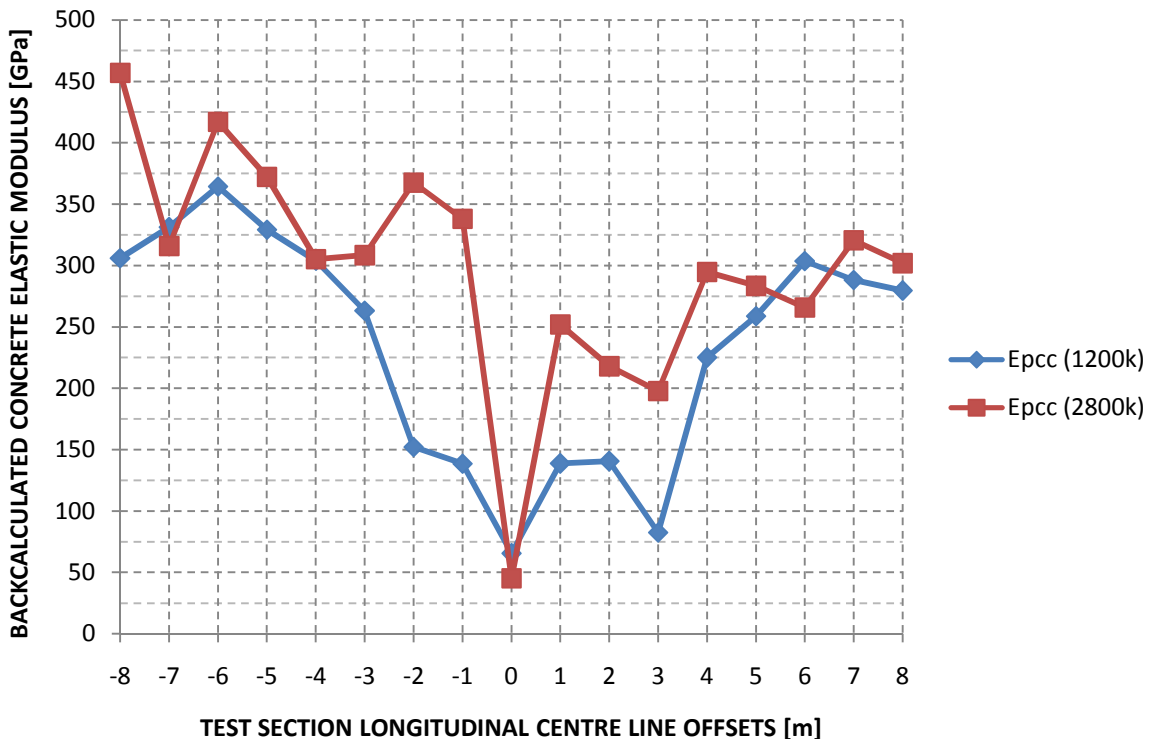
Figure C.26 Backcalculated concrete elastic modulus for the DL-model (60 kN FWD deflection bowls)
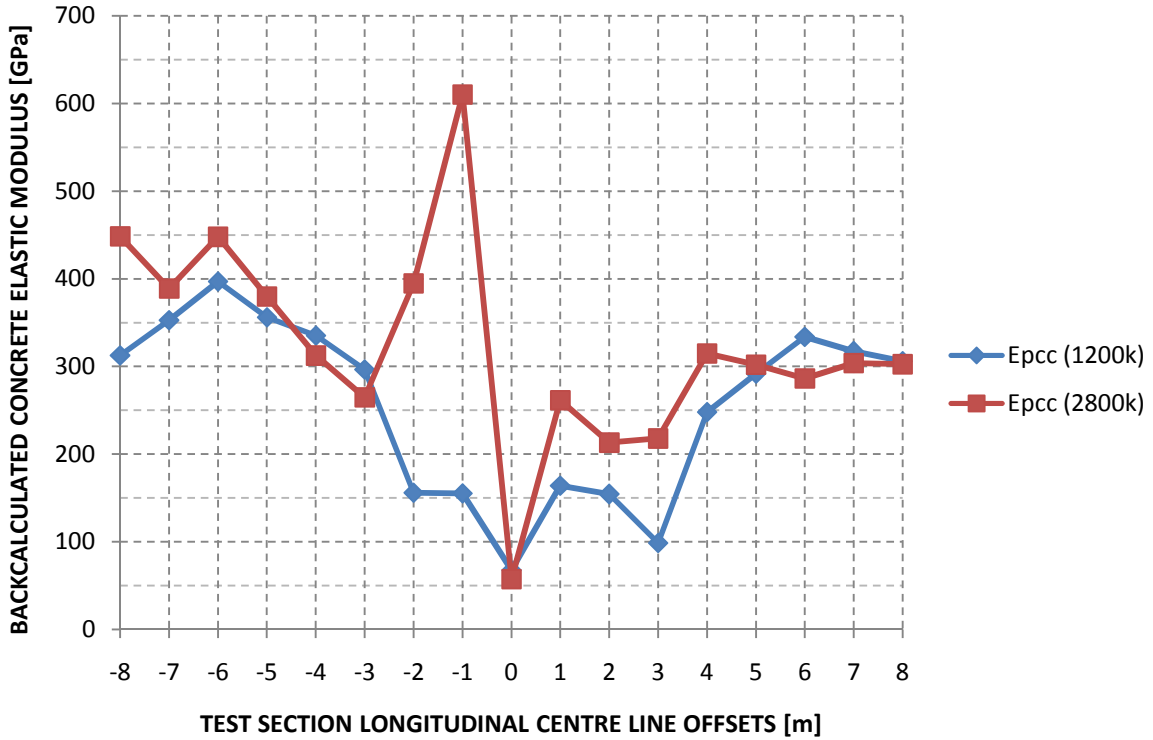
Figure C.27 Backcalculated concrete elastic modulus for the DL-model (80 kN FWD deflection bowls)
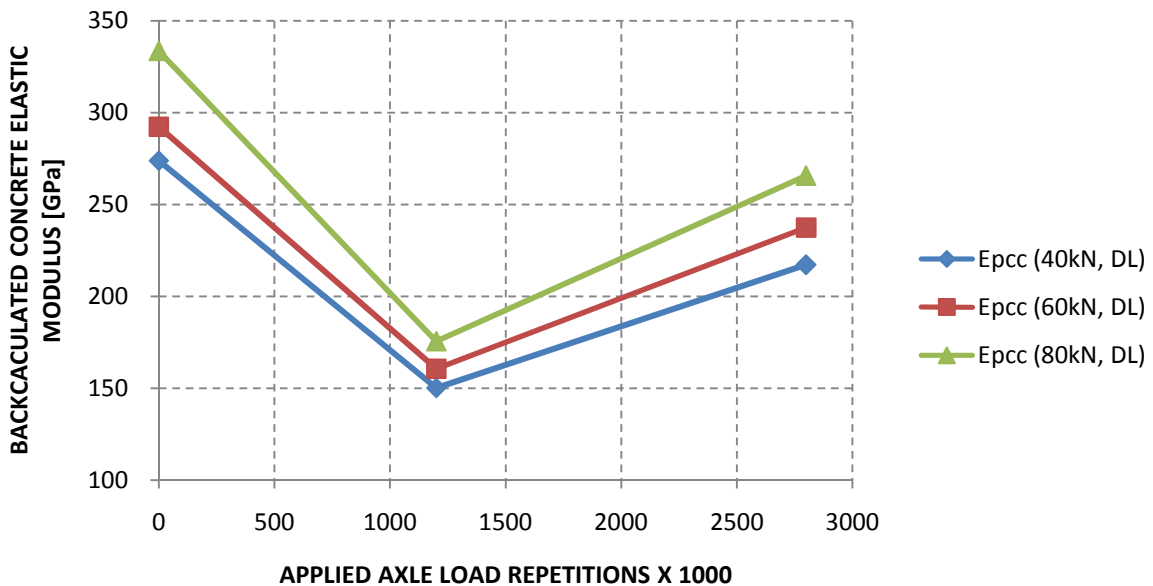
Figure C.28 Average backcalculated concrete elastic modulus for the DL-model at the indicated applied axle load repetition interval and specified FWD loading

C.3.2 ES-model concrete elastic modulus
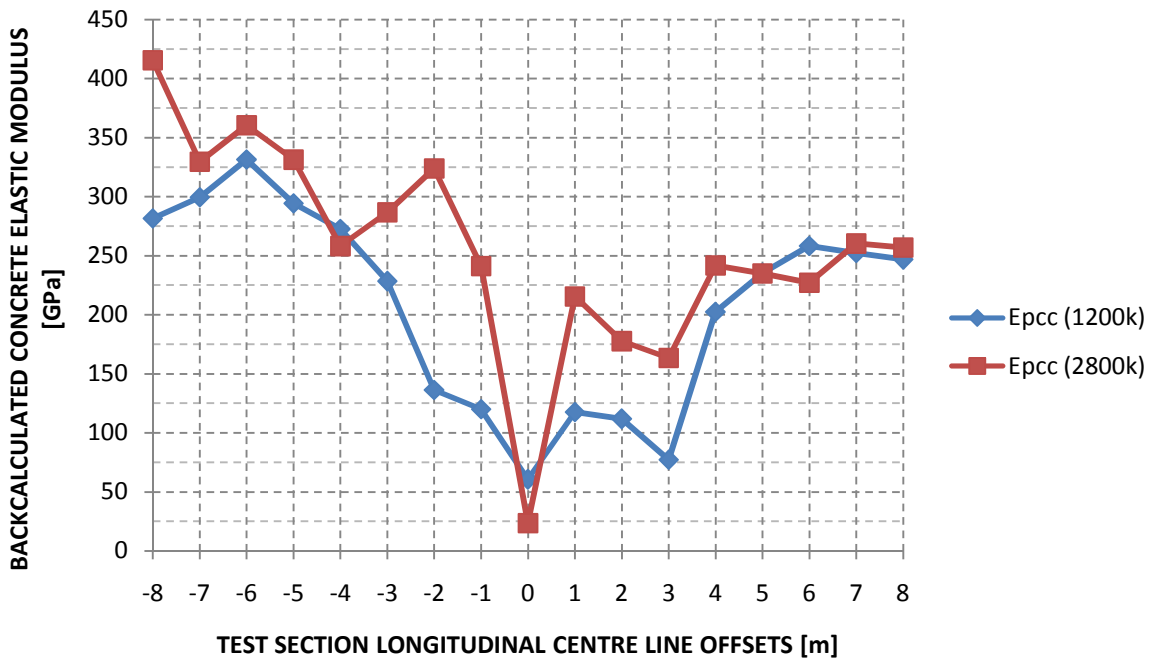
Figure C.29 Backcalculated concrete elastic modulus for the ES-model (40 kN FWD deflection bowls)
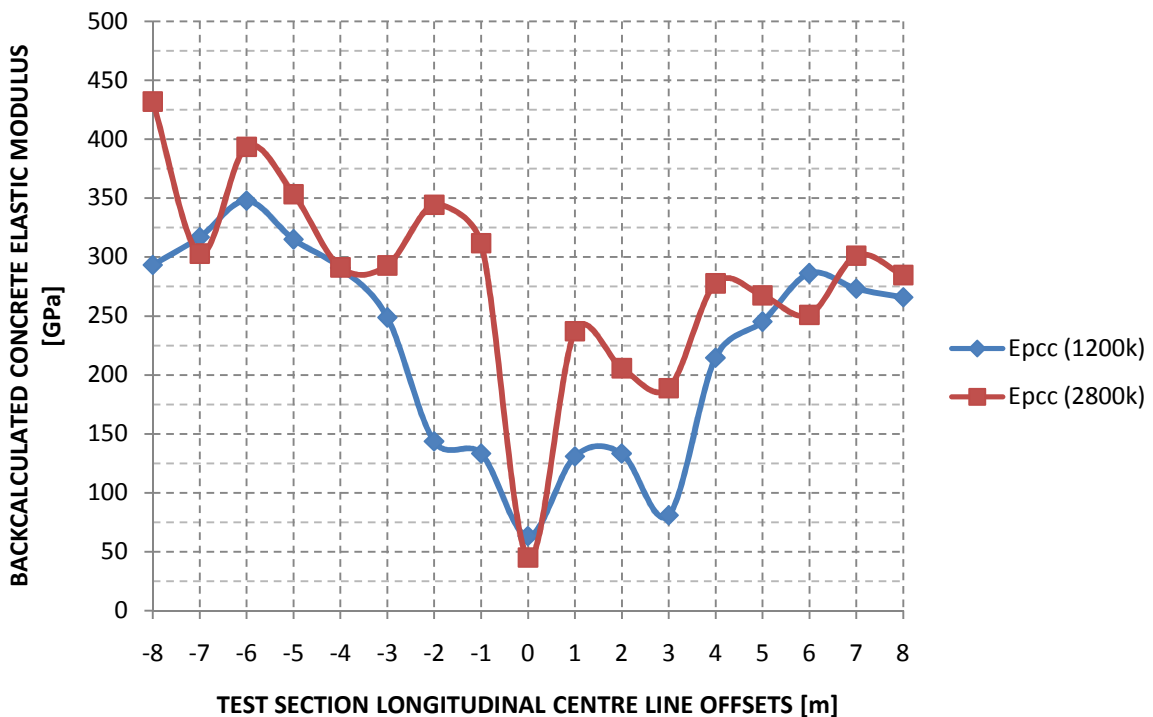
Figure C.30 Backcalculated concrete elastic modulus for the ES-model (60 kN FWD deflection bowls)
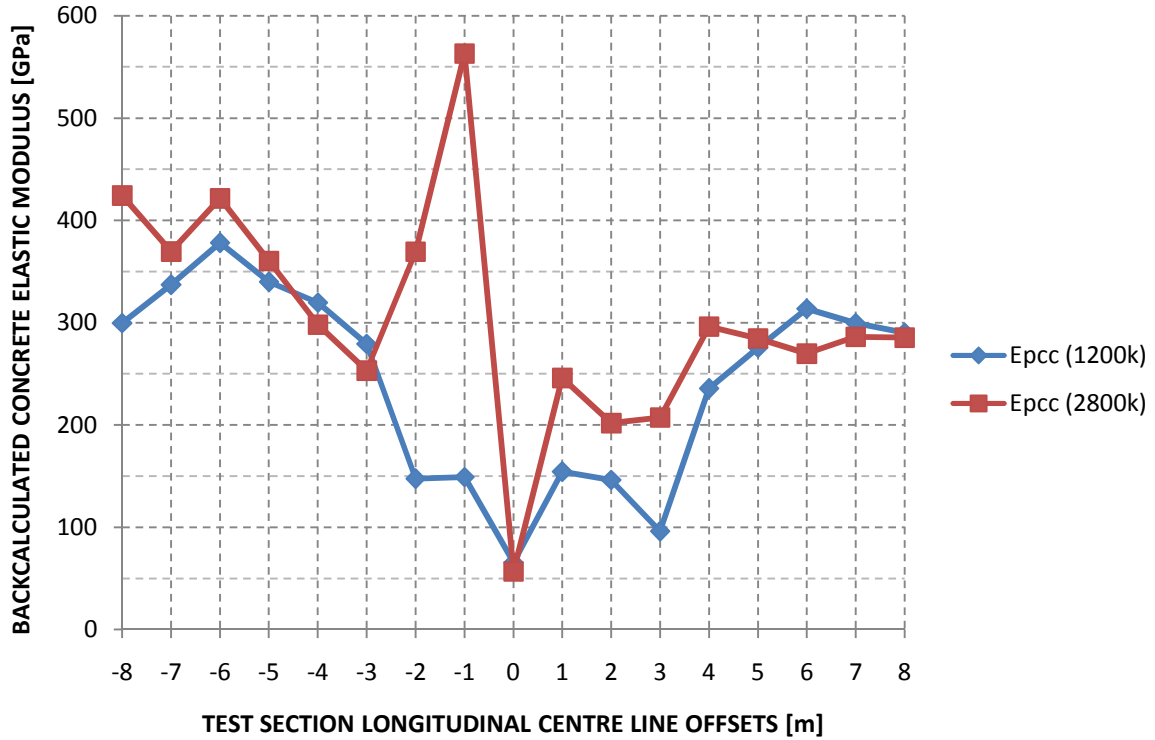
Figure C.31 Backcalculated concrete elastic modulus for the ES-model (80 kN FWD deflection bowls)
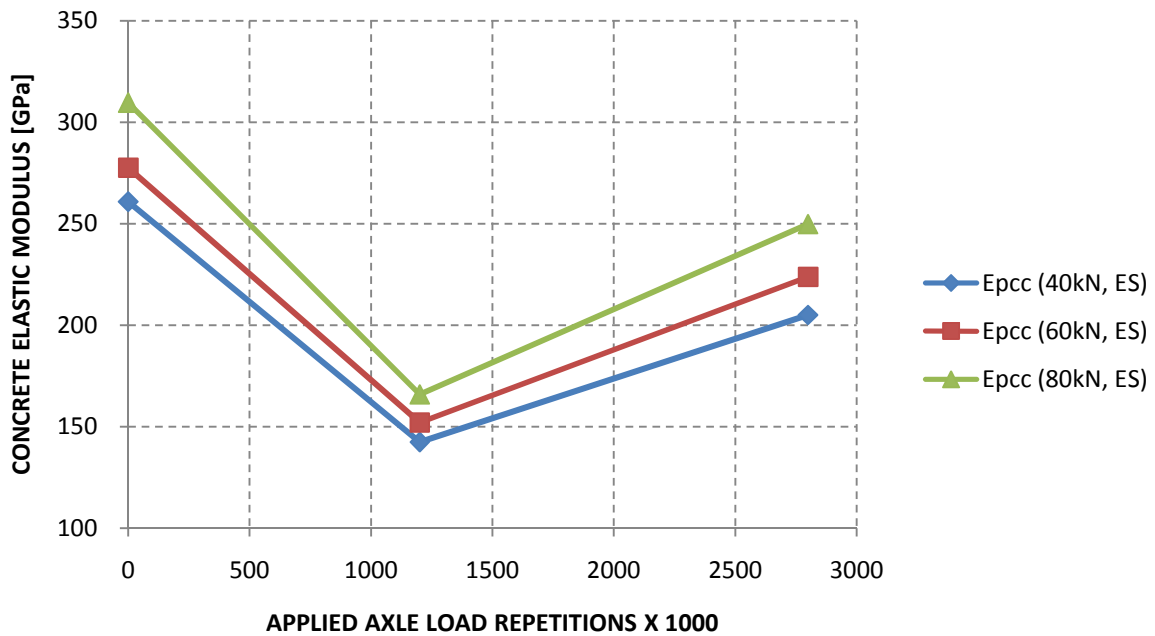
Figure C.32 Average backcalculated concrete elastic modulus for the DL-model at the indicated applied axle load repetition interval and specified FWD loading

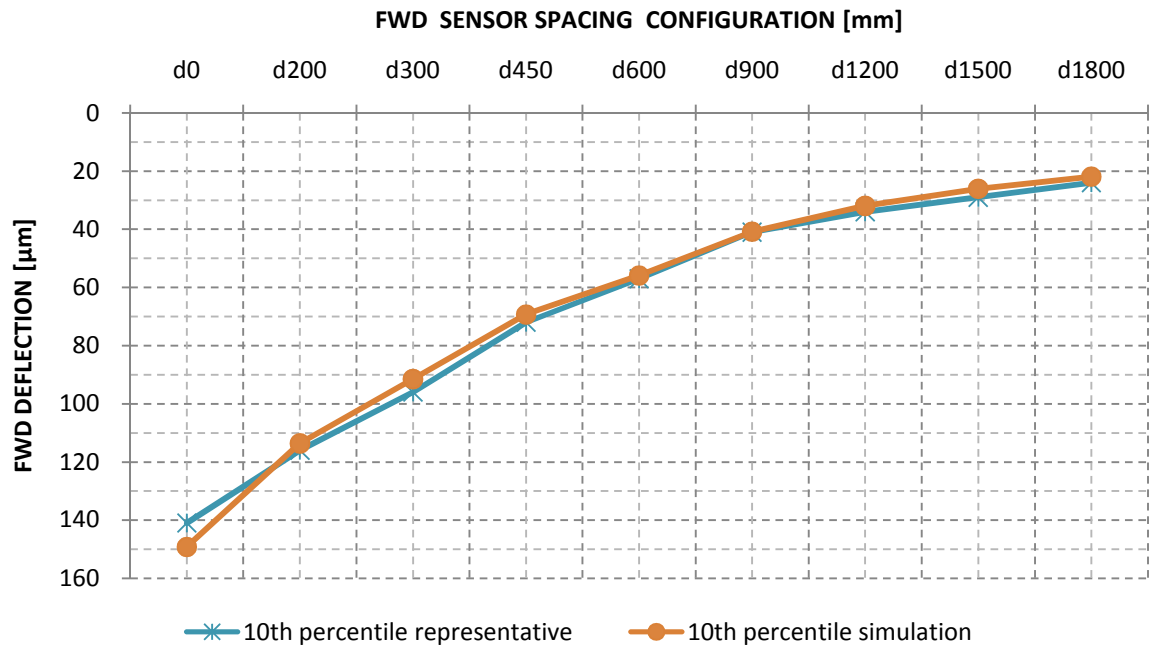## C.4 BISAR 3.0 Linear Elastic FWD Results

C.4.1 40 kN FWD simulated deflection profiles
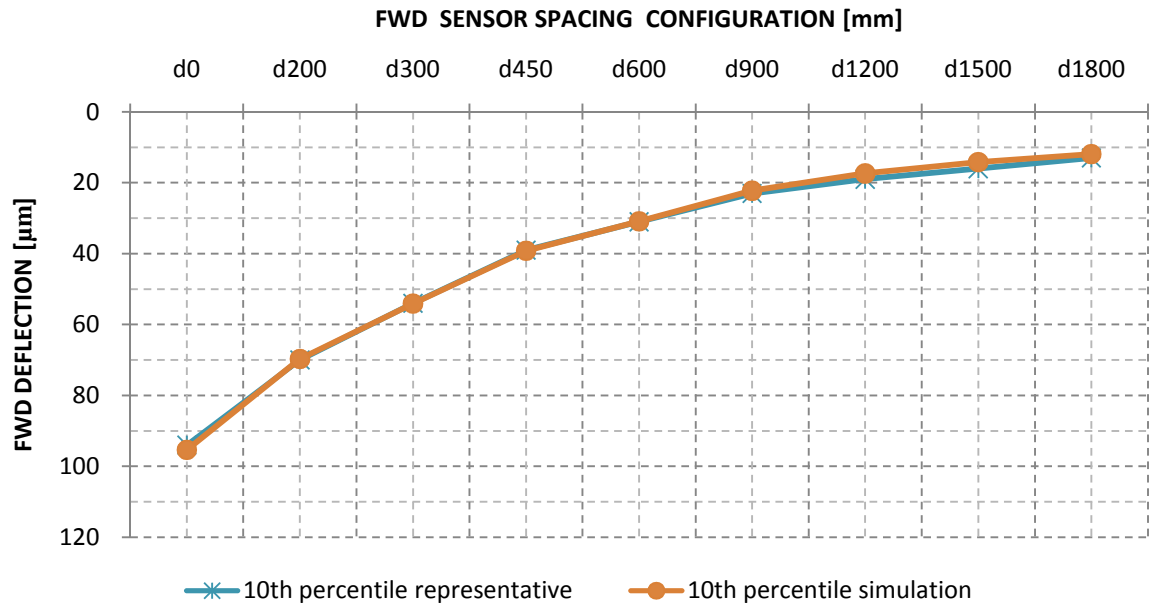
Figure C.33 Simulated FWD deflection profile versus the measured 10th percentile FWD profile for a 40 kN deflection bowl at 0k applied axle load repetition
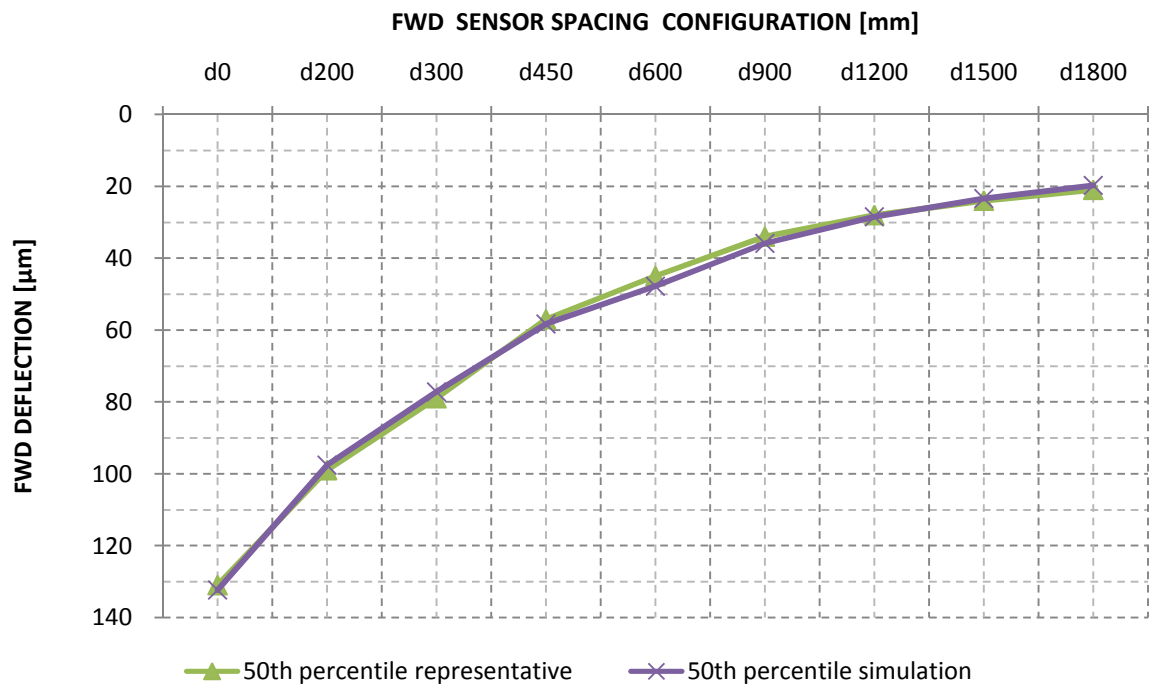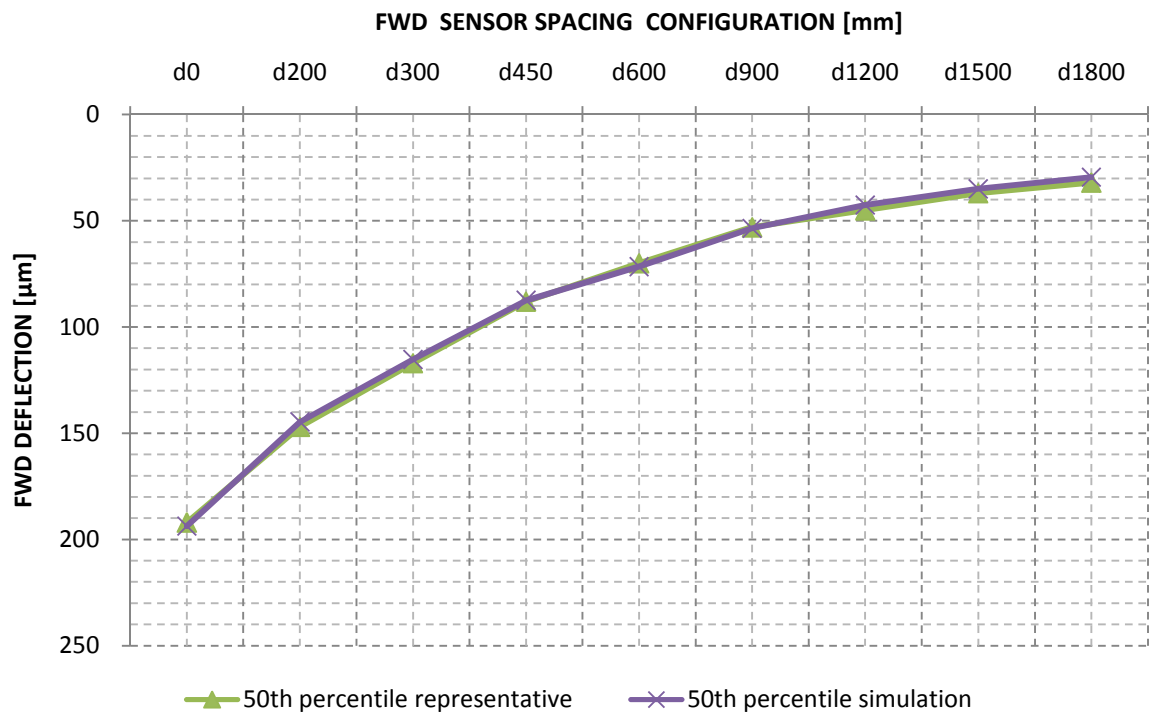

Figure C.34 Simulated FWD deflection profile versus the measured 50th percentile FWD profile for a 40 kN deflection bowl at 0k applied axle load repetition
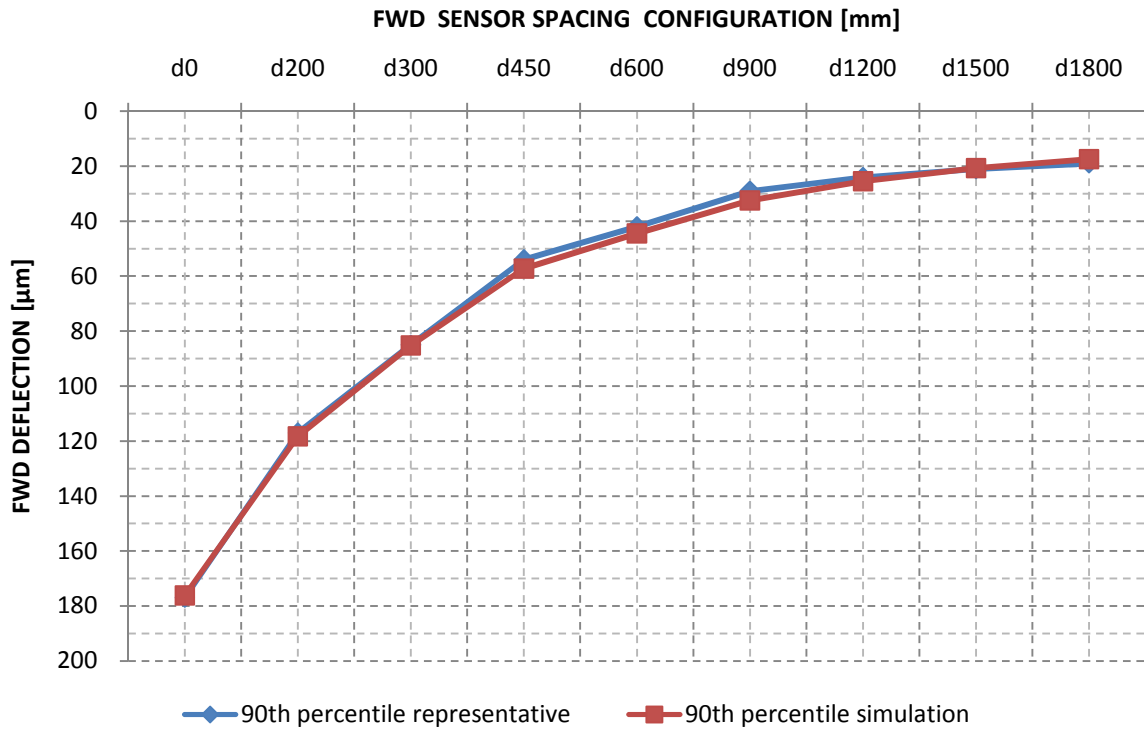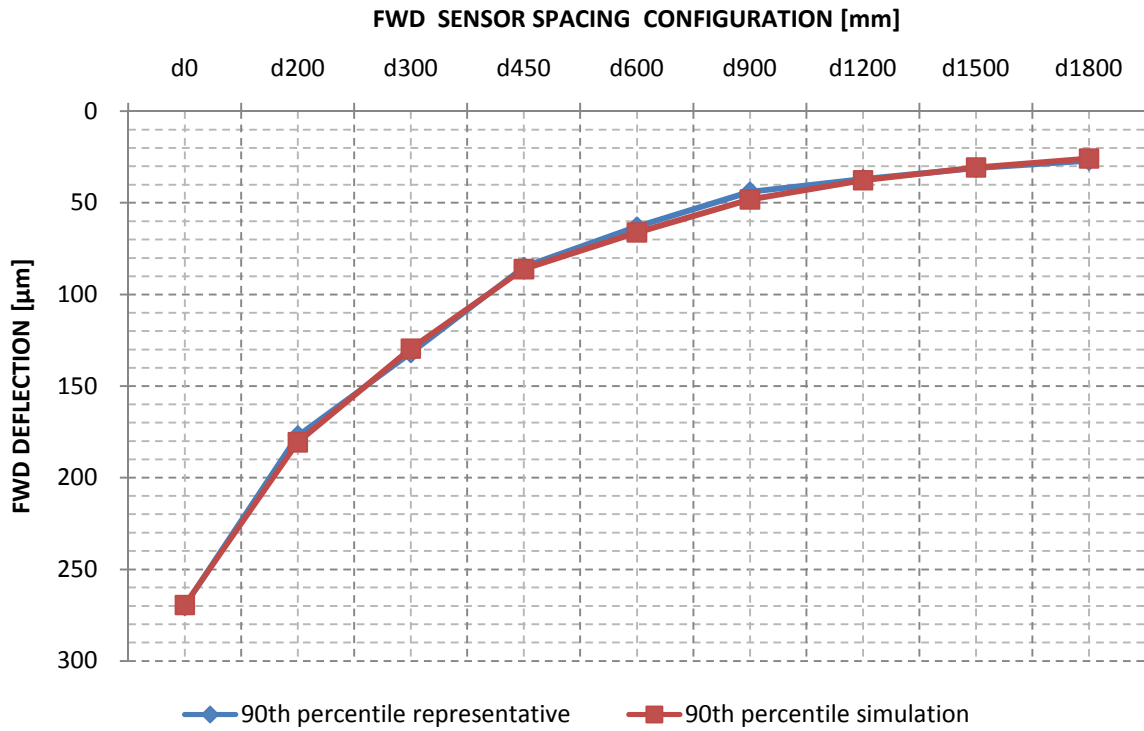
Figure C.35 Simulated FWD deflection profile versus the measured 90th percentile FWD profile for a 40 kN deflection bowl at 0k applied axle load repetition
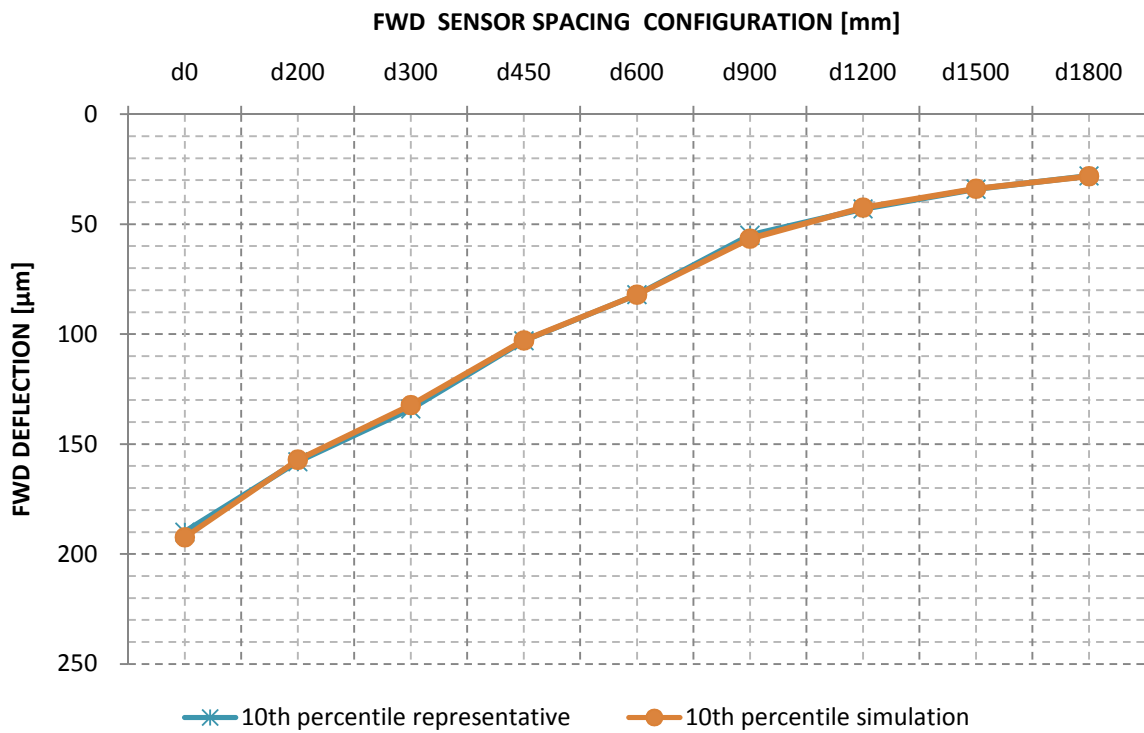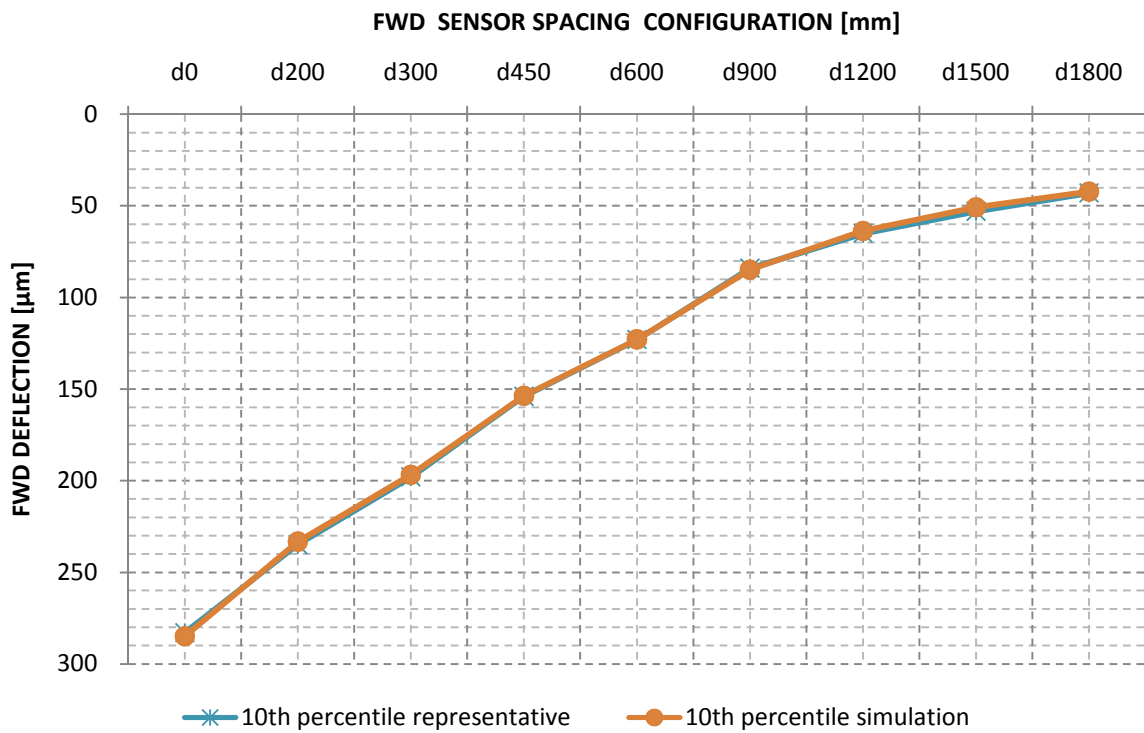

Figure C.36 Simulated FWD deflection profile versus the measured 10th percentile FWD profile for a 40 kN deflection bowl at 1200k applied axle load repetition

Figure C.37 Simulated FWD deflection profile versus the measured 50th percentile FWD profile for a 40 kN deflection bowl at 1200k applied axle load repetition
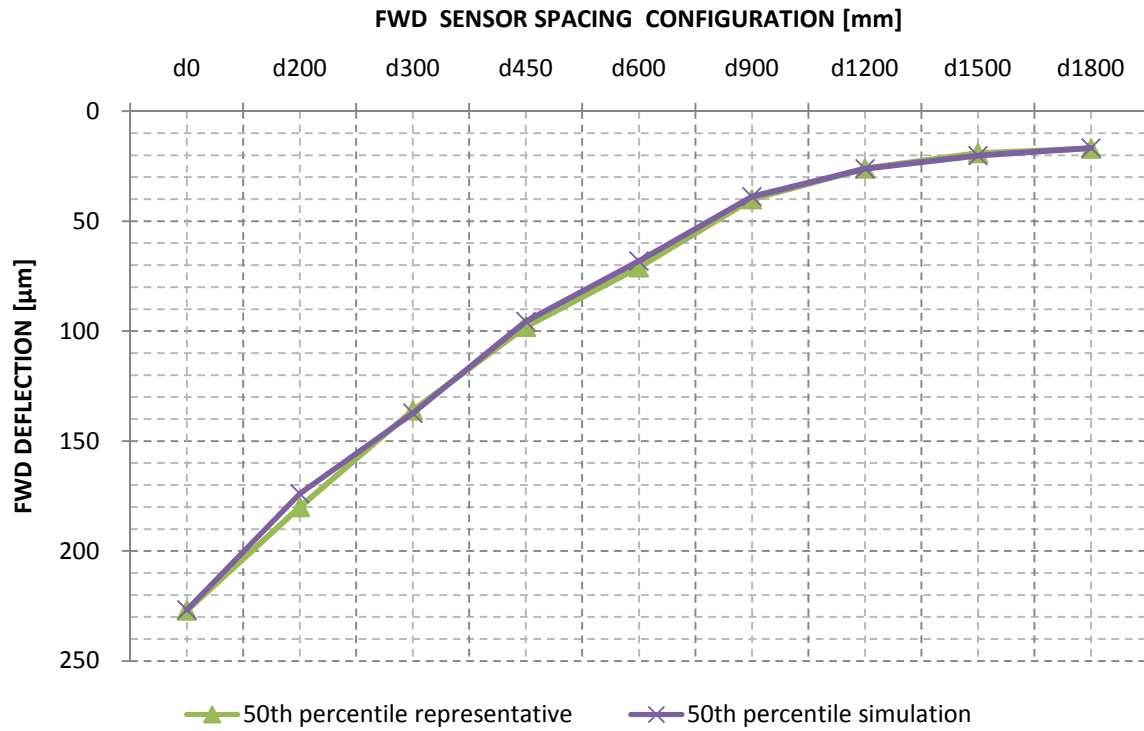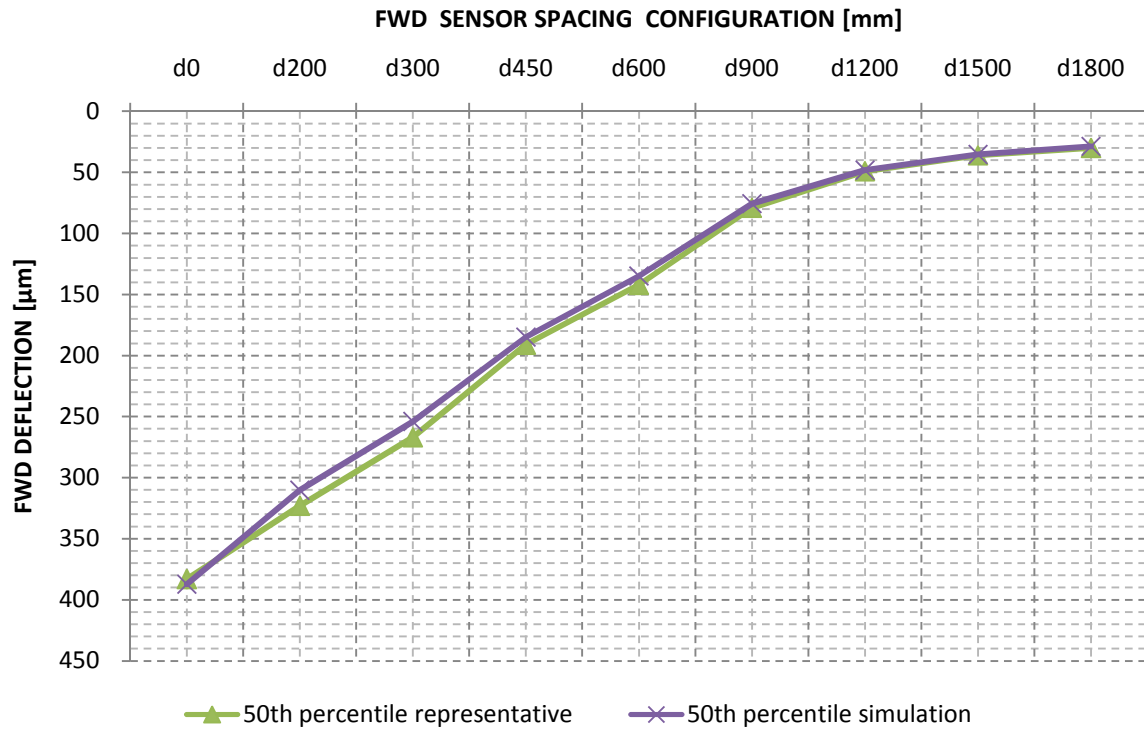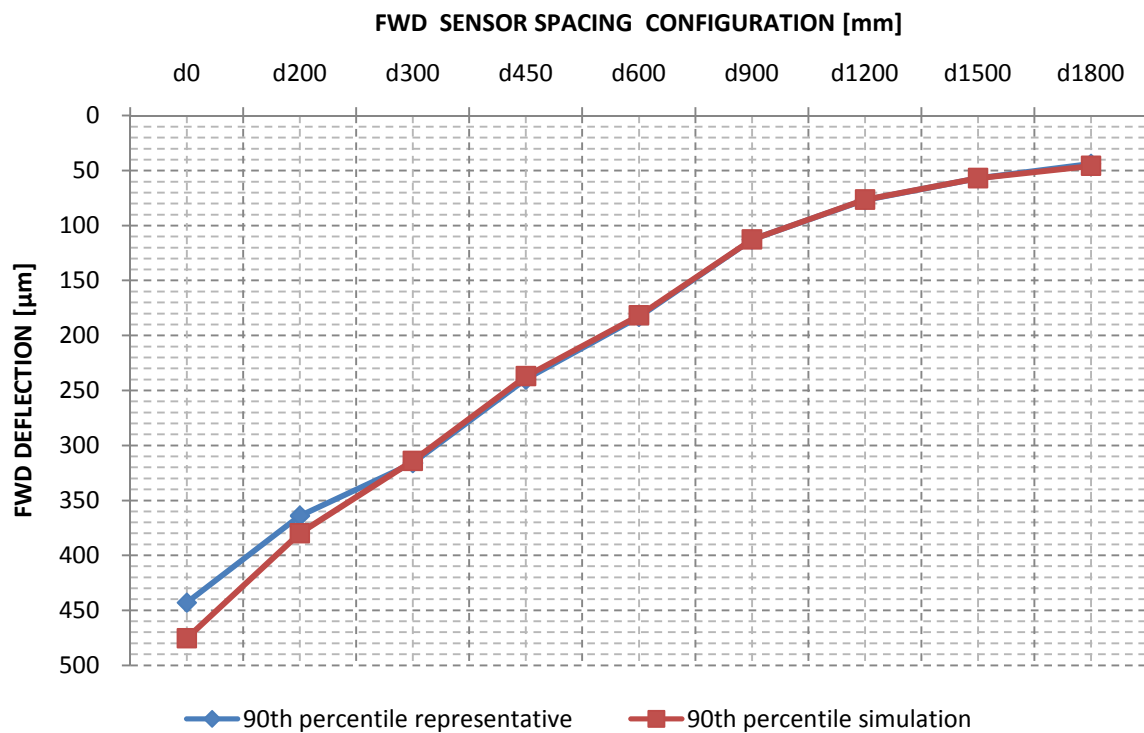
Figure C.37 Simulated FWD deflection profile versus the measured 50th percentile FWD profile for a 40 kN deflection bowl at 1200k applied axle load repetition
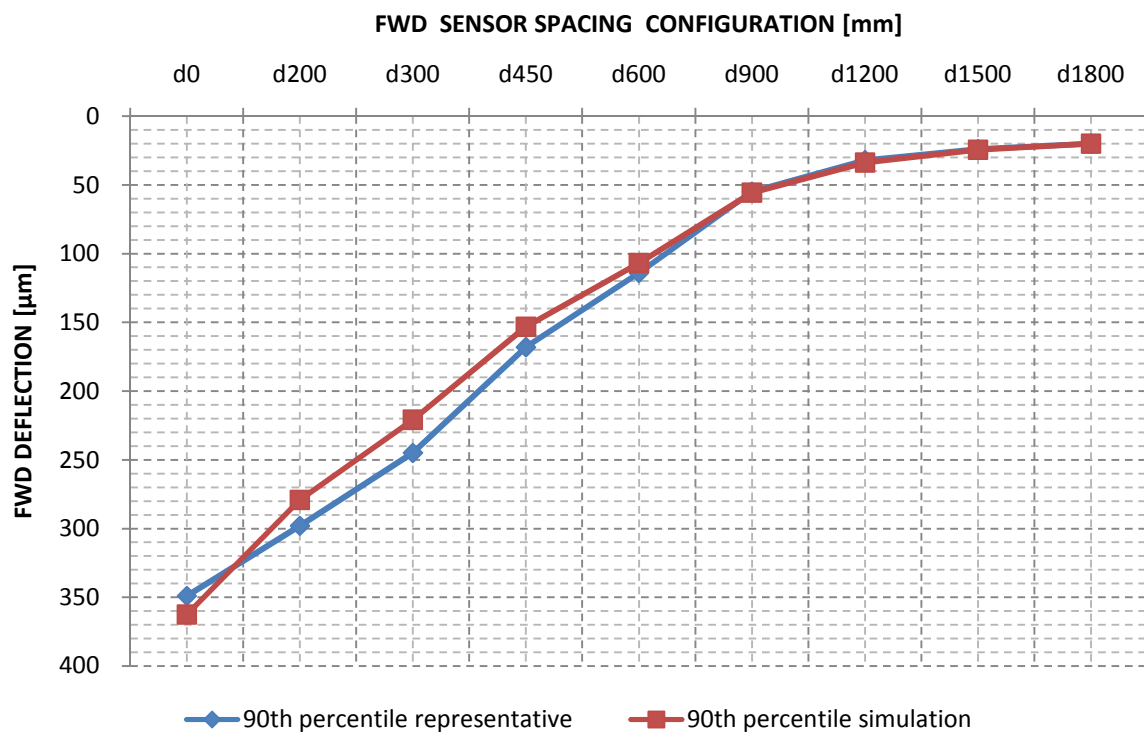
Figure C.38 Simulated FWD deflection profile versus the measured 90th percentile FWD profile for a 40 kN deflection bowl at 1200k applied axle load repetition
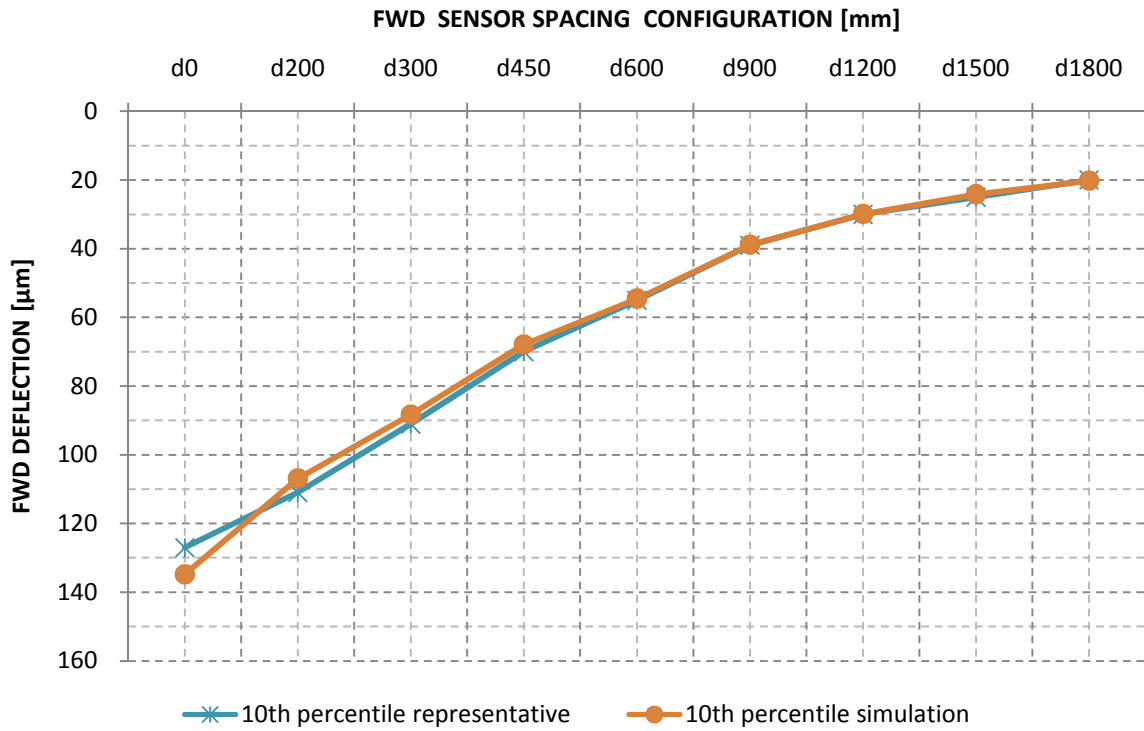
Figure C.39 Simulated FWD deflection profile versus the measured 10th percentile FWD profile for a 40 kN deflection bowl at 2800k applied axle load repetition
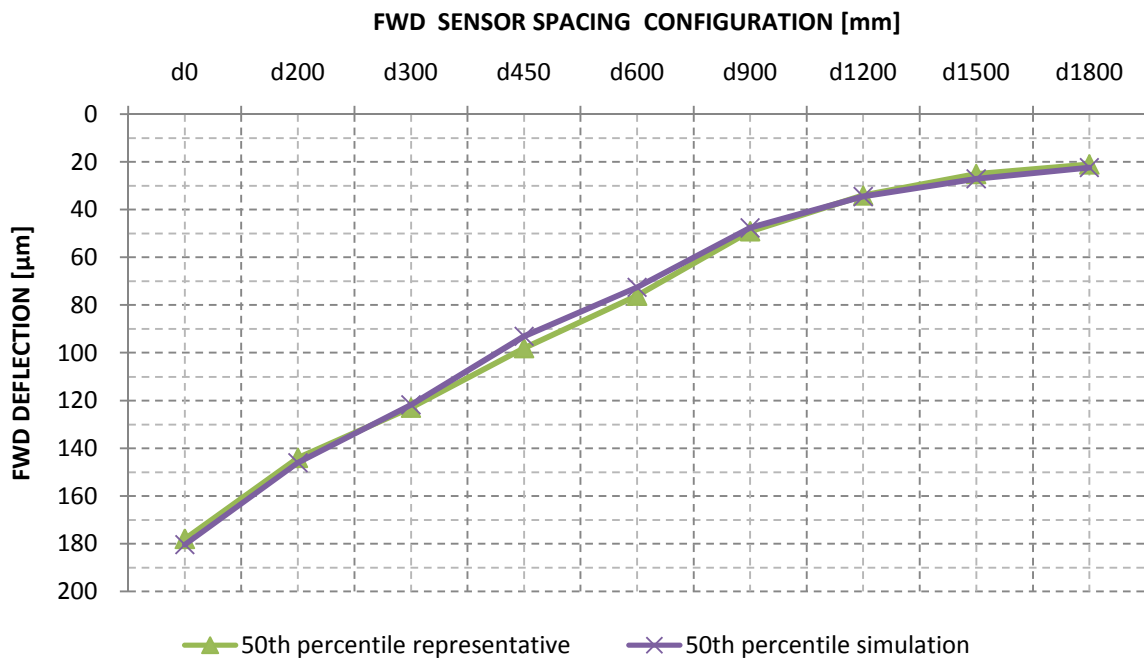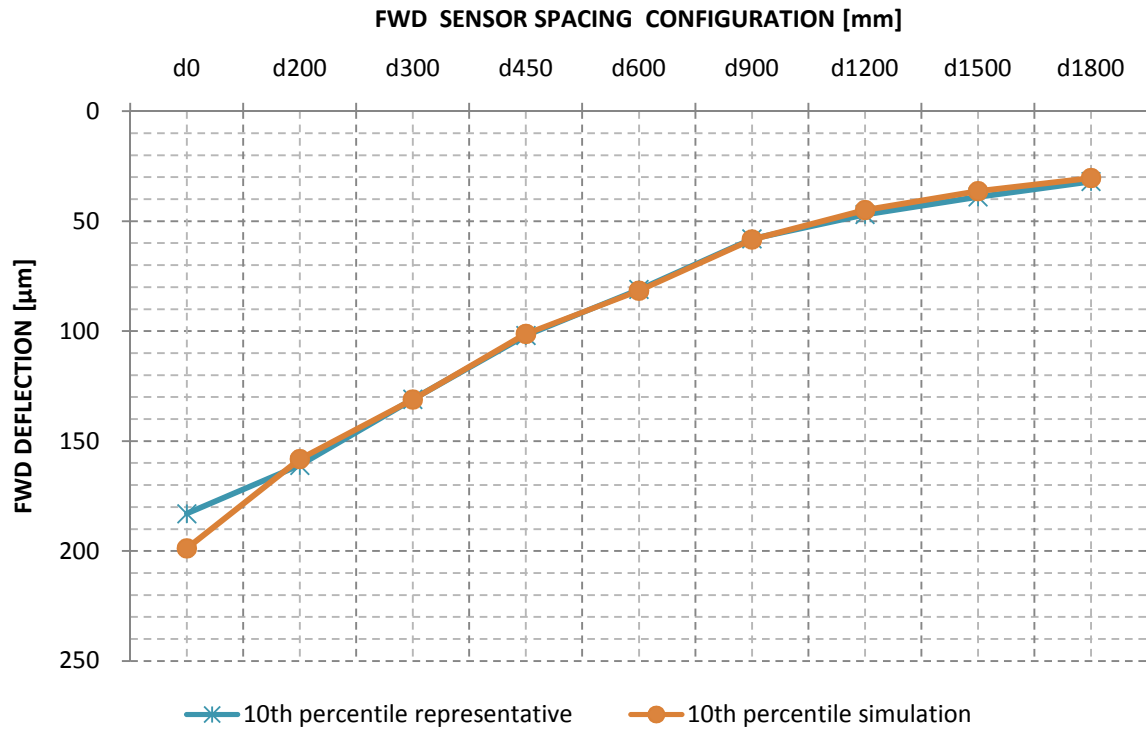

Figure C.40 Simulated FWD deflection profile versus the measured 50th percentile FWD profile for a 40 kN deflection bowl at 2800k applied axle load repetition

C.4.2 60kN FWD simulated deflection profiles

Figure C.41 Simulated FWD deflection profile versus the measured 10th percentile FWD profile for a 60 kN deflection bowl at 0k applied axle load repetition
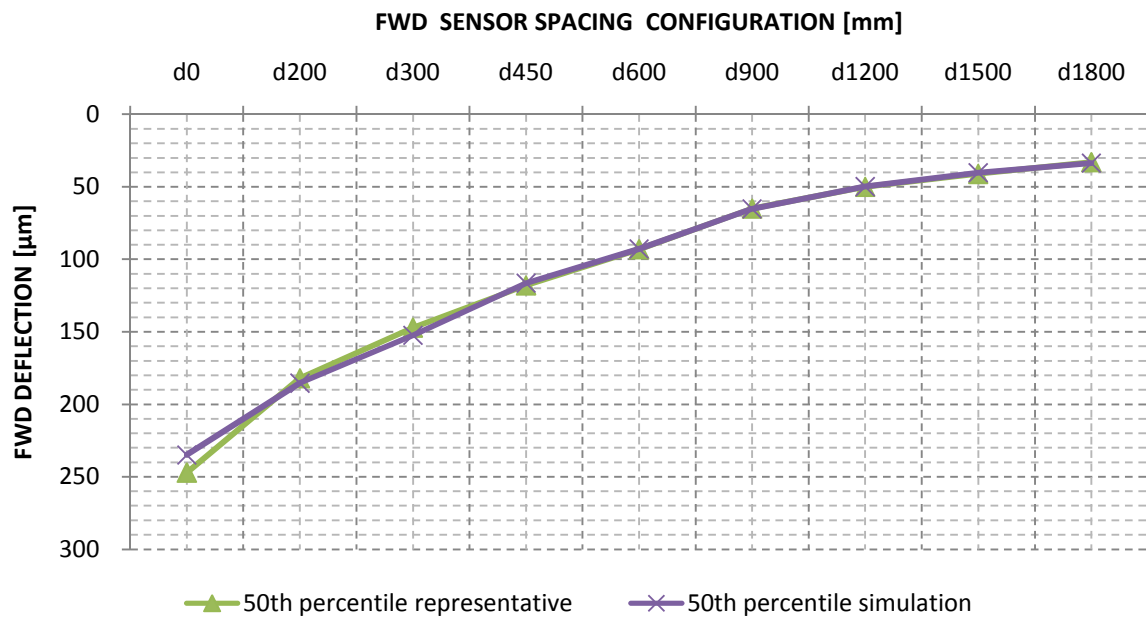

Figure C.42 Simulated FWD deflection profile versus the measured 50th percentile FWD profile for a 60 kN deflection bowl at 0k applied axle load repetition

Figure C.43 Simulated FWD deflection profile versus the measured 90th percentile FWD profile for a 60 kN deflection bowl at 0k applied axle load repetition
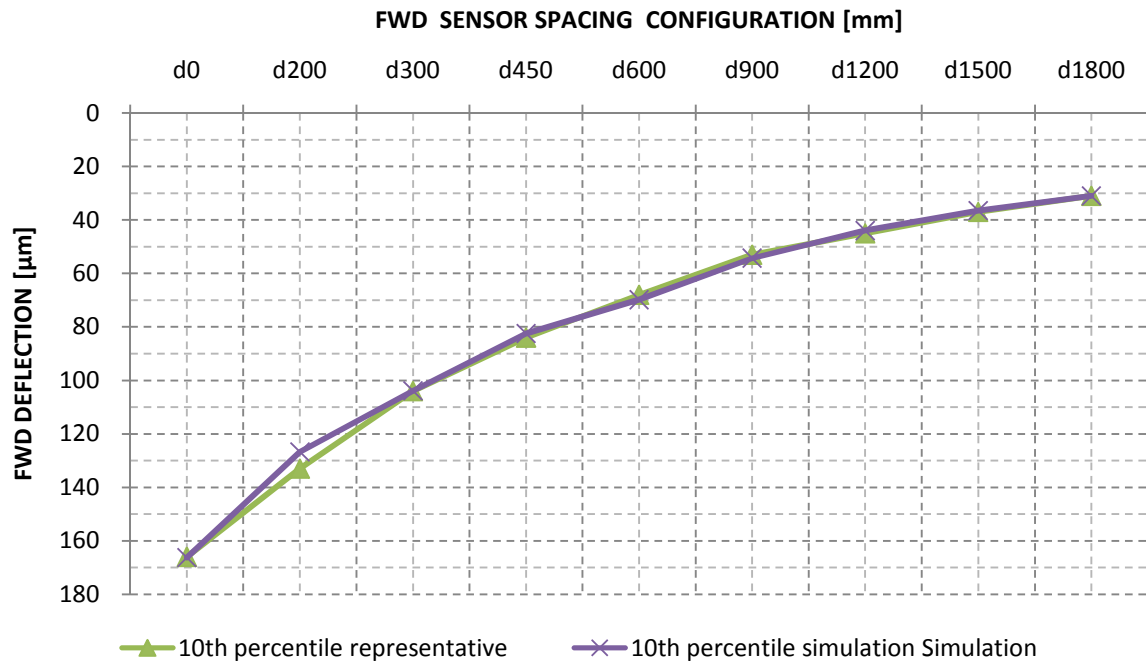

Figure C.44 Simulated FWD deflection profile versus the measured 10th percentile FWD profile for a 60 kN deflection bowl at 1200k applied axle load repetition
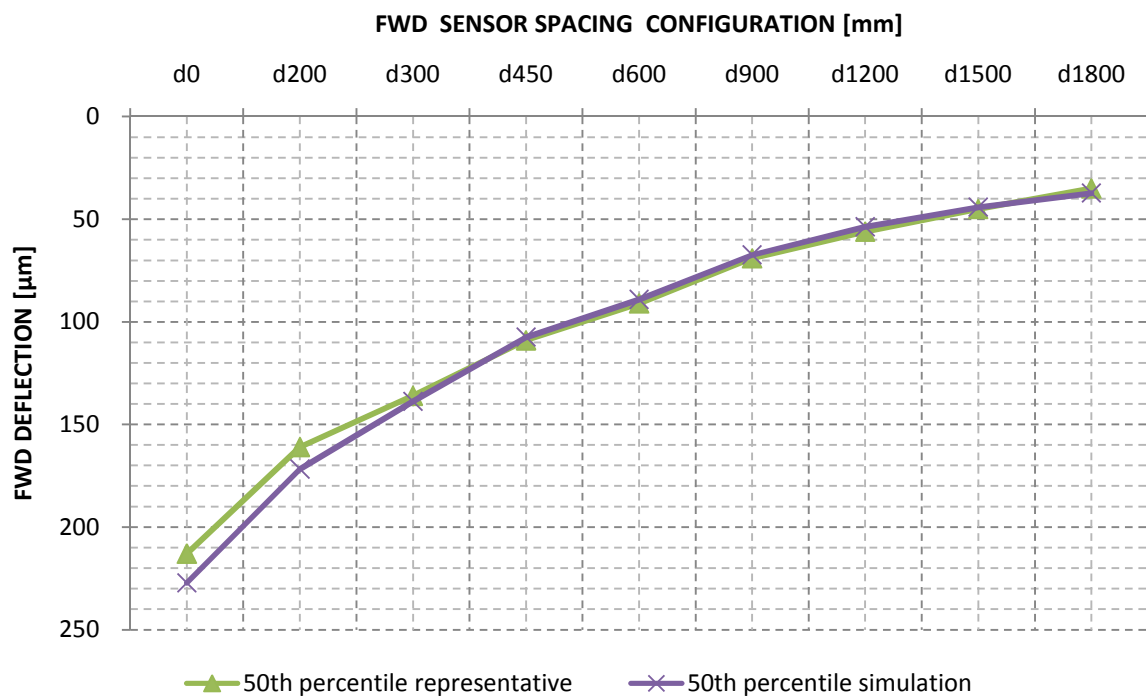
Figure C.45 Simulated FWD deflection profile versus the measured 50th percentile FWD profile for a 60 kN deflection bowl at 1200k applied axle load repetition

Figure C.46 Simulated FWD deflection profile versus the measured 90th percentile FWD profile for a 60 kN deflection bowl at 1200k applied axle load repetition

Figure C.47 Simulated FWD deflection profile versus the measured 10th percentile FWD profile for a 60 kN deflection bowl at 2800k applied axle load repetition

Figure C.48 Simulated FWD deflection profile versus the measured 50th percentile FWD profile for a 60 kN deflection bowl at 2800k applied axle load repetition
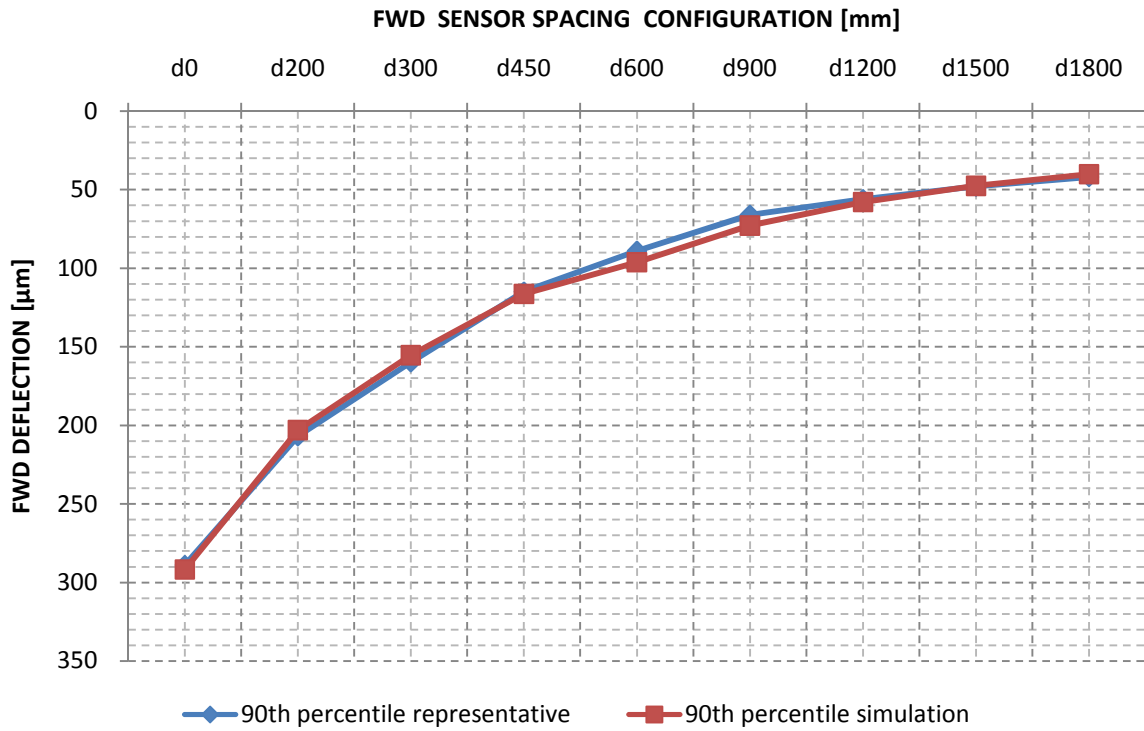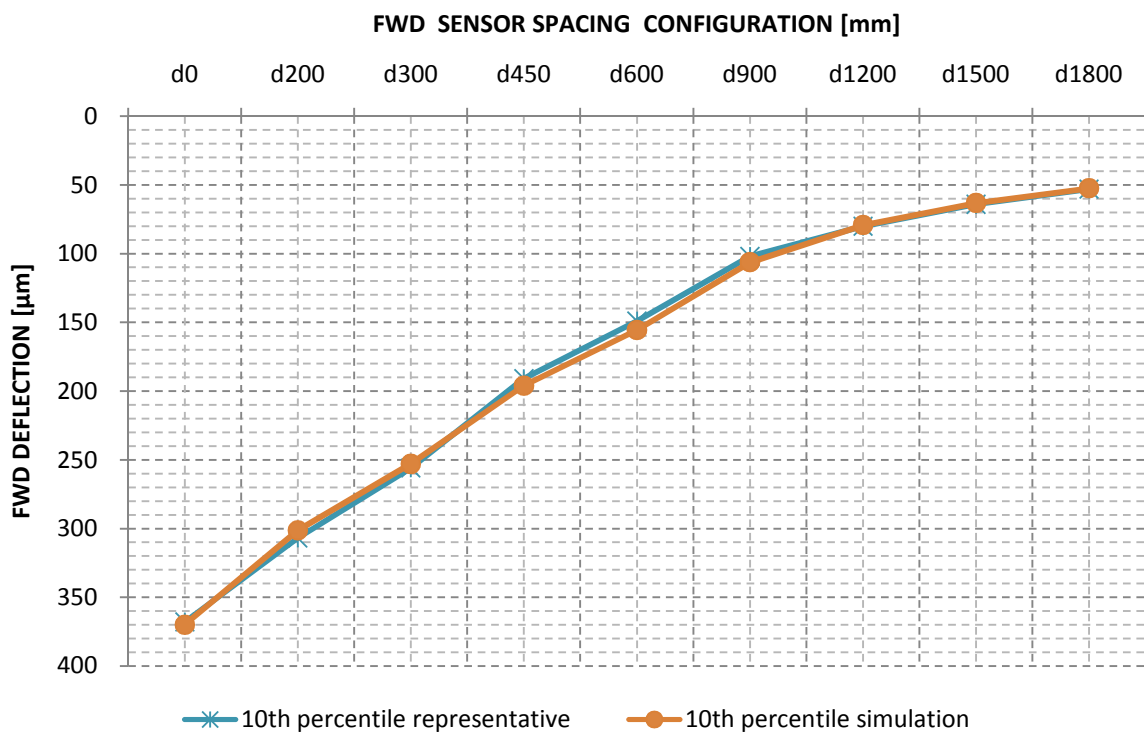
C.4.3 80kN FWD simulated deflection profiles

Figure C.49 Simulated FWD deflection profile versus the measured 10th percentile FWD profile for an 80 kN deflection bowl at 0k applied axle load repetition

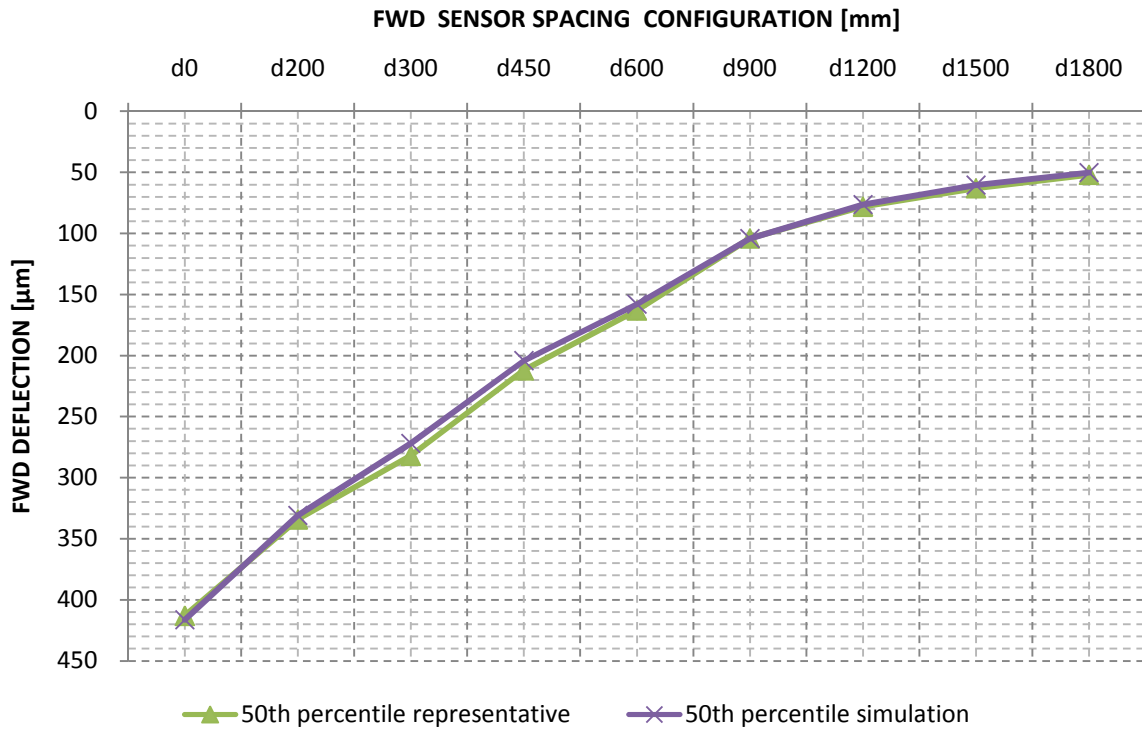**Figure C.50 Simulated FWD deflection profile versus the measured 50th percentile FWD profile for an 80 kN deflection bowl at 0k applied axle load repetition**

Figure C.51 Simulated FWD deflection profile versus the measured 90th percentile FWD profile for an 80 kN deflection bowl at 0k applied axle load repetition

Figure C.52 Simulated FWD deflection profile versus the measured 10th percentile FWD profile for an 80 kN deflection bowl at 1200k applied axle load repetition
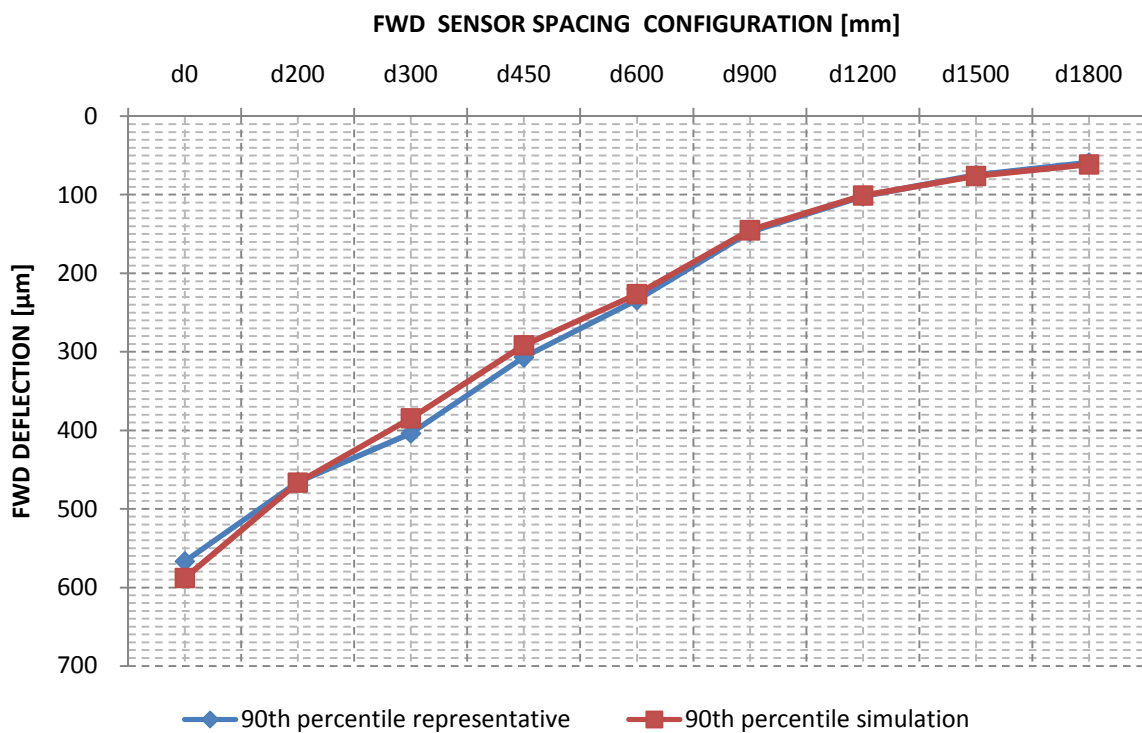
FWD SENSOR SPACING CONFIGURATION [mm]

Figure C.53 Simulated FWD deflection profile versus the measured 50th percentile FWD profile for an 80 kN deflection bowl at 1200k applied axle load repetition
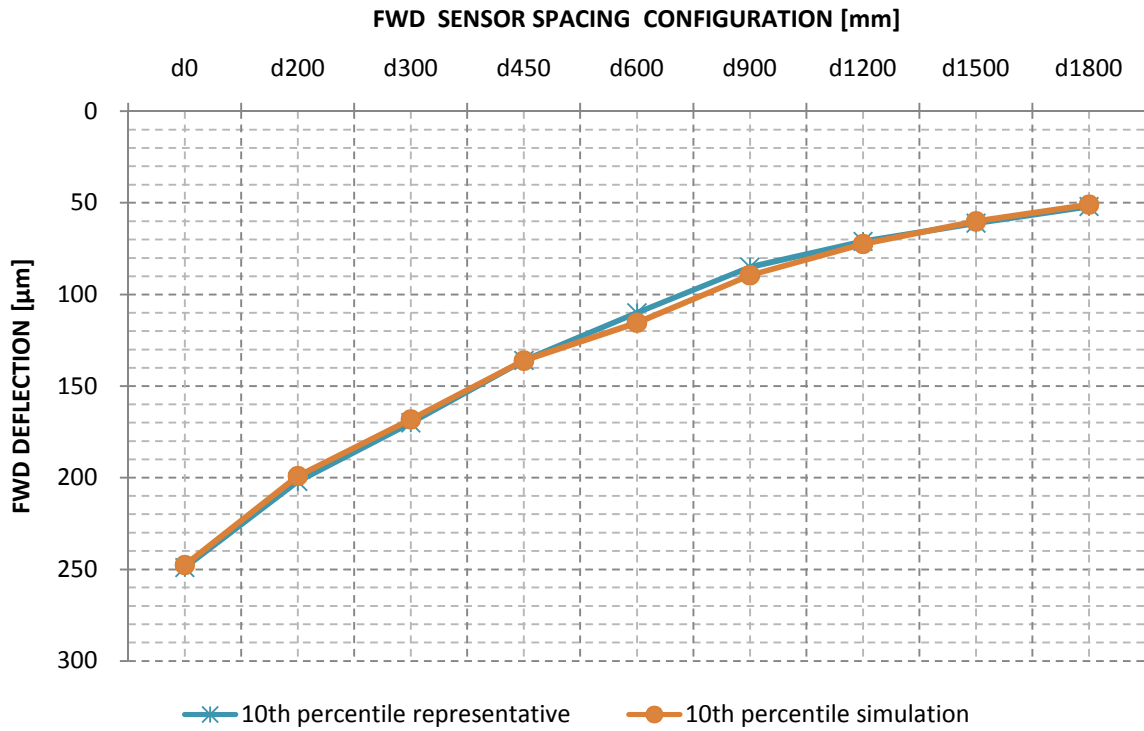
FWD SENSOR SPACING CONFIGURATION [mm]

Figure C.54 Simulated FWD deflection profile versus the measured 90th percentile FWD profile for an 80 kN deflection bowl at 1200k applied axle load repetition

Figure C.55 Simulated FWD deflection profile versus the measured 10th percentile FWD profile for an 80 kN deflection bowl at 2800k applied axle load repetition
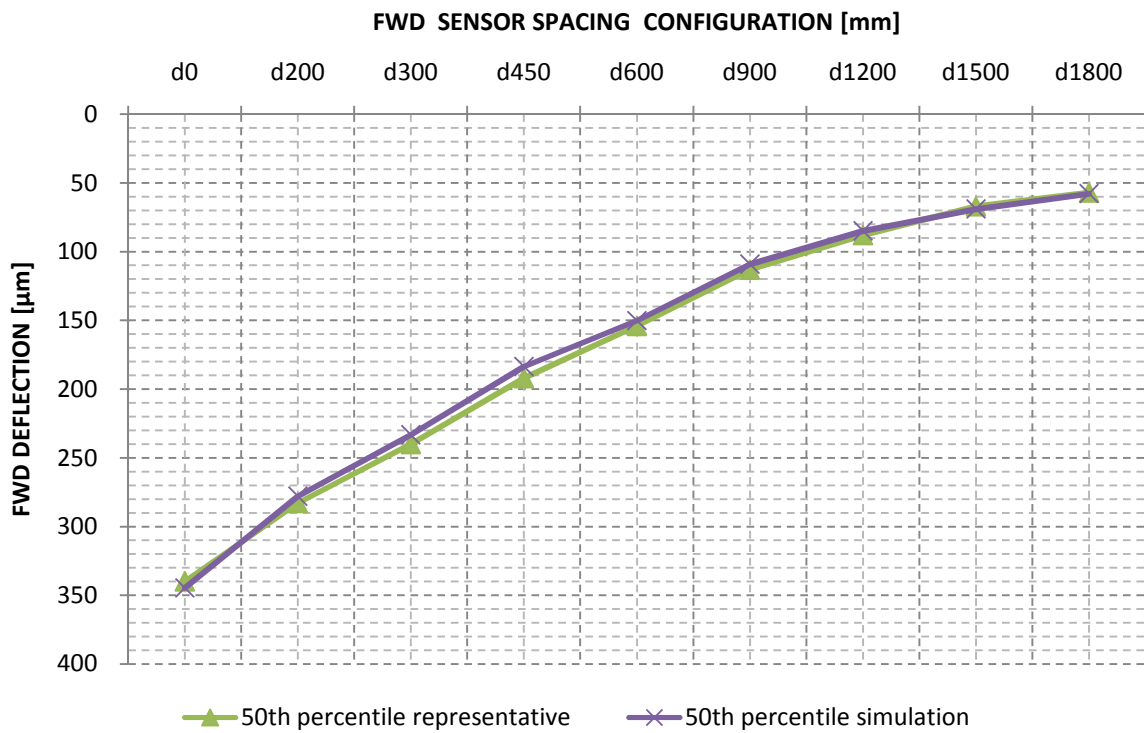

Figure C.56 Simulated FWD deflection profile versus the measured 50th percentile FWD profile for an 80 kN deflection bowl at 2800k applied axle load repetition
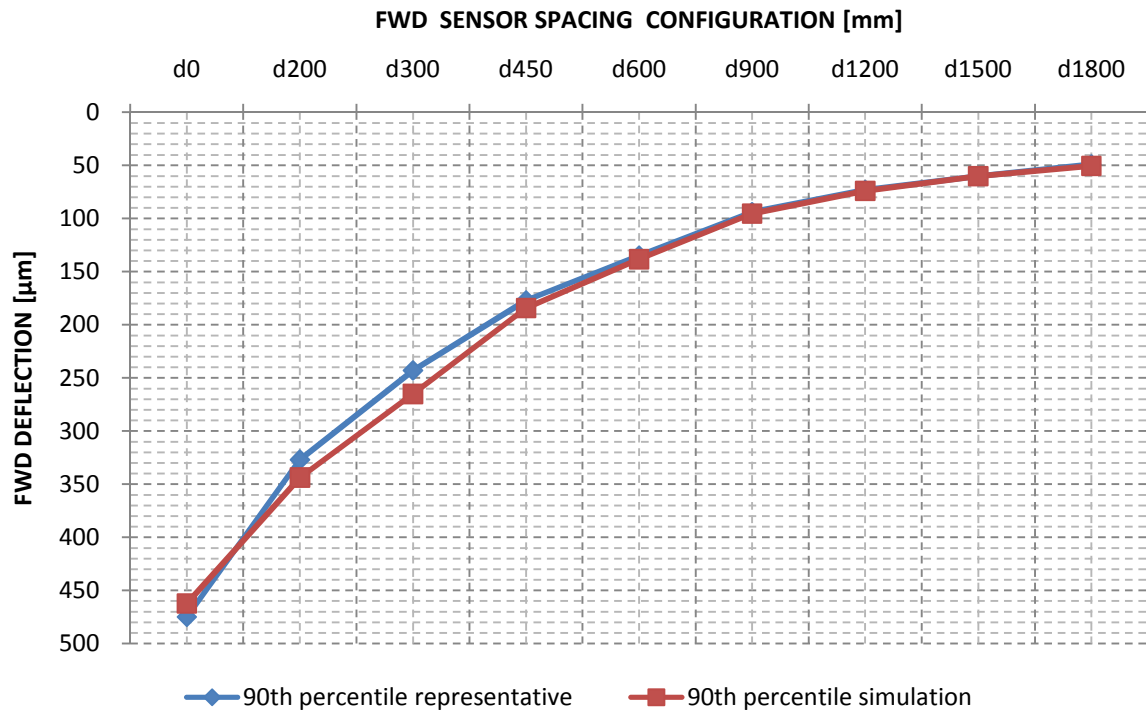
Figure C.57 Simulated FWD deflection profile versus the measured 90th percentile FWD profile for an 80 kN deflection bowl at 2800k applied axle load repetition